Investigation on Electromagnetic Performance of Doubly Salient Synchronous Reluctance Machines

Xi-Yun Ma

A thesis submitted for the degree of Doctor of Philosophy

Department of Electronic and Electrical Engineering

The University of Sheffield, UK

June 2018

Acknowledgements

Firstly, I would like to express my greatest and sincerest gratitude to my supervisor Dr. Guang-Jin Li for his guidance, supervision, motivation, encouragement and continuous support during the whole Ph.D study. I deeply appreciate his insightful comments, valuable suggestions through weekly meetings, critical proof reading of weekly reports and this thesis, as well as all the publications resulting from this work. Under his professional guidance, I have learned and improved a lot. I could not have imagined having a better supervisor and mentor for my Ph.D study.

Besides my first supervisor, I would like to thank Prof. Geraint Jewell, and Prof. Zi-Qiang Zhu for their guidance, instructive advice and support of this thesis, as well as proof reading of the publications from this work.

Also, I am grateful to my colleagues of the EMD research group: Mr. John Wilkinson, and Mr. Richard Garraway for their technical assistance of building the prototypes. In addition, thanks are due to Dr. Han-Lin Zhan, Dr. Pei-Lin Xu, Dr. Yang Guan, Dr. Yan-Jian Zhou and Dr. Yan-Xin Li, for technical discussions and experimental assistance.

Last but not the least, I deeply appreciate the constant and spiritual support of my parents throughout my years of study and the life in general. Also, a special gratitude goes to my boyfriend, Dr. Bo Ren for his encouragement and support.

Xi-Yun Ma

University of Sheffield, UK

June 2018

Abstract

This thesis investigates the electromagnetic performance of the novel doubly salient synchronous reluctance machines (DSRMs) with different winding configurations, excitation methods, stator and rotor structures, and slot/pole number combinations. Both the well-established DSRMs with double layer conventional and mutually-coupled windings, as well as the fully-pitched winding have been compared against those proposed DSRMs. Different current waveforms such as rectangular wave and sinewave excitations have been considered in the comparison. It is worth mentioning that with rectangular wave excitation, the DSRM is in effect a classic switched reluctance machine (SRM).

With rectangular wave excitation, different conduction angles such as unipolar 120° elec., unipolar/bipolar 180° elec., bipolar 240° elec., and bipolar 360° elec., have been adopted and the most appropriate conduction angles have been obtained for the SRMs with different winding configurations. In order to achieve improved machine performance, simpler manufacturing process and better fault tolerant capability, several novel modular SRMs have been proposed with different slot/pole number combinations, flux gap widths, and winding configurations. With appropriate conduction angles, the modular SRMs with higher rotor pole number than stator slot number are found to produce similar average torque, but much lower torque ripple, iron loss and radial force when compared with non-modular SRMs.

With sinewave excitation, both the static and dynamic performances (torque-speed curve, efficiency map, etc.) of the DSRMs with different winding configurations have been investigated in-depth. In order to obtain the maximum efficiency, appropriate winding configuration can be selected for different speed range applications. In order to compare with the conventional synchronous reluctance machines (SynRMs) having flux barriers inside the rotor, the appropriate rotor topologies together with different winding configurations and slot/pole number combinations for maximum average torque generation have been obtained. Moreover, for better understanding of the nature of the DSRMs and distinguishing the double/single layer conventional and mutually-coupled winding configurations, analytical models on the basis of magneto-motive force (MMF) and airgap permeance have been developed to analyse the contribution of airgap flux density harmonics to average torque and torque ripple. Furthermore, some prototypes have been built with different winding

configurations, stator structures (modular and non-modular) and slot/pole number combinations to validate the predictions.

List of Abbreviations

2D FEA	Two-dimensional finite element analysis
AC	Alternating current
AFB	Angled flux barrier
CSRM	Conventional switched reluctance machine
d-axis	Direct axis
DC	Direct current
DLC	Double layer conventional
DLMC	Double layer mutually-coupled
DSRM	Doubly salient synchronous reluctance machine
elec. deg.	Electrical degree
EV	Electrical vehicle
FG	Flux gap
FP	Fully-pitched
HEV	Hybrid electrical vehicle
MCSRM	Mutually-coupled switched reluctance machine
mech. deg.	Mechanical degree
MMF	Magneto-motive force
q-axis	Quadrature axis
RFB	Round flux barrier

SLC	Single layer conventional
SLMC	Single layer mutually-coupled
SRM	Switched reluctance machine
SynRM	Synchronous reluctance machine
UNET	Unequal tooth

Nomenclatures

h_s	Slot height	mm
θ_r	Rotor pole pitch	mech. deg.
θ_s	Stator pole pitch	mech. deg.
$\Lambda_{resultant}$	Resultant airgap permeance	mm^{-1}
B_{pp}	Peak to peak value of flux density	T
B_r	Radial flux density	T
B_t	Tangential flux density	T
F_r	Radial force on one stator pole	N
I_A, I_B, I_C	Magnitudes of phase currents	A
I_d, I_q	*d*- and *q*-axis currents	A
I_{max}	Maximum current	A
I_{ph}	Stator phase current	A
I_{pk}	Peak current	A
I_{rms}	RMS current	A
K_w	Ratio of rotor flux barrier width to rotor iron width	
L_a, L_b, L_c	Self-inductances of phases A, B, and C	mH
L_d, L_q	*d*- and *q*-axis inductances	H
MMF_a	Single-phase MMF	AT
MMF_{abc}	Three-phase MMF	AT

M_{ab}, M_{bc}, M_{ca}	Mutual-inductances between phases	mH
N_c	Number of turns per coil	
N_r	Rotor pole number	
N_s	Stator slot number	
P_{copper}	Copper loss	W
P_{iron}	Iron loss	W
P_{mech}	Mechanical loss	W
P_{out}	Output power	W
R_{ph}	Phase resistance	Ω
R_{ro}	Rotor outer radius	mm
R_{si}	Stator inner radius	mm
$T_{a\&b}$	Torque produced by phases A and B connected in series	Nm
T_a, T_b	Self-torques of phases A and B	Nm
T_{ab}	Mutual-torque produced by phases A and B	Nm
T_{av}	Average torque	Nm
T_{max}	Maximum instantaneous torque	Nm
T_{min}	Minimum instantaneous torque	Nm
T_{mutual}	Mutual-torque	Nm
T_{rc}	Contribution of i^{th} order harmonic to torque ripple	
T_{ripple}	Torque ripple	

T_{self}	Self-torque	Nm
V_{DC}	DC link voltage	V
V_a, V_b	Voltages of phases A and B	V
V_d, V_q	d- and q-axis voltages	V
V_{max}	Maximum voltage	V
V_{ph}	Phase voltage	V
W'	Co-energy	J
W_s	Average stator slot width	mm
W_t	Stator tooth width	mm
i_a, i_b, i_c	Instantaneous phase currents	A
k_{h1}, k_{h2}	Hysteresis loss coefficients	A/m, Am/Vs
k_e	Eddy current loss coefficient	Am/V
l_g	Airgap length	mm
p_{iron}	Iron loss density	W/m^3
β_r	Rotor slot opening coefficient	
β_s	Stator slot opening coefficient	
δ_r	Additional airgap due to rotor slotting effect	mm
δ_s	Additional airgap due to stator slotting effect	mm
μ_0	Free space permeability	H/m
ψ_A, ψ_B, ψ_C	Flux linkages of phases A, B and C	Wb-turn

ψ_d, ψ_q	d- and q-axis flux linkages	Wb-turn
ΔT_{result}	Difference between the maximum and minimum resultant torques	Nm
H	Strength of magnetizing field	A/m
r	Airgap radius	mm
α	Phase advanced angle	elec. deg.
γ	Stator slot opening	mech. deg.
η	Machine efficiency	
Λ	Airgap permeance	mm^{-1}
μ	Radial displacement	μm
σ	Mechanical stress	MPa
φ	Angle between initial rotor position and rotor aligned position	mech. deg.
Ω	Mechanical rotor speed	r/min
ω	Rotation speed	Rad/s
L	Active length	mm
T	Instantaneous torque	Nm
i	Instantaneous phase current	A
m	Number of phases	
p	Pole pair number	
θ	Rotor position	mech. deg.

ϕ	Phase angle between phase current and voltage	elec. deg.

CONTENTS

Chapter 1. INTRODUCTION

This chapter starts with the research background of this thesis and an overview of switched reluctance machines (SRMs), followed by a summary of literature review which includes both the SRMs (different topologies and current supply modes) and also the synchronous reluctance machines (SynRMs). The SRMs, with both internal and external rotor structures, have been introduced in terms of winding configurations, slot/pole number combinations, multiphase structures and also modular structures. In addition, the current supply modes, particularly the sinewave current supply, have been introduced in detail, and compared with that adopted to the SynRMs. Moreover, the SynRMs have been reviewed that cover different shapes of flux barriers inside the rotor core, number of flux barrier layers, slot/pole number combinations and also winding configurations. Furthermore, the research scope and contributions of this thesis have been given at the end of this chapter.

1.1 BACKGROUND AND OVERVIEW

The first record of switch reluctance machine (SRM), Davidson's Locomotive, can be traced back to 1842 [1]. Different from other electrical machines, the torque of the SRMs is solely produced by the tendency of the rotor to move to its aligned position where the inductance of the stator winding is maximum [2] [3]. The reluctance torque is produced in the SRMs due to their doubly salient structure (both the stator and rotor have salient poles) [2] [4]. In terms of mechanical construction and even simply from the perspective of appearance, the SRMs are attractive since they have only stator winding and there are neither permanent magnets nor field windings on the rotor [5]. As a result, the SRMs have simple and robust rotor structure and can be low cost as well when compared with other counterparts such as induction machines and permanent magnet machines. Consequently, the SRMs are suitable for harsh environment and safety-critical applications [3], [6]. Nowadays, the SRMs are predominately used in a variety of applications ranging from automotive, renewable energy, aerospace and domestic appliances sectors [3] [2] [4] [6] [7] [8].

Despite these and other attractive features, the SRMs have arguably yet to gain the foothold in the market that one might have expected. One important limiting factor for conventional SRMs is that the power converter stage is nonconventional. In addition, the SRMs tend to exhibit high levels of vibration and acoustic noise when compared with permanent magnet machines and induction machines due to doubly salient structure and unipolar phase current waveforms [9] [10] [11] [12] [13]. This has to some extent, limited their wider industrial applications. It is well-established that the main source of vibration and the consequent acoustic noise is the abrupt change of radial magnetic force around the airgap. In addition, the unipolar phase current waveforms of the SRMs can have the abrupt change in phase current as well. Moreover, the stator vibration can also be excited by torque ripple, subsequently emitting acoustic noise [9]. In order to reduce the vibration and acoustic noise, several noise mitigation strategies have been proposed in literature such as stator lamination shape optimization [10], rotor and stator skewing [14], hybrid excitation with a C-dump inverter to reduce the rapid change of radial magneto-motive force (MMF) [15], two-stage commutation [16], voltage smoothing using pulse-width modulation (PWM) [9], and active vibration damping using piezoelectric actuators [17] - [18].

Numerous methods have already been investigated in the literature in order to improve machine performance and make the SRMs more suitable for various industrial applications.

These include optimizing the control strategies for the SRM drives and also other methods from the aspects of machine design such as increasing rotor pole number to be higher than slot pole number, increasing phase number, varying winding configurations, employing modular machine structure with segmented stator/rotor poles, etc., which will be detailed in the following sections.

1.2 RESEARCH SCOPE AND CONTRIBUTIONS

1.2.1 RESEARCH SCOPE

The main topic of this thesis is to investigate the electromagnetic performances of the novel doubly salient synchronous reluctance machines (DSRM) with different winding configurations, current excitation methods and also machine topologies. According to the three established SRMs with short-pitched conventional winding and mutually-coupled winding, as well as fully-pitched distributed winding, two novel 12-slot/8-pole SRMs with single layer conventional and mutually-coupled winding configurations have been proposed. In addition, different conduction angles of both the unipolar and bipolar rectangular wave currents have been adopted to the three established and two novel SRMs for a comprehensive investigation on the machine performances. Moreover, several novel modular SRMs have been proposed with different winding configurations, slot/pole number combinations and flux gap widths, and also supplied with different current waveforms.

With sinewave excitation, both the dynamic and static performances of the DSRMs (which is in effect short-pitched SynRMs with doubly salient machine structure) with double/single layer conventional and mutually-coupled, as well as fully-pitched winding configurations have been investigated in-depth. Additionally, the SynRMs with different rotor structures, winding configurations and slot/pole number combinations have also been studied. Furthermore, for better understanding of the nature of the DSRMs, some analytical models have also been developed to analyse the contribution of airgap flux density harmonics to the torque (average torque and also torque ripple) for different winding configurations.

This thesis is comprised of 7 chapters as follows:

- Chapter 1 provides a general background and overview of the SRMs, followed by a literature review about the SRMs with different machine topologies, current excitation methods of both the SRMs and SynRMs, and key design parameters of the SynRMs.
- Chapter 2 proposes two novel 3-phase, 12-slot/8-pole SRMs with single layer conventional and mutually-coupled winding configurations, which combine the merits of double layer mutually-coupled SRM (short end-windings) and fully-pitched SRM (high torque capability). In addition, the influence of conduction angles (e.g. unipolar 120° elec., unipolar 180° elec., bipolar 180° elec., bipolar 240° elec., and bipolar 360° elec.) on the electromagnetic performances has been investigated and compared between the SRMs. Both single and double layer machine prototypes have been built to validate the predictions.
- Chapter 3 proposes several 3-phase modular SRMs with E-core segmented stators. Different slot/pole number combinations such as greater stator slot number than rotor pole number (12-slot/8-pole and 12-slot/10-pole) and greater rotor pole number than stator slot number (12-slot/14-pole and 12-slot/16-pole) have been adopted to the modular SRMs. In addition, different flux gap widths and conduction angles have been employed to the modular SRMs with both conventional and mutually-coupled winding configurations. The 12-slot/8-pole and 12-slot/14-pole SRMs with both non-modular and modular structures have been built and the predictions have been validated by experimental tests.
- Chapter 4 comprehensively investigates the electromagnetic performances of the DSRM topologies with double/single layer conventional and mutually-coupled, as well as fully-pitched winding configurations. Comparisons of static and dynamic performances in terms of *d*- and *q*-axis inductances, torque performances, loss calculations, torque-speed curve and efficiency map have been obtained. Two prototypes have also been built to validate the predictions.
- Chapter 5 investigates the influence of rotor topologies and winding configurations on the electromagnetic performances of 3-phase SynRMs with different slot/pole number combinations, e. g. 12-slot/4-pole and 12-slot/8-pole. Transversally laminated synchronous reluctance rotors with both round and angled flux barriers have been considered, as well as the rotor with salient poles used in the SRMs. The 12-slot/8-pole SynRMs with salient pole rotor have been built to validate the predictions in terms of inductance and torque.

- Chapter 6 adopts simple analytical modelling to investigate the contribution of airgap field harmonics to the torque production in 3-phase 12-slot/8-pole DSRMs with both double/single layer conventional and mutually-coupled winding configurations. The airgap flux density has been calculated by analytically obtained MMF and doubly salient airgap permeance. The contribution of airgap field harmonics to average torque and torque ripple has been validated by direct finite element analysis.
- Chapter 7 gives a general conclusion and future work.

1.2.2 CONTRIBUTIONS

The main contributions of this thesis can be summarized as follows:

- Two novel 3-phase, 12-slot/8-pole SRMs have been proposed with single layer conventional and mutually-coupled winding structures. For the same copper loss, the proposed single layer SRMs can produce higher average torque than conventional SRMs without heavy magnetic saturation (unsaturated). However, the performance of the proposed SRMs deteriorates markedly with increasing phase current under saturation.
- Appropriate conduction angles (for better torque performance) can be selected for the SRMs with different winding configurations at both low and high current levels. This can increase the average torque and/or reduce the torque ripple coefficient.
- Novel modular SRMs have been proposed with improved machine performance, simpler manufacturing process and better fault tolerant capability. With appropriate conduction angles (for better torque performance), the modular SRMs with higher rotor pole number than stator slot number can produce similar average torque to non-modular SRMs, but with much lower torque ripple, lower iron loss and lower radial force. Due to this lower radial force, the modular SRMs have the potential to generate lower vibration and acoustic noise. However, the mechanical integrity of the modular SRMs stator may limit the machine for very high speed applications.
- In order to obtain maximum machine efficiency, appropriate winding configuration of the DSRMs can be selected for different speed range applications. The double layer mutually-coupled DSRMs achieves the highest efficiency between 6000 and 8000rpm. The single layer DSRMs are suitable for middle speed applications over the range of 3000 to 4500 rpm. Fully-pitched DSRM achieves a more modest efficiency at lower speed around 2000rpm.

- The appropriate rotor topologies (for better torque performance) among synchronous reluctance rotors with round and angled flux barrier, as well as the rotor used in SRMs can be selected in order to obtain the maximum average torque for different winding configurations and slot/pole number combinations.
- A better understanding has been achieved by analytical modelling for distinguishing single/double layer conventional and mutually-coupled winding configurations. According to the MMF model, it is found that the working harmonic orders of mutually-coupled windings are doubled than those of the conventional windings. In addition, the harmonic orders of the double layer machines are doubled than those of the single layer ones. Moreover, it is found that the dominant MMF harmonics with positive rotating speed (forward rotating) produce positive torque. However, the dominant MMF harmonics with backward rotating produce negative torque.

During the PhD study, based on the above contributions, 8 papers in total have been published, which include 7 journal papers and 1 conference paper. The publication list is given as below:

1. **X. Y. Ma,** G. J. Li, G. W. Jewell and Z. Q. Zhu, "Comparative study of short-pitched and fully-pitched SRMs supplied by sine wave currents," in *ICIT15*, Sevilla, Spain, Mar. 17-19, 2015. [Chapter 4]
2. **X. Y. Ma**, G. J. Li, G. W. Jewell, Z. Q. Zhu and H. L. Zhan, "Performance comparison of doubly salient reluctance machine topologies supplied by sinewave currents," *IEEE Trans. Ind. Electron.,* vol. 63, no. 7, pp. 4086-4096, Mar. 2016. [Chapter 4]
3. G. J. Li, **X. Y. Ma**, G. W. Jewell, Z. Q. Zhu and P. L. Xu, "Influence of conduction angles on single layer switched reluctance machines," *IEEE Trans. Magn.,* vol. 52, no. 12, pp. 1-11, Jul. 2016. [Chapter 2]
4. G. J. Li, Z. Q. Zhu, **X. Y. Ma** and G. W. Jewell, "Comparative study of torque production in conventional and mutually coupled SRMs using frozen permeability," *IEEE Trans. Magn.,* vol. 52, no. 6, pp. 1-9, Jun. 2016.
5. **X. Y. Ma**, G. J. Li, Z. Q. Zhu, G. W. Jewell and J. Green, "Investigation on synchronous reluctance machines with different rotor topologies and winding configurations," *IET Elec. Power Appl.*, vol. 12, no. 1, pp. 45-53, Jul. 2017. [Chapter 5]

6. G. J. Li, **X. Y. Ma**, G. W. Jewell and Z. Q. Zhu, "Novel modular switched reluctance machines for performance improvement," *IEEE Trans. Energy Convers.*, vol. 33, no. 3, pp. 1255-1265, Jan. 2018. [Chapter 3]

7. **X. Y. Ma**, G. J. Li, G. W. Jewell and Z. Q. Zhu, "Recent development of reluctance machines with different winding configurations, excitation methods, and machine structures", *CES Trans. Electrical Machines and Systems,* vol. 2, no. 1, pp. 82-92, Mar. 2018. [Chapters 2, 3, 4 and 5]

8. **X. Y. Ma**, G. J. Li, G. W. Jewell, and Z. Q. Zhu, 'Quantitative analysis of contribution of air-gap field harmonics to torque production in three-phase 12-slot/8-pole doubly salient synchronous reluctance machines', *IEEE Trans. Magn.,* vol. 54, no. 9, pp. 1-11, Jul. 2018. [Chapter 6]

1.3 SWITCHED RELUCTANCE MACHINE (SRM) TOPOLOGIES

The most common SRMs are designed with an internal rotor structure. However, in order to achieve better torque performance for low-speed in-wheel application, the SRMs can also have an external rotor structure. Both structures are very much similar in terms of magnetic circuit, and most topologies if not all of internal rotor SRMs can be applicable to external rotor SRMs. Therefore, this thesis will mainly focus on the internal rotor SRMs.

In terms of mechanical construction, the SRMs with internal rotor structure can be classified as non-modular and modular ones, as shown in Fig. 1.1. In addition, different winding configurations, slot/pole number combinations, and phase numbers can be employed in the SRMs to achieve different machine performances. The well-established conventional and mutually-coupled SRMs are designed with double layer winding structures. It can be found in Fig. 1.1 that the winding arrangement of the double layer conventional machine is A+A-B-B+C-C+… (where '+' stands for GO conductor while '-' stands for RETURN conductor). However, for the mutually-coupled winding, it is A+A-B+B-C+C-… The difference in winding configurations results in variation in flux distribution. With conventional winding, the flux will only flow through phase A when phase A is energized. While with mutually-coupled winding, the flux will flow through not only phase A but also phases B and C, leading to short flux path. Therefore, different from the conventional machine, not only the self-flux (self-

inductance) but also the mutual-flux (mutual-inductance) will contribute to torque production in the mutually-coupled machine. With similar winding configurations as shown in Fig. 1.1, both conventional and mutually-coupled machines can employ the single layer structure. Fully-pitched SRM has been proposed in [19] with single layer winding structure and the mutual-inductance can be fully utilized for torque generation. With this winding arrangement, the self-inductance is nearly independent of rotor position. As a result, only the mutual-inductance will contribute to torque production. Both the conventional and mutually-coupled windings can be employed with single layer structures and will be detailed in Chapter 2. It is worth mentioning that the fully-pitched winding with double layer structure has similar electromagnetic performance in terms of flux, inductance and output torque as the single layer structure but with slightly shorter end-windings. In order to achieve simplified manufacture process, better fault tolerant capability and potentially reduced material consumption, the SRMs can be constructed with modular structure with E-core and C-core segmented stators or rotors, leading to variable flux distributions and also different machine performances.

In this section, different SRM machine topologies will be summarized according to different winding configurations, slot/pole number combinations, multiphase structures and also modular topologies.

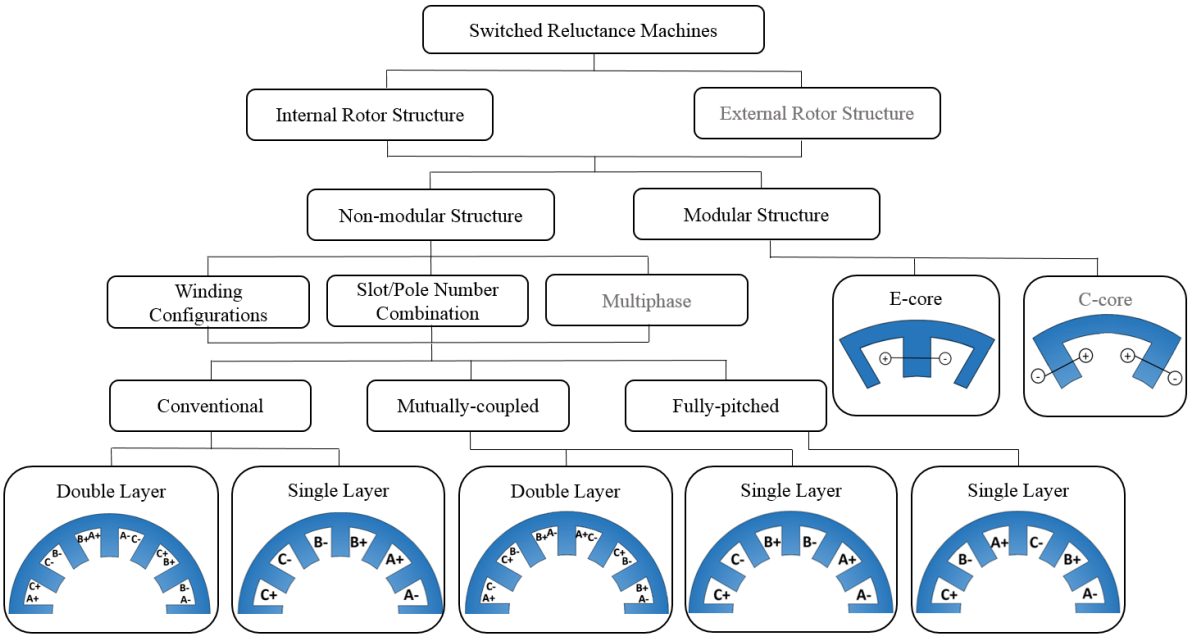

Fig. 1.1 Categorization of switched reluctance machines (SRMs). The topologies investigated in this thesis are in black.

1.3.1 WINDING CONFIGURATIONS

For a very common 3-phase, 6-slot/4-pole SRMs, there are three well-established winding configurations in the literature. They are the double layer conventional SRM, the double layer mutually-coupled SRM, and the single layer fully-pitched SRM as shown in Fig. 1.2 [11] [19] [20].

It can be found that for the conventional and mutually-coupled SRMs, each phase winding consists of 2 coils, and each coil is wound around one stator tooth, and hence two coils belonging to two different phases are located in one stator slot – double layer winding. This also means that the coil pitch equals to the slot pitch ($2\pi/N_s$, N_s is the stator slot number), which is smaller than the pole pitch ($2\pi/N_r$, N_r is the rotor pole number) – short-pitched winding. In addition, the magnetic polarities of coils of one phase, e.g. phase A, for conventional SRM are NS, while for mutually-coupled SRM, they are NN. In a fully-pitched SRM, each phase winding comprises of 1 coil and each coil spans 3 slot pitches, leading to a fully-pitched winding. Moreover, only one coil is located in one stator slot, leading to a single layer winding structure.

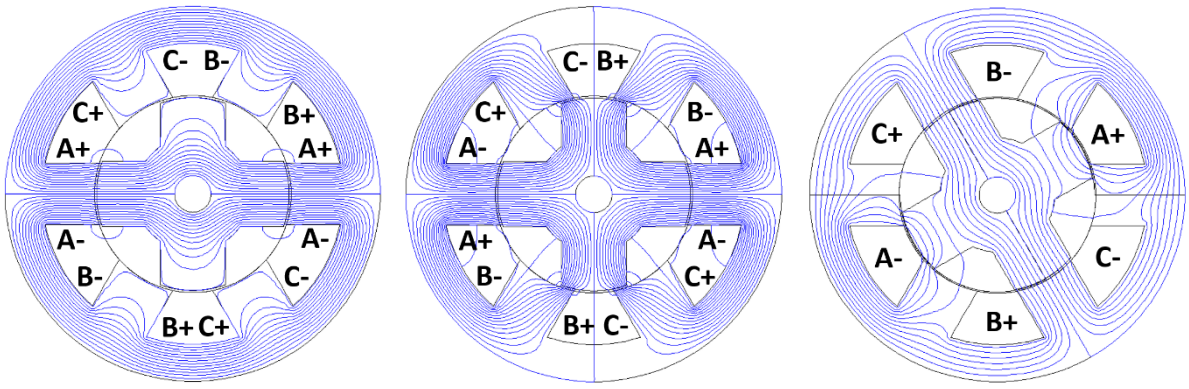

(a) (b) (c)

Fig. 1.2 3-phase, 6-slot/4-pole SRMs. (a) Conventional SRM, (b) mutually-coupled SRM, (c) fully-pitched SRM [11] [19] [20].

As mentioned previously, it can be found in Fig. 1.2(a) that the magnetic flux in the conventional machine is essentially self-linked by the excitation coil and the mutual flux between phases is very low and largely negligible. However, in the mutually-coupled machine, the magnetic flux is mutually coupled between adjacent coils. This magnetically mutual coupling will produce mutual-inductance between phases so that the output torque of the machine could be increased. Moreover, the mutually-coupled machine is less sensitive to

magnetic saturation due to the fact that the flux in stator yoke is separated into different flux paths [11]. As a result, the MMF in the stator yoke and flux density are less than that of the conventional one with the same number of turns per phase and also the same phase current. This means that the mutually-coupled machine can resist a higher saturation current and can achieve better overload capability [21], with an enhancement by around 77% up to $40A_{rms}$ (which is 4 times of the rated current) [22]. However, the torque ripple of the mutually-coupled machine is relatively higher because of the nature of the self- and mutual-inductance variations, and hence could potentially generate higher noise. Different from these, the torque in the fully-pitched machine is produced only by the derivatives of mutual-inductance with respect to rotor position. In addition, due to single layer winding structure, the fully-pitched machine can produce higher average torque when it is not heavily saturated [22]. But the considerably longer end-winding leads to larger phase resistance and hence higher copper loss than other machines with the same phase current [19].

1.3.2 SLOT/POLE NUMBER COMBINATIONS

The stator slots and rotor poles are typically designed to be symmetrical and evenly distributed. Under the rules constraining the pole number, pole arc and phase number, the regular slot/pole number selection for the SRMs can be given in Table 1.1 [23] - [24].

TABLE 1.1 TYPICAL SLOT/POLE NUMBER COMBINATIONS

Number of Phase	Slot/pole number combinations
3	6-slot/2-pole; 6-slot/4-pole; 6-slot/8-pole; 6-slot/14-pole; 12-slot/8-pole; 18-slot/12-pole; 24-slot/16-pole
4	8-slot/6-pole; 8-slot/10-pole; 16-slot/12-pole; 24-slot/18-pole; 32-slot/24-pole
5	10-slot/4-pole; 10-slot/6-pole; 10-slot/8-pole; 10-slot/12-pole
6	12-slot/10-pole; 12-slot/14-pole; 24-slot/20-pole;
7	14-slot/4-pole; 14-slot/10-pole; 14-slot/12-pole; 14-slot/16-pole;

In order to enhance machine performance, several design adjustments have been proposed with variable slot/pole number combinations. By way of example, 12-slot/4-pole and 6-slot/2-pole combinations in [25] and a 6-slot/14-pole SRM in [26] have been proposed with redundant poles for lower acoustic noise generation. In [24], novel SRMs with higher number of rotor

poles than stator poles have been introduced. Compared with the conventional 6-slot/4-pole SRM, the proposed novel SRM has the same stator slot number but with increased rotor pole number (10-pole). With the same phase number and volume constraints, the 6-slot/10-pole machine exhibits higher torque capability while with lower torque ripple. Although the regular slot/pole number combinations generally have the best overall machine performance, there still exist some unconventional slot/pole number combinations such as 12-slot/9-pole, 9-slot/5-pole, and 12-slot/7-pole configurations, which have been proposed in [27] to reduce the vibration and acoustic noise.

1.3.3 MULTIPHASE SRMS

Employing appropriate slot/pole number combination, the multi-phase SRMs can produce lower torque ripple when compared with the 3-phase SRMs due to the fact that higher phase number can give rise to the interaction between phases, hence, the torque dips between phases can be reduced [28]. In addition, machine reliability and fault tolerant capability can be improved [29] - [30]. However, due to the increase in phase number, the drive systems become complicated and the increase in power electronic devices might lead to higher cost [28].

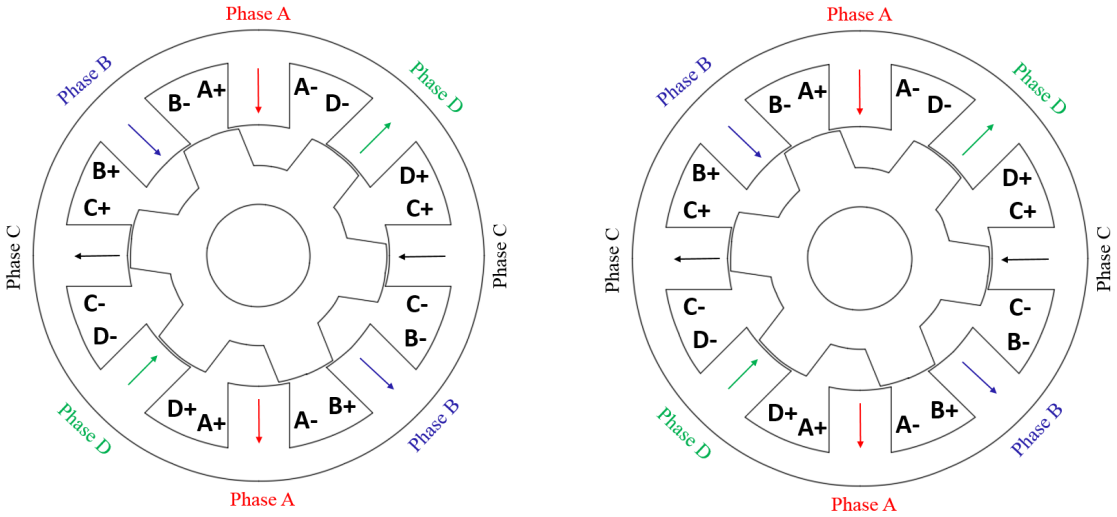

Fig. 1.3 Winding configurations of 4-phase 8-slot/6-pole SRMs with magnetic polarities of (a) NSNSSNSN, (b) NNNNSSSS [31].

Similar to the 3-phase SRMs, different winding configurations can also be employed for the multiphase SRMs. However, compared with the machines with odd phase numbers such as a 3-phase 6-slot/4-pole (coil magnetic polarities can be NSNSNS), the magnetic field is

naturally asymmetric in the machine with even phase number [31]. For 4-phase, 8-slot/6-pole SRMs, two winding configurations have been investigated in [31] and their magnetic polarities such as NSNSSNSN and NNNNSSSS are shown in Fig. 1.3. It can be seen in Fig. 1.3(a) that only the phases A and B have the magnetic polarities of NN (or SS), which will lead to long flux path during two-phase excitation, and hence result in lower instantaneous torque. However, the magnetic polarities are NS (or SN) for other two phases (such as phase A and D), which will lead to short flux path, and result in higher instantaneous torque. Similarly, in Fig. 1.3(b), both short and long flux paths are presented during two-phase excitation. Therefore, the asymmetric magnetic fields will result in irregular and asymmetric instantaneous torque waveforms for both winding configurations. The torque performance can be improved by adjusting the phase currents individually. By way of example, for the case in Fig. 1.3(a), it can be realized by increasing the currents of phases A and B when the transient torque produced by these two phases is low.

The mutual coupling and its effect on torque performance have also been investigated in [32] for some 6-phase 12-slot/10-pole SRMs with different winding configurations. For clearer explanation, [29] introduced five winding configurations for 6-phase 12-slot/10-pole SRMs. Fig. 1.4 shows three windings among them which have relatively better torque performance.

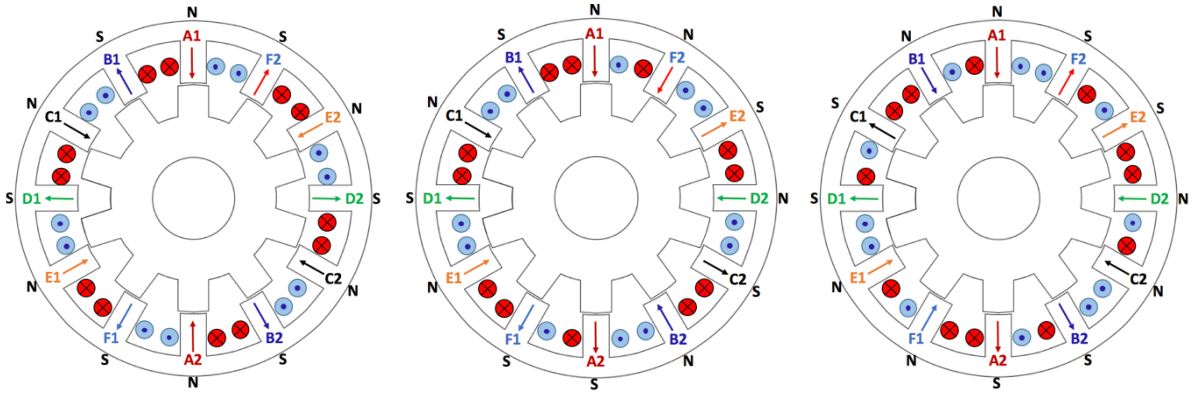

(a) (b) (c)

Fig. 1.4 Winding configurations of 6-phase 12-slot/10-pole SRMs with magnetic polarities of (a) NSNSNSNSNSNS, (b) NSNSNSSNSNSN, (c) NNSSNNSSNNSS [29].

Under single-phase excitation, e.g. phase A is excited, the winding configurations in Fig. 1.4 (b) and (c) with single-phase magnetic polarities of NS present long flux path through the stator and rotor cores, as shown in Fig. 1.5(a). However, the winding configuration in Fig. 1.4(a) with single-phase magnetic polarities of NN leads to short flux path, as shown in Fig. 1.5 (b). In addition, it has been found by 2D FEA that with NS connections, there is only self-

inductance. However, with NN connections, the self-inductance becomes slightly lower but there is considerable mutual-inductance, both of them will influence the torque generation.

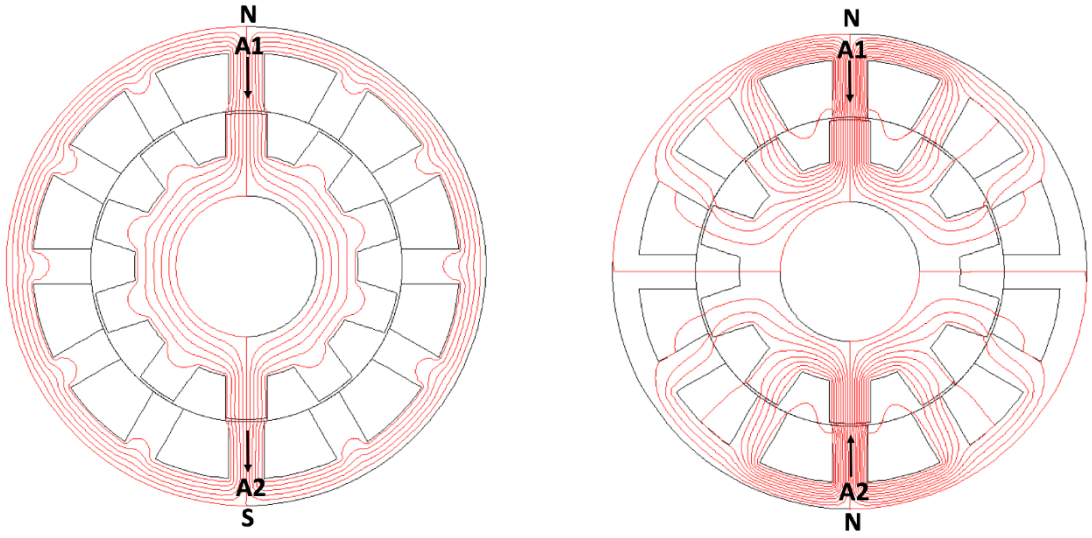

(a) (b)

Fig. 1.5 Comparison of flux distribution between winding configurations of (a) NS (long flux path), and (b) NN (short flux path), under single phase excitation [29].

Under 6-phase excitation, the average torque performance of the winding connection in Fig. 1.4 (a) (with NN) with short flux path has negative effect from mutual coupling but still produce higher average torque than others. In addition, machine with this winding connection has the lowest core losses due to lower flux density in the core back. However, employing winding connections in Fig. 1.4 (b) and (c) (with NS) can have reasonable average torque but with less mutual-inductance.

1.3.4 Modular SRMs

1.3.4.1 Modular SRMs with Segmented Stators

Different from the aforementioned classic non-modular SRMs, the novel modular SRMs become increasingly attractive due to their simplified manufacture process, higher reliability, enhanced fault tolerance capability and potentially reduced material consumption. As shown in Fig. 1.1, modular topologies are normally designed with E-core or C-core (also called U-core in some research papers) stators [33] - [34]. By way of example, a 2-phase, 6-slot/10-pole modular SRM has been proposed in [33], as shown in Fig. 1.6(a). The phase windings are wound on the narrower teeth of the two E-core stator segments. It has been found that using

such topology can save 22% steel compared with a non-modular 2-phase SRM of the same stator outer diameter, hence reducing the total cost. Moreover, the modular machine can produce higher average torque and efficiency. However, the major drawback of this structure is the deformation of stator segments caused by radial force, which will cause acoustic noise and ovalization of the stator, which may lead to mechanical crashes.

In order to improve the mechanical durability and to reduce the acoustic noise, an alternative structure of the 2-phase modular SRM has been proposed in [35], which is constructed as a 2-phase, 9-slot/12-pole, E-core SRM, as shown in Fig. 1.6(b). This modular machine is made of three similar E-core segments as shown in Fig. 1.6(a) and each phase has three coils connected in series. In order to reduce flux leakage between two adjacent E-core segments, the zero flux region can be replaced with non-ferromagnetic material.

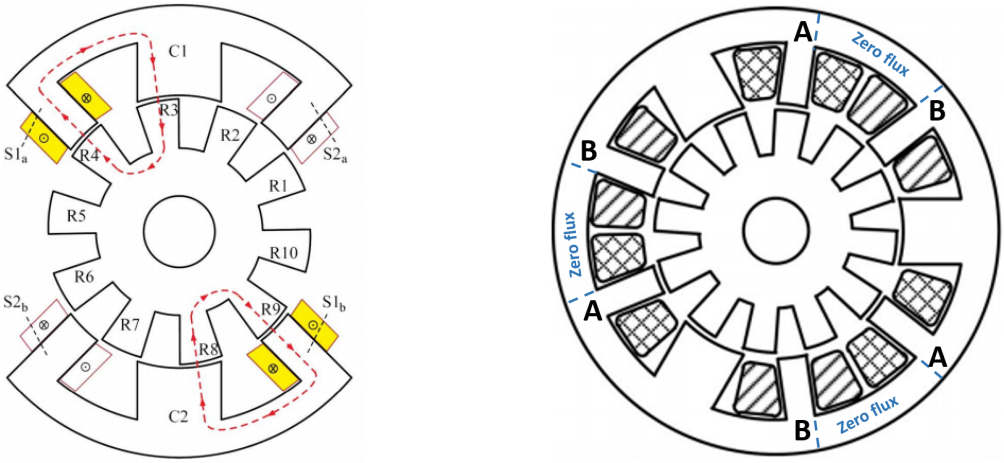

(a) (b)

Fig. 1.6 2-phase modular SRMs with E-core segmented stators. (a) 6-slot/10-pole (b) 9-slot/12-pole [33] [35].

Due to the difficulties in assembling the 2-phase, 6-slot/10-pole modular SRM, the magnetic structure has been optimized in [36] for mechanical robustness, manufacturability and performance improvement, as shown in Fig. 1.7. The straight back irons in I- and L-shaped segmented stator yokes enhance assembling capability and mechanical robustness without variation in flux paths, as shown in Fig. 1.7 (a) and (b), respectively. The non-modular (non-segmented) L-shaped stator yoke with two more common poles in Fig. 1.7 (c) forms two additional flux paths to reduce the overall reluctance during phase excitation, and hence can generate more positive torque than the L-shaped segmented yoke.

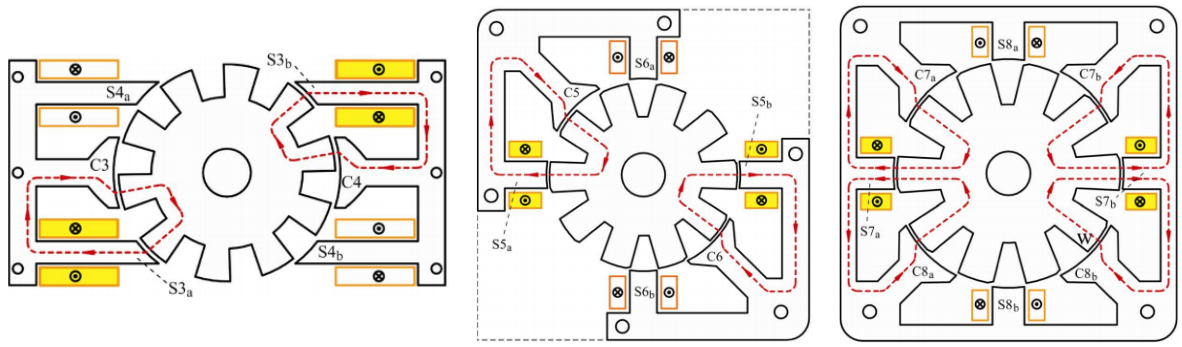

(a) (b) (c)

Fig. 1.7 Optimized magnetic structure of E-core SRMs with (a) I-shaped yoke, (b) L-shaped yoke, (c) L-shaped yoke with two more common poles [36].

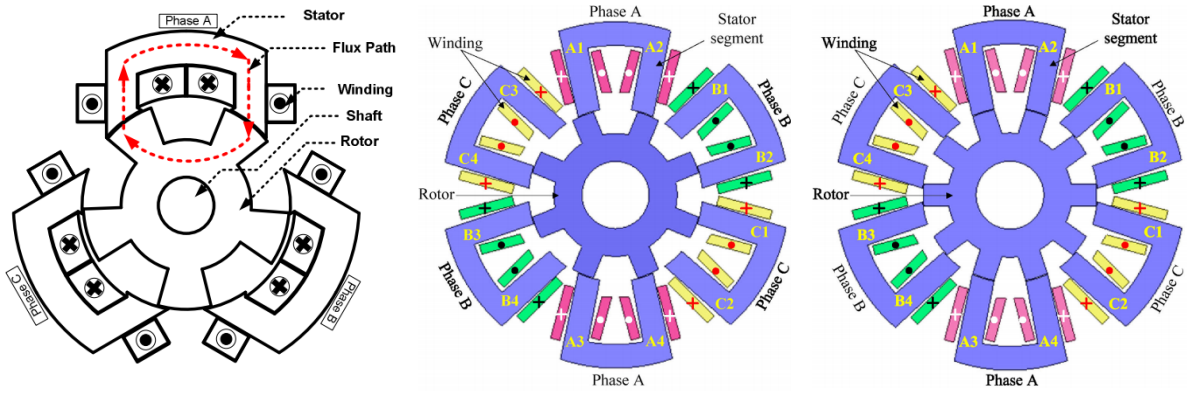

(a) (b) (c)

Fig. 1.8 3-phase modular SRMs with C-core segmented stators. (a) 6-slot/5-pole, (b) 12-slot/8-pole, (c) 12-slot/10-pole [34], [37].

In order to create a large slot space for winding and assembly individually, the SRMs with C-core modular structure have also been proposed. As shown in Fig. 1.8(a), a 3-phase, 6-slot/5-pole modular SRM with C-core segmented stators has been proposed in [34], where two coils are wound on one C-core segment. Due to the fact that the phase windings are totally independent from each other, the flux only flows through the excited pole and hence, there is no mutual-flux between phases. Therefore, the unbalanced radial force exists, leading to the fact that the proposed C-core machine produces higher acoustic noise than the conventional SRMs. However, the proposed machine is found to have higher torque production when compared with conventional SRMs with the same outer diameter. Similar to the C-core topology in [34], [37] introduced and compared two modular SRMs with 3-phase, 12-slot/8-pole and 12-slot/10-pole, as shown in Fig. 1.8(b) and (c), respectively. With the same phase winding configurations, it has been found that the 12-slot/10-pole machine achieves better

torque performance than the 12-slot/8-pole machine at low speed due to higher phase inductance.

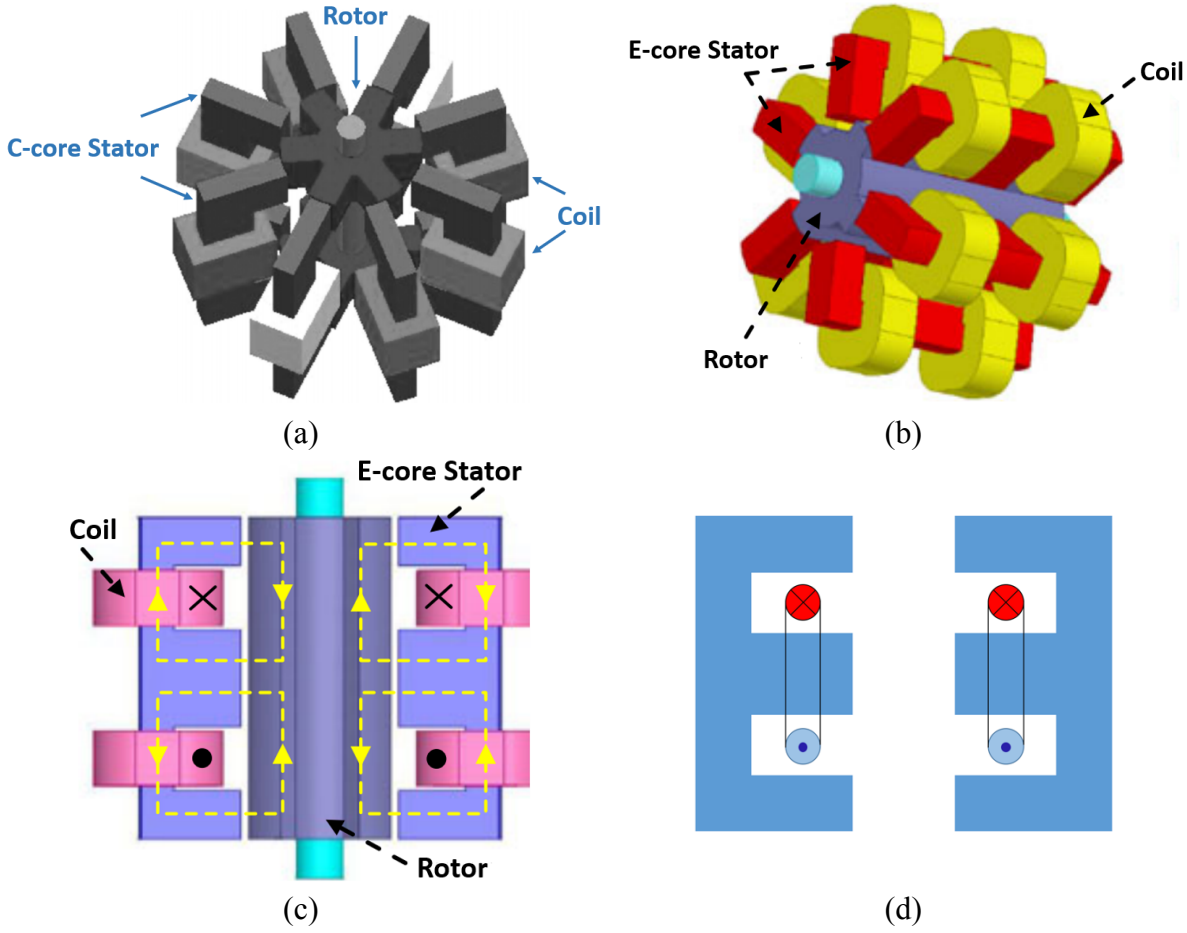

Fig. 1.9 Modular machines with toroidally constructed stators. (a) 4-phase, 8-slot/6-pole SRM with C-core segmented stators, (b) 3-phase, 6-slot/4-pole SRM with E-core segmented stators, (c) flux path of (b) from side view, (d) winding along axial direction of (b) from side view [38], [40].

Different from the conventional concentrated windings in the above modular machines, Fig. 1.9(a) shows a C-core modular SRM with toroidal winding, which has been proposed in [38]. This 4-phase, 8-slot/6-pole modular SRM consists of 8 independent stator segments which are constructed toroidally with the phase winding wound in the middle of the C-core. When compared with a conventional 8-slot/6-pole SRM with the same size, the modular machine can obtain higher fill factor and result in higher number of turns per phase. Therefore, for the same torque production, the modular SRM requires less current than the conventional SRM. Similarly, E-core segmented stators have also been constructed toroidally in [40] and [39], as shown in Fig. 1.9(b). It can be seen that for the 6-slot/4-pole modular SRM, there are two coils

wound on the E-core stator yoke and each phase consists of four coils. Fig. 1.9(c) shows the flux paths of one phase from the side view of the machine. Different from the conventional machine, the flux in such machine flows in both axial and radial directions. Due to the independent flux paths between phases, it can be predicted that the fault tolerant capability will be strong. However, the machine overall outside diameter is large due to the toroidally constructed coil. Therefore, it would be a better way to have the phase winding along the axial direction, as shown in Fig. 1.9(d).

1.3.4.2 MODULAR SRMS WITH SEGMENTED ROTORS

Modular SRMs can also be constructed with segmented rotors [41]. By way of example, two modular SRMs with segmented rotors have been proposed in [42] and [43] with different slot/pole number combinations, as shown in Fig. 1.10. The segmented rotors are magnetically isolated and connected with non-magnetic support structure. Different slot/pole number combinations and winding configurations such as fully-pitched and single layer short-pitched winding configurations have been employed in [42]. It has been found that with higher number of segmented rotor poles than stator slots such as 12-slot/14-pole and 12-slot/16-pole, the torque performance can be improved when compared with the conventional 12-slot/8-pole SRM. However, with higher electrical frequency due to increased rotor pole numbers, these machines are limited for high speed application owing to higher iron loss. The multiplicity of slot/pole number combinations such as 18-slot/12-pole and 24-slot/16-pole has been proposed in [43] for wider speed range applications.

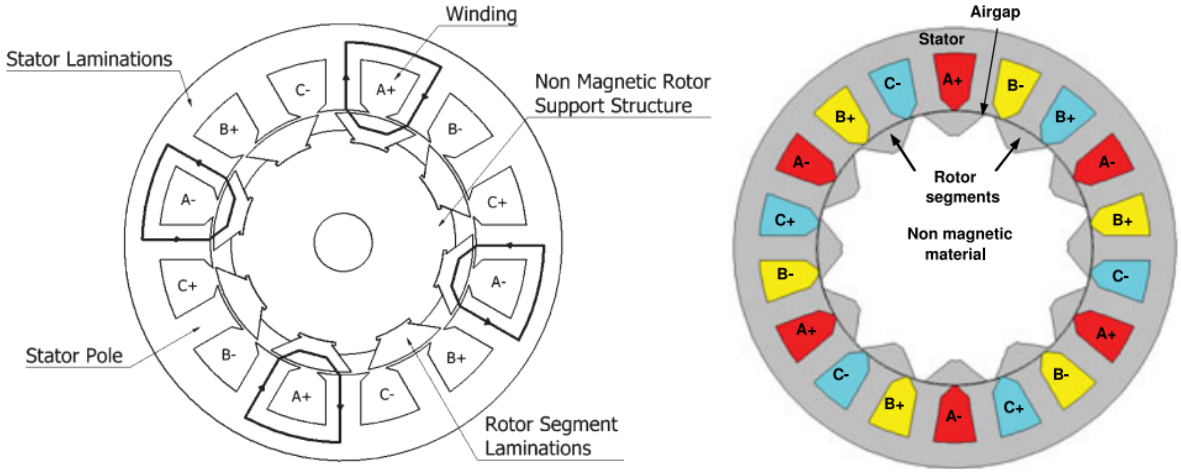

(a) (b)

Fig. 1.10 3-phase modular SRMs with segmented rotors. (a) 12-slot/8-pole, (b) 18-slot/12-pole [42] [43].

1.3.5 EXTERNAL ROTOR SRMS

The most common machines are designed with an internal rotor. However, in order to achieve high torque at low speed for in-wheel application, the external rotor SRM can also be employed as shown in Fig. 1.11 [44]. It is worth mentioning that almost all topologies for internal rotor SRMs can be equally applicable for external rotor SRMs.

Generally, the comparison between inner and external rotor SRMs is focused on geometry, cooling efficiency and electromagnetic behaviour. With regard to the winding, slot area of inner rotor SRMs cannot be fully used so that to some extent reduce the torque density. Also, the airgap radius is limited for coils spacing and cooling inside the housing. In contrast, both the coils and cooling can be placed near the shaft in the external rotor SRMs so that the airgap radius can be increased and hence improving the torque density and also machine efficiency. In addition, the improved torque per ampere ratio reduces the voltage-ampere requirement of the converter, and hence the size and cost of the converter can be reduced [45]. However, the cooling capability of external rotor SRMs is weakened when compared with inner rotor SRMs [45]. For air cooling system, this is mainly due to the fact that the heat (copper losses) in the stator slot needs to cross the airgap (bad thermal conductor) before being dissipated by the cooling system, leading to higher temperature rise in the stator slots. For liquid cooling system, a higher cooling efficiency can be achieved but the reliability could be lower such as the failure of any auxiliary cooling loop component, and more complicated mechanical structure.

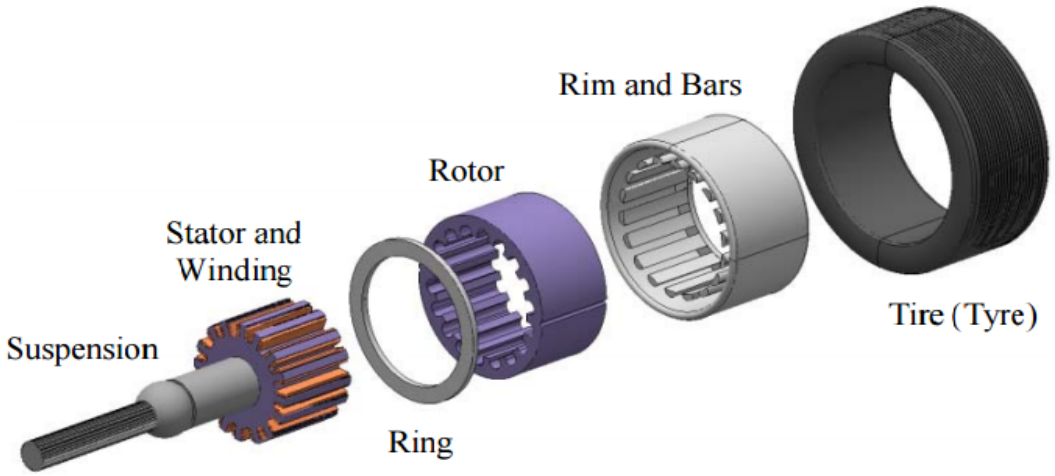

Fig. 1.11 External rotor SRM arrangement for in wheel drive application [44].

Fig. 1.12 shows some examples of external rotor SRMs with conventional concentrated winding configuration. In order to achieve lower torque ripple, the number of rotor poles is

generally selected to be higher than that of stator slots for external rotor SRMs. However, the higher number of rotor poles will cause high frequency and hence increase the iron loss, but the iron loss is not the dominant one for modest speed applications. Fig. 1.12(a) is a 3-phase 6-slot/8-pole SRM. It was designed for a fan in an air conditioner [46], [47]. In [48], a 3-phase 6-slot/10-pole SRM, as shown in Fig. 1.12(b), was designed for electric bicycles which achieves high torque and power density and operates at low speed. In [44], a 4-phase 16-slot/18-pole SRM, as shown in Fig. 1.12(c), was proposed for electric bus application with reduced torque ripple and increased machine efficiency.

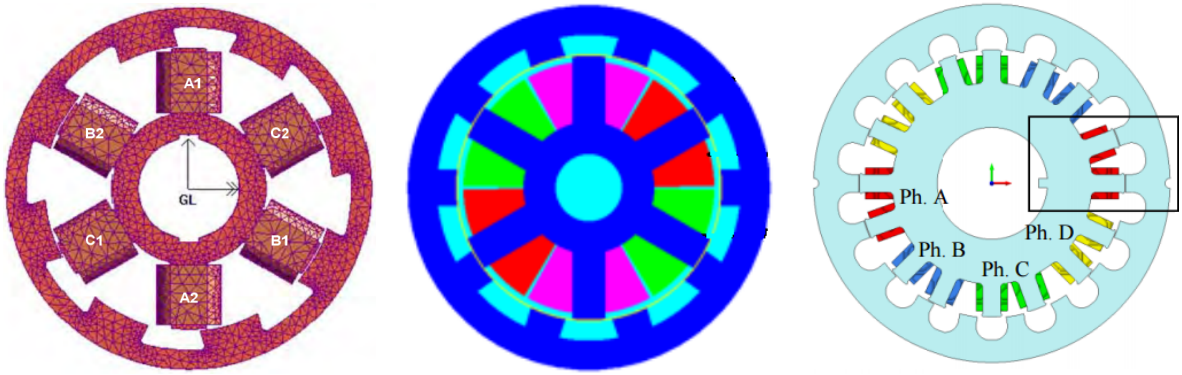

(a) (b) (c)

Fig. 1.12 Examples of external rotor SRMs. (a) 3-phase 6-slot/8-pole [46], (b) 3-phase 6-slot/10-pole [48], (c) 4-phase 16-slot/18-pole [44].

1.4 SYNCHRONOUS RELUCTANCE MACHINES (SYNRMS)

The advantage of using the SynRMs and SRMs over the permanent magnet machines is that the magnets are not needed. However, compared with the SRMs, the rotor structures of the SynRMs may be more complex and difficult for manufacturing. The major types of synchronous relucatance rotors are constructed with salient pole, axially laminated, and transverally laminated with flux barriers inside, as shown in Fig. 1.13. Although the salient pole rotor has the simplest and most robust structure, the doubly salient structure might result in higher vibration and acoustic noise. The axially laminated rotor in Fig. 1.13 (b) has advantages such as increased saliency ratio, hence improved power density and power factor [49]. However, it is very complex for industrial manufacturing. In addition, the eddy current losses are larger than other structures owing to axially laminated structure. As can be seen from Fig. 1.13 (c) that the rotor sheets of transversally laminated rotor are equipped with several air barriers (also called flux barriers), and there is a narrow rib between the rotor outer diameter and the ends of flux barriers in order to maintain a minimum rotor mechanical strength for medium and high speed operations. On the basis of machine performance and manufacturing process, transversally laminated rotor is the best choice from the perspective of manufacturability and will be detailed further in next section.

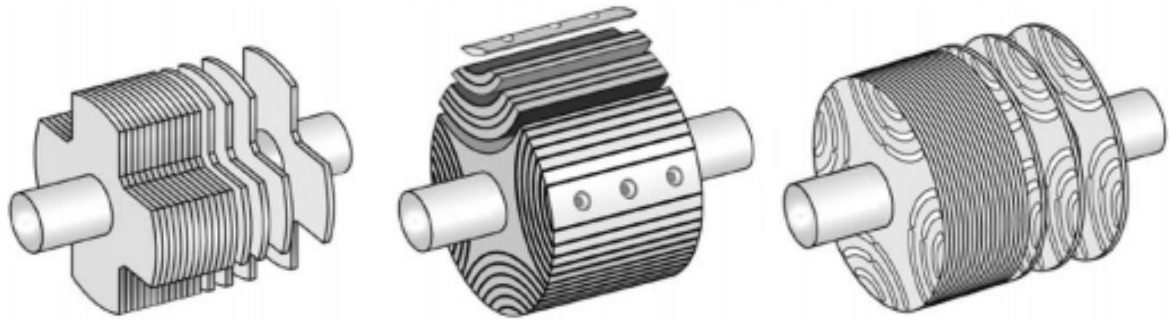

(a) (b) (c)

Fig. 1.13 Schematics of synchronous reluctance rotors with (a) salient pole, (b) axially laminated, (c) transversally laminated with flux barriers inside [49].

In the SynRMs, electromagnetic torque is directly proportional to the difference between *d*- and *q*-axis inductances and power factor is closely related to the saliency ratio [50]. Both of them can be enhanced by optimizing the machine parameters, such as the flux barrier shape, flux barrier layer number, slot/ pole number combination as well as winding configuration.

1.4.1 DIFFERENT SHAPES OF FLUX BARRIERS

For transversally laminated rotor, the literature shows two different flux barrier shapes: round flux barriers, as shown in Fig. 1.14 (a), and angled flux barriers, as shown in Fig. 1.14 (b). A comparison between these two flux barrier shapes has been carried out in [51] and [52]. In addition, some 24-slot/4-pole SynRMs with both flux barrier shapes have been investigated and tested in [53]. Regardless of the slot/pole number combinations, the rotor with round and angled flux barriers can have comparable average torque and torque ripple performances, which is relative to the ratio of rotor flux barrier width to rotor iron width, and hence the saliency ratio. However, it is found in [53] that the mechanical performances could be improved with angled flux barriers such as the stress in the rib. In addition, the angled flux barriers are also used for some permanent magnet-assisted SynRMs to achieve wider constant power speed range and better power factor performance.

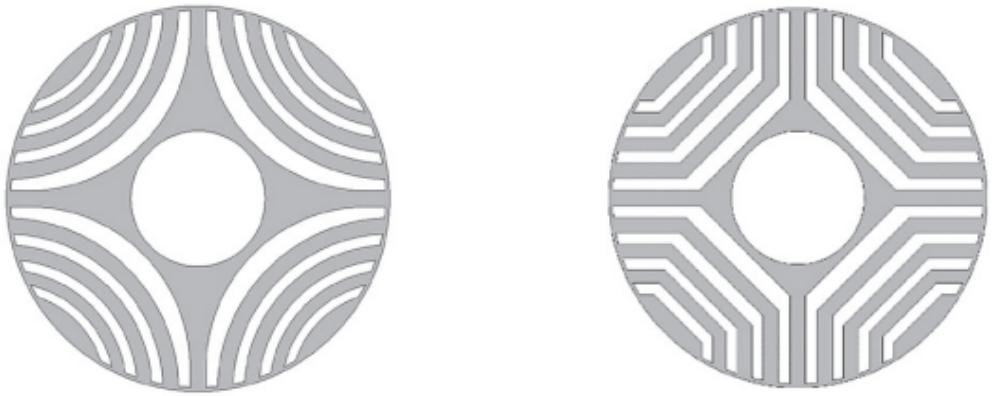

Fig. 1.14 Different flux barrier shapes in transversely laminated rotor. (a) Round flux barriers, (b) angled flux barriers [51].

1.4.2 DIFFERENT NUMBERS OF FLUX BARRIER LAYERS

The influence of number of flux barrier layers on the electromagnetic performance in terms of average torque and torque ripple has been studied in [54]. For fairness, the optimization of the SynRMs with different layers is constrained with a fixed ratio of total flux barrier thickness to total iron lamination thickness, as shown in Fig. 1.15. With the same ratio, the results showed that the SynRMs with different number of flux barrier layers can produce almost the same average torque. However, they can be distinguished by the performance of torque ripple. The SynRM with two-layer flux barriers is found to have higher torque ripple than the others. While

with three-layer flux barriers, the torque ripple is the lowest and it is only about 16% of that with two-layer flux barriers.

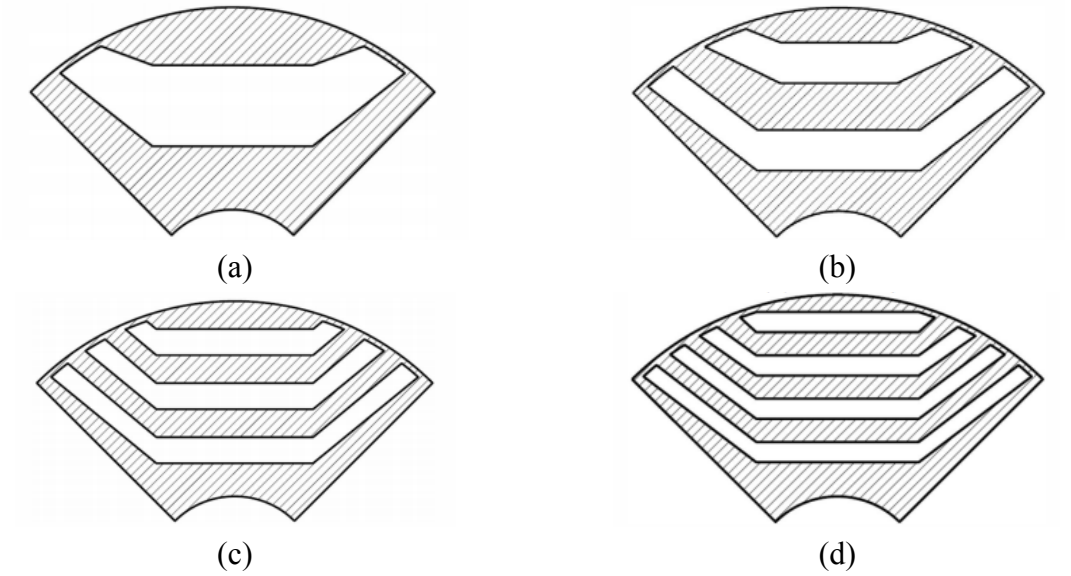

Fig. 1.15 Different number of flux barrier layers in the transversally laminated rotor. Design with the constraint of a fixed ratio of total flux barrier thickness to total iron lamination thickness (a) One-layer, (b) two-layer, (c) three-layer, (d) four-layer [54].

1.4.3 DIFFERENT SLOT/POLE NUMBER COMBINATIONS

Different slot/pole number combinations can result in variable flux paths, leading to different *d*- and *q*-axis inductances. Several research works about the influence of slot/pole number combinations on machines' electromagnetic performance have been carried out. With the same number of slots per pole per phase, a comparative study has been done in [54] between 12-slot/4-pole, 18-slot/6-pole and 24-slot/8-pole SynRMs with the same flux barrier layer. The conclusion has been obtained that the average torque is the highest for the 12-slot/4-pole combination and it is reduced with increasing rotor pole number. In addition, with this combination, a modest torque ripple can be achieved.

The SynRMs with different stator slot numbers but with the same rotor pole number have also been investigated in [54]. A comparison has been made between the 4-pole SynRMs with 12-slot, 24-slot and 36-slot. The average torque is similar for these machines but the lower torque ripple can be obtained with the increasing stator slot number. Considering both the average torque and torque ripple performance, it can be concluded that the 24-slot/4-pole SynRM performs better than other slot/pole number combinations.

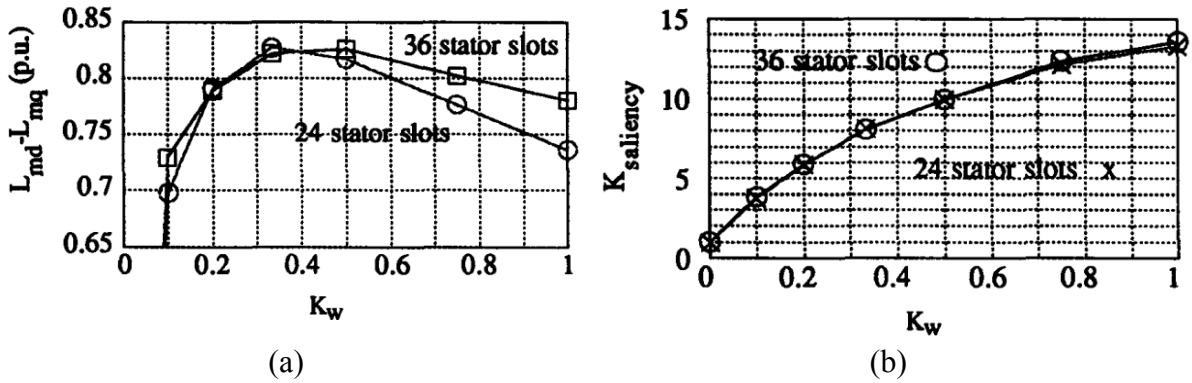

(a) (b)

Fig. 1.16 Influence of different stator slot numbers on (a) inductance difference between *d*- and *q*-axis against K_w, (b) saliency ratio against K_w [55].

In addition, the influence of stator slot number on the two key design factors of the SynRM, e.g. difference between *d*- and *q*-axis inductances and the saliency ratio, has been investigated in [55], with varying K_w (which is the ratio of rotor flux barrier width to rotor iron width). The results in Fig. 1.16 (a) clearly shows that a better torque production can be achieved when K_w is in the range of 0.2 to 0.6, due to higher inductance difference. In addition, the inductance difference is quite independent of the stator slot number. It can be seen from Fig. 1.16 (b) that the saliency ratio is also independent of the stator slot number, but a higher saliency ratio can be achieved with higher K_w.

1.4.4 DIFFERENT WINDING CONFIGURATIONS

Similar to the induction machines, the classic SynRMs often employ the distributed stator windings, in which the coils often span a few slot pitches [56]. However, many permanent magnet machines and DSRMs adopt the fractional slot concentrated windings, in which the coils are concentrated around one single stator tooth, due to their inherent advantages such as higher slot fill factor, shorter end-winding, smaller machine overall footprint, etc. [57] [58] [59].

In [60], a 6-slot/4-pole SynRM was equipped with fractional slot, double layer concentrated winding configuration, as shown in Fig. 1.17 (b). When compared with the conventional 24-slot/4-pole SynRM with distributed winding in Fig. 1.17 (a), it has been found that the higher fill factor can be achieved by adopting the concentrated winding. Moreover, the torque density, and thermal characteristics can also be improved. However, the drawbacks of the concentrated winding are lower winding factor and lower saliency ratio, and hence reduced power factor. In

addition, it can cause higher torque ripple, higher iron loss due to higher armature MMF harmonics

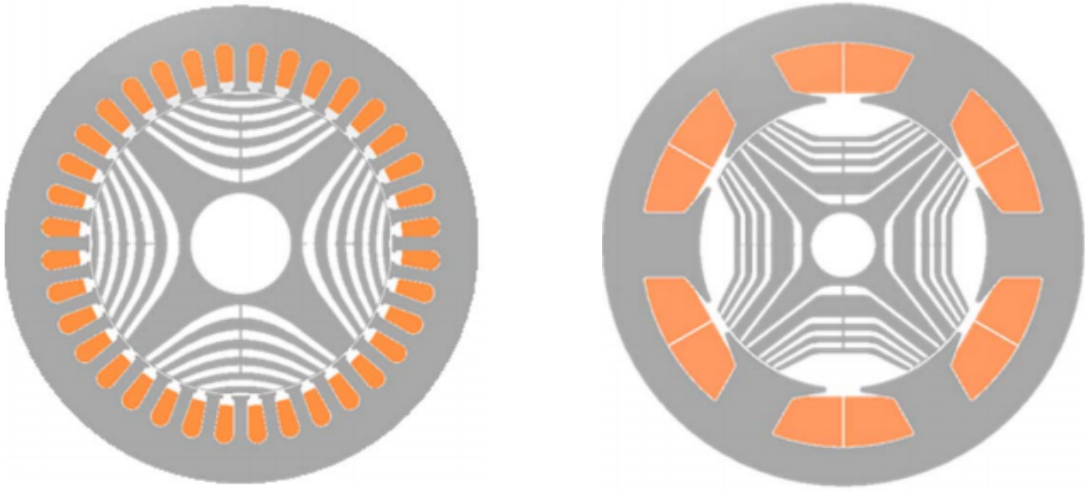

(a) (b)

Fig. 1.17 SynRMs with (a) distributed and (b) concentrated winding [60].

1.5 CURRENT SUPPLY MODES

1.5.1 EXCITATION METHOD FOR SRM

In general, the SRMs are supplied with unipolar rectangular wave phase current with 120° elec. conduction when the phase number is three. Therefore, different phases are excited successively and only the self-inductance has been considered for torque generation. As mentioned previously, the conventional winding configuration with double layer structure in Fig. 1.2 (a) has only self-inductance and almost null mutual-inductance. Consequently, the unipolar excitation without considering mutual-inductance will be appropriate for this winding configuration. By way of example, Fig. 1.18 shows the unipolar excitation for conventional SRM with conduction angle of 120° elec. With this excitation method, positive torque can be generated by the self-inductance, e.g. $\frac{1}{2} {i_a}^2 dL_a/d\theta$, if phase A is energized when $dL_a/d\theta$ is positive.

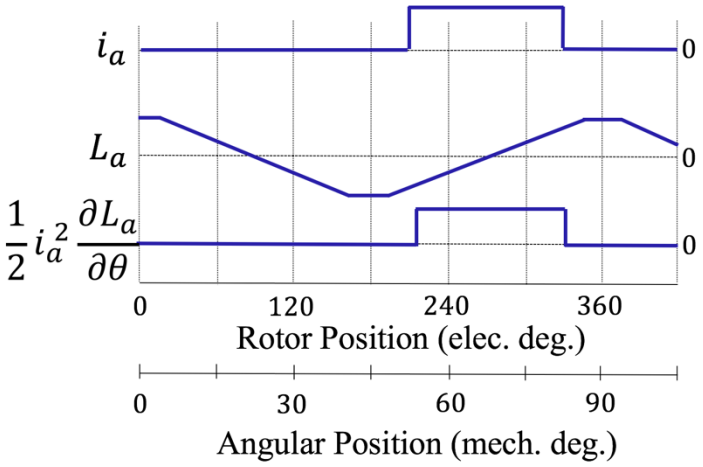

Fig. 1.18 Unipolar excitation for conventional SRM with conduction angle of 120° elec.

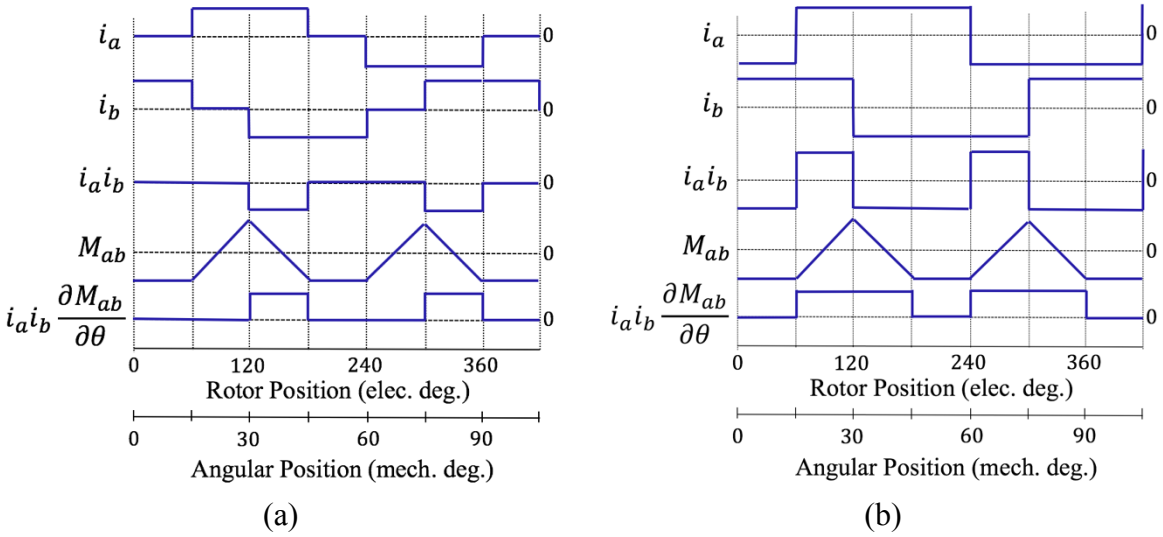

Fig. 1.19 Bipolar excitation for fully-pitched SRM with conduction intervals of (a) 120° elec., (b) 180° elec. [61].

Different from the conventional winding configuration, the fully-pitched SRM is proposed in [62] and shown in Fig. 1.2 (c) with dominant mutual-inductance while the self-inductance does not contribute to torque production. Therefore, the commonly used unipolar excitation with conduction angle of 120° elec. will not be suitable due to the fact that in order to use the mutual-inductance for torque production, at least two phases should be energized simultaneously at any time. As a result, the conduction angle of the phase current should be higher than 120° elec. In [61], bipolar excitations with intervals of 120° elec. and 180° elec.

conductions have been applied to the fully-pitched SRM, as shown in Fig. 1.19. With such excitation methods, the mutual-inductance has been considered, which can generate positive torque, e.g. $i_a i_b dM_{ab}/d\theta$ if phases A and B are energized.

In order to consider both the self- and mutual-inductances for torque production, a two-phase excitation method for a 3-phase 6-slot/4-pole mutually-coupled SRM has been proposed in [20]with bipolar excitation and different conduction angles. Since the electromagnetic torque of the SRM is closely related to both the self- and mutual-inductances, a higher torque performance can be achieved by considering the influence of both the self- and mutual-inductances through the two-phase excitation. Moreover, with such excitation mode, the abrupt change of phase current can be reduced, leading to lower torque ripple and lower vibration and acoustic noise [20].

1.5.2 Excitation Method for Synchronous Reluctance Machine (SynRM)

Similar to permanent magnet and induction machines, the synchronous reluctance machines (SynRMs) are rotating field machines and hence are always supplied with sinewave current, as shown in Fig. 1.20.

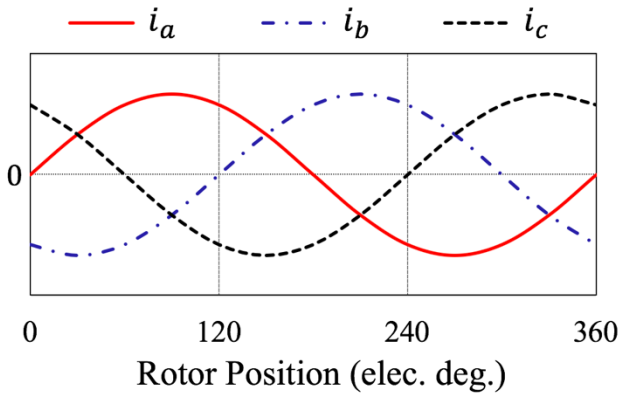

Fig. 1.20 Excitation method for the SynRMs.

Different from the SRM drive with 3-phase asymmetric half-bridge inverter, the 3-phase standard inverter such as that used for permanent magnet machines and also induction machines is used for the SynRMs with less current sensors and connection [28]. It is also found that the vibration and acoustic noise of the SRMs can actually be reduced by adopting sinewave excitation [63]. It is worth mentioning that with sinewave excitation, the SRMs are in effect

short-pitched SynRMs while classic SynRMs often employ distributed windings to achieve higher saliency ratio and also larger difference between *d*- and *q*-axis inductances and hence higher reluctance torque. In addition, the SRMs have a doubly salient machine structure with both salient stator and rotor poles, while the SynRMs can have salient pole rotor or with flux barriers inside the rotor core. Therefore, the SRMs with sinewave excitation are named as doubly salient synchronous reluctance machines (DSRMs) in this thesis. In [6] and [11], different winding configurations such as double layer conventional and mutually-coupled DSRMs have been investigated with sinewave excitation. The double layer mutually-coupled DSRM is found to have better torque performance and lower vibration and acoustic noise levels.

Chapter 2. COMPARISON OF INFLUENCE OF CONDUCTION ANGLES BETWEEN DOUBLE LAYER AND SINGLE LAYER SWITCHED RELUCTANCE MACHINES

In this chapter, two novel single layer SRMs with conventional winding (SLC-SRM), and mutually-coupled winding (SLMC-SRM) have been proposed on the basis of the well-established SRMs: double layer conventional SRM (DLC-SRM), double layer mutually-coupled SRM (DLMC-SRM), and fully-pitched SRM (FP-SRM). Additionally, the influence of conduction angles on the performances of the two novel 3-phase 12-slot/8-pole single layer SRMs has been investigated. Both unipolar and bipolar excitations are employed for the SRMs with different conduction angles such as unipolar 120° elec., unipolar 180° elec., bipolar 180° elec., bipolar 240° elec., and bipolar 360° elec. Their flux distributions, self- and mutual-flux linkages and inductances are analysed, and followed by a performance comparison between the two single layer SRMs in terms of on-load torque, average torque, and torque ripple, using two-dimensional finite element analysis (2D FEA). Copper loss, iron loss and machine efficiency have also been investigated with different phase currents and rotor speeds. The predicted results show that the conduction angle of unipolar 120° elec. is the best excitation approach for the SLC-SRM at low current and also modest speed, as its double layer counterpart. However, at high current, the higher average torque is achieved by a conduction angle of unipolar 180° elec. For the SLMC-SRM, bipolar 180° elec. conduction is the most appropriate excitation method to generate a higher average torque but lower torque ripple than others. The lower iron loss is achieved by unipolar excitation for both machines, and the SLC-SRM with unipolar 120° elec. conduction achieves the highest efficiency than others at $10\mathrm{A}_{\mathrm{rms}}$. In addition, the performances of single layer machines have been compared with the established double layer SRMs with conventional and mutually-coupled windings. The prototype SRMs, for both the SLC-SRM and SLMC-SRM, have been built and tested to validate the predictions.

This chapter was published in [64].

2.1 INTRODUCTION

In order to minimize the torque ripple, several reduction strategies have been proposed such as modifying stator and rotor pole geometry [21] [65], employing high rotor pole numbers [24], and profiling the current waveforms [66] [67]. Generally, the SRMs are supplied with unipolar current using an asymmetric bridge inverter as shown in Fig. 2.1, and the conduction angle of phase current for conventional SRMs is less than 120° elec. without any phase overlapping. In order to extend the overlapping time during the commutation for torque ripple reduction, bipolar excitation is applied to the SRMs and a three-phase standard inverter as shown in Fig. 2.2 needs to be employed [20] [68].

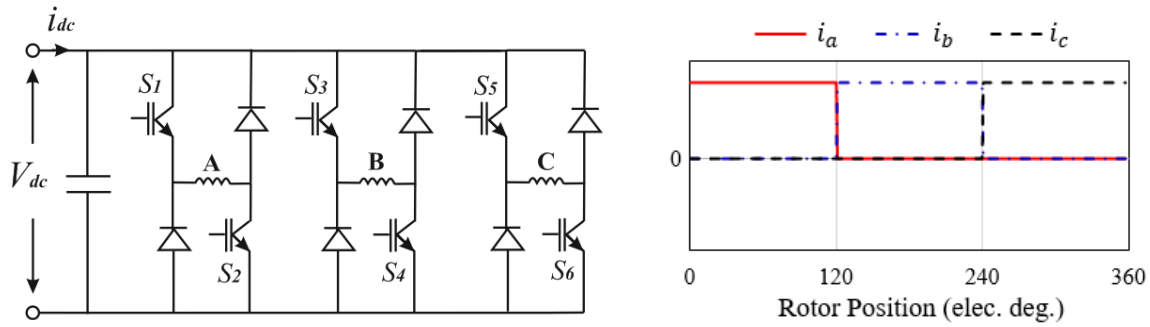

(a) (b)

Fig. 2.1 Unipolar rectangular wave excitation. (a) Asymmetric bridge inverter (b) rectangular current waveform with unipolar 120° elec. conduction [68].

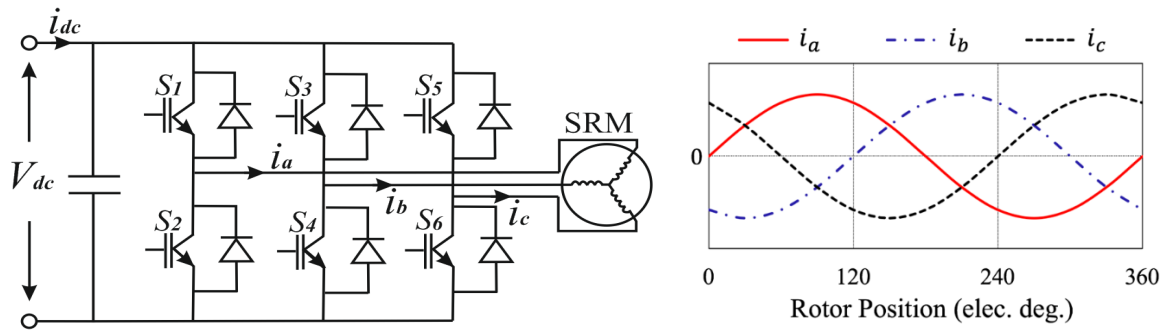

(a) (b)

Fig. 2.2 Sinewave excitation. (a) Three-phase standard inverter, (b) sinewave current waveform [68].

Two bipolar excitations have been investigated in literature, i.e. rectangular and sinusoidal waveforms. In [20], two phases of the SRM are excited simultaneously. Hence, the torque is produced by both self- and mutual-inductances. Moreover, mechanical stress can be mitigated

due to the reduced abrupt change of phase excitation. Similarly, indicated by this hybrid excitation, the vibration and acoustic noise are reduced [15]. It has also been found that with sinusoidal bipolar excitation, torque ripple of the DLC-SRM can be reduced when compared with unipolar and bipolar excitations with rectangular waveforms [69]. In addition, the DLMC-SRM with sinusoidal bipolar excitation produced higher average torque but lower torque ripple than that supplied with rectangular waveforms current [70]. However, the average torque of the DLC-SRM is often lower than that of the DLMC-SRM due to the nature of self- and mutual-inductances [22]. In order to further improve the torque capability, the FP-SRM with single layer winding structure has been proposed [19]. It has much higher position varying mutual-inductance and can produce high average torque but low torque ripple [22] [19] [62]. However, the longer end-winding of the FP-SRM will lead to higher copper loss, limiting the machine efficiency.

Combined with the merits of single layer FP-SRM and short-pitched DLC-SRM/DLMC-SRM, two novel short pitched, single layer SRMs have been proposed. In addition, due to the different waveforms of the derivatives of self- and mutual-inductances with respect to rotor positions, the current waveforms can be tailored accordingly in order to improve the torque performance. In this chapter, the single layer SRMs will be supplied with both the unipolar and bipolar excitations with rectangular waveforms and variable conduction angles such as unipolar 120° elec., unipolar and bipolar 180° elec., bipolar 240° elec. and bipolar 360° elec. will be employed. Hence, the contribution of this chapter is to comprehensively investigate two novel single layer SRMs supplied with different unipolar and bipolar excitations. The influence of conduction angles on the machine performance is studied and compared in terms of instantaneous torque, average torque and torque ripple at both low current and high current levels. Furthermore, after the calculation of copper loss and iron loss, machine efficiency has been investigated under different speeds and currents. Based on the obtained results, the appropriate excitation method can be found for different machines in order to achieve higher torque, lower torque ripple and also higher efficiency under different conditions.

2.2 WINDING CONFIGURATIONS OF SRMS

As previously mentioned, different winding configurations have significant impact on the electromagnetic performances of the SRMs. For consistency and clarity, all the machines have the same leading dimensions and design features as listed in TABLE 2.1. The winding configurations and flux distributions of the established 3-phase, 12-slot/8-pole SRMs are

shown in Fig. 2.3(a), (b), and (e) with double layer conventional (DLC-), double layer mutually-coupled (DLMC-) and fully-pitched (FP-) windings, respectively. While, the two novel SRMs with single layer conventional (SLC-) and single layer mutually-coupled (SLMC-) windings are shown in Fig. 2.3 (c) and (d), respectively. The rotors of the SRMs are at the aligned position and the phase A is supplied with a 10A DC current. Moreover, the different flux paths in the SRMs result in different coil magnetic polarities, as shown in TABLE 2.2.

TABLE 2.1 MACHINE LEADING DIMENSIONS AND DESIGN PARAMETERS

Stator slot number	12	Active length (mm)	60
Rotor pole number	8	Turn number per phase	132
Stator outer radius (mm)	45	Coil packing factor	0.37
Airgap length (mm)	0.5	Rated RMS current (A)	10
Rotor outer radius (mm)	26.5	Current density (A_{rms}/mm^2)	5.68
Rotor inner radius (mm)	15.7		

TABLE 2.2 INFLUENCE OF WINDING CONFIGURATIONS ON COIL MAGNETIC POLARITIES OF THE PHASE A

Winding configurations	Coil magnetic polarities
DLC	SNSN
DLMC	SSSS
SLC	SN
SLMC	SS
FP	NN

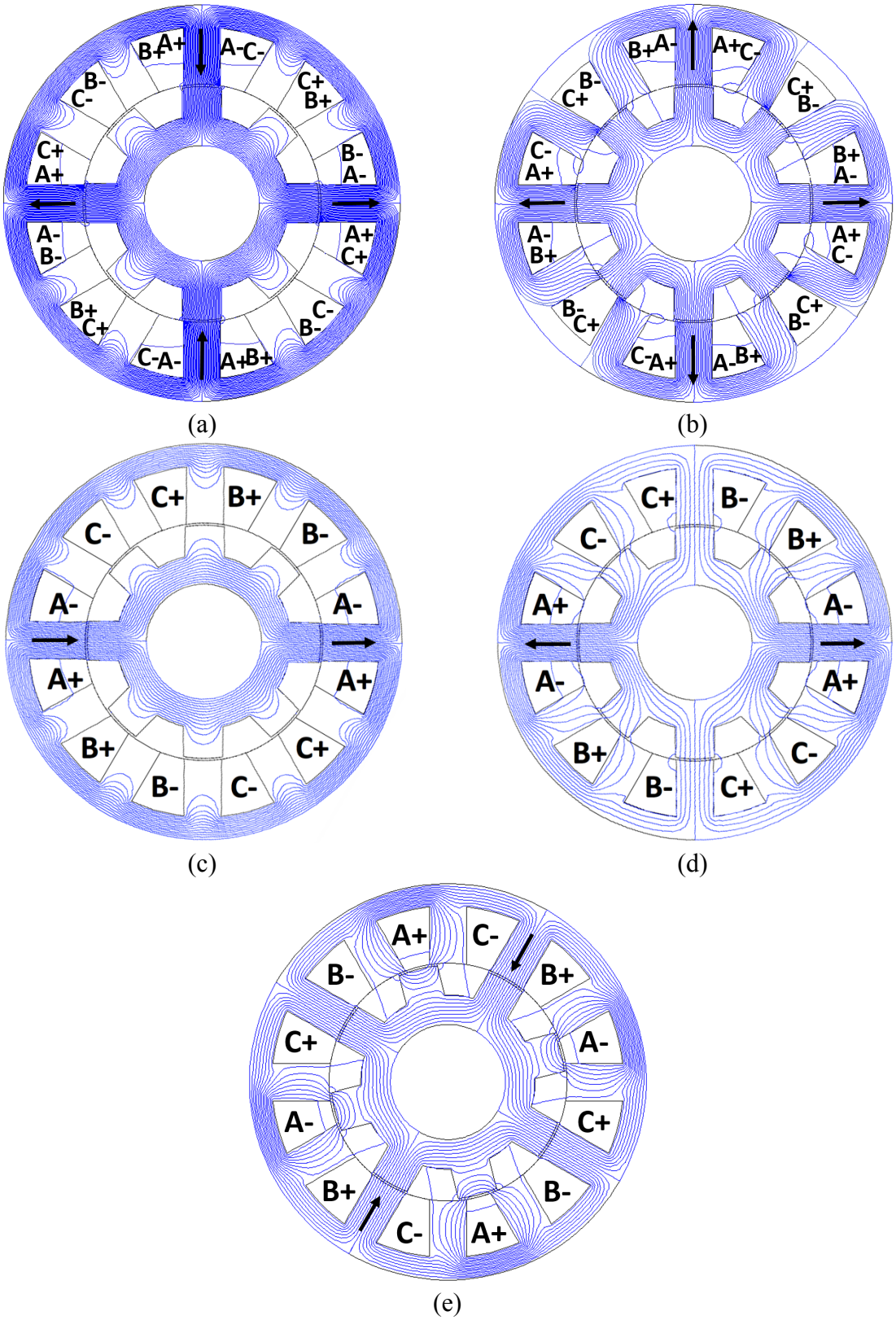

Fig. 2.3 Comparison of winding configurations and flux distributions between 3-phase 12-slot/8-pole (a) DLC-SRM, (b) DLMC-SRM, (c) SLC-SRM, (d) SLMC-SRM and (e) FP-SRM. The rotor is at aligned position and the phase A is supplied with a 10A DC current.

2.2.1 REVIEW OF THE ESTABLISHED SRMS

In the two well-established 3-phase, 12-slot/8-pole double layer SRMs (DLC- and DLMC-SRMs), each phase winding consists of 4 concentrated coils, and each stator tooth is wound with one coil. As a result, two coils belonging to two different phases are located in a given stator slot, leading to, at least in terms of MMF distribution, an arrangement akin to a double layer winding. This also dictates that the coil pitch is equal to the slot pitch ($2\pi/N_s$ where N_s is the stator slot number), which is smaller than the pole pitch ($2\pi/N_r$ where N_r is the rotor number). Hence, this gives rise to a short-pitched winding. In addition, the magnetic polarities of the coils of one phase, e.g. phase A, for the DLC-SRM are SNSN, while for DLMC-SRM, they are SSSS ("+" stands for GO conductor while "-" stands for RETURN conductor in Fig. 2.3).

In contrast, for the FP-SRM, each phase winding comprises 2 coils and each coil spans 3 slot pitches, leading to a fully-pitched winding. Moreover, it can be regarded as a single layer winding since only one coil is located in a given stator slot and the coil magnetic polarities of phase A are NN. However, as a consequence of the fully-pitched winding, the end-windings of the FPSRM will be significantly longer than those of a corresponding short-pitched SRMs, in turn leading to higher copper loss.

In addition, it will be apparent that there is little mutual coupling flux between phases in the DLC-SRM, as shown in Fig. 2.3(a). However, as will be apparent from Fig. 2.3(b) and (e), the fluxes of phase A in the DLMC-SRM and the FP-SRM also link the coils of phases B and C. As a consequence, appreciable mutual flux is present and this will contribute to torque generation as noted previously and has been detailed in [21] and [62].

2.2.2 TWO NOVEL SINGLE LAYER SRMS

The winding configurations of the two single layer SRMs were designed based on the aforementioned DLC- and DLMC-SRMs, as shown in Fig. 2.3(a) and (b), respectively. The magnetic flux distribution in the aligned position for the SLC-SRM and SLMC-SRM is shown in Fig. 2.3 (c) and (d), respectively. Again, only the phase A is supplied by a 10A DC current. Similar to the established DLC-SRM, it is found that there exists almost no mutual flux in the SLC-SRM, hence better fault tolerant capability [71]. However, as was the case with the DLMC-SRM discussed above, appreciable mutual flux is present in the SLMC-SRM, which will contribute to torque generation.

In addition, the coil magnetic polarities of phase A are SN for the SLC-SRM (similar to the DLC-SRM), and SS for the SLMC-SRM (similar to the DLMC-SRM). However, it can be found that each phase of the single layer SRMs comprises 2 coils, which is half of that of the double layer SRMs, and each coil is wound around one stator tooth, leading to concentrated winding structure. Therefore, their end-windings are much shorter than the same sized FP-SRM, leading to lower copper loss [72]. Moreover, similar to the FP-SRM, the single layer SRMs also have one coil located in one stator slot, and can potentially have higher inductance variation against rotor position (number of turns per phase is the same for all the SRMs) and hence higher torque production without magnetic saturation. However, in order to maintain the same number of turns per phase as for the established double layer SRMs, each coil of the single layer SRMs has double number of turns compared with the double layer SRMs. This leads to higher spatial concertation of MMF. Thus, the SLC-SRM and SLMC-SRM, in particular the former, are more sensitive to magnetic saturation and hence will have lower overload torque capability, as will be investigated later. In contrast, the less MMF concentration in the double layer SRMs indicates less flux density, and hence less sensitivity to magnetic saturation, in particular the DLMC-SRM can have better overload torque capability.

2.3 Influence of Winding Configurations on Self- and Mutual-Flux Linkages

Due to magnetic saturation, the flux linkage loci with increasing phase current are nonlinear. They are also determined by the rotor position due to the doubly salient structure. The maximum flux linkage is achieved at aligned position while the minimum occurs at unaligned position, as shown in Fig. 2.4, where the phase A is supplied with an increasing DC current.

Fig. 2.4 and Fig. 2.5 show the self- and mutual-flux linkages against phase DC currents up to 40A of the SRMs, where only the phase A is energized. It can be found that the saturation current of the DLMC-SRM is much higher than that of the DLC-SRM and also the FP-SRM. In addition, the SLMC-SRM can resist a higher saturation current than the SLC-SRM because it is less sensitive to magnetic saturation. Moreover, it is worth noting that since the single layer SRMs have doubled number of turns per coil compared with the double layer SRMs, leading to higher MMF concentration. As a result, it can be observed that the single layer SRMs are more prone to magnetic saturation than their double layer counterparts.

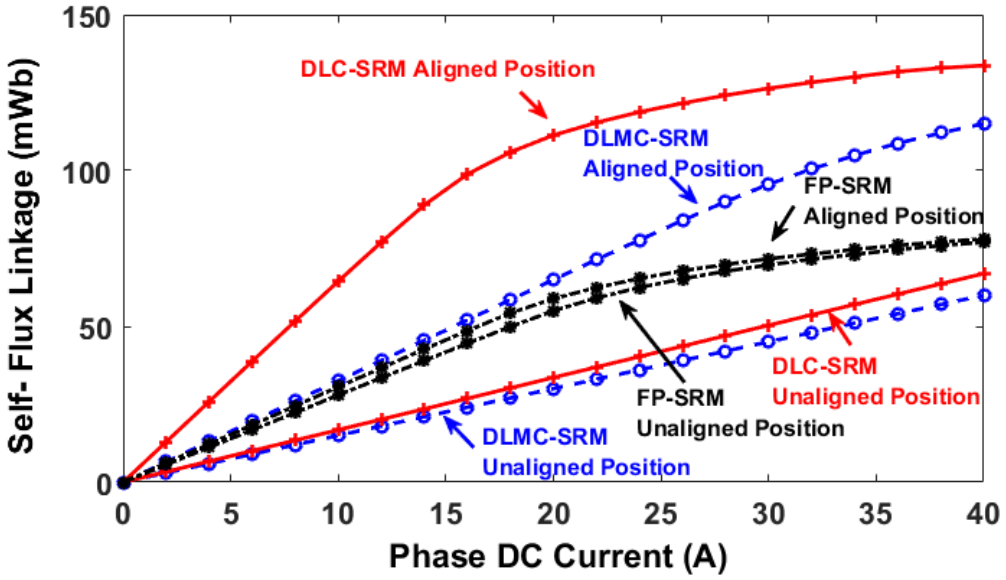

(a)

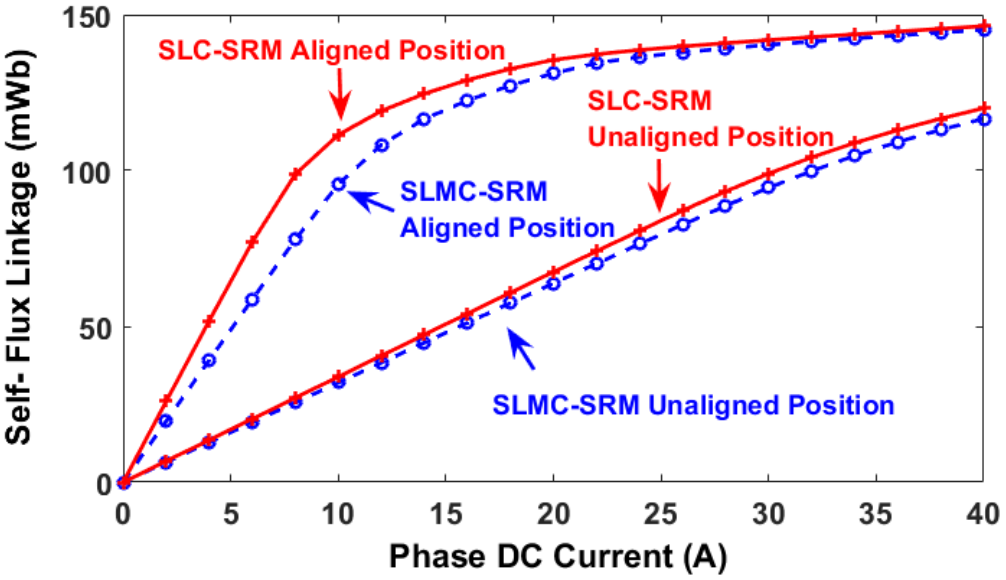

(b)

Fig. 2.4 Phase A self-flux linkage against phase DC current. (a) Double layer SRMs and FP-SRMs, (b) single layer SRMs.

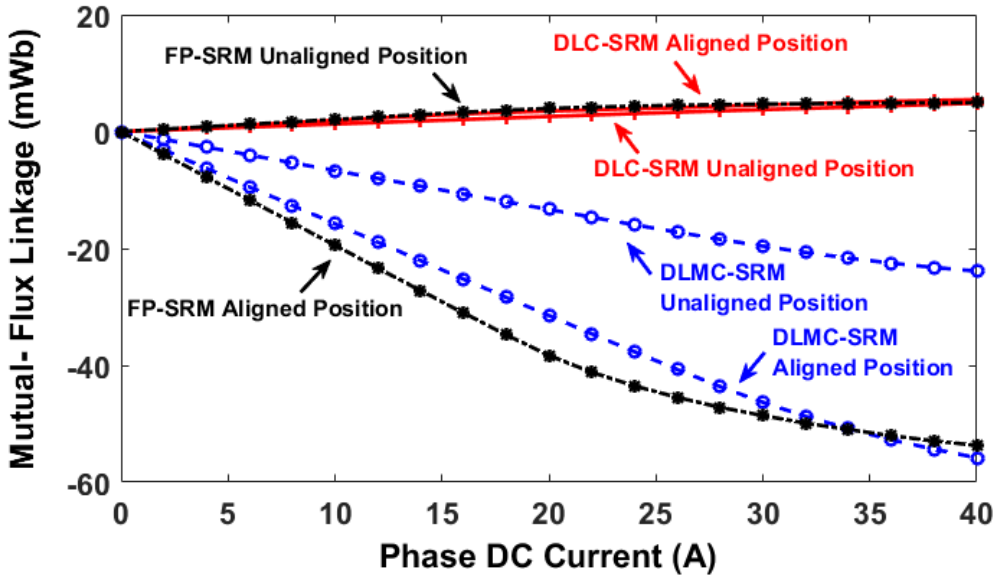

(a)

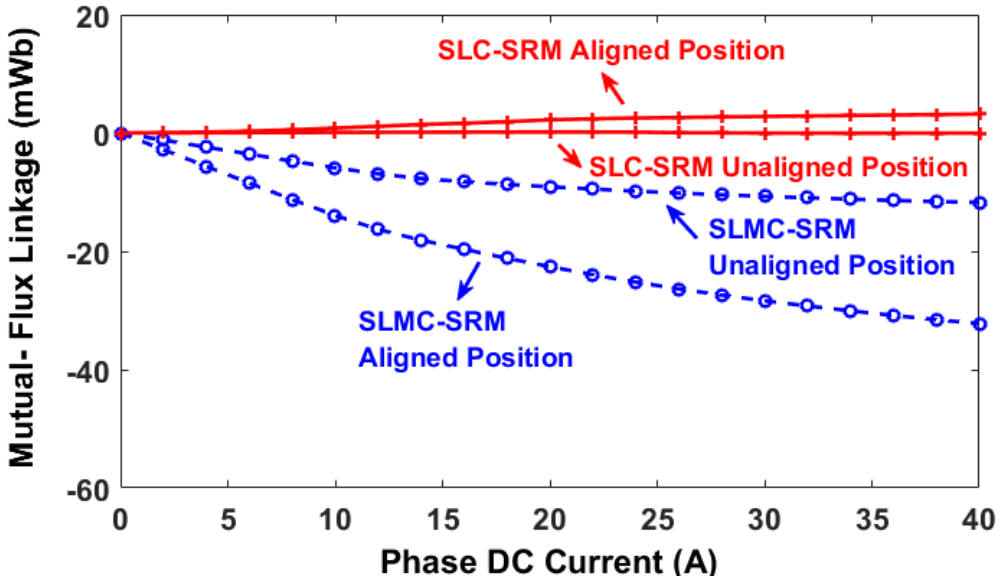

(b)

Fig. 2.5 Mutual-flux linkage against phase DC current. (a) Double layer SRMs and FP-SRMs, (b) single layer SRMs.

The area enclosed by the loci between aligned and unaligned positions is the co-energy (W'), which converts the electrical energy to mechanical energy of the SRMs, or vice versa. According to the co-energy theory, the instantaneous torque T and average torque T_{av} can be given by [3] [73]:

$$T = \left.\frac{\partial W'(i,\theta)}{\partial \theta}\right|_{i=constant} \tag{2.1}$$

$$T_{av} = \frac{mp}{2\pi} \times W' \tag{2.2}$$

where i is the instantaneous phase current, θ is the rotor position, m is number of phase, and p is pole pair number.

Therefore, the torque produced by self-flux linkage (self-inductance) of the DLC- and SLC-SRMs will be slightly higher than that of the DLMC- and SLMC-SRMs, respectively, due to the bigger area enveloped by the aligned and unaligned self-flux linkages in Fig. 2.4. However, the torque produced by self-flux linkage of FP-SRM will be nearly null due to the smallest enveloped area.

The area enclosed by the aligned and unaligned mutual-flux linkages of both the DLC-SRM and SLC-SRM is significantly smaller than the DLMC- and SLMC-SRMs, respectively, as shown in Fig. 2.5. In addition, the area of both the double layer SRMs and single layer SRMs is smaller than that of the FP-SRM. Hence, it can be predicted that the FP-SRM, DLMC-SRM and SLMC-SRM could have higher torque produced by mutual-flux linkage (mutual-inductance). This means that the current waveforms will have significantly different influences on the performance of the SRMs, as will be detailed in the following sections.

2.4 Influence of Winding Configurations on Self- and Mutual-Inductances

In order to employ the appropriate current waveforms for the SRMs, self- and mutual-inductances have been analysed separately. The different flux paths as shown in Fig. 2.3 will have a profound impact on the self- and mutual-inductances. This is mainly due to the fact that the relationship between the phase flux linkage and the apparent inductances, which can be described by

$$L_a = \frac{\psi_A}{I_A} \tag{2.3}$$

$$M_{ab} = \frac{\psi_B}{I_A} \tag{2.4}$$

where L_a is self-inductance of the phase A, and M_{ab} is mutual-inductance between the phases A and B. I_A is phase current of the phase A. ψ_A and ψ_B are flux-linkages of the phases A and B, respectively. Here, only the phase A is selected as an example, the inductances of other phases can be calculated using the same method.

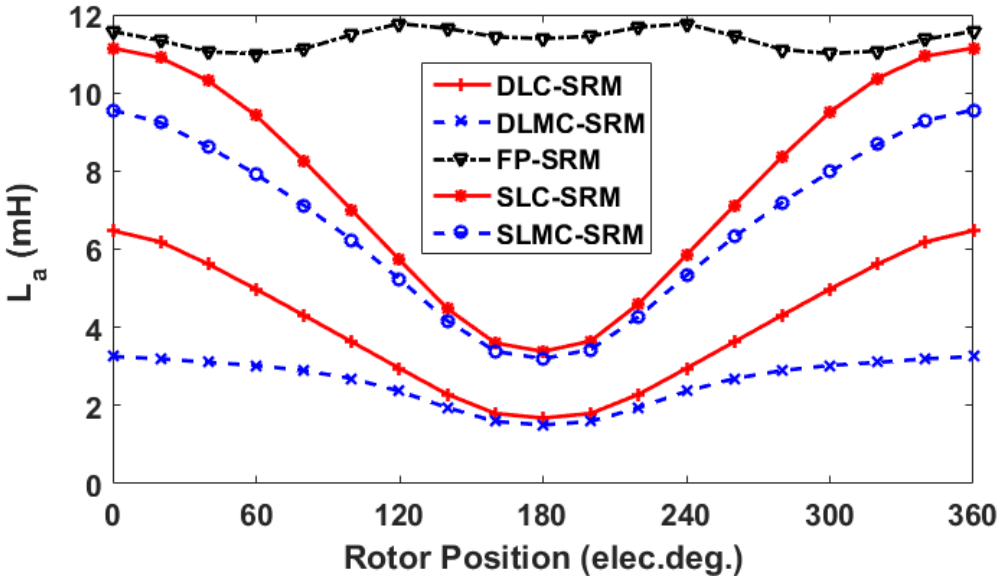

(a)

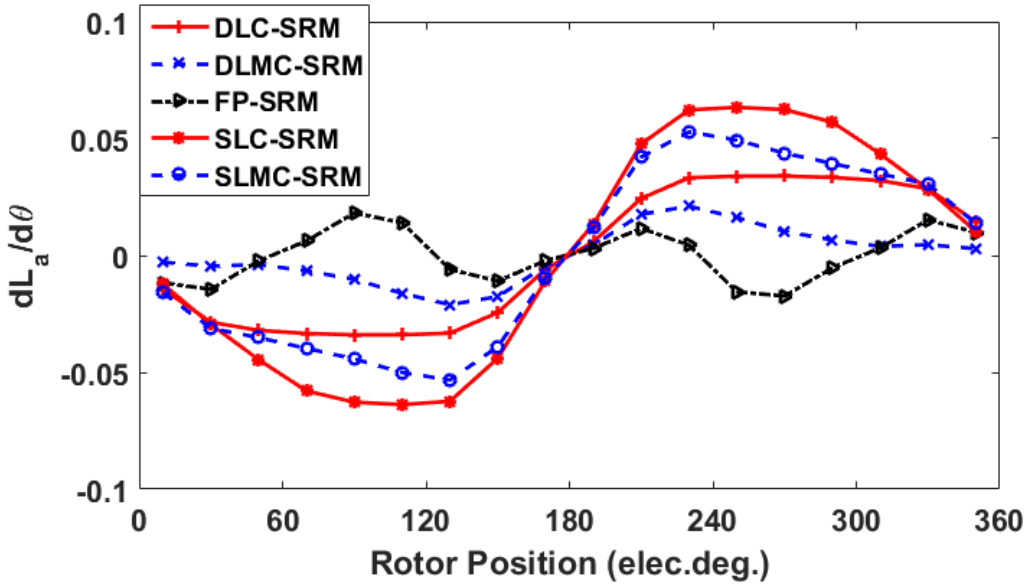

(b)

Fig. 2.6 Comparison of (a) $L_a$and (b) $dL_a/d\theta$. Phase A is supplied with a 10A DC current.

The comparison of L_a, M_{ab} and their derivatives with respect to rotor position for the DLC-, DLMC-, FP-, SLC-, and SLMC-SRMs have been carried out, as shown in Fig. 2.6 and Fig. 2.7, in which the phase A is supplied with a 10A DC current. In addition, the 0° elec. represents the rotor aligned position. The self-inductances L_b and L_c, and mutual-inductances M_{bc} and M_{ca} are respectively shifted from L_a and M_{ab} by 120° elec. while with the same amplitudes. Therefore, they are not shown here to avoid duplication.

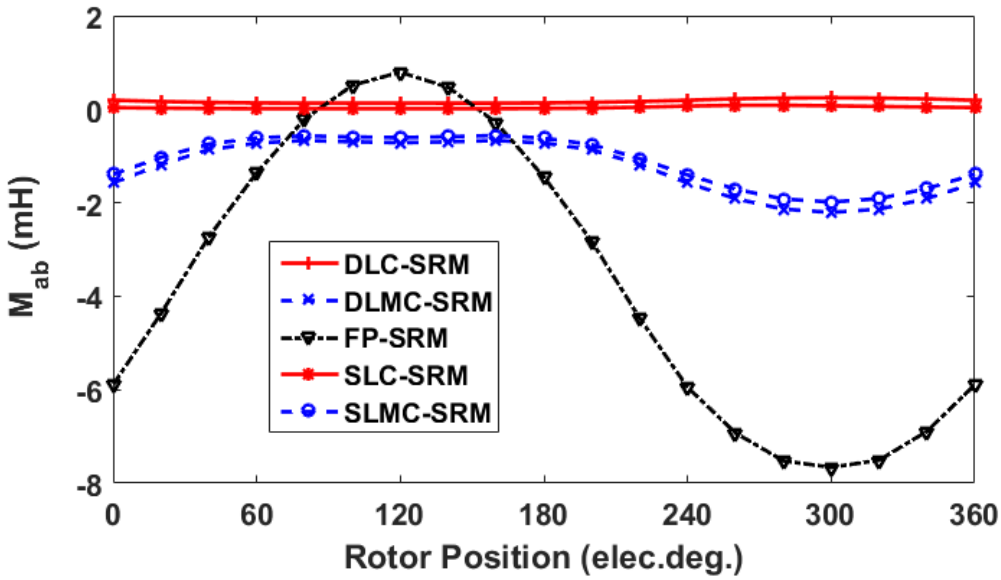

(a)

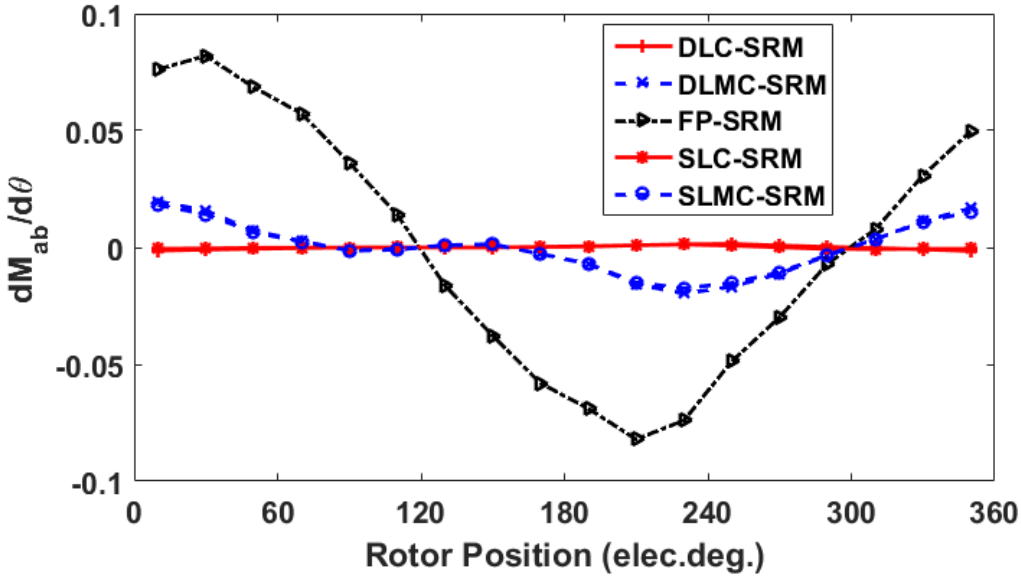

(b)

Fig. 2.7 Comparison of (a) M_{ab} and (b) $dM_{ab}/d\theta$. Phase A is supplied with a 10A DC current.

The inductance comparison shows that the amplitude of self-inductance of the FP-SRM is the highest, as shown in Fig. 2.6 (a), but it varies hardly with rotor positions, as shown in Fig. 2.6 (b). Moreover, it has different frequency compared with other SRMs and therefore will not contribute to torque production. For the double and single layer SRMs, the amplitude of $dL_a/d\theta$ of the DLC- and SLC-SRMs is slightly higher than that of the DLMC- and SLMC-SRMs, respectively. It is worth noting that for the SRMs, the derivatives of self- and mutual-inductances to rotor position will largely determine the torque production. Hence, the DLC- and SLC-SRMs are likely to produce higher self-torque (torque produced by self-inductance) than the DLMC- and SLMC-SRMs, respectively [22].

Fig. 2.7 (a) shows that the absolute value of amplitude of mutual-inductance of the FP-SRM is much higher than that of the DLMC-SRM and the SLMC-SRM, but it is close to zero of the DLC-SRM and SLC-SRM. This is the same case for the derivatives of relevant mutual-inductances, as shown in Fig. 2.7 (b). Therefore, although $dL_a/d\theta$ of the FP-SRM is negligible for electromagnetic torque production, the significantly higher $dM_{ab}/d\theta$ hence higher mutual-torque (torque produced by mutual-inductance) would still allow the FP-SRM to produce higher resultant output torque. On the contrary, $dM_{ab}/d\theta$ of the DLC-and SLC-SRMs is nearly null and will not contribute to torque production. Hence, the DLC- and SLC-SRMs will only have the self-torque. Accordingly, the DLMC- and SLMC-SRMs have the potential to produce higher torque than the DLC- and SLC-SRMs, respectively, since both the self- and mutual-inductances could contribute to torque.

Furthermore, the amplitude of the $dL_a/d\theta$ in the SLC- and SLMC-SRMs are nearly twice as high as that in the DLC- and DLMC-SRMs, respectively. However, the amplitudes of $dM_{ab}/d\theta$ remain almost the same. Therefore, it can be predicted that the SRMs with single layer winding structures could produce higher torque than their relevant double layer counterparts if heavy magnetic saturation does not occur. However, it is worth noting that the torque can be produced by both the derivatives of self- and mutual-inductances with respect to rotor position, and also directly depends on the current waveforms. In addition, in order for the mutual-inductance to contribute positively to the resultant torque, the 3-phase current waveforms need to be properly designed, as will be detailed in the following section.

2.5 RECTANGULAR CURRENT WAVEFORMS WITH DIFFERENT CONDUCTION ANGLES

2.5.1 ON-LOAD TORQUE EXPRESSION

The electromagnetic torque of the SRMs on the basis of self- and mutual-inductances is given by:

$$T = \overbrace{\frac{1}{2}{i_a}^2\frac{dL_a}{d\theta} + \frac{1}{2}{i_b}^2\frac{dL_b}{d\theta} + \frac{1}{2}{i_c}^2\frac{dL_c}{d\theta}}^{T_{self}} + \overbrace{i_a i_b\frac{dM_{ab}}{d\theta} + i_b i_c\frac{dM_{bc}}{d\theta} + i_a i_c\frac{dM_{ac}}{d\theta}}^{T_{mutual}} \tag{2.5}$$

where i_a, i_b and i_c are 3-phase instantaneous currents. It can be seen that the resultant torque can be divided into two components, i.e. self-torque T_{self} and mutual-torque T_{mutual}. Due to the foregoing difference in self- and mutual-inductances, the components of electromagnetic torque for the SRMs can be summarized in TABLE 2.3. Since there is no mutual-inductance in the DLC- and SLC-SRMs, the torque of which will be purely produced by self-inductances. However, the self-inductances of the FP-SRM although exist but have negligible variation against rotor position. Therefore, the torque of the FP-SRM can be assumed purely due to the mutual-inductance. The DLMC- and SLMC-SRMs will take advantage of both the self- and mutual-inductances to produce the torque.

TABLE 2.3 ELECTROMAGNETIC TORQUE COMPARISON

Machine Type	Electromagnetic Torque
DLC-SRM, SLC-SRM	$T = T_{self}$
FP-SRM	$T = T_{mutual}$
DLMC-SRM, SLMC-SRM	$T = T_{self} + T_{mutual}$

2.5.2 CURRENT WAVEFORMS WITH DIFFERENT CONDUCTION ANGLES

As mentioned previously, not only the self- and mutual-inductances but also the current waveforms will have influence on the electromagnetic torque. Different conduction angles will

lead to various performances for different SRMs due to their specific features of self- and mutual-inductances. The two novel single layer SRMs, i.e. SLC-SRM and SLMC-SRM are selected for comprehensive investigation in this chapter.

2.5.2.1 DIFFERENT CONDUCTION ANGLES

For rectangular wave excitation, the value of RMS current is determined by the conduction angle. TABLE 2.4 shows the peak current, at the same RMS current of 10A, for conduction angle of $120°$, $180°$, $240°$ and $360°$ elec. which are 17.3A, 14.1A, 12.2A and 10A respectively.

TABLE 2.4 CONDUCTION ANGLE VS PEAK CURRENT FOR THE SAME RMS CURRENT (10A)

Conduction angle (elec. deg.)	I_{pk}
120	$\sqrt{3}I_{rms}$=17.3A
180	$\sqrt{2}I_{rms}$=14.1A
240	$\sqrt{3/2}I_{rms}$=12.2A
360	I_{rms}=10A

2.5.2.2 CURRENT WAVEFORMS WITH RESPECT TO SELF- AND MUTUAL-INDUCTANCES

Based on the torque equation (2.5), the self-torque is independent of the sign of the current. It depends only on the sign of $dL/d\theta$. It is found in Fig. 2.6 (b) that the positive $dL/d\theta$ of both single layer SRMs lasts for $180°$ elec. and the two rotor positions for $dL/d\theta = 0$ can be expressed as

$$\begin{bmatrix}\theta_1\\ \theta_2\end{bmatrix} = \begin{bmatrix}(\pi/N_r - \varphi/2)\times N_r\\ (2\pi/N_r - \varphi/2)\times N_r\end{bmatrix} \tag{2.6}$$

where N_r is rotor pole number and φ is angle between initial rotor position and rotor aligned position in mechanical degrees (θ_1 and θ_2 are illustrated in Fig. 2.9 (a)).

When the rotor poles are approaching the aligned position, $dL/d\theta$ is positive, and hence a positive self-torque is produced, regardless of the sign of the current. In contrast, when the rotor poles are approaching the unaligned position, the self-torque is negative, again regardless of

the sign of the current [23]. Hence, the phase current should be applied when $dL/d\theta$ is positive in order to make sure $\frac{1}{2}{i_a}^2\frac{dL_a}{d\theta}$ is positive. Furthermore, a positive mutual-torque relating to two phases, e.g. phases A and B, can be produced when $i_a i_b \frac{dM_{ab}}{d\theta}$ is positive. This requires i_a and i_b to have the same sign when $\frac{dM_{ab}}{d\theta}$ is positive, or i_a and i_b to have opposite signs when $\frac{dM_{ab}}{d\theta}$ is negative. It can be found that $dM/d\theta$ is positive when the rotor pole approaches the position from Fig. 2.8(a) to (b). Hence, 3-phase currents should be considered together with the signs of $dM/d\theta$ to ensure an optimized positive output torque.

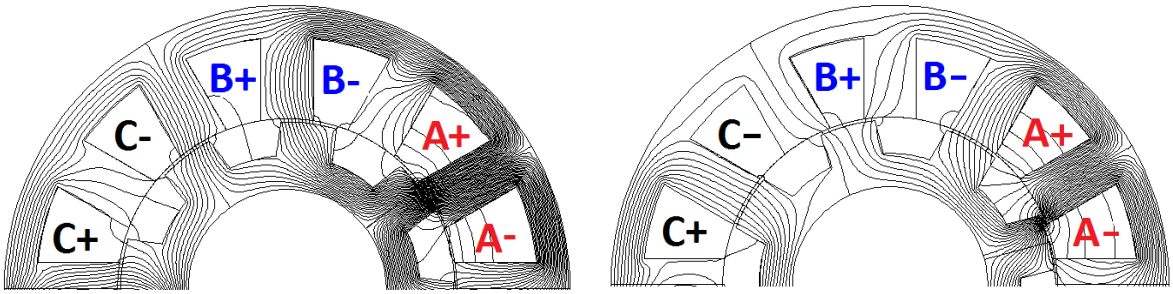

(a) (b)

Fig. 2.8 Rotor positions of the SLMC-SRM when $\frac{dM}{d\theta} = 0$, (a) at maximum $|M_{ab}|$, (b) at minimum $|M_{ab}|$. Phase A is supplied with 10A DC current.

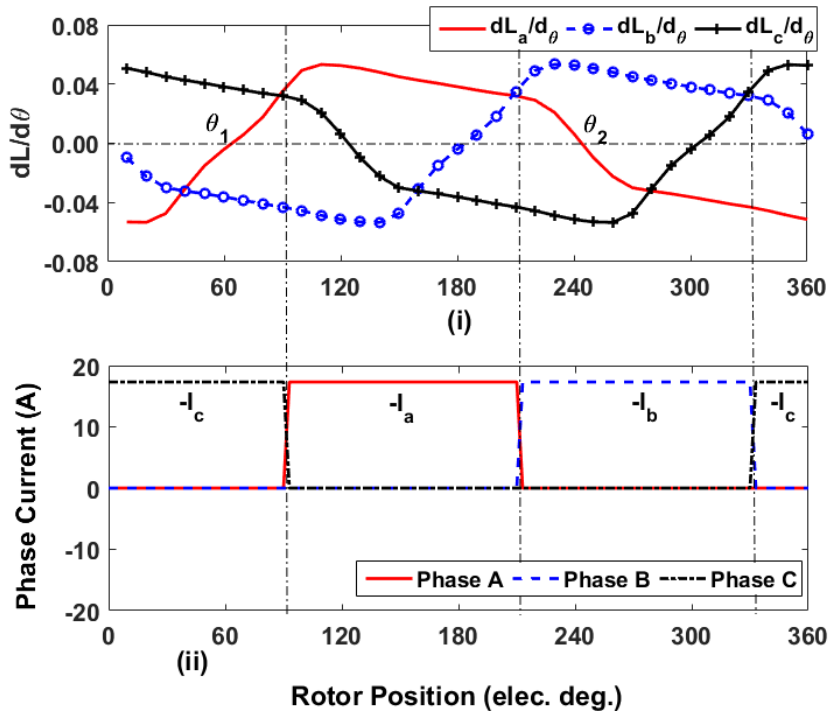

(a)

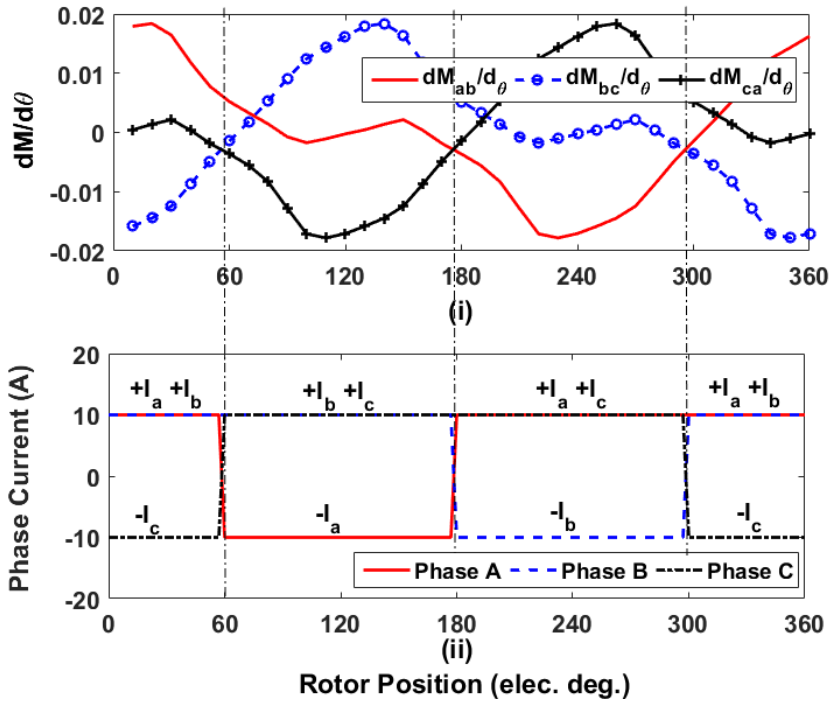

(b)

Fig. 2.9 Derivatives of inductance of the SLMC-SRM with respect to rotor position and relevant current waveform for (a) high self-torque generation: (i) $dL/d\theta$, (ii) phase currents with unipolar 120° elec. conduction, (b) high mutual-torque generation: (i) $dM/d\theta$, (ii) phase currents with bipolar 360° elec. conduction. Phases A, B and C are supplied with a $10A_{rms}$ current, respectively.

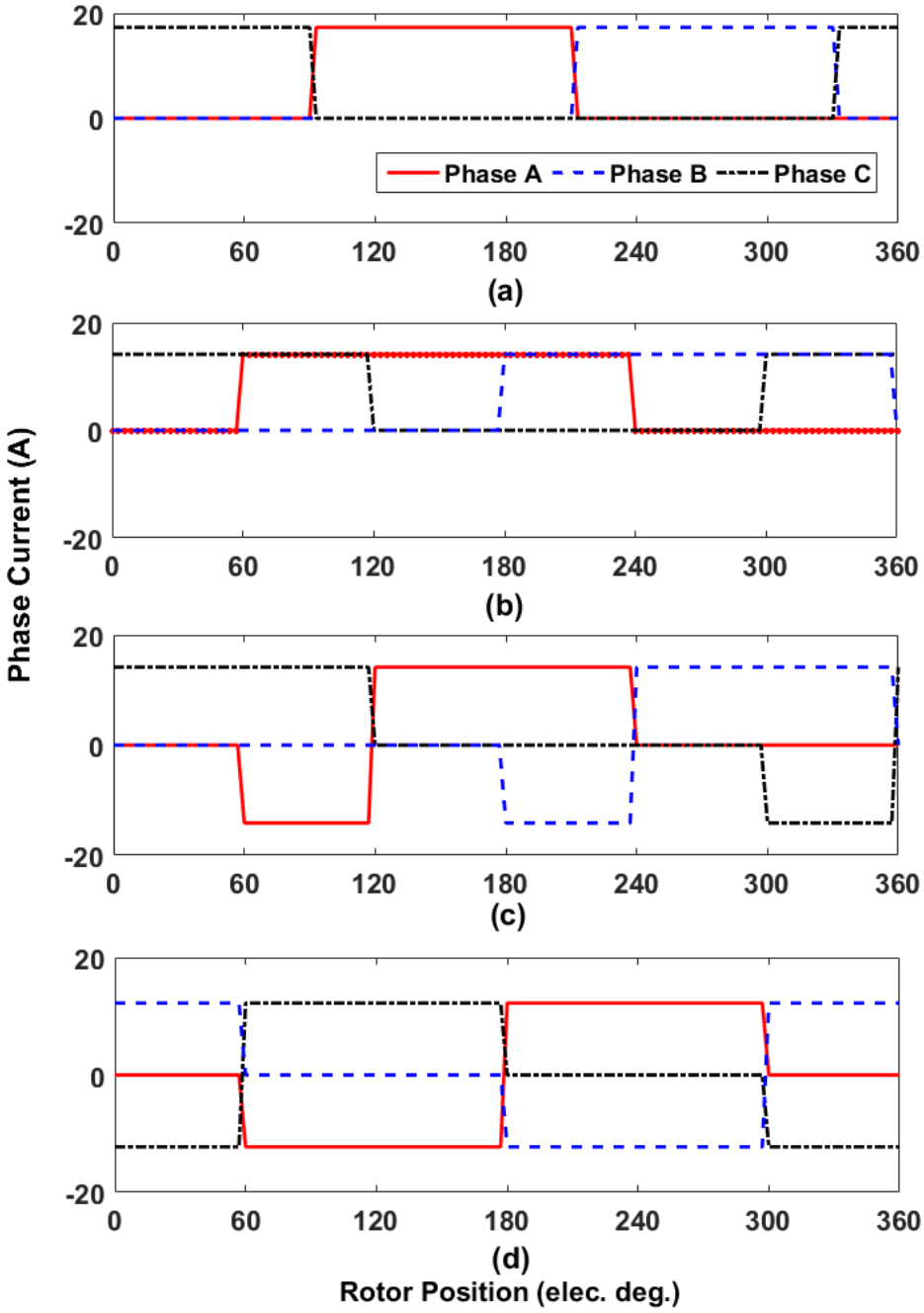

Fig. 2.10 Unipolar and bipolar excitations with rectangular waveforms and different conduction angles for the SLC-SRM and SLMC-SRM. (a) Unipolar 120° elec., (b) unipolar 180° elec., (c) bipolar 180° elec., (d) bipolar 240° elec.

Fig. 2.9 (a) and (b) are the examples to analyse the high self-torque and mutual-torque generation of the SLMC-SRM, respectively. The unipolar 120° elec. is proposed for only the self-torque generation since no mutual-torque can be generated without two phases are

simultaneously excited. For high self-torque generation, it can be found in Fig. 2.9 (a) that the phase current has been injected when the $dL/d\theta$ has positive and also the highest magnitude. However, the bipolar 360° elec. is proposed to have a negative 120° elec. conduction and a positive 240° elec. conduction in order to fully utilize the mutual-inductance for torque generation. For example, from rotor position 60° elec. to 180° elec., $dM_{bc}/d\theta$ is positive. Hence, in order to produce a positive mutual-torque between phases B and C, positive i_b and i_c are applied. Additionally, i_a needs to be negative to achieve a positive mutual-torque between phases A and C due to negative $dM_{ac}/d\theta$. The mutual-torque between phases A and B in this region will be negligible regardless the signs of i_a and i_b since $dM_{ab}/d\theta$ is nearly null. Similarly, it can be found that positive mutual-torques are also generated at other rotor positions when supplied by the bipolar 360° elec. conduction.

According to both the self- and mutual-inductance variations, rectangular current waveforms have been carried out in Fig. 2.10, which aim to achieve a balance between the self-torque and the mutual-torque so to maximize the resultant output torque. It can be found that the bipolar 180° elec. excitation consists of a negative 60° elec. conduction followed by a positive 120° elec. conduction. The bipolar 240° elec. excitation is comprised of a negative and a positive 120° elec. conduction angles.

For simplicity, these conduction methods can be further expressed as below.

(1) Unipolar x° elec. conduction ($x \leq 180$)

$$i_A(\theta) = \begin{cases} 0 & 0 \leq \theta < \frac{1}{2}[(\theta_1 + \theta_2) - x] \\ I_{pk} & \frac{1}{2}[(\theta_1 + \theta_2) - x] \leq \theta < \frac{1}{2}[(\theta_1 + \theta_2) + x] \\ 0 & \frac{1}{2}[(\theta_1 + \theta_2) + x] \leq \theta < 360 \end{cases} \tag{2.7}$$

(2) Bipolar 180° elec. conduction

$$i_A(\theta) = \begin{cases} 0 & 0 \le \theta < \theta_1 \\ -I_{pk} & \theta_1 \le \theta < \theta_1 + 60 \\ I_{pk} & \theta_1 + 60 \le \theta < \theta_2 \\ 0 & \theta_2 \le \theta < 360 \end{cases} \tag{2.8}$$

(3) Bipolar 240° elec. conduction

$$i_A(\theta) = \begin{cases} 0 & 0 \le \theta < \theta_1 \\ -I_{pk} & \theta_1 \le \theta < \theta_1 + 120 \\ I_{pk} & \theta_1 + 120 \le \theta < \theta_2 + 60 \\ 0 & \theta_2 + 60 \le \theta < 360 \end{cases} \tag{2.9}$$

(4) Bipolar 360° elec. conduction

$$i_A(\theta) = \begin{cases} I_{pk} & 0 \le \theta < \theta_1 \\ -I_{pk} & \theta_1 \le \theta < \theta_1 + 120 \\ I_{pk} & \theta_1 + 120 \le \theta < 360 \end{cases} \tag{2.10}$$

The phases B and C will have the same amplitude but out of phase of 120^o elec.

2.6 PERFORMANCE COMPARISON BETWEEN SRMS WITH DIFFERENT CONDUCTION ANGLES

2.6.1 ON-LOAD TORQUE

On-load torques of the single layer SRMs have been calculated by 2D FEA at 10A phase RMS current, as shown in Fig. 2.11. It can be found that the on-load torques have different waveforms due to different current waveforms. TABLE 2.5 summarizes the comparison of average torque at rated current $10A_{rms}$. The SLC-SRM produces its highest average torque with unipolar 120° elec. conduction. The SLMC-SRM supplied by bipolar 180° elec. conduction achieves its highest average torque.

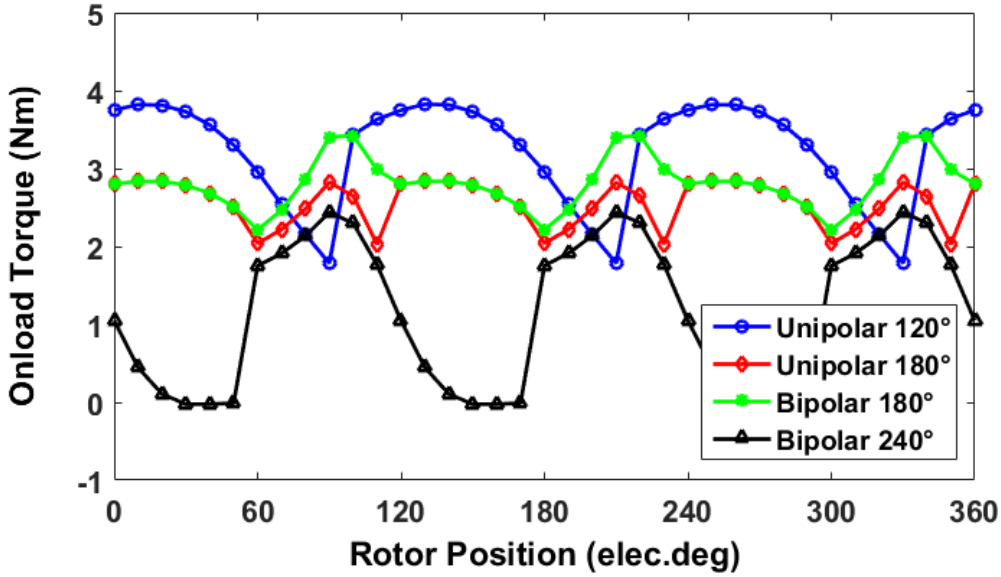

(a)

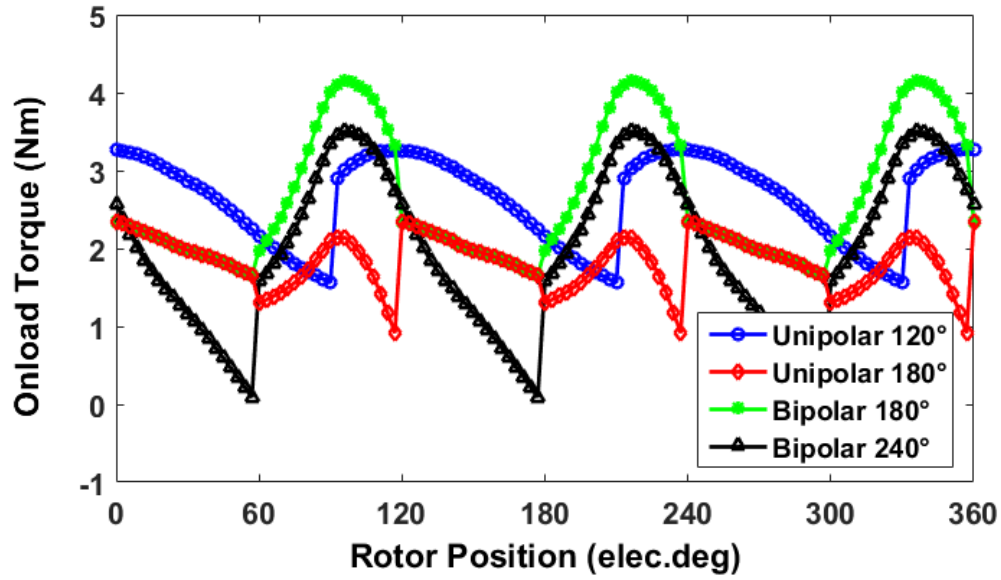

(b)

Fig. 2.11 On-load torque comparison of (a) SLC-SRM, and (b) SLMC-SRM at 10A phase RMS current.

TABLE 2.5 AVERAGE TORQUE AT RATED CURRENT $10A_{RMS}$

Conduction Angle (elec.)	Rated Average Torque (Nm)	
	SLC-SRM	SLMC-SRM
Unipolar 120°	3.22	2.62
Unipolar 180°	2.82	1.88
Bipolar 180°	2.57	2.65
Bipolar 240°	1.15	2.06

2.6.2 AVERAGE TORQUE AND TORQUE RIPPLE

With different current waveforms in Fig. 2.10, average torque and torque ripple of the single layer SRMs from 0A to 40A phase RMS current have been investigated, as shown in Fig. 2.12 and Fig. 2.13. Torque ripple is calculated according to maximum (T_{max}), minimum (T_{min}) and average torque (T_{av}) for an electrical period as shown below:

$$T_{ripple} = \frac{T_{max} - T_{min}}{T_{av}} \times 100\% \tag{2.11}$$

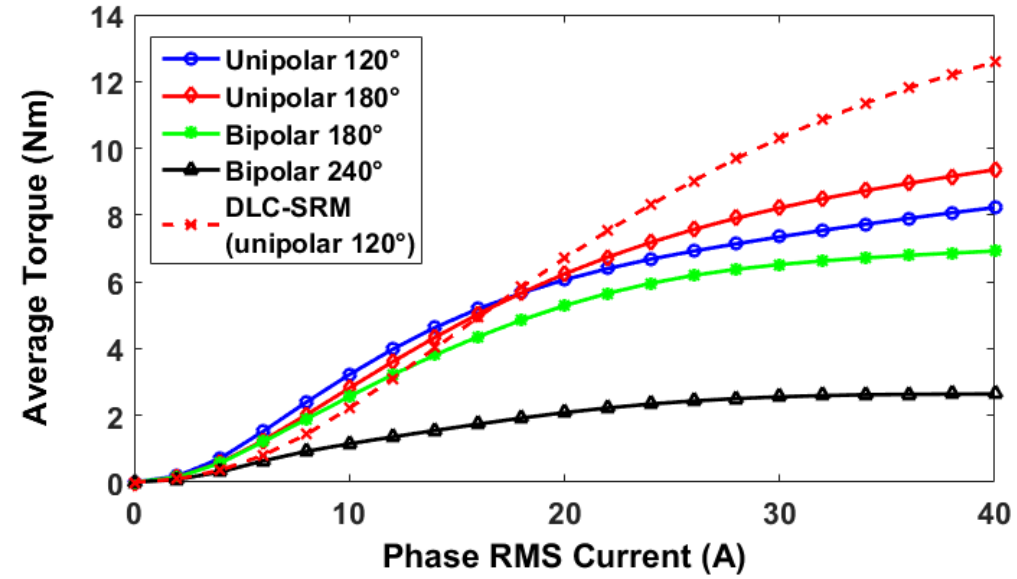

(a)

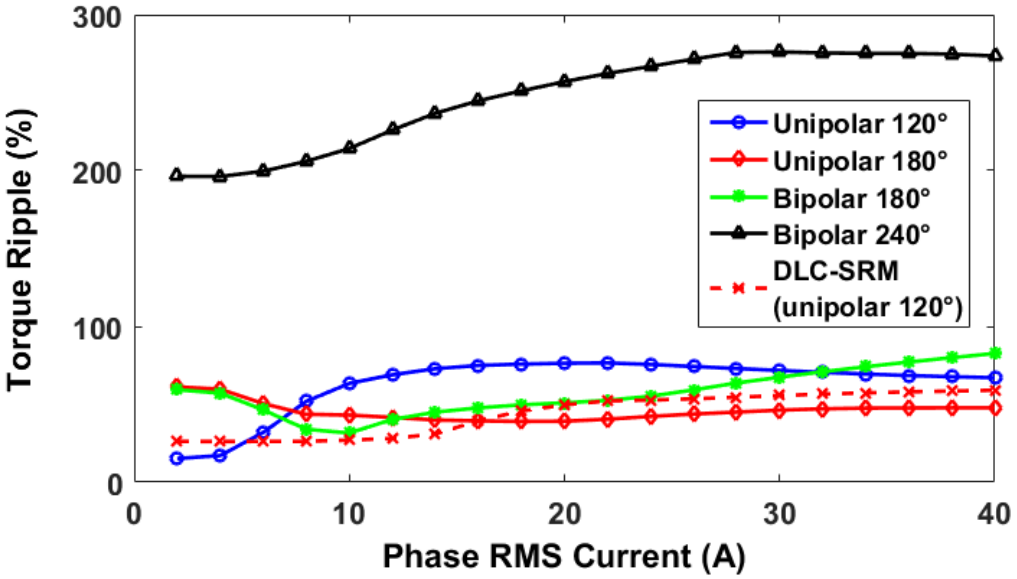

(b)

Fig. 2.12 Comparison of (a) average torque and (b) torque ripple coefficient of the SLC-SRM against phase RMS current varying from 0A to 40A.

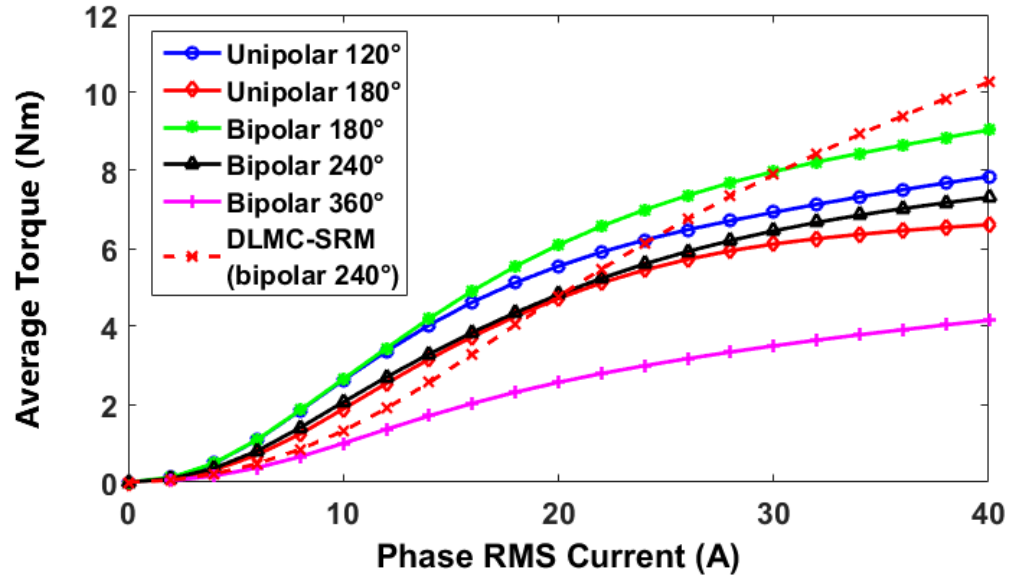

(a)

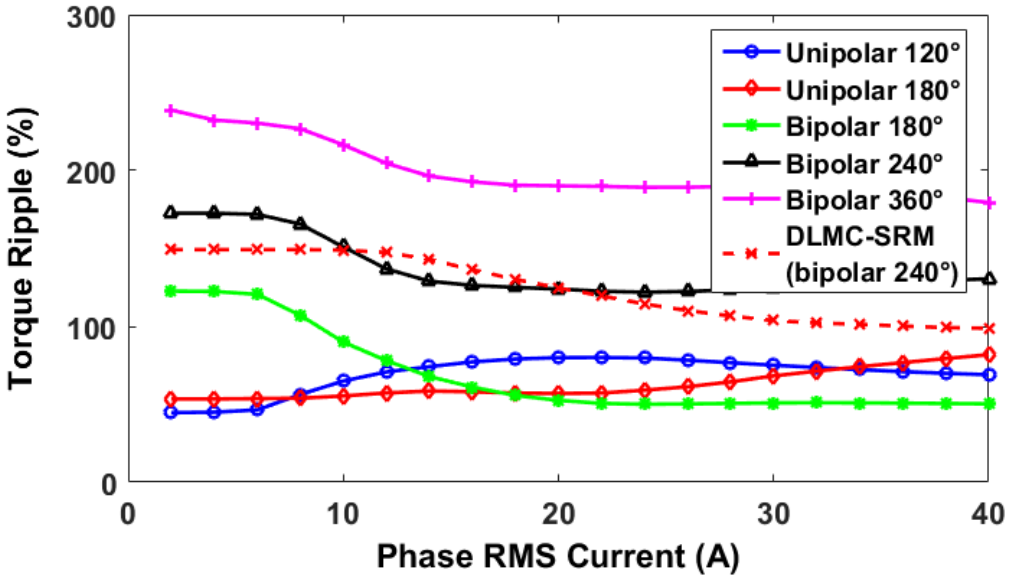

(b)

Fig. 2.13 Comparison of (a) average torque and (b) torque ripple coefficient of the SLMC-SRM against phase RMS current varying from 0A to 40A.

At low current, the SLC-SRM excited by unipolar 120° elec. conduction achieves higher average torque than others as shown in Fig. 2.12. However, at high current, the SLC-SRM supplied by unipolar 180° elec. conduction exhibits better torque capability, i.e. higher average torque while with lower torque ripple. According to the nature of self- and mutual-inductance variations, the SLC-SRM with bipolar 180°, 240° and 360° elec. conductions have gradually deteriorated performances since negative self-torque has been produced which reduces the average torque (bipolar 360° elec. conduction is not shown here because the average torque is

close to zero). For completeness, a DLC-SRM, supplied by unipolar 120° elec. conduction has been selected, which produces the highest average torque for this class of SRM. It can be found that, with appropriate conduction angle, the SLC-SRM can even produce higher torque than the DLC-SRM at low current. However, due to the fact that the SLC-SRM is more sensitive to magnetic saturation, the DLC-SRM can produce higher torque at high current.

It can be found in Fig. 2.13 that the SLMC-SRM supplied by bipolar 180° elec. conduction produces the highest average torque but modest torque ripple, particularly at high phase current. Compared with the DLMC-SRM (which achieves its highest average torque by bipolar 240° elec. conduction if rectangular wave currents are employed), the SLMC-SRM with most appropriate conduction angle generates higher torque. However, at high phase current, e.g. 40A, the DLMC-SRM can produce even higher average torque than the SLMC-SRM. Moreover, it can be concluded that the SLMC-SRM has lower torque ripple than the DLMC-SRM when supplied with most appropriate conduction angles.

TABLE 2.6 SUMMARY OF MACHINE AVERAGE TORQUE WITH DIFFERENT CONDUCTION ANGLES

	DLC-SRM		DLMC-SRM		FP-SRM		SLC-SRM		SLMC-SRM	
	Low	High	Low	High	Low	High	Low	High	Low	High
Unipolar 120°	1	1	4	4	5	5	1	2	2	2
Unipolar 180°	2	2	5	5	2	2	2	1	4	4
Bipolar 180°	3	3	2	2	4	4	3	3	1	1
Bipolar 240°	4	4	1	1	3	3	4	4	3	3
Bipolar 360°	5	5	3	3	1	1	5	5	5	5

Note: Number 1-5 represents relative average torque from the highest to the lowest. 'Low' stands for low current at $10A_{rms}$, 'High' stands for high current at $40A_{rms}$.

For completeness, TABLE 2.6 summarizes the machine average torques with different conduction angles at different current levels. It can be found that the FP-SRM with bipolar 360° elec. conduction can have the best torque performance, while the unipolar 120° elec. is the worst due to negligible contribution of self-inductance in the FP-SRM. In contrast, with nearly null mutual-inductance, the unipolar 120° elec. conduction is the most appropriate one for the DLC-SRM. While for the DLMC-SRM, the bipolar 240° elec. conduction is the most appropriate one, in which the contributions of both the self- and mutual-inductances have been considered. Similar to the DLC-SRM, the SLC-SRM produces the highest average torque with

the unipolar 120° elec. conduction at low current, while the unipolar 180° elec. becomes the most appropriate conduction angles at high current level due to magnetic saturation. Moreover, the SLMC-SRM with bipolar 180° conduction achieves its best performance at both low and high current levels.

2.6.3 COPPER LOSS

With different winding structures, the copper losses of a given sized SRM with different winding configurations will be different at the same phase current due to different end-winding structures, as shown in Fig. 2.14. In addition, the phase resistance depends on the mean length per turn, which consists of two active conductors in stator slots and two end-windings.

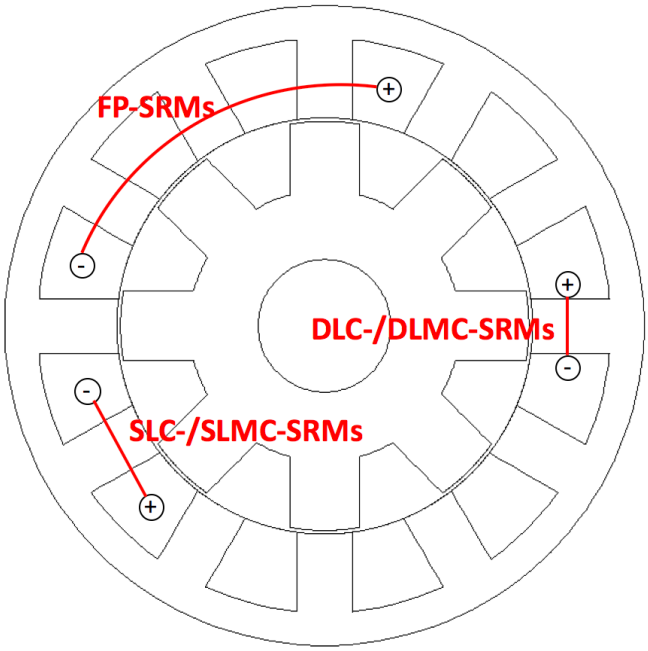

Fig. 2.14 Example of the end-windings of the SRMs with different winding configurations.

Accordingly, TABLE 2.7 summarizes the average value of one end-winding length of both the double and single layers, as well as the FP-SRMs, where W_s is average stator slot width (trapezoidal slot shape) and W_t is stator tooth width. For the FP-SRM, the end winding consists of $\frac{1}{2}\pi W_s$ plus an arc length of the span range of a coil where R_{si} is the stator inner radius, h_s is the slot height, N_s is the slot number, and γ is the stator slot opening in mechanical degree. It can be found that the end-windings of the single layer SRMs are slightly higher than that of the double layer SRMs, but are significantly shorter than that of the FP-SRM.

TABLE 2.7 INFLUENCE OF WINDING CONFIGURATIONS ON END-WINDINGS

Winding configurations	Expression of end-windings	End-winding length (m)
DLC/DLMC	$\frac{1}{4}\pi W_s + W_t$	0.015
SLC/SLMC	$\frac{1}{2}\pi W_s + W_t$	0.023
FP	$\frac{1}{2}\pi W_s + 2\pi(R_{si} + \frac{1}{2}h_s)\times\frac{360°/N_s\times 3-\gamma}{360°}$	0.058

TABLE 2.8 shows a comparison of copper loss between the SRMs under rated condition for a coil temperature of 20°C. The nature of the end-windings in a FP-SRM dictate that for this relatively short axial length of stator core, the total mean length per turn which consists of two end winding length plus two active length is much longer when compared with both the double and single layer SRMs, with consequent adverse implications for the phase resistance of the FP-SRM. However, the double layer winding has the lowest phase resistance amongst all the winding configurations, and hence could produce the lowest copper loss at the same phase current. Due to single layer winding configuration, the SLC-SRM and SLMC-SRM have slightly longer end-windings than that of the double layer SRMs if the number of turns per phase is the same. Therefore, the phase resistance and hence the copper loss of the SLC-SRM/SLMC-SRM is slightly higher than that of the DLC-SRM/DLMC-SRM.

TABLE 2.8 COMPARISON OF COPPER LOSS WITH COIL TEMPERATURE OF 20℃ AT 10 A_{rms}

Items	DLC &DLMC-SRMs	FP-SRM	SLC &SLMC-SRMs
Mean length per turn (m)	0.15	0.24	0.17
Copper wire Length (m)	19.95	31	21.83
Phase resistance (Ω)	0.53	0.82	0.57
Rated copper loss (W)	159	246	171

In order to investigate the influence of the copper loss on the torque performances, Fig. 2.15 shows the comparison of average torque and torque ripple against copper loss of the single and double layer SRMs. In order to investigate for the full current range, the appropriate conduction

angles for high current level as shown in TABLE 2.6 have been selected for the single layer SRMs. Additionally, the double layer SRMs with the most appropriate conduction angles have also been shown for comparison. It can be found that the copper loss of the single layer SRMs is lower than that of the double layer SRMs for a given average torque, e.g. 2.5Nm. Moreover, the DLMC-SRM has the worst torque against copper loss performance at low copper loss region with the highest torque ripple. However, the DLC-SRM supplied by unipolar 120° conduction produces the lowest copper loss at higher average torque, e.g. 8Nm.

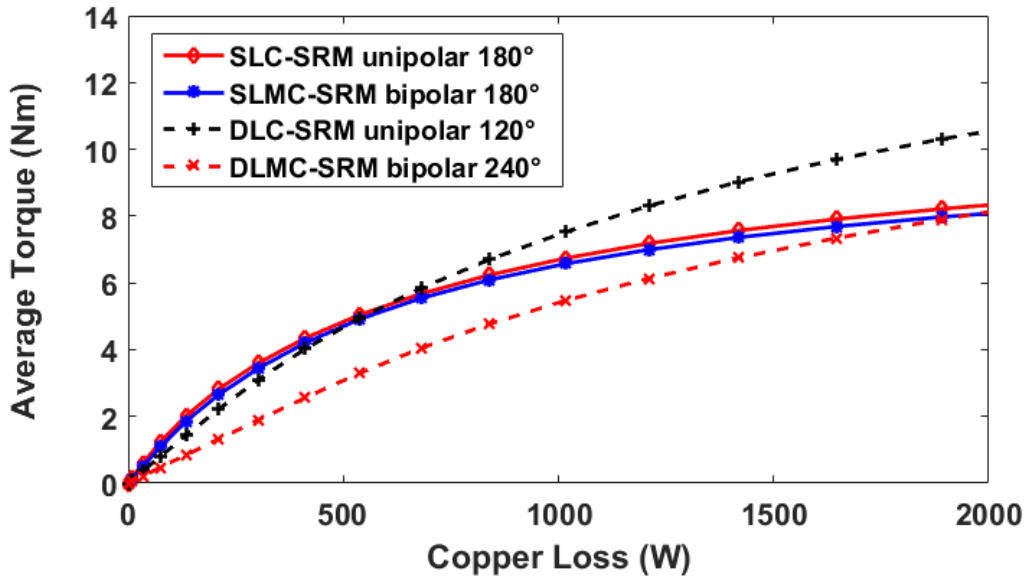

(a)

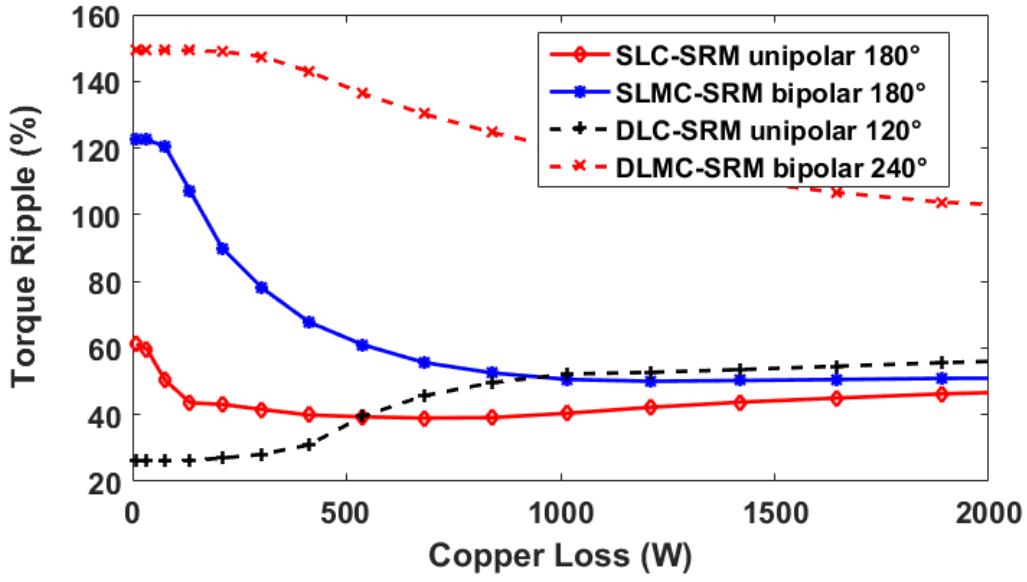

(b)

Fig. 2.15 Comparison of (a) average torque and (b) torque ripple coefficient against copper loss of the SRMs for varying phase RMS current.

2.6.4 IRON LOSS

Due to different excitations, the flux density waveforms in different parts of the machine can be unipolar, asymmetric, and can contain minor-loop excursions. In order to deal with the non-sinusoidal flux density waveform, approaches have been proposed in [74] [75]. In this chapter, the harmonic flux densities of each FE mesh element within the stator and rotor have been calculated using Fourier analysis [76] [77], (2.12) is then used for calculating iron loss in each FE mesh element [6]. The total stator and rotor iron losses can be obtained by summing the losses in all the stator and rotor mesh elements.

$$p_{iron}(W/m^3) = \sum_{n=1,2,3\ldots} (nf_x)\left(k_{h1}\Delta B_{pp,n} + k_{h2}\Delta B_{pp,n}^2\right) + k_e \sum_{n=1,2,3\ldots} (nf_x)\int_0^{\frac{1}{nf_x}} \left(\frac{\partial B_n}{\partial t}\right)^2 dt \tag{2.12}$$

where n is the harmonic order, f is the stator or rotor iron core flux density frequency, B_{pp} is the peak to peak value of the flux density. For silicon iron core considered in this thesis, the hysteresis loss coefficients k_{h1} and k_{h2} are $5A/m$ and $40Am/Vs$, respectively. The eddy current loss coefficient k_e is $0.022\ Am/V$.

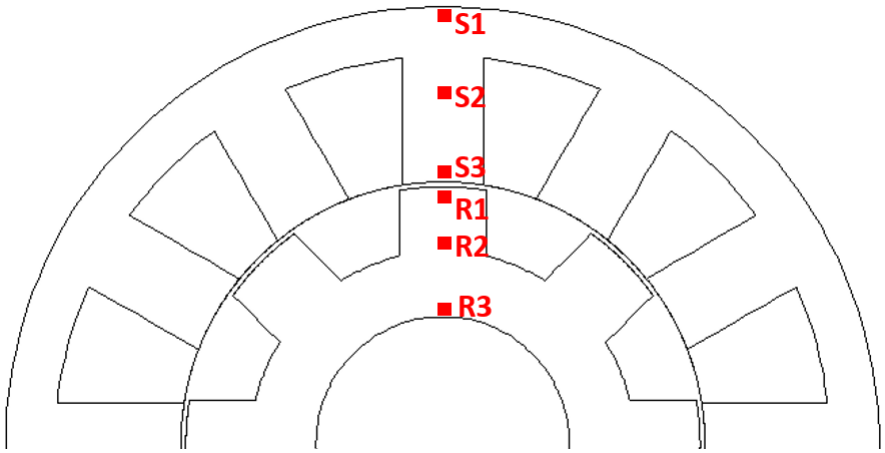

Fig. 2.16 Cross-section of a 12-slot/8-pole single layer SRM. Points S1, S2, and S3 of stator back iron, tooth body, and tooth tip are selected as examples for stator flux density observation. Points R1, R2, and R3 of rotor tooth tip, rotor body and rotor yoke are selected for rotor flux density observation.

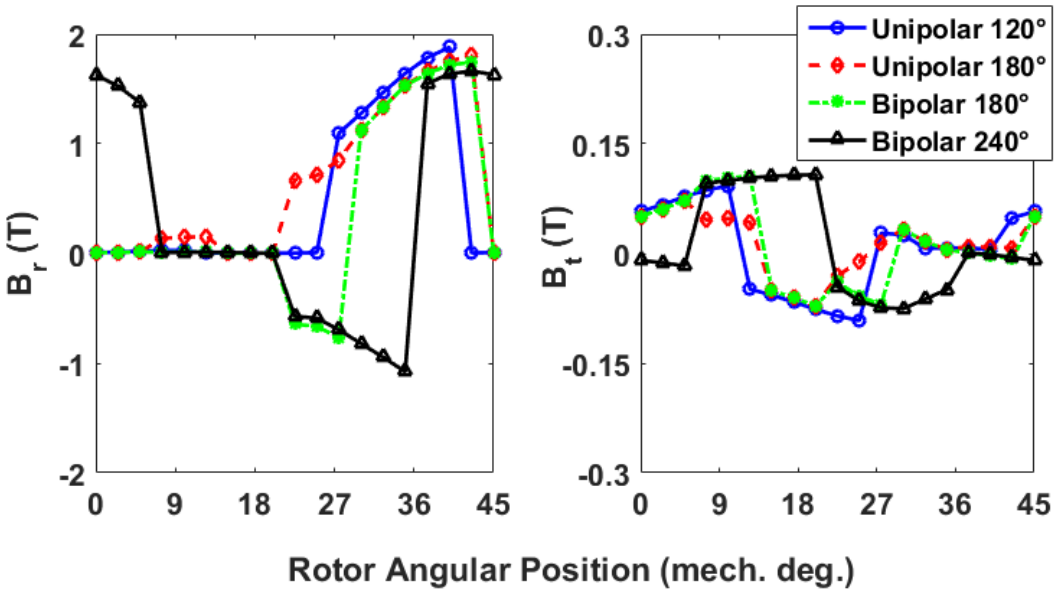

(a)

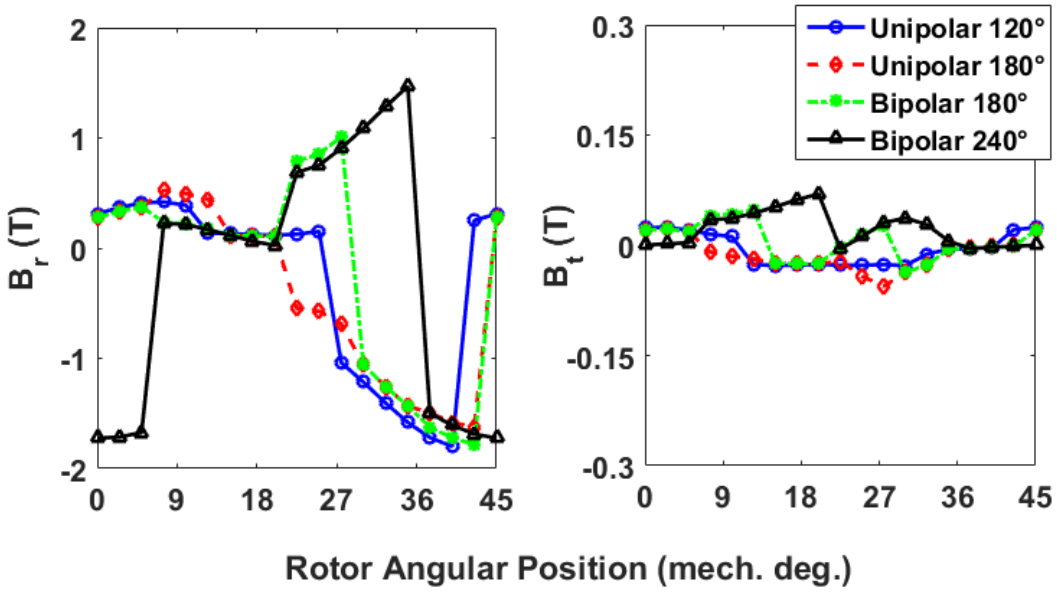

(b)

Fig. 2.17 B_r and B_t vs rotor position at point S2. (a) SLC-SRM, (b) SLMC-SRM. The phase RMS current is 10A for different conduction angles.

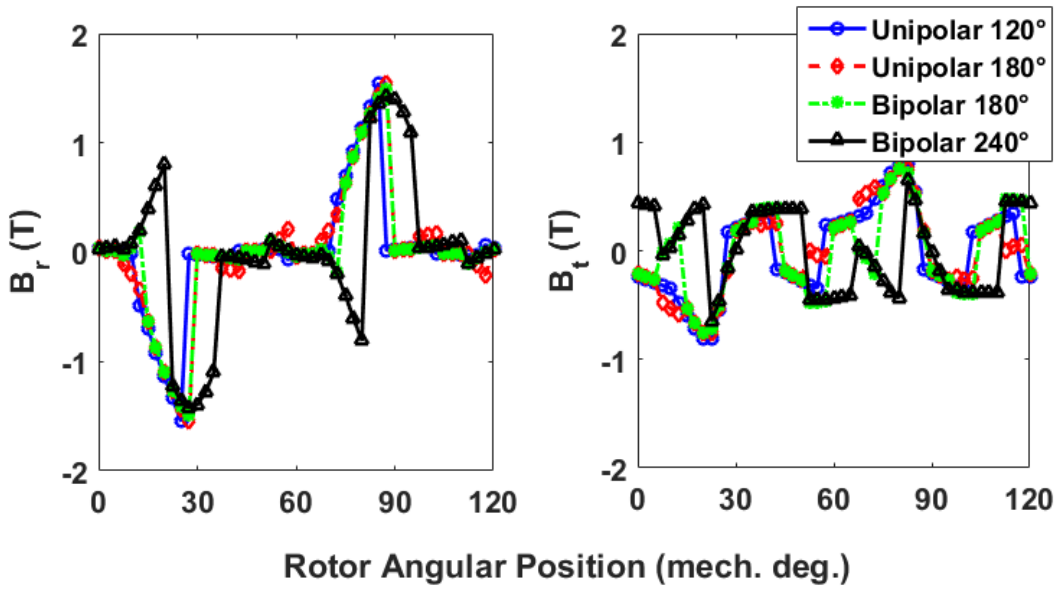

(a)

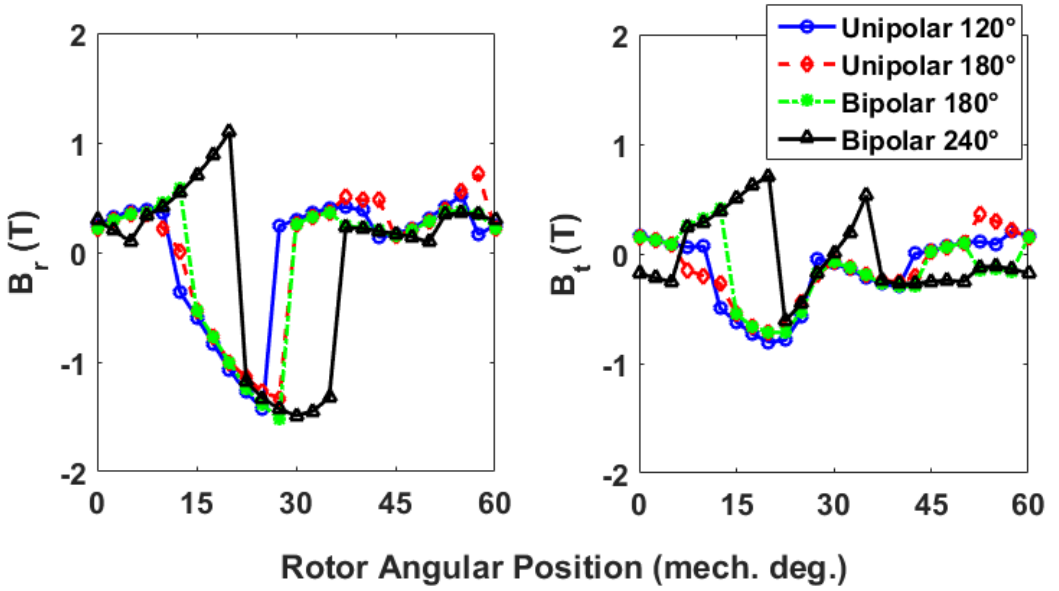

(b)

Fig. 2.18 B_r and B_t vs rotor position at point R2. (a) SLC-SRM, (b) SLMC-SRM. The phase RMS current is 10A for different conduction angles.

In general, iron losses of the stator and rotor are calculated separately since their flux densities have different frequencies. Hence, both the radial (B_r) and tangential (B_t) flux densities of the stator and rotor are investigated for the selected points shown in Fig. 2.16. By way of example, one period of flux density variations of the stator and rotor tooth bodies of the single layer SRMs are shown in Fig. 2.17 and Fig. 2.18, respectively. It is found that one period of both the stator B_r and B_t of the single layer SRMs is 45 mech. deg., regardless of conduction

angles. However, the period of rotor flux densities of the SLC-SRM is 120 mech. deg., which is twice as high as that of the SLMC-SRM.

TABLE 2.9 SUMMARY OF FLUX DENSITY FREQUENCIES

Machine type	B_r/B_t frequency (Hz)	
	Stator	Rotor
SLC-SRM	f_0	$0.375f_0$
SLMC-SRM	f_0	$0.75f_0$

TABLE 2.10 IRON LOSS OF SINGLE LAYER SRMS AT $10A_{rms}$, 400RPM

Machine type	Conduction angle (elec.)	Iron loss (W)		
		Stator	Rotor	Total
SLC-SRM	Unipolar 120°	3.58	0.48	4.05
	Unipolar 180°	3.16	0.40	3.57
	Bipolar 180°	4.82	0.60	5.42
	Bipolar 240°	5.90	0.76	6.67
SLMC-SRM	Unipolar 120°	2.33	0.85	3.18
	Unipolar 180°	1.90	0.80	2.71
	Bipolar 180°	3.52	1.13	4.65
	Bipolar 240°	5.03	1.63	6.66

For simplicity, the stator and rotor flux density frequencies are summarized in TABLE 2.9. For both the single layer SRMs, the stator flux density frequency is equal to $f_0 = \frac{\Omega p}{60}$ (where Ω is mechanical speed and p is rotor pole number), which is 53.33Hz at 400rpm. However, the rotor flux density has lower frequency than the stator. In addition, rotor flux density frequency of the SLMC-SRM is two times higher than that of the SLC-SRM since the effective pole number of the SLMC-SRM is twice as high as that of the SLC-SRM.

In TABLE 2.10, the stator, rotor and total iron losses have been calculated by 2D FEA at $10A_{rms}$ and 400rpm, supplied by rectangular wave current with different conduction angles. It is apparent that both the single layer SRMs have higher stator iron loss than rotor iron loss.

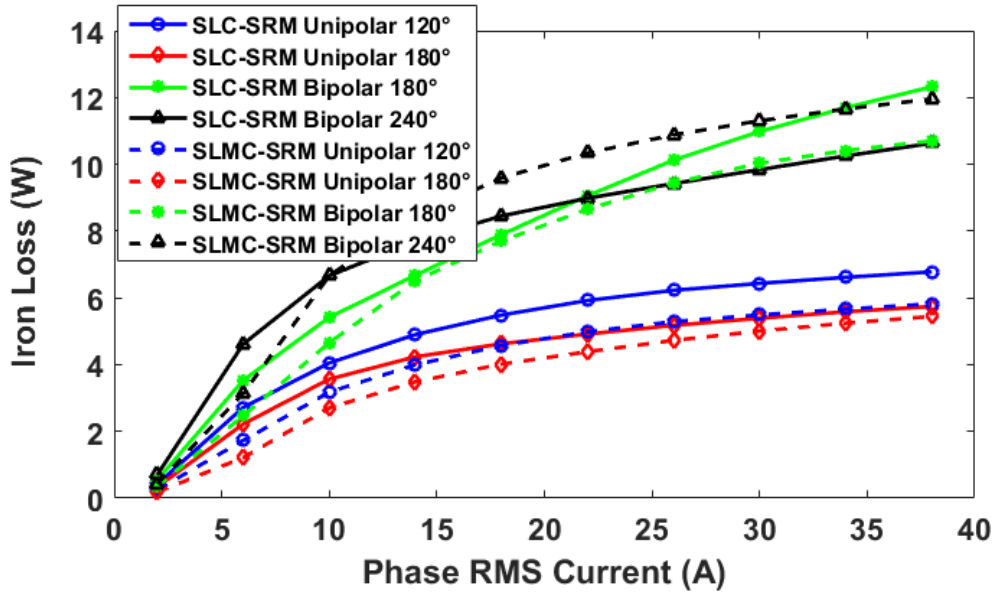

(a)

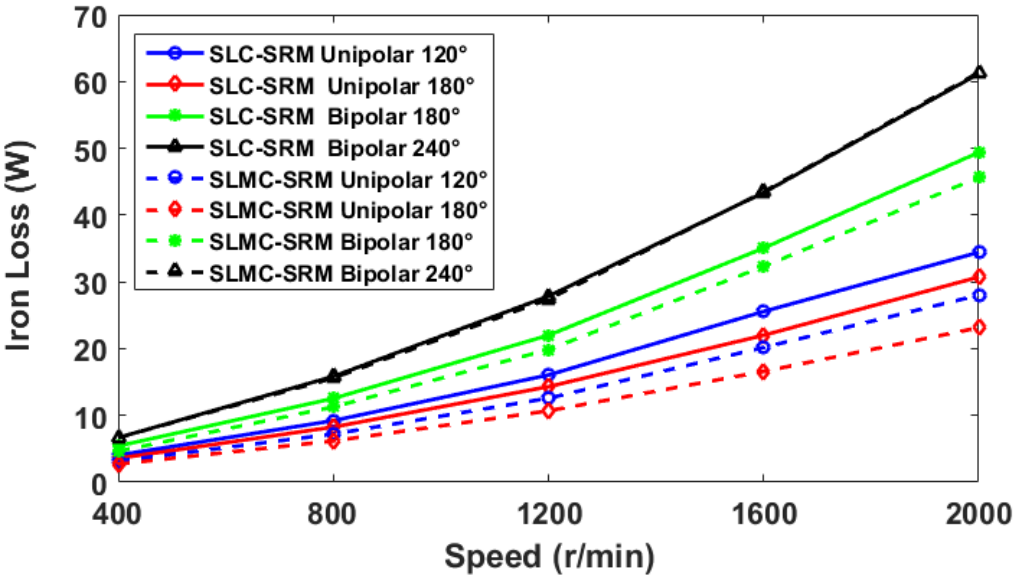

(b)

Fig. 2.19 Influence of conduction angles on iron loss of single layer SRMs. (a) At 400 rpm with increasing phase RMS current, (b) at 10 $A_{rms}$with increasing speed.

For completeness, the iron loss variations with increasing phase RMS current at 400rpm are shown in Fig. 2.19 (a). It is found that both the single layer SRMs supplied by conduction angles of unipolar 120° elec. and unipolar 180° elec. produce lower iron losses than others at different phase RMS currents. With increasing rotor speed at fixed $10A_{rms}$, the iron loss is increased as shown in Fig. 2.19 (b). It can also be found that the SLMC-SRM produces lower iron loss than the SLC-SRM with the same conduction angle at different rotor speeds. At 2000rpm, the highest iron loss is around 60W, which is supplied with conduction angle of

bipolar 240° elec. However, the copper loss still could be the dominant loss of this relatively small machine at modest speed. Nevertheless, for larger and higher speed machines, the iron loss could be the dominant loss [78].

2.6.5 EFFICIENCY

The machine efficiency can be calculated based on output power and the previously calculated machine losses. TABLE 2.11 shows the influence of conduction angles on machine efficiency at $10A_{rms}$ under 400rpm rotor speed. Moreover, Fig. 2.20 shows the efficiency curves with varying rotor speeds at $10A_{rms}$. At 2000rpm, efficiency of >70% can be achieved by both the single layer SRMs with appropriate current excitations. In addition, with a unipolar 120° elec. conduction angle, the SLC-SRM produces its highest efficiency of 76% at 2000rpm, while the SLMC-SRM can achieve 72%. Hence, in order to produce higher efficiency, the appropriate conduction angles of the SLC-SRM are unipolar 120° elec. and unipolar 180° elec., whilst for the SLMC-SRM, they are unipolar 120° elec. and bipolar 180°elec.

TABLE 2.11 EFFICIENCY OF SINGLE LAYER SRMS @ $10A_{rms}$ & 400RPM

Machine type	Conduction angle (elec. deg.)	Output power (W)	Efficiency (%)
SLC-SRM	Unipolar 120°	134.88	41.90
	Unipolar 180°	118.12	38.77
	Bipolar 180°	107.65	36.36
	Bipolar 240°	48.17	20.25
SLMC-SRM	Unipolar 120°	109.75	37.09
	Unipolar 180°	78.75	29.78
	Bipolar 180°	111.00	37.17
	Bipolar 240°	86.29	31.27

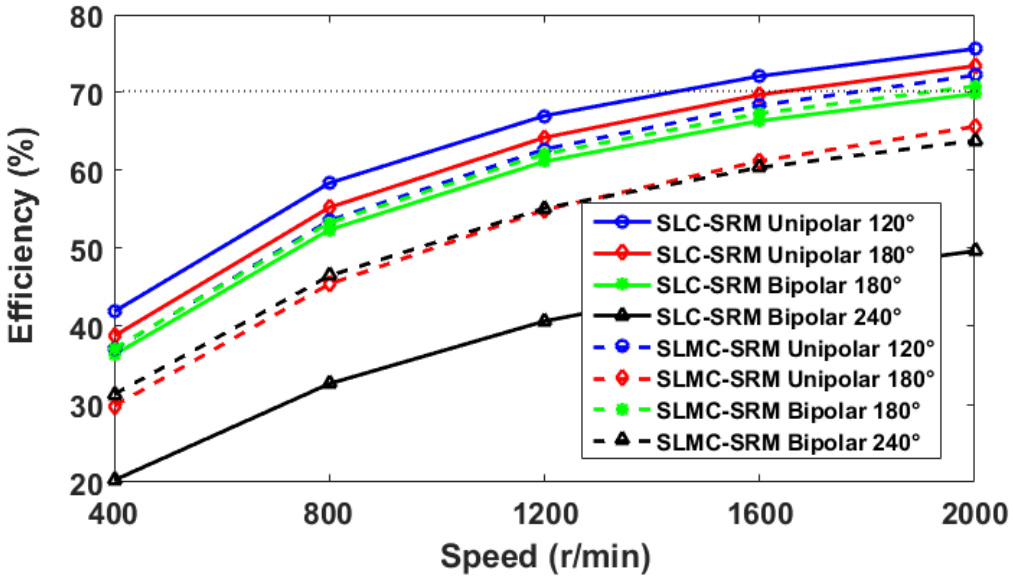

Fig. 2.20 Influence of conduction angles on machine efficiency with varying speed at $10A_{rms}$.

2.7 EXPERIMENTAL VALIDATION

2.7.1 PROTOTYPES OF SRMS

In order to validate the predictions, two 12-slot/8-pole machines with the design parameters in TABLE 2.1 were built. The wound stator of the SLC-SRM and SLMC-SRM is shown in the Appendix, Fig. I (c). The two single layer SRMs can be realized with the same wound stator by reconnecting the coils as detailed in Fig. 2.3. The common rotor for both machines is shown in Fig. III (b).

2.7.2 SELF-AND MUTUAL-INDUCTANCES

The self-inductance $L_a(\theta)$ and mutual-inductance $M_{ab}(\theta)$ are measured according to (2.13) and (2.14) as shown below [79]:

$$L_a(\theta) = \frac{\sqrt{(V_a/I_a)^2 - {R_{ph}}^2}}{2\pi f} \tag{2.13}$$

$$M_{ab}(\theta) = \frac{V_b}{2\pi f I_a} \tag{2.14}$$

where V_a and V_b are the voltages of the phases A and B, respectively. I_a is the amplitude of the phase current in phase A, and f is the frequency of phase voltage. Phase resistance R_{ph} is measured as 1.48Ω for the single layer SRMs.

During the tests, the sinusoidal voltage source injected into the phase A has a peak-peak value of 9.2V with a frequency of 106.6Hz for the SLC-SRM and 105.5Hz for the SLMC-SRM. Hence, the measured amplitude of phase current is around 1.8A. Fig. 2.21 shows the predicted and measured self- and mutual-inductances of the single layer SRMs, a generally good agreement can be observed. The discrepancy between measured and predicted self-inductances is mainly due to the end-windings which have not been taken into account in the simulations.

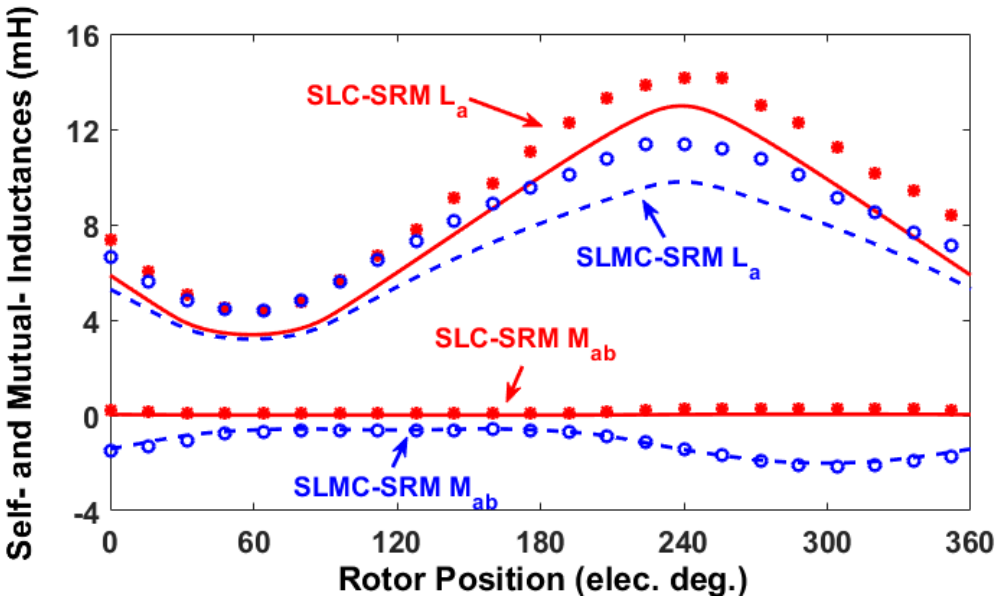

Fig. 2.21 Predicted and measured self-inductance L_a and mutual-inductance M_{ab} at 1.8A phase peak current of the single layer SRMs. (solid lines: predicted results, marks: measured results).

2.7.3 Self- and Mutual-Torques

In order to measure the torque produced by self-inductance, the phase A is selected as an example. The method of static torque measurement detailed in [80] was adopted for undertaking all torque measurements in this study and Fig. 2.22 shows the test rig. A balance beam is connected to the rotor shaft. It is levelled and the bar at one end is rested on the tray of a digital gauge. The stator is clamped in the jaws of a lathe enabling it to be rotated in precise step instead of rotating rotor shaft. By measuring the force using the digital gauge and knowing the distance of the balance beam from shaft center to the pointer, the static torque can be obtained. Power supply is used to inject DC current of 10A into the phase A. Fig. 2.23 shows

the self-torque comparison between the SLC-SRM and SLMC-SRM. The measured results are slightly higher than predicted results due to measurement error but this discrepancy is within an acceptable range.

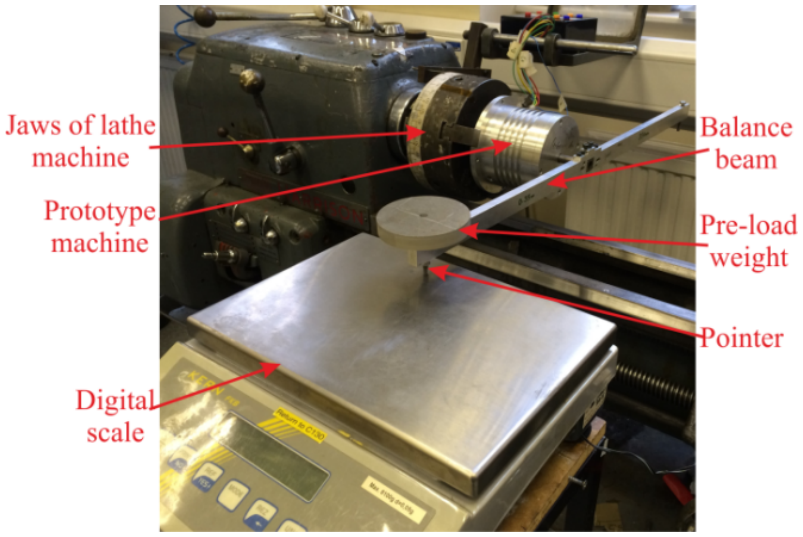

Fig. 2.22 Test rig for static torque measurements.

Mutual-torque produced by mutual-inductance is given in (2.15) if the saturation is neglected.

$$T_{ab} = T_{a\&b(series)} - T_a - T_b \tag{2.15}$$

where $T_{a\&b(series)}$ is the torque when the phases A and B are connected in series as shown in Fig. 2.24, T_a and T_b are the self-torques of the phases A and B, respectively. Fig. 2.25 shows the comparison of the mutual-torque between the SLC-SRM and SLMC-SRM, where the phase current of 1A has been used in order to minimize the influence of magnetic saturation. It can be found that the measured results match well with the predictions.

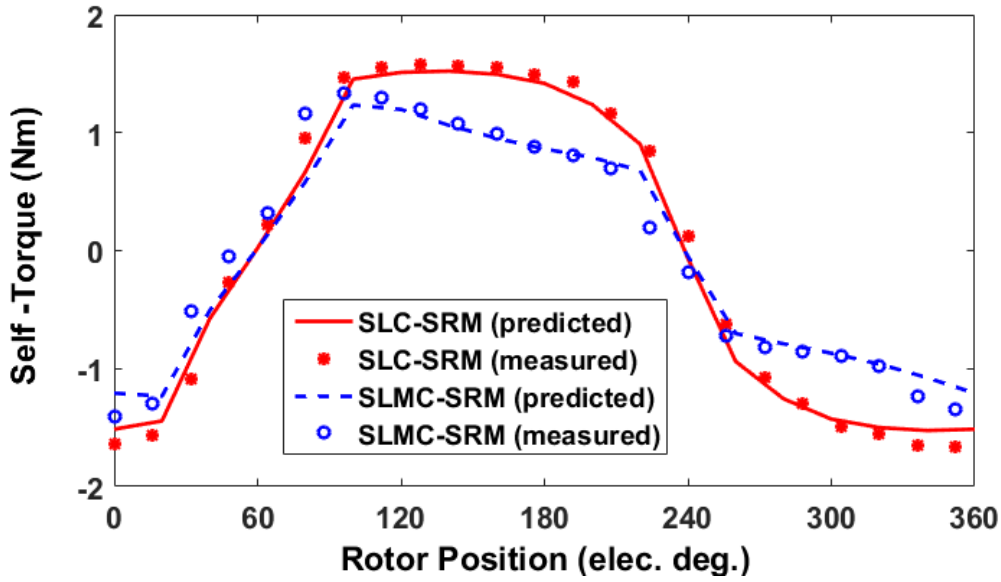

Fig. 2.23 Predicted and measured self-torques versus rotor position of the single layer SRMs at 10A DC current.

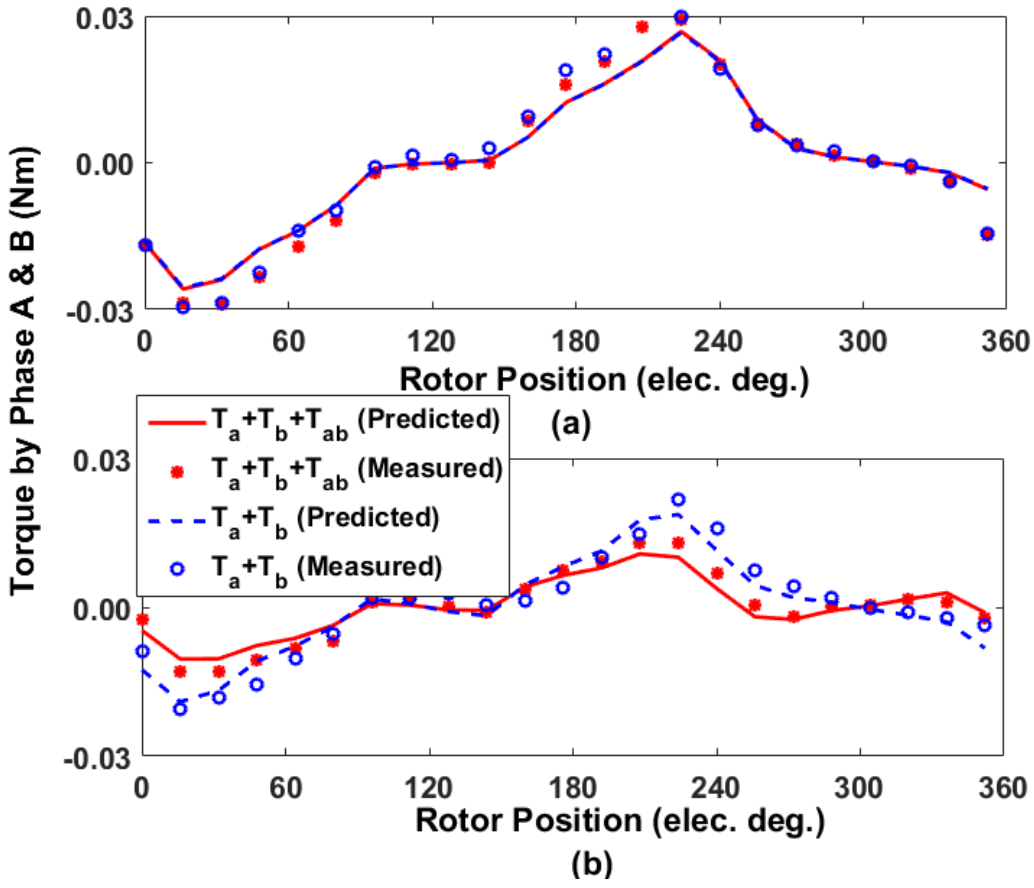

Fig. 2.24 Predicted and measured torques produced by phase A and phase B versus rotor position at 1A DC current. (a) SLC-SRM, (b) SLMC-SRM.

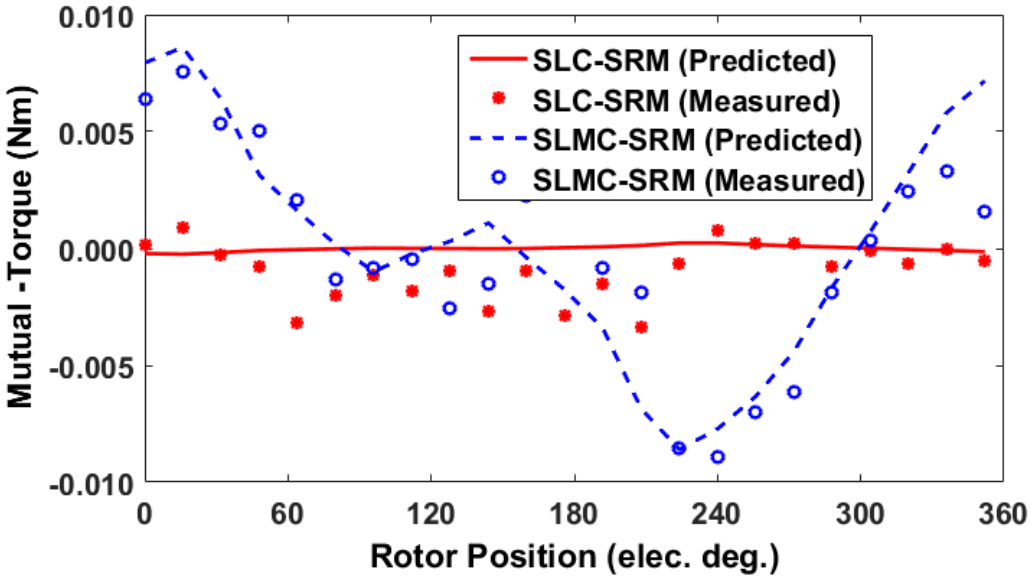

Fig. 2.25 Predicted and measured mutual-torques versus rotor position at 1A DC current. (a) SLC-SRM, (b) SLMC-SRM.

2.7.4 STATIC ON-LOAD TORQUE

According to the current waveforms with different conduction angles as shown in Fig. 2.10, the on-load torques of the SLC-SRM and SLMC-SRM have been measured at different rotor positions as shown in Fig. 2.26. The aligned rotor position of phase A can be tested by injecting current only into the phase A. This will cause the rotor to rotate to the aligned position of the phase A. In addition, the DC current can be injected into each phase at different rotor positions according to the current waveforms with relevant conduction angles in order to obtain the torque waveforms shown in Fig. 2.26. The phase RMS current of all the currents with different conduction angles is 4A, and the DC current is injected into each phase at different rotor positions corresponding to the current waveforms shown in Fig. 2.10.

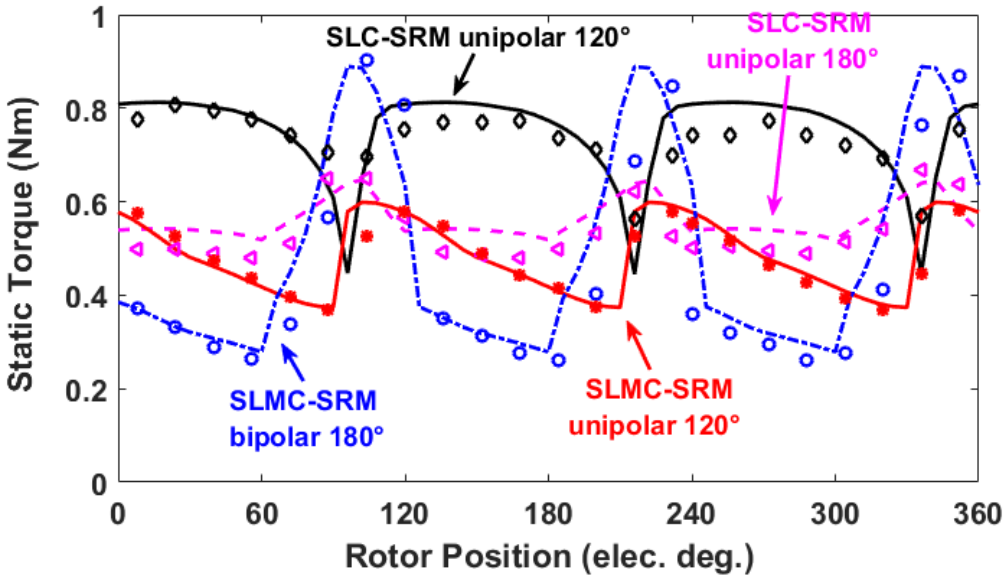

Fig. 2.26 Predicted and measured static torques versus rotor position at 4A phase RMS current. (Lines: predicted results, marks: measured results).

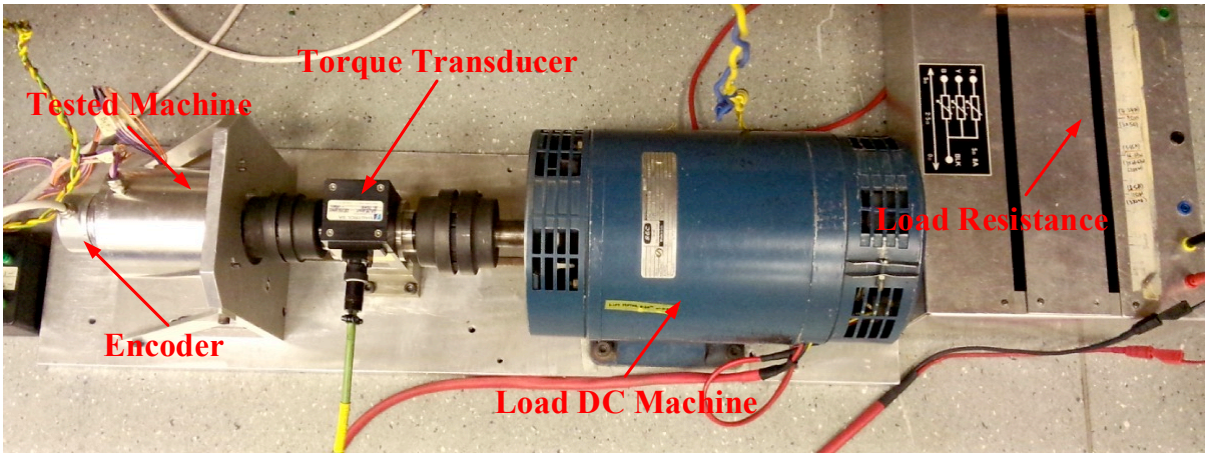

Fig. 2.27 Dynamic test rig.

2.7.5 DYNAMIC TEST

Fig. 2.27 shows the dynamic test rig. The load is provided via a DC machine and a resistor bank. Load torque is measured by using a torque transducer and the position sensor is an incremental photoelectric rotary encoder. Limited by the load-torque capacity of the DC machine used for dynamic test, a DC voltage of 38V has been used and the phase RMS current is 4A for all the tests. By way of example, Fig. 2.28 shows the 3-phase current waveforms of the SLC-SRM with different conduction angles at 100rpm. The average torque of predicted, static (as shown in Fig. 2.26) and dynamic tests at $4A_{rms}$ are compared in TABLE 2.12. With

the appropriate conduction angles, the average torque of the SLC-SRM can be higher than that of the SLMC-SRM, at low current level of $4A_{rms}$. Both the static and dynamic test results match well with the predicted ones. The difference is mainly due to the fact that the end-winding effect has not been taken into account in the 2D FEA. In addition, the torque sensor accuracy in dynamic test and the measuring error also contribute to this discrepancy.

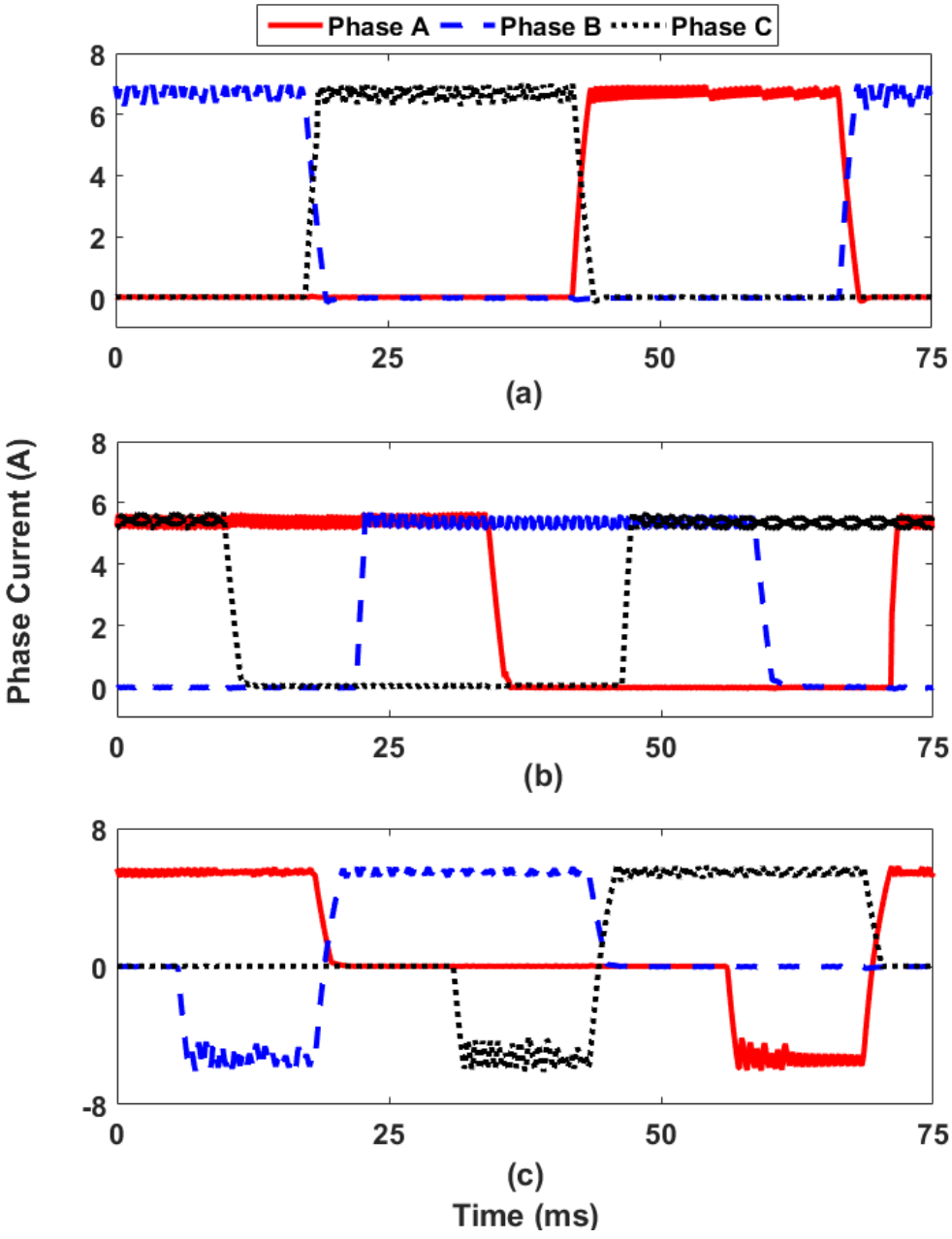

Fig. 2.28 Transient 3-phase currents with conduction angles of (a) unipolar 120°elec., (b) unipolar 180°elec. and (c) bipolar 180°elec. at 100rpm. The phase RMS current is 4A.

TABLE 2.12 AVERAGE TORQUE COMPARSION AT $4A_{rms}$

Machine type	Conduction angle (elec. deg.)	Predicted (Nm)	Static test (Nm)	Dynamic test (Nm)
SLC-SRM	Unipolar 120°	0.75	0.74	0.71
	Unipolar 180°	0.56	0.54	0.55
SLMC-SRM	Unipolar 120°	0.49	0.48	0.47
	Bipolar 180°	0.50	0.47	0.48

The predicted and measured efficiency-speed curves of both the SLC-SRM and SLMC-SRM have been compared in Fig. 2.29. The measured results have relatively good agreement with the predictions. However, the difference becomes larger at higher speed due to the higher distortion in the transient current waveforms and also the mechanical losses that have not been taken into account in the predictions.

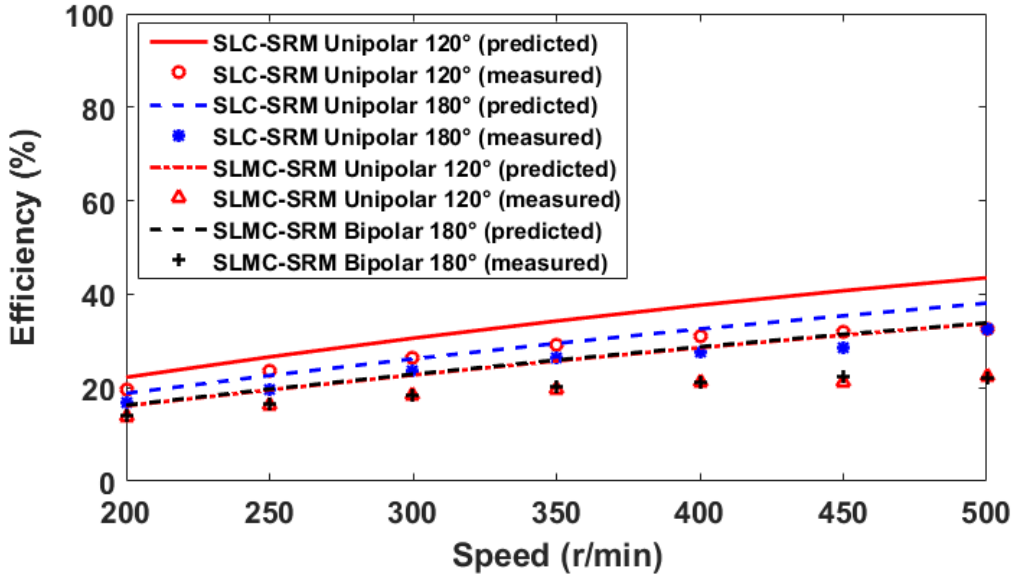

Fig. 2.29 Predicted and measured efficiency-speed curves of the single layer SRMs with different conduction angles. The phase RMS current is 4A.

2.8 CONCLUSION

Two novel single layer, short-pitched SRMs: SLC-SRM and SLMC-SRM have been proposed on the basis of the well-established DLC-SRM and DLMC-SRM. In this chapter, the two single layer SRMs supplied by unipolar and bipolar rectangular wave currents with different conduction angles have been investigated and compared.

Due to the nature of the self- and mutual-inductance variations, it is found that the SLC-SRM supplied by unipolar 120° elec. conduction obtained its highest average torque at low current level. However, at high current level, the higher average torque is achieved by unipolar 180° elec. conduction. In addition, the SLC-SRM can achieve higher efficiencies when supplied by these conduction angles at different rotor speeds. For the SLMC-SRM, bipolar 180° elec. conduction is the most appropriate one to generate a higher average torque and relative higher efficiency while with lower torque ripple than other conduction angles. When compared with their double layer counterparts, the single layer SRMs have better torque performances at low current. But due to magnetic saturation, the double layer SRMs can produce higher average torque at high current.

In order to achieve simplified manufacture process, better fault tolerant capability and potentially reduced material consumption, both the single layer winding configurations will be adopted to the SRMs with modular structure, as will be studied in chapter 3.

Chapter 3. NOVEL MODULAR SRMS FOR PERFORMANCE IMPROVEMENT

Compared with non-modular machines, modular topologies become increasingly attractive due to their simplified manufacture process, better fault tolerant capability and potentially reduced material consumption. In order to maintain or even enhance the machine performance and achieve high fault tolerant capability, novel modular, single layer winding SRMs with different rotor pole numbers are proposed, which are supplied with rectangular wave current with different conduction angles. The influences of the pole number and flux gap width between E-core segmented stators on the electromagnetic performance have been investigated in terms of self- and mutual-inductances, electromagnetic torque, copper loss, iron loss, and radial force. It has been found that the modular structures with higher rotor pole number than stator slot number (12-slot/14-pole and 12-slot/16-pole SRMs) can maintain and even improve the average torque due to the nature of self- and mutual-inductances. In addition, the torque ripple of modular machines is significantly reduced (below 50%), so do the iron loss and radial force, leading to potentially lower vibration and acoustic noise. Two prototypes with 12-slot/8-pole and 12-slot/14-pole have been built with both non-modular and modular structures to validate the predictions in terms of inductances and static torques.

This chapter was published in [81].

3.1 INTRODUCTION

It is worth noting that all the aforementioned SRMs employ double layer winding configuration (two coils sharing one stator slot), a winding arrangement which is also referred to as 'all stator teeth wound'. However, higher torque capability can be achieved by adopting single layer windings (only one side of a coil in each stator slot) as a consequence of the higher self-inductance [22] [72]. Additionally, the single layer winding structure can have the improved fault tolerant capability since the phases are physically separated, hindering a fault such as local over-heating in one coil from propagating to the adjacent coils. Apart from the above advantages, single layer winding also provides the opportunity to adopt the modular machine topologies. These topologies can enhance further the fault tolerant capability and simplify the manufacturing of electrical machines, particularly their winding processes [82]. Moreover, if the slot and pole number combination is appropriately selected, modular machines have the ability to retain, or even improve machine performance compared with a corresponding non-modular design [79].

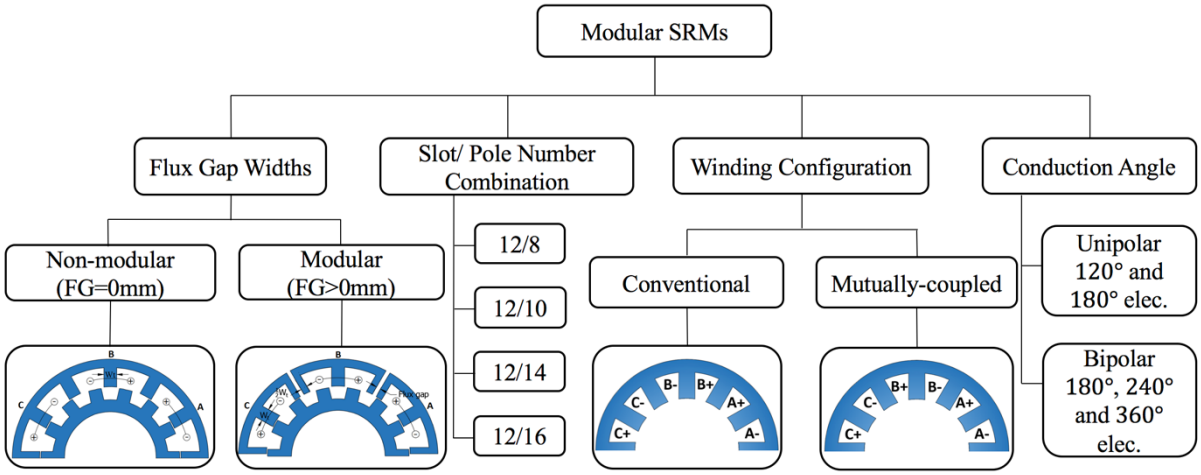

Fig. 3.1 Investigation variables of the modular SRMs. The SRMs are equipped with rectangular excitation.

Modular SRMs have also been proposed with E-core segmented stators in [35] [36], and C-core segmented stators in [34] [83]. These various segmented stators result in a reduction in core mass compared with non-modular SRMs with the same stator outer diameter, in turn leading to reduced cost and core losses. Moreover, the short flux paths which arise due to the gaps between segmented stators require lower MMF to generate a given torque. However, the existing modular SRMs are not designed with conventional stator/rotor pole combination, and

the influence of flux gap (FG) widths on the machine performances has not been investigated in detail. Moreover, due to relative large FG width, stator deformation can be problematic in some modular structures.

A series of novel 3-phase modular single layer SRMs are proposed in this chapter, combining the merits of single layer winding configuration (high torque capacity) and modular structure (enhanced fault tolerant capability). For clarity, a diagram including FG widths, slot/pole number combinations, winding configurations, and conduction angles for all the investigated modular SRMs is shown in Fig. 3.1. The trends of electromagnetic performance of 12-slot/10-pole and 12-slot/16-pole machines with different FGs are not shown in this chapter, since they are very similar to those of the 12-slot/8-pole and 12-slot/14-pole machines, respectively. In order to achieve enhanced machine performance, specifically higher average torque but with lower torque ripple, rectangular wave current with different conduction angles are employed according to the nature of the rate of change of self- and mutual-inductances [64]. For consistency and fair comparison between non-modular (FG=0mm) and modular (FG>0mm) machines, the most appropriate conduction angle for high current level has been employed. According to TABLE 2.6, the unipolar 180° elec. and bipolar 180° elec. conductions have been selected for the 12-slot/8-pole conventional SRMs (CSRMs) and mutually-coupled winding SRMs (MCSRMs), respectively. However, for the 12-slot/14-pole machines, the bipolar 180° elec. conduction is adopted for the CSRMs, while the unipolar 180° elec. conduction is for the MCSRMs. With the most appropriate conduction angles, the influences of FG widths and slot/pole number combinations are investigated in terms of electromagnetic torque, copper loss, iron loss and radial force. For completeness, the iron bridges, which have the advantage of yielding a single-piece cross-section, have also been added in the FGs to investigate their influence on machine performance.

3.2 FEATURES OF NON-MODULAR AND MODULAR MACHINES

3.2.1 STRUCTURES OF NON-MODULAR AND MODULAR MACHINES

A series of 3-phase, 12-slot SRMs with rotor pole numbers: 8, 10, 14 and 16, are proposed with different FG widths in this chapter although other slot/pole number combinations can also be deployed with appropriate modifications. All the machines have the same overall size and

number of turns, but are optimized individually with FG=0 mm (corresponds to a non-modular structure without FGs as a baseline) and single layer conventional (SLC) winding configuration, supplied with unipolar rectangular wave currents with conduction angle of $120°$ elec.

TABLE 3.1 MACHINE DIMENSIONS FOR THE SRMS WITH FG = 0 MM

Stator slot number	12	Shaft outer radius (mm)	21.1
Rotor pole number	14	Active length (mm)	60
Stator outer radius (mm)	45	Turn number per phase	132
Split ratio	0.72	Rated RMS current (A)	10
Airgap length (mm)	0.5	Current density (A_{rms}/mm^2)	5.68
Rotor outer radius (mm)	31.9		

By way of example, the key design parameters for an optimized 12-slot/14-pole machine with FG=0 mm are summarized in TABLE 3.1 and the machine structure is shown in Fig. 3.2(a), which adopts the SLC windings. The investigation described in this chapter is limited to single layer winding configurations.

A variation on the baseline 3-phase 12-slot non-modular structure, using an E-core modular stator structure with flux-gaps is shown in Fig. 3.2 (b). In refining this design, the tooth body iron section width W_t will be kept constant for different FG widths so to maintain similar level of magnetic saturation in stator teeth with FGs. It is inevitable that the flux path will change with increasing FG widths. In addition, it is worth noting that for a fixed Ampere-turn per slot, the current density will be increased with the increasing FG widths due to the reduced slot area (increased from $5.68A_{rms}/mm^2$ to $7.33A_{rms}/mm^2$ with increasing FGs from 0mm to 6mm). For completeness, iron bridges are added in the FGs as shown in Fig. 3.2 (c). In this case, the FGs act as dummy slots. It is apparent that the modular structures in Fig. 3.2 (b) have no iron bridge. However, when the iron bridge height is equal to the stator core height – the FGs are fully replaced by iron, the machine stator tooth widths will be unequal, leading to an unequal tooth (UNET) width structure. This structure has been used in permanent magnet machines in order to achieve higher winding factor and also higher average torque. For the SRMs in this chapter, the influence of UNET on machine performance will also be investigated.

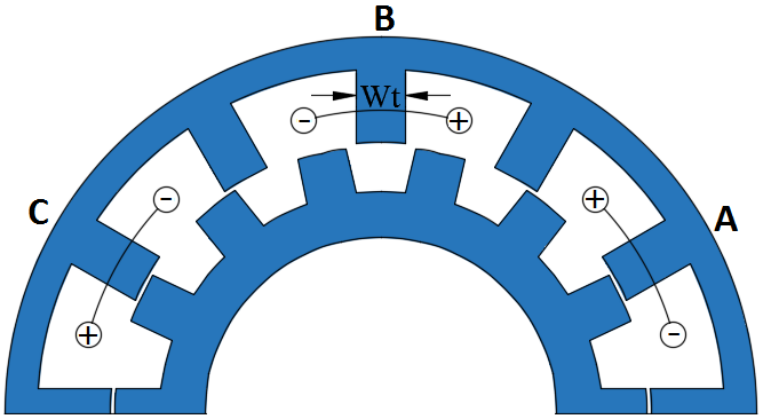

(a)

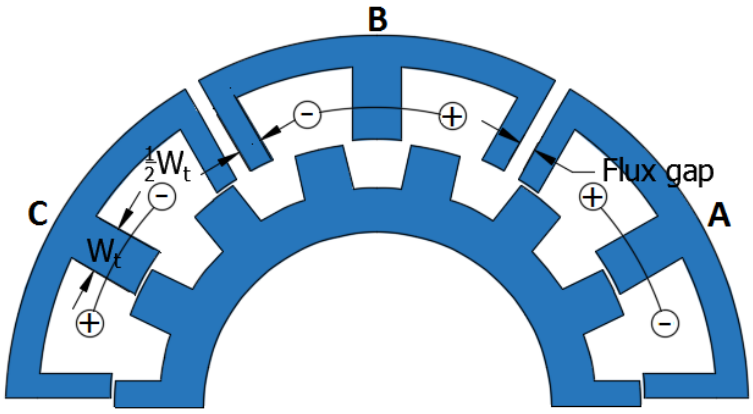

(b)

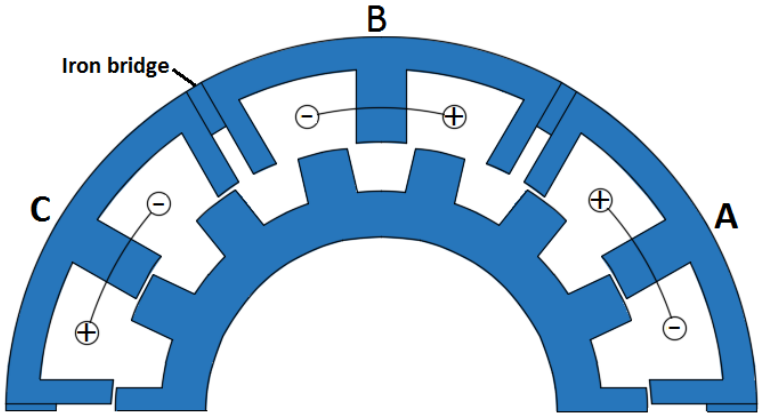

(c)

Fig. 3.2 Cross-sections (half) of 12-slot/14-pole SRMs with (a) non-modular structure, (b) modular structure without iron bridges and (c) modular structure with iron bridges. All the machines have SLC winding topologies.

3.2.2 FLUX DISTRIBUTION

By way of example, two-dimensional finite element (2D FE) predicted flux distributions are shown in Fig. 3.3, for the particular cases of the 12-slot/8-pole and 12-slot/14-pole CSRMs.

Two variants of each design were considered, viz. a non-modular variant with FG=0 mm and a modular variant with FG=2 mm. For all machines, the rotors are at the aligned positions of the phase A, which is supplied with a 10A DC current.

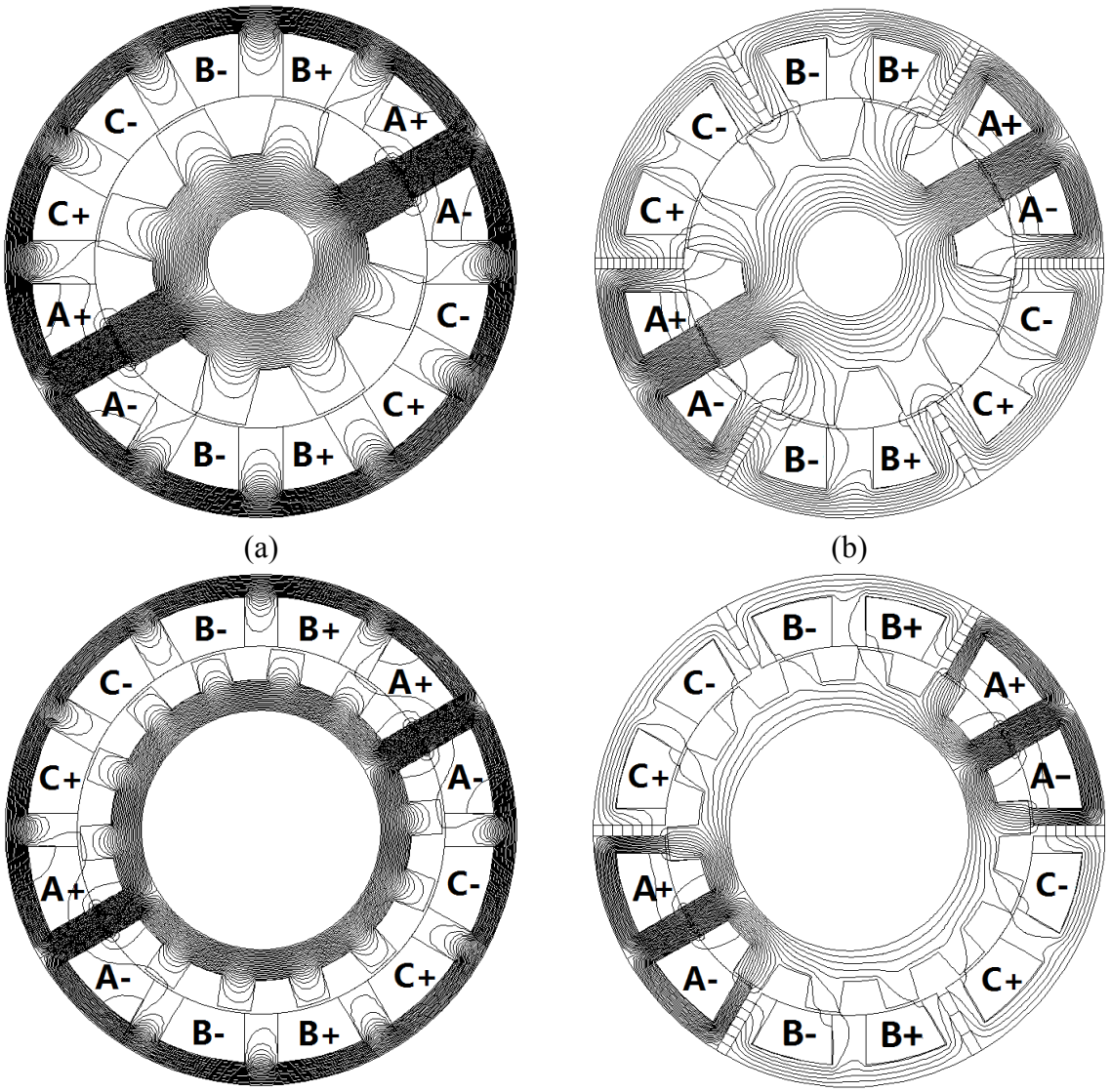

Fig. 3.3 Comparison of 2D FE predicted flux distributions between 12-slot/8-pole CSRMs with (a) FG=0 mm and (b) FG= 2mm, and 12-slot/14-pole CSRMs with (c) FG=0 mm and (d) FG= 2mm. The rotor is at the aligned position and phase A alone is supplied with a 10A DC current.

It can be established that for both machines, the flux of the phase A is not linked with the phases B and C to any meaningful extent in the non-modular CSRM (i.e. when FG=0 mm) as shown in Fig. 3.3 (a) and (c). However, due to the presence of FGs in the modular variants, the flux path is dramatically changed as shown in Fig. 3.3 (b) and Fig. 3.3 (d). The shorter flux

path and less concentrated flux lead to lower MMF across the stator back iron. As a result, the flux density in the stator back iron of the modular machines is lower than that of the non-modular counterparts. This in turn dictates that they will be less sensitive to magnetic saturation and with improved overload torque capability.

3.2.3 SELF- AND MUTUAL-INDUCTANCES

Due to the relationship between flux linkage and apparent inductances, the varying flux paths will have influence on self-inductance L_a and mutual-inductance M_{ab}. The self- and mutual-inductances and their derivatives with respect to rotor positions for the 12-slot/8-pole and 12-slot/14-pole CSRMs have been calculated using 2D FEA, as shown from Fig. 3.4 to Fig. 3.6, where 0 elec. deg. represents the rotor aligned position. In $dL/d\theta$ and $dM/d\theta$, the units for L and M are mH and for θ is in elec. deg. The FG widths increase from 0mm to 6mm and only the phase A is supplied with DC currents of both 10A and 40A. The trend in inductances and their derivatives for different FG widths of the 12-slot/10-pole and 12-slot/16-pole machines, although not shown in this chapter, are very similar to those of the 12-slot/8-pole and 12-slot/14-pole machines, respectively. In addition, the self-inductances and their derivatives of the MCSRMs with different FG widths are not shown because they are similar to those of the CSRMs but the mutual-inductances and their derivatives are shown in Fig. 3.7.

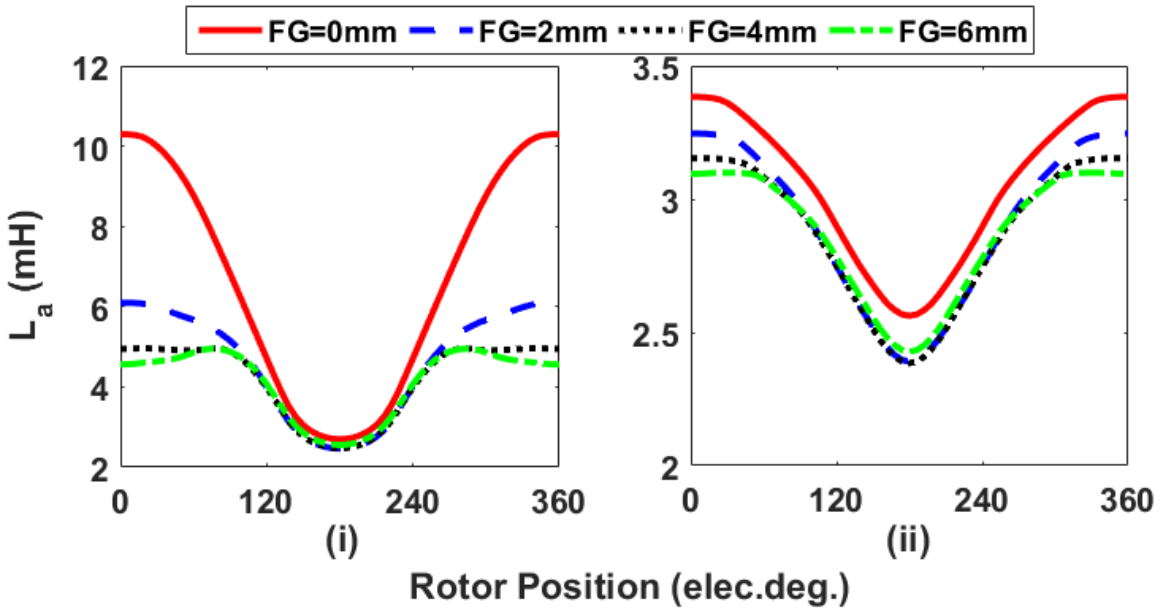

(a)

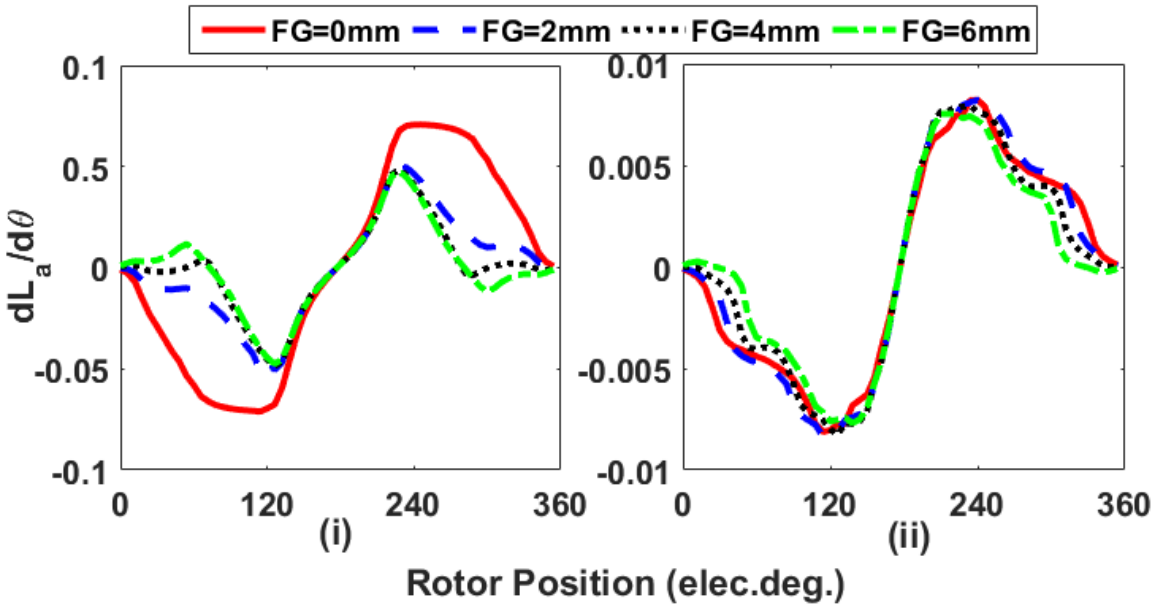

(b)

Fig. 3.4 Comparison of (a) L_a and (b) $dL_a/d\theta$ between the 12-slot/8-pole modular CSRMs with different FG widths. Phase A is supplied with a (i) 10A and (ii) 40A DC current.

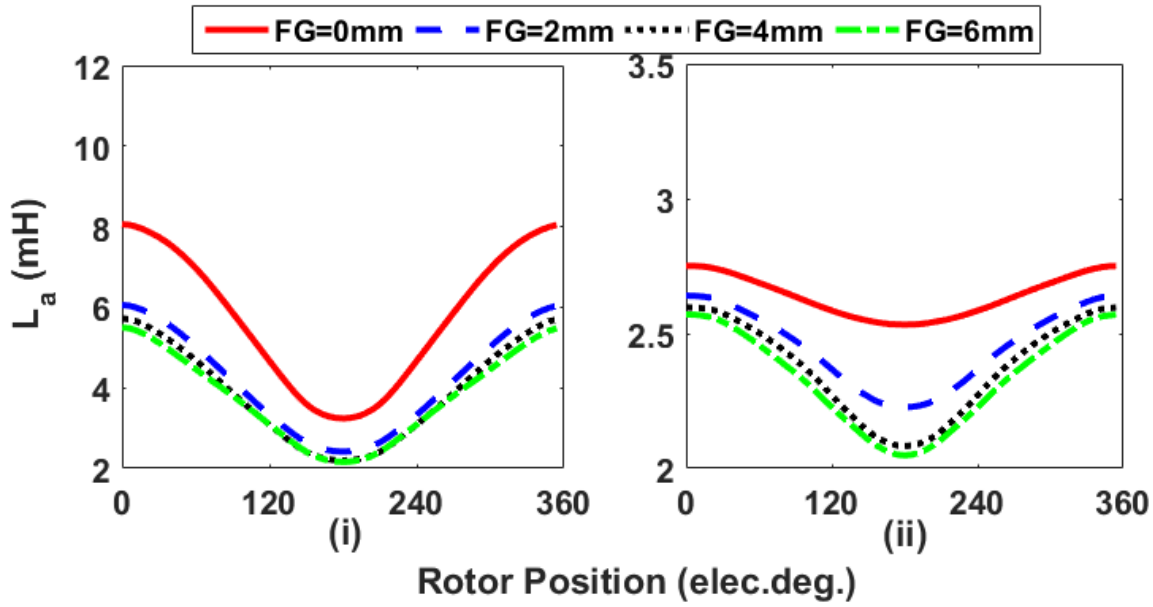

(a)

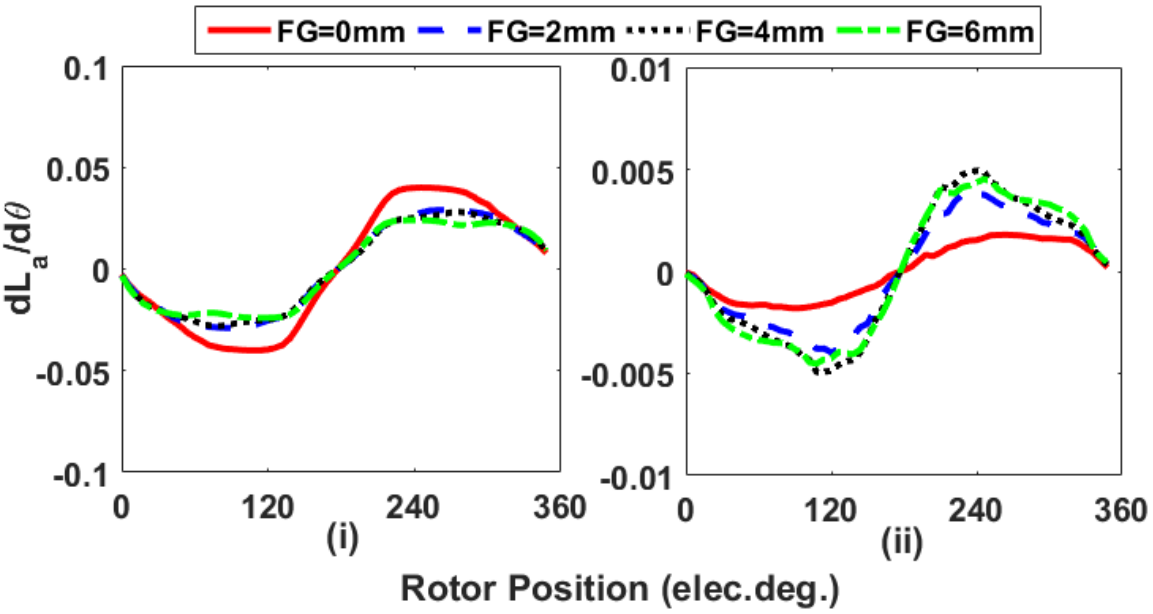

(b)

Fig. 3.5 Comparison of (a) L_a and (b) $dL_a/d\theta$ between the 12-slot/14-pole modular CSRMs with different FG widths. Phase A is supplied with a (i) 10A and (ii) 40A DC current.

Regardless of the rotor pole number, it is apparent that the amplitudes of self-inductances of the non-modular CSRMs (FG=0mm) as shown in Fig. 3.4(a) and Fig. 3.5(a) are higher than that of the modular CSRMs (FG >0mm) at both low (10A) and high (40A) phase currents. In Fig. 3.4(b) and Fig. 3.5(b), the amplitudes of $dL_a/d\theta$ for both the 12-slot/8-pole and 12-slot/14-pole CSRMs decrease with increasing FG widths at low current (<15A). In addition, at low current without heavy magnetic saturation, the FG width only has significant effect on the amplitudes of $dL_a/d\theta$ when it is varying from 0mm to 2mm since the flux path has been

changed significantly from non-modular to modular machines due to the FGs in the stator. However, there is no significant effect between modular machines (FG=2mm and FG=4mm) since the increase in FG widths does not have significant influence on the flux path anymore.

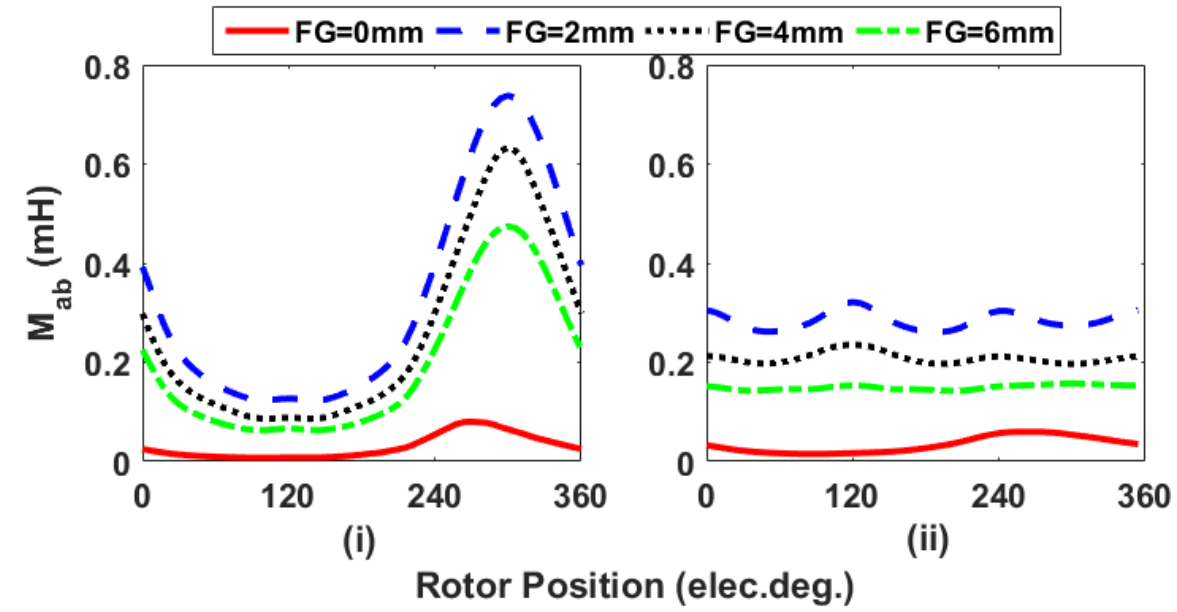

(a)

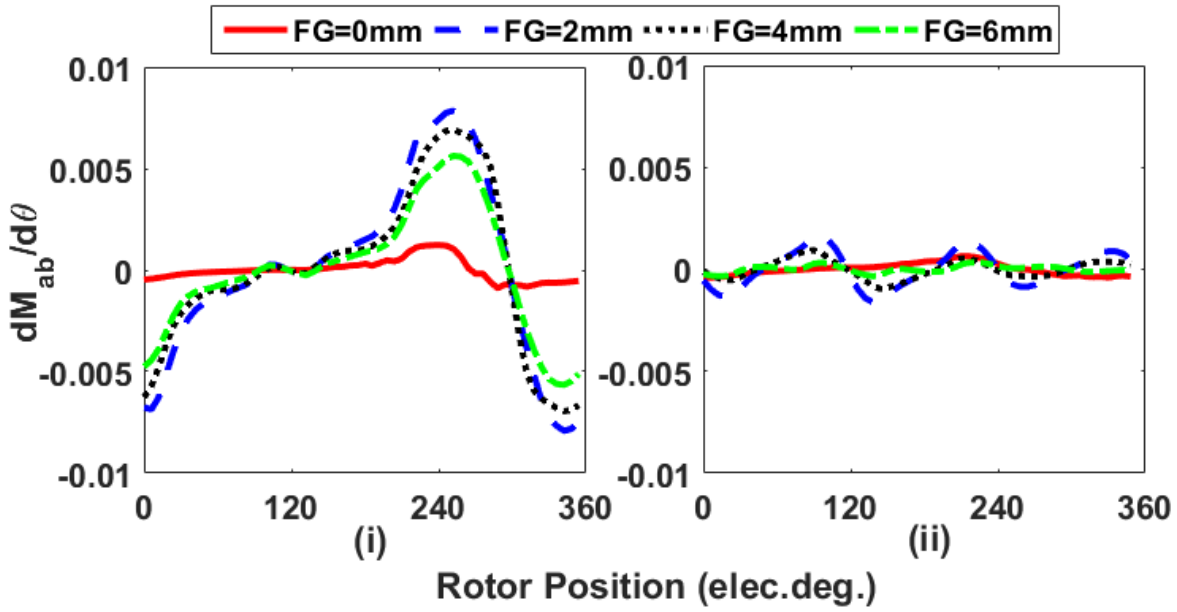

(b)

Fig. 3.6 Comparison of (a) M_{ab} and (b) $dM_{ab}/d\theta$ between the (i) 12-slot/8-pole and (ii)12-slot/14-pole modular CSRMs with different FG widths. Phase A is supplied with a 10A DC current.

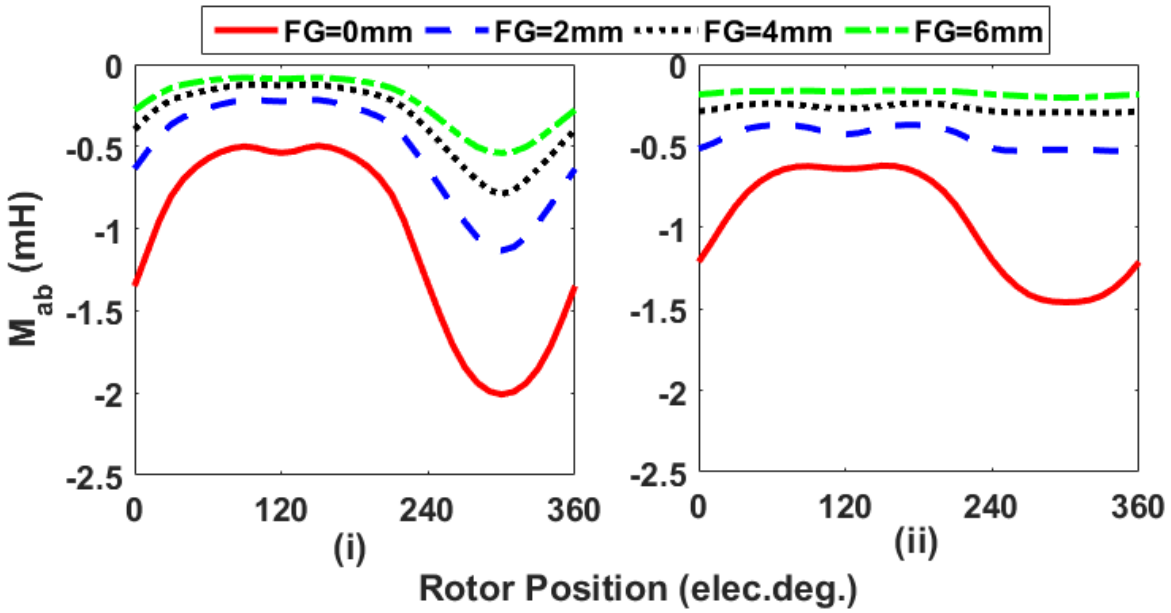

(a)

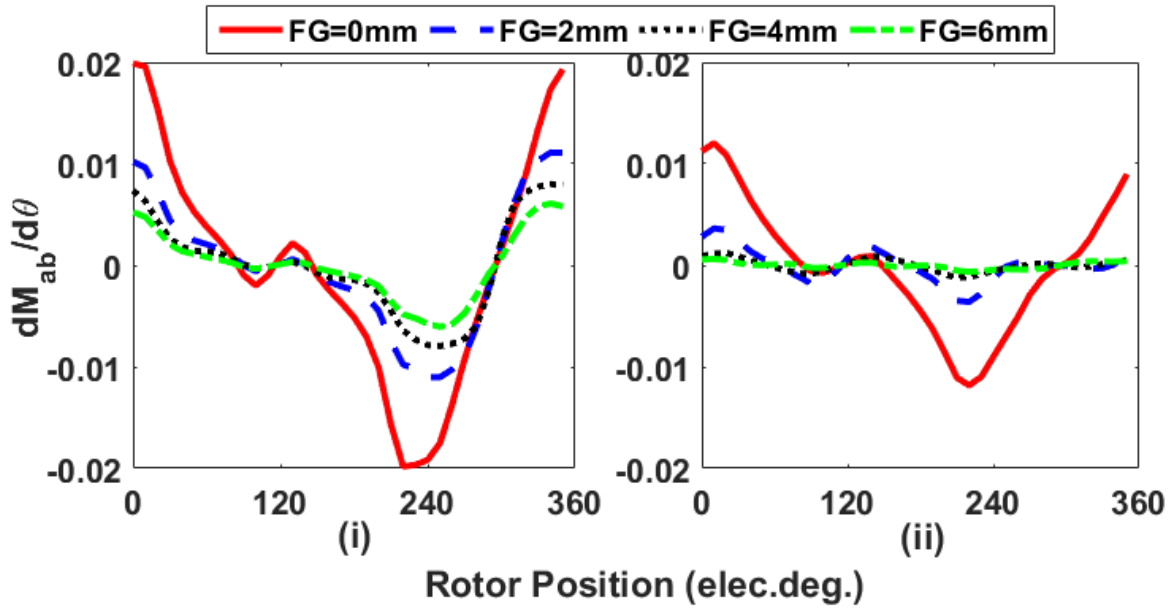

(b)

Fig. 3.7 Comparison of (a) M_{ab} and (b) $dM_{ab}/d\theta$ between the (i) 12-slot/8-pole and (ii)12-slot/14-pole modular MCSRMs with different FG widths. Phase A is supplied with a 10A DC current.

At high current, the amplitude of $dL_a/d\theta$ for the 12-slot/8-pole CSRMs is only marginally influenced by the width of the FGs. However, in the case of the 12-slot/14-pole CSRMs, the modular machines have higher amplitudes of $dL_a/d\theta$ compared with the non-modular machine which is due to the fact that the 14-pole modular machines can be less sensitive to magnetic saturation than their non-modular counterpart.

The variations of the M_{ab} and $dM_{ab}/d\theta$ at 10A DC current of the CSRMs and MCSRMs are shown in Fig. 3.6 and Fig. 3.7, respectively. This single value of current is sufficient to demonstrate this aspect of behaviour since this measure is not influenced to any meaningful degree by the current levels that are likely to be encountered in this machine. Moreover, it is worth noting that compared with $dL_a/d\theta$, the very modest contribution from $dM_{ab}/d\theta$ is usually neglected for non-modular CSRMs. According to the waveforms of $dL_a/d\theta$, it can be predicted that the 12-slot/14-pole CSRMs will have the potential to produce higher electromagnetic torque with FGs than a corresponding non-modular design. For both the 12-slot/8-pole and 12-slot/14-pole MCSRMs, the amplitudes of the M_{ab} and $dM_{ab}/d\theta$ are decreased with increasing FG widths. However, the similar trend in the $dL_a/d\theta$ still make the modular 12-slot/14-pole MCSRMs possible to produce higher electromagnetic torque than the non-modular machine if appropriate current waveforms are employed.

3.3 ELECTROMAGNETIC PERFORMANCE INVESTIGATION OF NON-MODULAR AND MODULAR MACHINES

3.3.1 ON-LOAD TORQUE BY DIFFERENT CONDUCTION ANGLES

According to the general expression of electromagnetic torque of a SRM as shown in (2.5)**,** the definition of torque ripple deployed in this chapter can be calculated on the basis of the maximum (T_{max}), the minimum (T_{min}) and the average torque (T_{av}) over an electrical period as presented in (2.11)**.**

Given the nature of the waveforms of self- and mutual-inductance derivatives, the conduction angles of rectangular wave current supply have been optimized and selected according to the method stated in [64], as shown in TABLE 3.2. For unipolar excitation, the current has the positive magnitude and is always in the same direction. However, the current has both positive and negative pulses for bipolar excitation, e.g. the current waveform with conduction angle of bipolar 180° elec. consists of a negative current pulse for 60° elec. and a positive current pulse for 120° elec. Moreover, both the current pulses are supplied when $dL_a/d\theta \geq 0$ in order to generate positive torque. With conduction angle of unipolar 120° elec., the mutual-inductance does not make a net contribution to electromagnetic torque. Hence, the torque is only produced by the change in self-inductance. However, both unipolar and bipolar

180° elec. conduction make full use of both the changes in self- and mutual-inductances for torque generation.

TABLE 3.2 CONDUCTION ANGLES FOR RECTANGULAR WAVE EXCITATION

Conduction angle (elec.)	Component (elec.)
Unipolar 120°	Positive 120°
Unipolar 180°	Positive 180°
Bipolar 180°	Negative 60° + positive 120°

In order to select the most appropriate conduction angle for different machines, 2D FE calculations were performed to establish the average torque over one cycle for each machine as function of the magnitude of current. Fig. 3.8 shows the resulting comparison of average torques between non-modular CSRMs. It is evident that with conduction angle of unipolar 120° elec., the non-modular 12-slot/8-pole and 12-slot/14-pole SRMs have greater average torque performances at low current. However, at high current, the highest average torque of the 12-slot/8-pole non-modular SRM is achieved by adopting the conduction angle of unipolar 180° elec., while for the 12-slot/14-pole machine it is the bipolar 180° elec. Additionally, as shown in TABLE 3.3, the lowest torque ripples for both the 12-slot/8-pole and 12-slot/14-pole machines are achieved by adopting the conduction angle of unipolar 180° elec., while the highest torque ripple are generated when adopting the conduction angle of bipolar 180° elec.

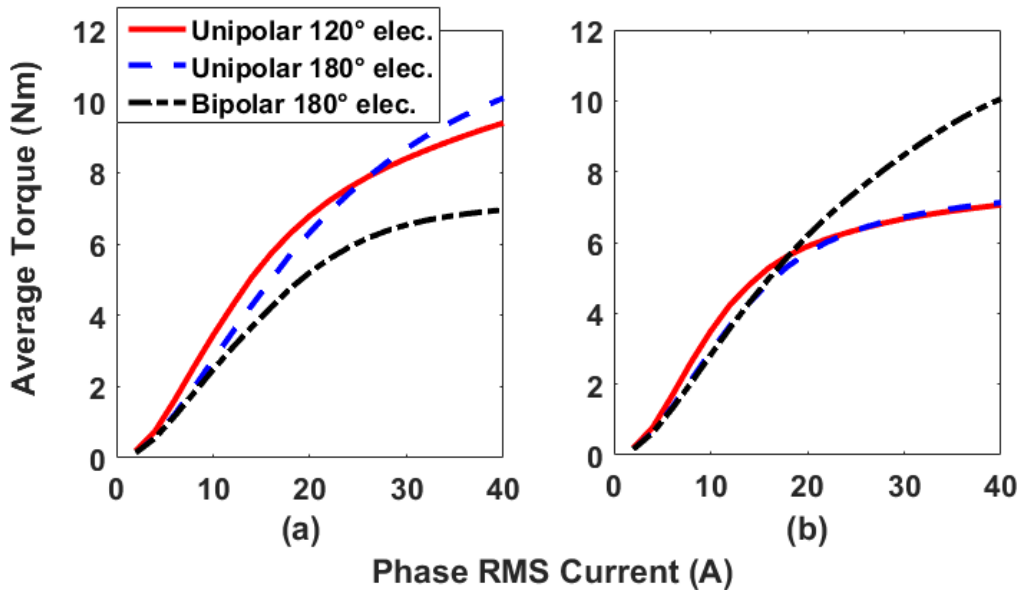

Fig. 3.8 Influence of conduction angles on average torque between (a) 12-slot/8-pole and (b) 12-slot/14-pole non-modular CSRMs.

TABLE 3.3 TORQUE RIPPLE OF NON-MODULAR CSRMS AT $40A_{RMS}$

Machine type	Conduction angle (elec. deg.)		
	Unipolar 120	Unipolar 180	Bipolar 180
12-slot/8-pole	81.59%	35.77%	123.2%
12-slot/14-pole	51.24%	37.49%	67.96%

TABLE 3.4 APPROPRIATE CONDUCTION METHODS OF THE CSRMS

Machine type	Low current	High current
12-slot/8-pole	unipolar 120° elec.	unipolar 180° elec.
12-slot/10-pole	unipolar 120° elec.	bipolar 180° elec.
12-slot/14-pole	unipolar 120° elec.	bipolar 180° elec.
12-slot/16-pole	unipolar 120° elec.	unipolar 180° elec.

TABLE 3.5 APPROPRIATE CONDUCTION METHODS OF THE MCSRMS

Machine type	Low current	High current
12-slot/8-pole	bipolar 180° elec.	bipolar 180° elec.
12-slot/10-pole	bipolar 180° elec.	unipolar 180° elec.
12-slot/14-pole	bipolar 180° elec.	unipolar 180° elec.
12-slot/16-pole	bipolar 180° elec.	bipolar 180° elec.

Furthermore, as shown in TABLE 3.4, the unipolar 120° elec. is the most effective conduction angle for all the CSRMs with different slot/pole number combinations at low current. However, at high current, the unipolar 180° elec. conduction is preferred for the 12-slot/8-pole and 12-slot/16-pole CSRMs, while the bipolar 180° elec. conduction is preferred for the 12-slot/10-pole and 12-slot/14-pole CSRMs. Similarly, it can be found in TABLE 3.5 that the bipolar 180° elec. is the most appropriate conduction angle for all the MCSRMs with different slot/pole number combinations at low current. However, at high current, the bipolar 180° elec. conduction is preferred for the 12-slot/8-pole and 12-slot/16-pole MCSRMs, while the unipolar 180° elec. conduction is preferred for the 12-slot/10-pole and 12-slot/14-pole MCSRMs. For consistency, the preferred conduction angles for high current are adopted for the following on-load torque investigation for the modular machines with different FG widths.

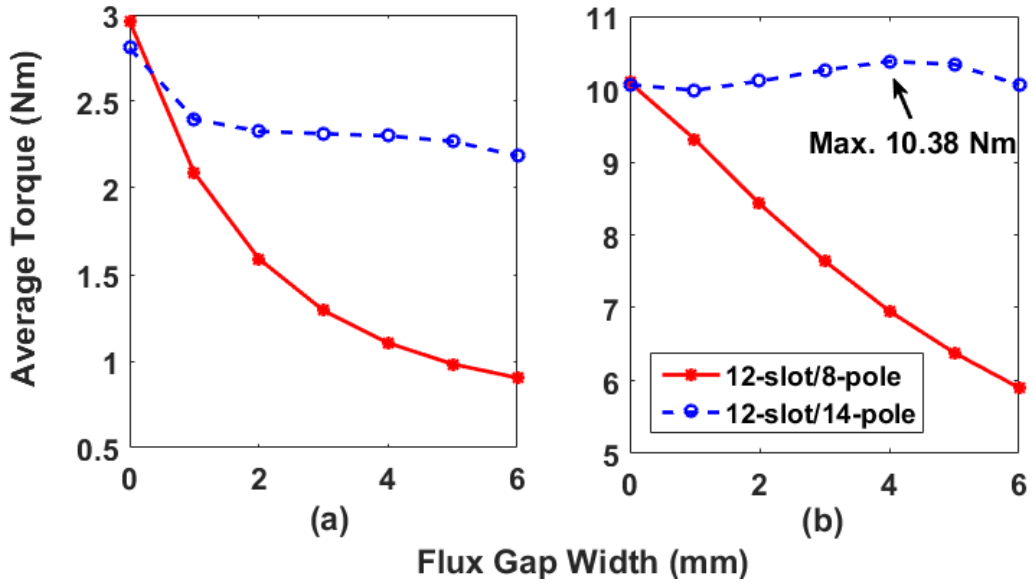

Fig. 3.9 Comparison of average torque between the 12-slot/8-pole and 12-slot/14-pole CSRMs against FG widths at (a) $10\mathrm{A_{rms}}$ and (b) $40\mathrm{A_{rms}}$.

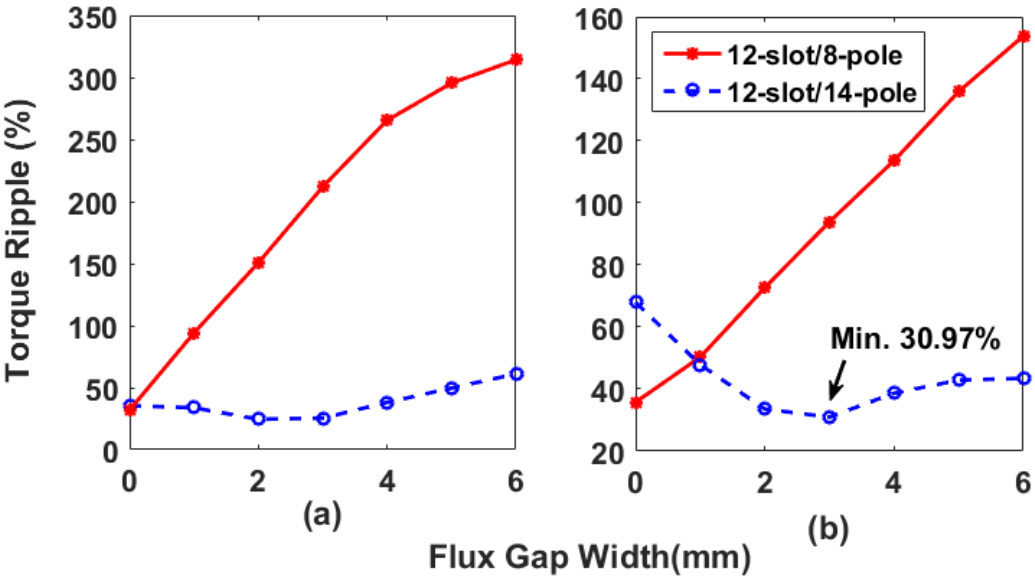

Fig. 3.10 Comparison of torque ripple between 12-slot/8-pole and 12-slot/14-pole CSRMs against FG widths at (a) $10A_{rms}$ and (b) $40A_{rms}$.

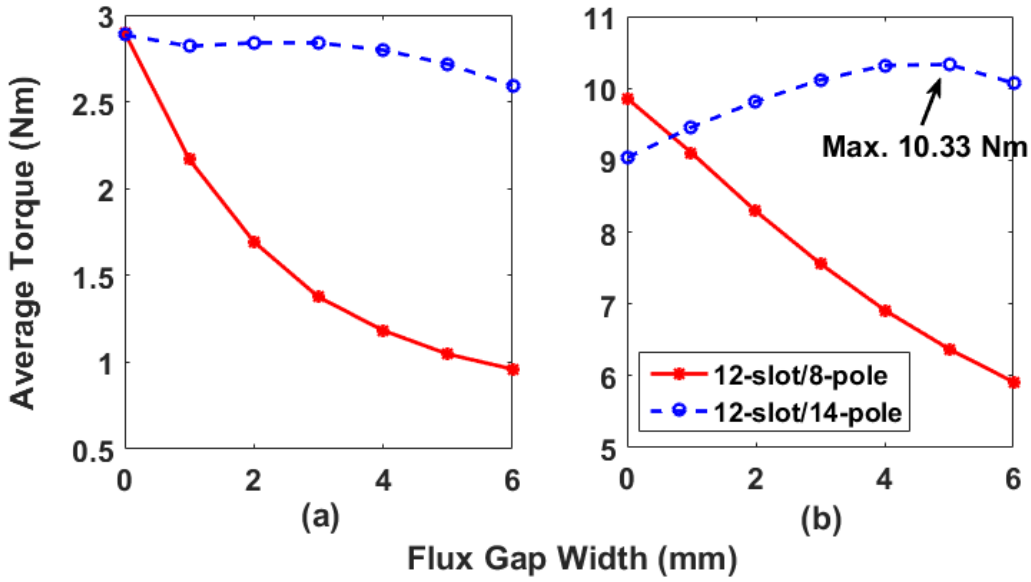

Fig. 3.11 Comparison of average torque between the 12-slot/8-pole and 12-slot/14-pole MCSRMs against FG widths at (a) $10\mathrm{A_{rms}}$ and (b) $40\mathrm{A_{rms}}$.

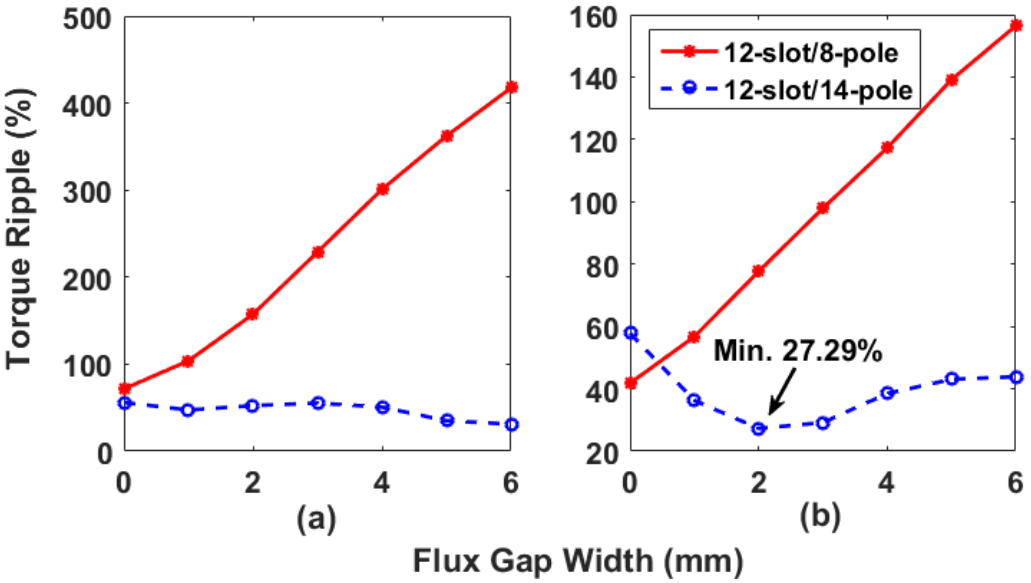

Fig. 3.12 Comparison of torque ripple between 12-slot/8-pole and 12-slot/14-pole MCSRMs against FG widths at (a) $10A_{rms}$ and (b) $40A_{rms}$.

The average torque and torque ripple at different current levels were predicted by 2D FEA. The resulting outcomes are shown in Fig. 3.9 to Fig. 3.12, from which it is evident that the 12-slot/8-pole CSRM and MCSRM with non-modular structure achieve better performance than their modular counterparts regardless of phase RMS current employed. In order to investigate the sensitivity to magnetic saturation and overload torque capability, the 12-slot/14-pole

modular CSRM with FG=3 mm and MCSRM with FG=4mm were selected as the in-depth design for copper loss calculation.

3.3.2 COPPER LOSS

The machines are optimized with non-modular structure for a fixed current density of 5.68A/mm^2. Hence, with increasing FGs, the slot area is slightly reduced, leading to reduced wire diameter. Fig. 3.13 shows the copper loss for different SRMs for a phase current of $10A_{rms}$. It is evident that the copper losses at rated current for all modular machines are higher than those of their non-modular counterparts irrespective of the number of poles. However, previous results demonstrated that the average torque is also influenced by the dimensions of the FGs. Hence, in order to provide a consistent basis for comparing design, the relationship between torque and copper loss needs to be investigated.

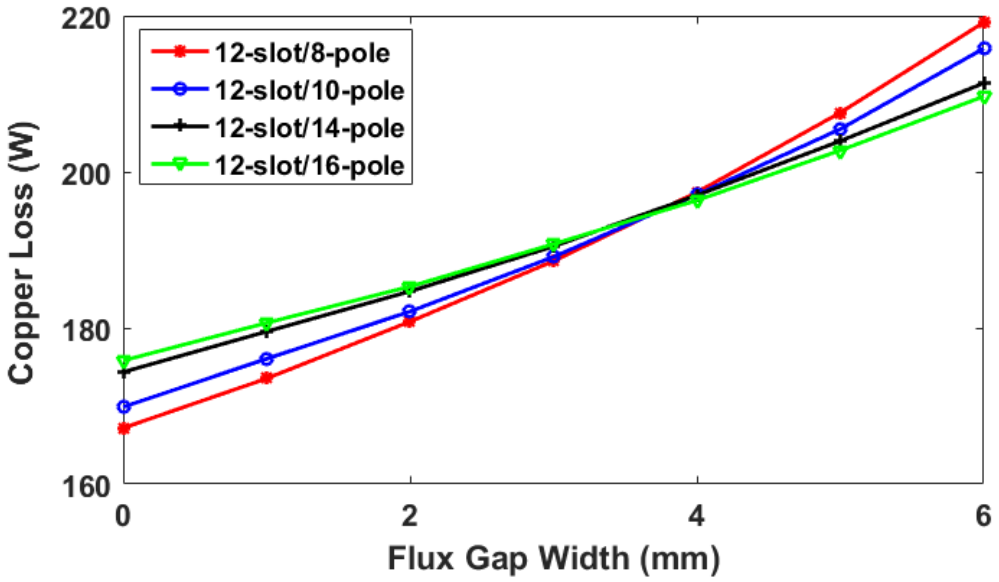

Fig. 3.13 Copper loss of non-modular and modular SRMs with different pole numbers and FG widths at $10A_{rms}$ current.

With the optimized conduction angles, the variation in the average torques as a function of copper loss for non-modular 8-pole SRMs and modular 14-pole SRMs (CSRM with FG=3mm and MCSRM with FG=4mm) are shown in Fig. 3.14. It is apparent that both non-modular and modular machines can produce similar average torque values for the same copper loss, regardless of winding configurations. However, with conventional winding, the torque ripple in modular 12-slot/14-pole machine can be much lower than that in non-modular 12-slot/8-pole machine when the copper loss (phase current) is higher than around 170W (10A). While,

the torque ripple in modular 12-slot/14-pole machine can be much lower than that in non-modular 12-slot/8-pole machine at any copper loss (phase current) with mutually-coupled winding configurations.

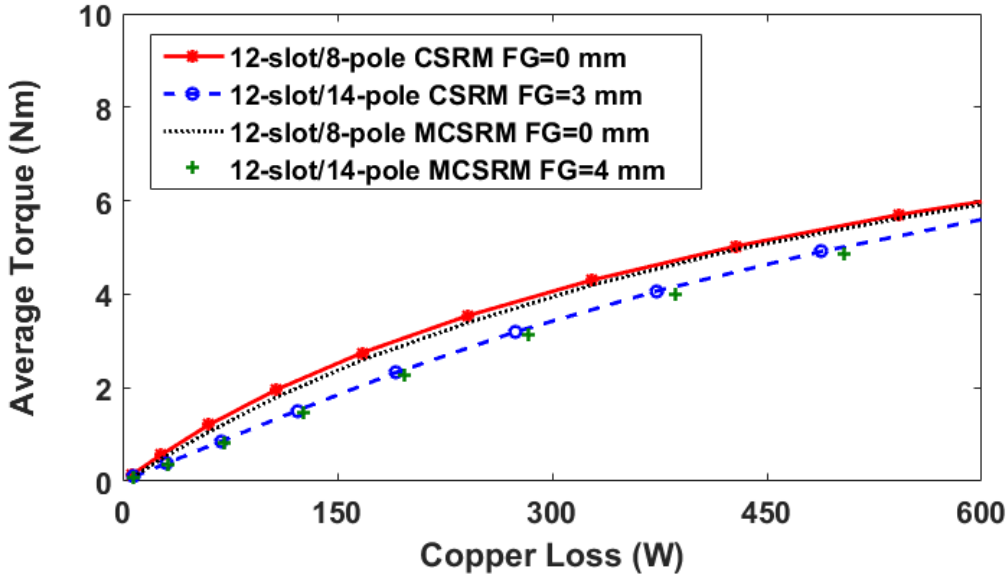

(a)

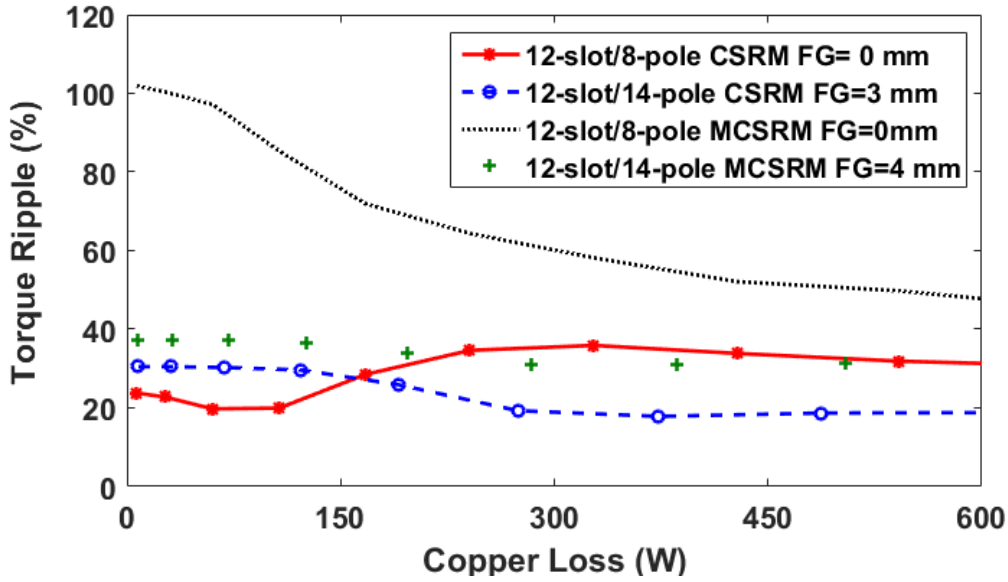

(b)

Fig. 3.14 Comparison of (a) average torque and (b) torque ripple as a function of copper loss.

3.3.3 IRON LOSS

The method of iron loss calculation in this chapter is similar to that in Chapter 2, and (2.12) is used for calculating the iron loss density in each element of the FE element model [6]. The overall loss is obtained from a summation of the losses in each finite element in the stator and rotor core regions. For silicon iron core considered in this thesis, the hysteresis loss coefficients k_{h1} and k_{h2} are $5A/m$ and $40Am/Vs$ respectively. The eddy current loss coefficient k_e is $0.022\ Am/V$.

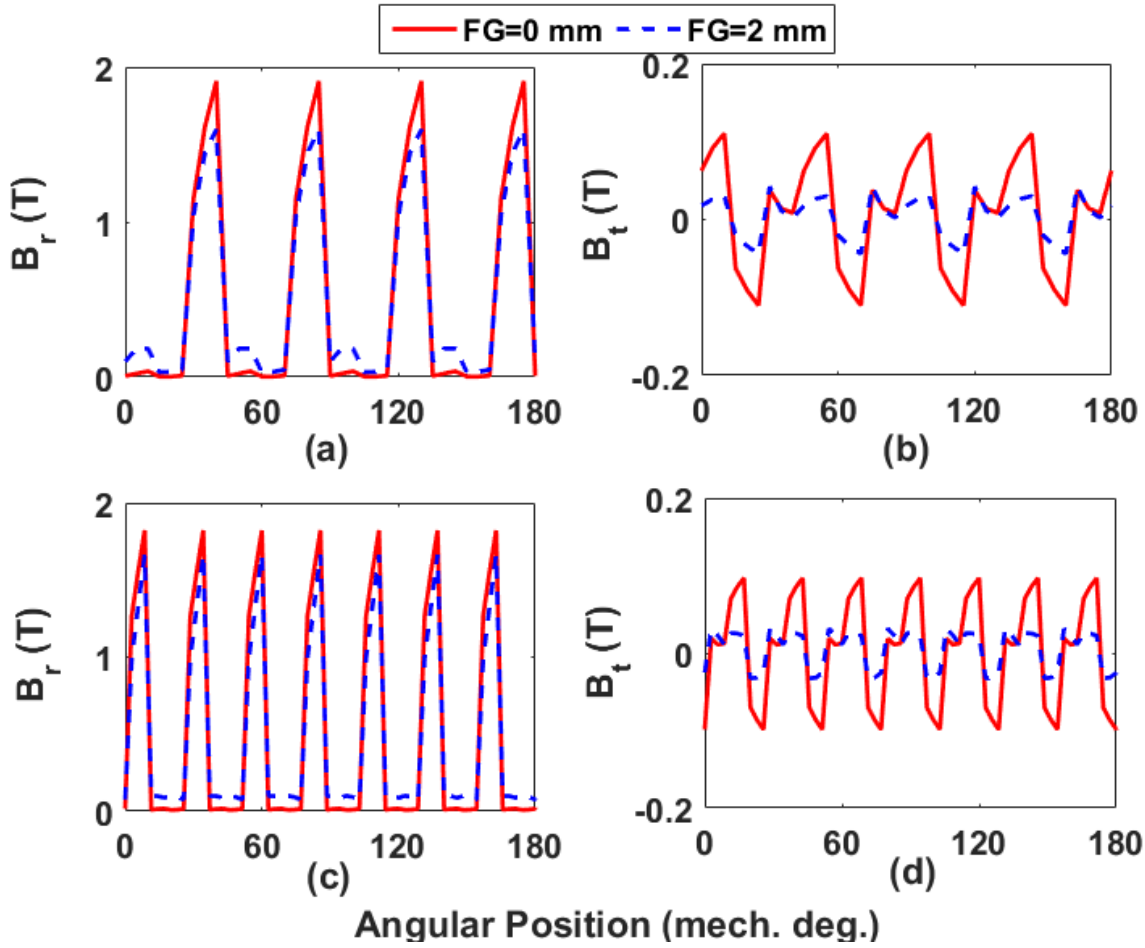

Fig. 3.15 Radial and tangential flux densities in **stator tooth** of (a) and (b) 12-slot/8-pole, (c) and (d) 12-slot/14-pole CSRMs. 3-phases are supplied with rectangular wave currents with conduction angle of unipolar 120° elec.

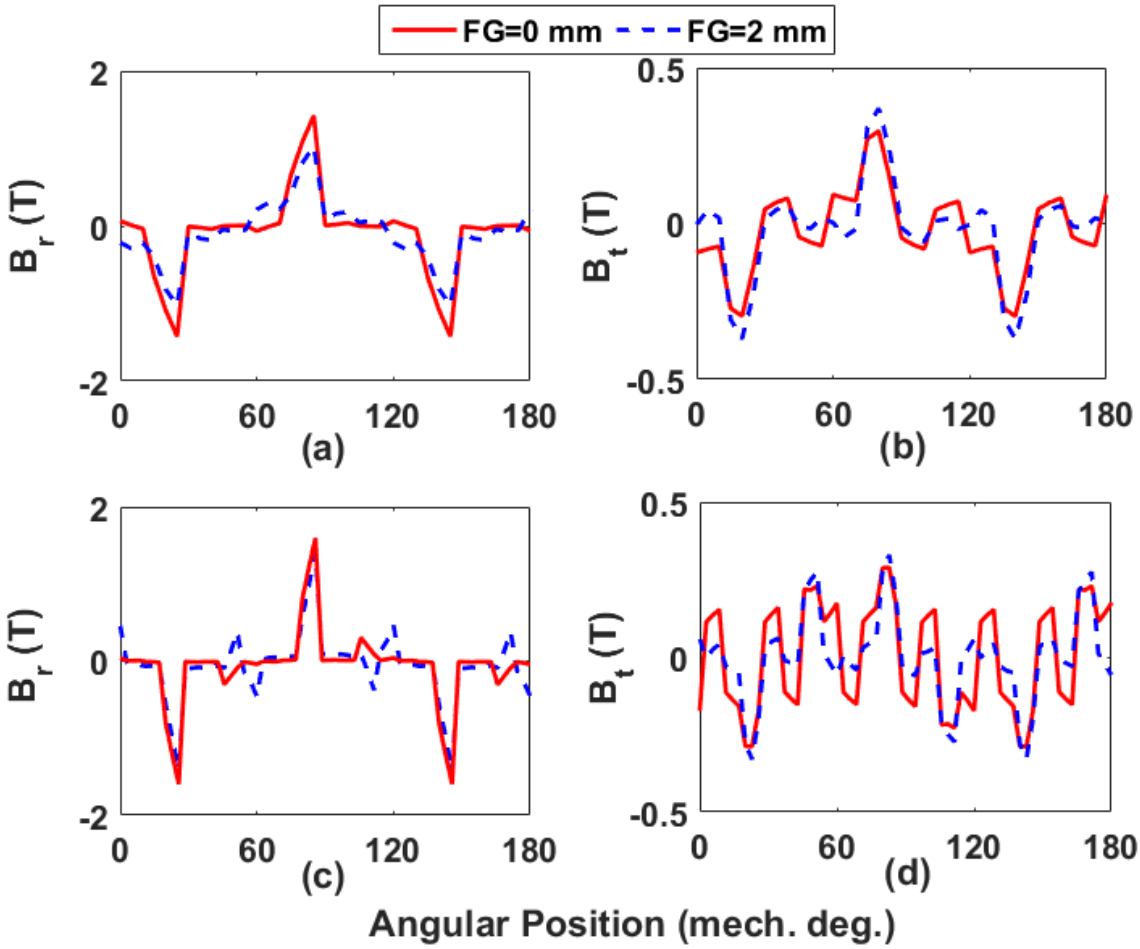

Fig. 3.16 Radial and tangential flux densities in **rotor tooth** of (a) and (b) 12-slot/8-pole, (c) and (d) 12-slot/14-pole CSRMs. 3-phases are supplied with rectangular wave currents with conduction angle of unipolar 120° elec.

The flux densities have been investigated in different parts of the stator and rotor iron cores. By way of example, the flux densities at the middle of the stator and rotor teeth for 12-slot/8-pole and 12-slot/14-pole CSRMs with different FG widths are shown in Fig. 3.15 and Fig. 3.16. It is apparent from these waveforms that the modular machines have lower amplitude of radial flux densities in both the stator and rotor teeth than their non-modular counterparts. However, for a given slot/pole number combination, the periodicities of flux densities are the same between non-modular and modular machines. With different rotor pole numbers, the stator flux densities have different periodicities. However, the rotor flux densities exhibit 3 full cycles in one mechanical cycle (360 mech. deg.) for both the CSRMs. The resulting flux density frequencies at 400rpm are given in TABLE 3.6 for both the CSRM and the MCSRM with different rotor pole numbers. Furthermore, TABLE 3.7 shows the iron loss at $10A_{rms}$ and 400 rpm.

TABLE 3.6 SUMMARY OF FLUX DENSITY FREQUENCIES AT A ROTATIONAL SPEED OF 400RPM

Slot/pole number combination	Machine type	B_r/B_t frequency (Hz)	
		Stator	Rotor
12-slot/8-pole	CSRM	53.3	20
	MCSRM	53.3	40
12-slot/14-pole	CSRM	93.3	20
	MCSRM	93.3	40

TABLE 3.7 IRON LOSS (W) @ $10A_{rms}$ AND 400RPM

Slot/pole number combination	Machine type	FG (mm)			
		0	2	4	6
12-slot/8-pole	CSRM	4.05	1.48	1.18	1.26
	MCSRM	3.18	1.60	1.39	1.46
12-slot/14-pole	CSRM	6.61	2.47	1.84	1.49
	MCSRM	4.41	2.66	2.05	1.68

It can be found in TABLE 3.6 that although the stator flux density has different frequencies between 8-pole and 14-pole machines, it is the same between the CSRM and MCSRM. The rotor flux density frequency are 20Hz for the CSRM, and 40Hz for the MCSRM, regardless of the rotor pole numbers. Accordingly, TABLE 3.7 shows that the iron loss of the non-modular CSRM is higher than that of the non-modular MCSRM. However, the modular CSRMs present lower iron loss than that of the modular MCSRMs. Regardless of the machine winding configurations, both the 12-slot/8-pole and 12-slot/14-pole modular machines can produce lower iron loss than the non-modular machines.

Fig. 3.17 and Fig. 3.18 show the variation of iron loss as functions of phase RMS current and speed for different FG widths. Due to similar trend in iron loss, the results for MCSRMs are not shown in this chapter to avoid duplication. It can be found that the 12-slot/14-pole machine produces higher iron loss than the 12-slot/8-pole machine due to the higher stator flux density frequency, as expected. However, with the increasing FG width, both machines produce significantly lower iron losses. For example, when FG=2mm, the iron loss of 12-slot/14-pole is reduced by around 63% when compared with the CSRMs with FG=0mm. This

is a very attractive feature, particularly for SRM used in high speed applications, where iron loss could constitute a significant proportion of the overall loss.

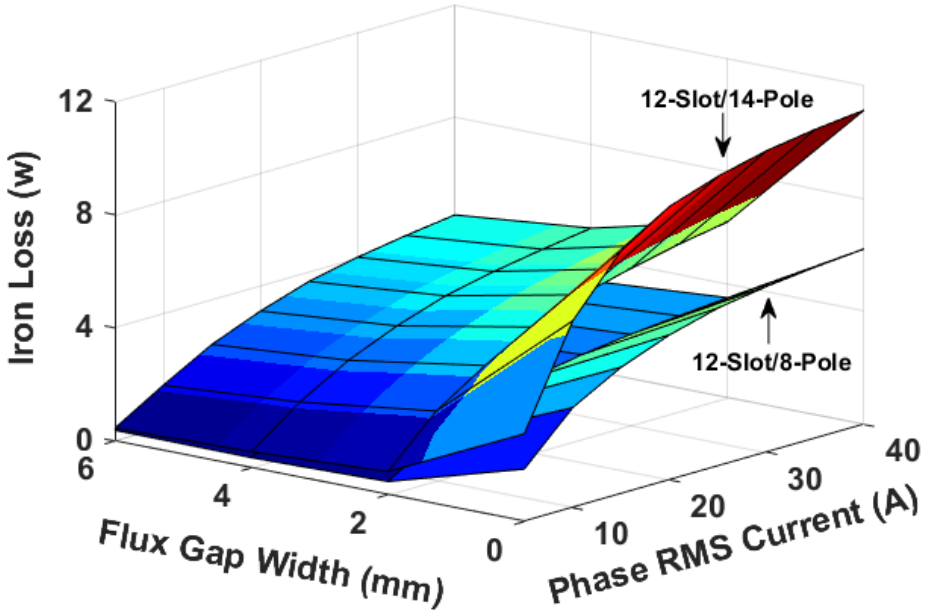

Fig. 3.17 Variation of iron loss against FG width and phase RMS current between the 12-slot/8-pole and 12-slot/14-pole CSRMs. The 3-phases are supplied by rectangular wave current with conduction angle of unipolar 120° elec., at a rotational speed of 400rpm.

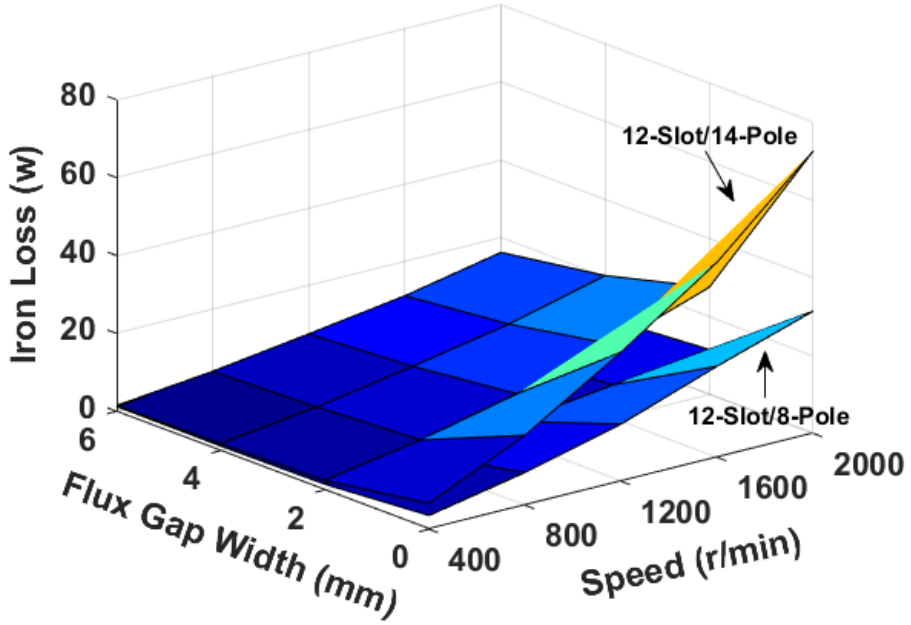

Fig. 3.18 Variation of iron loss against FG width and speed between the 12-slot/8-pole and 12-slot/14-pole CSRMs. The 3-phases are supplied by rectangular wave current with conduction angle of unipolar 120° elec., at $10A_{rms}$.

3.3.4 RADIAL FORCE

The change of flux path due to the presence of the FGs will not only influence the iron loss but also the radial force. Since the abrupt change of radial force acting on the stator as the rotor passes successive teeth is the main electromagnetic source of vibration and acoustic noise, an understanding of radial force is the key to investigate machine mechanical performance. According to Maxwell stress tensor, the radial force F_r on one stator pole is given by [84]:

$$F_r = \int_{-\frac{\theta_s}{2}}^{\frac{\theta_s}{2}} \frac{1}{2\mu_0} ({B_r}^2 - {B_t}^2) r_{si} L d\theta \tag{3.1}$$

where θ_s is the stator pole pitch, i.e. 30 mech. deg. for a SRM with 12-slot, $\mu_0$is the free space permeability, B_r and B_t are the radial and tangential flux densities in the airgap, r_{si} is the stator inner radius, and L is the active length.

According to (3.1), $({B_r}^2 - {B_t}^2)$ distribution in the airgap has been investigated, in which only the phase A is supplied with a DC current and the rotor is at the aligned position of the phase A. By way of example, the influence of FG widths on the airgap flux densities of the CSRMs at different current levels is shown in Fig. 3.19. Since the magnitude of the radial force is directly proportional to $({B_r}^2 - {B_t}^2)$, it can be observed that both the 12-slot/8-pole and 12-slot/14-pole modular machines are likely to have lower radial force distribution around the airgap. However, due to magnetic saturation, the non-modular and modular 12-slot/14-pole machines will produce similar peak radial force at high current.

In order to investigate the influence of FG widths on the radial force, Fig. 3.20 shows the localized radial force on one stator pole of the phase A predicted by 2D FEA. In this case, the 3-phases are supplied by currents with unipolar 120° elec. conduction. The 0° elec. rotor position corresponds to the rotor being aligned with the phase A. It can be seen that the radial force for both machines is decreased with increasing FG widths at low current, e.g. $10A_{rms}$. For the 12-slot/8-pole machines, the peak radial force is reduced by 35.2% when FG is changed from 0 mm to 2 mm. For the 12-slot/14-pole machines, it is reduced by 16.8%. However, the difference between peak radial force of different FG widths narrows at high current, e.g. $40A_{rms}$, again due to the onset of appreciable magnetic saturation. Moreover, at the same current level, the peak radial force of 12-slot/8-pole CSRM is higher than that of 12-slot/14-

pole CSRM. This is a consequence of the optimized stator pole arc being shorter with increasing rotor pole number, hence the radial force surface area is reduced.

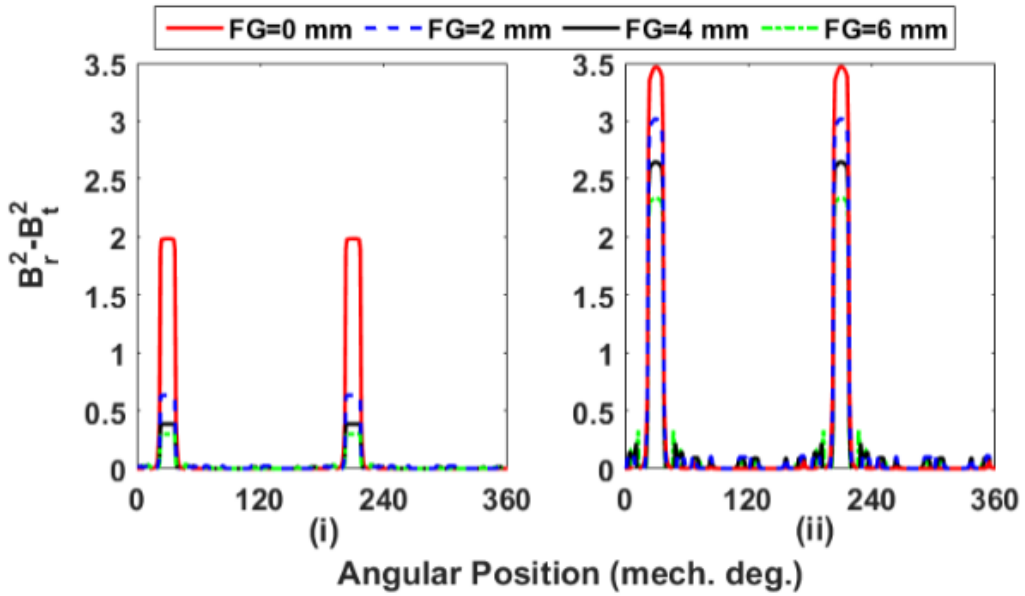

(a)

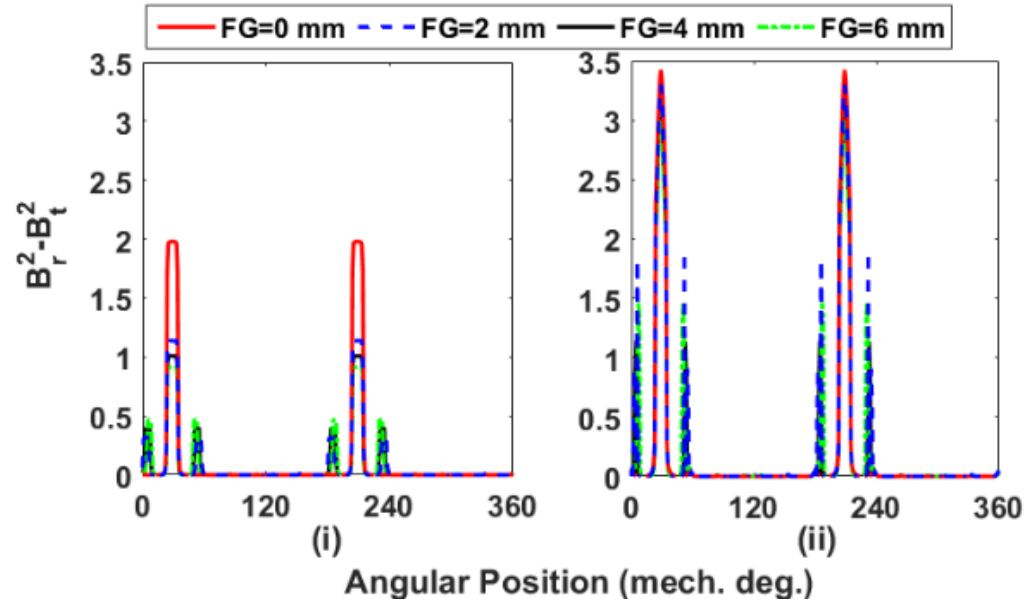

(b)

Fig. 3.19 ($B_r{}^2 - B_t{}^2$) distribution in the airgap of the (a) 12-slot/8-pole and (b) 12-slot/14-pole non-modular and modular CSRMs. Phase A is supplied with (i) 10A and (ii) 40A DC current and the rotor pole is aligned with phase A.

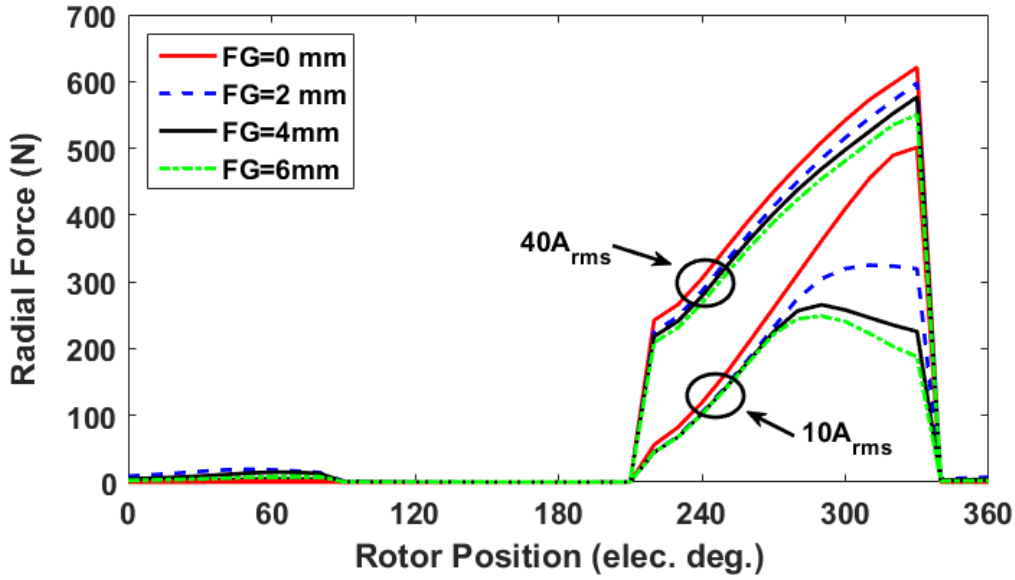

(a)

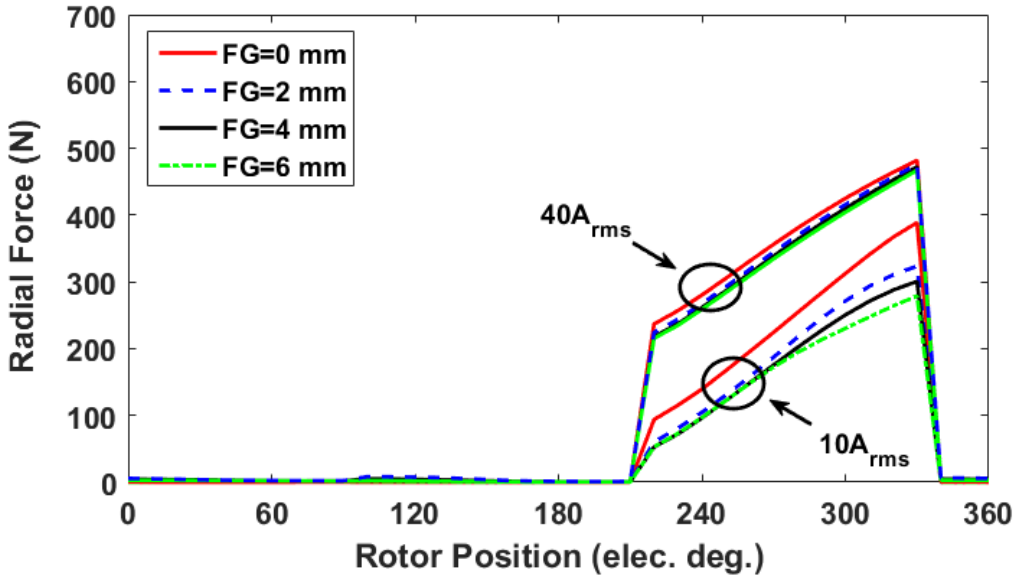

(b)

Fig. 3.20 Radial force on one stator pole of the phase A for different FG widths and currents of (a) 12-slot/8-pole and (b) 12-slot/14-pole CSRMs. The 3-phase rectangular wave current is supplied with conduction angle of unipolar 120° elec.

Due to the similar trend in radial force, the results for MCSRMs are not shown in this chapter. Instead, a comparison of the peak radial force between the CSRMs and MCSRMs, as well as the reduction of the peak radial force from FG=0mm to FG=2mm are shown in TABLE 3.8. It can be found that the MCSRMs have lower radial force than that of the CSRMs at low current. However, at high current, the MCSRMs have higher radial force since the CSRMs are more sensitive to magnetic saturation.

TABLE 3.8 COMPARISON OF PEAK RADIAL FORCE BETWEEN CSRM AND MCSRM WITH UNIPOLAR 120° ELEC. CONDUCTION

Slot/pole number combination	Machine type	Current (A)	FG(mm)		Reduction (%)
			0	2	
12-slot/8-pole	CSRM	10	501.3	325	35.2
		40	621.3	597.7	3.8
	MCSRM	10	455.2	309.3	32.1
		40	644.4	619.6	3.8
12-slot/14-pole	CSRM	10	388.8	323.5	16.8
		40	482.1	475.8	1.3
	MCSRM	10	356.3	316.9	11.1
		40	484.0	479.6	0.9

TABLE 3.9 INFLUENCE OF CONDUCTION ANGLES ON PEAK RADIAL FORCE FOR FG=2MM

	Conduction angle (elec. deg.)	Peak radial force at different current level (N)	
		$10A_{rms}$	$40A_{rms}$
12-slot/8-pole	Unipolar120	325	597.7
	Unipolar180	257.6	625.1
	Bipolar180	235.3	591.7
12-slot/14-pole	Unipolar120	323.5	475.8
	Unipolar180	297.1	517.6
	Bipolar180	264.1	499.3

TABLE 3.9 shows the influence of conduction angles on peak radial force at different current levels for modular CSRM with FG=2mm. This demonstrates that at low current, the lowest peak radial force is produced with a bipolar 180° elec. conduction angle. However, due to the different magnetic saturation levels, machines with different pole numbers have different preferred current conduction angles at high current.

3.4 MODULAR MACHINE WITH IRON BRIDGES

For completeness, iron bridges were added into the FGs to yield single-piece stator laminations. The resulting geometries become those shown previously in Fig. 3.2(c). With

different iron bridge heights and FG widths, the average torque of the 12-slot/8-pole and 12-slot/14-pole CSRMs varies as shown in Fig. 3.21.

The iron bridge height does not have significant influence on average torque especially for the height > 4mm. At low current, both machines have higher average torque with increasing iron bridge height ($\leq 4mm$), but the average torque is decreased with increasing FG width. However, at high current, the 12-slot/14-pole CSRM produces lower average torque with increasing iron bridge height ($\leq 4mm$). Hence, it can be concluded that the iron bridge has positive influence on average torque for both machines at low current, but negative influence for 12-slot/14-pole machine at high current.

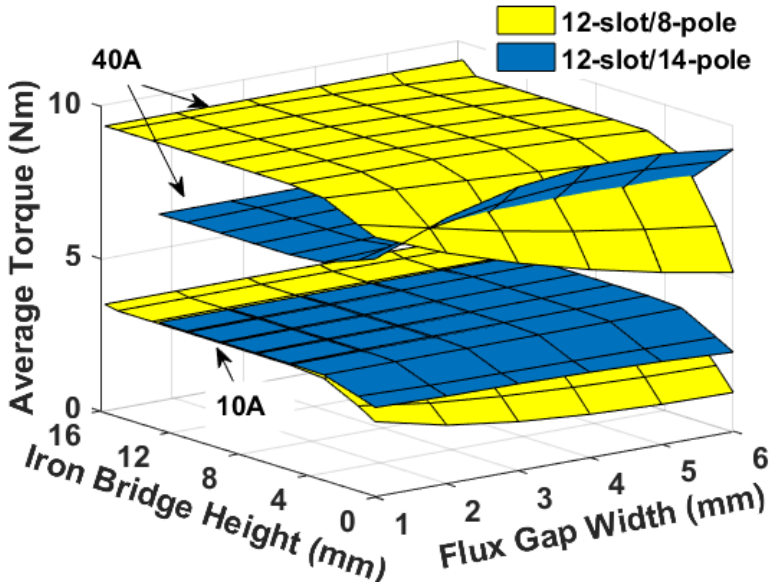

Fig. 3.21 Comparison of average torques between the 12-slot/8-pole and 12-slot/14-pole modular CSRMs with iron bridges.

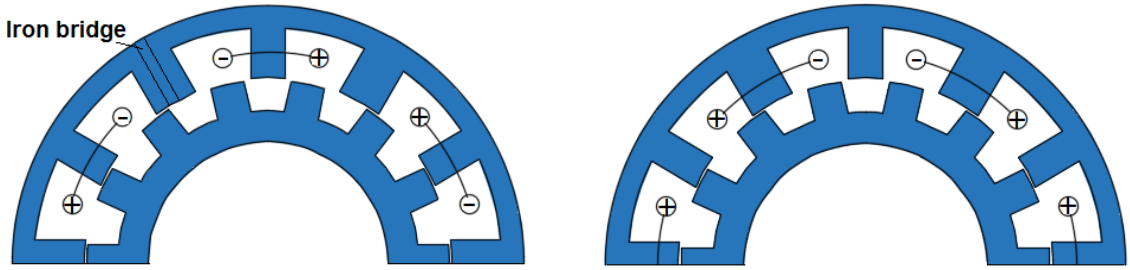

Fig. 3.22 Cross-sections of 12-slot/8-pole CSRM with UNET with (a) winding on narrower teeth (original teeth) (b) winding on wider teeth. The iron bridge (or FG) width is 2mm.

As aforementioned, when the FGs are fully replaced by iron, the stator tooth widths become unequal, leading to unequal tooth (UNET) width machines. Hence, the coils in the UNET machines can be wound around either the narrower or the wider stator teeth as shown in Fig. 3.22 and the torque performance has been compared with modular machines as shown in Fig. 3.23. It is found that for the 12-slot/8-pole, the UNET with coils on wider stator teeth can produce the highest torque with FG=1mm (virtual FGs in the UNET machines). However, for 12-slot/14-pole, the better torque performance (higher average torque but lower torque ripple) is achieved with a modular structure.

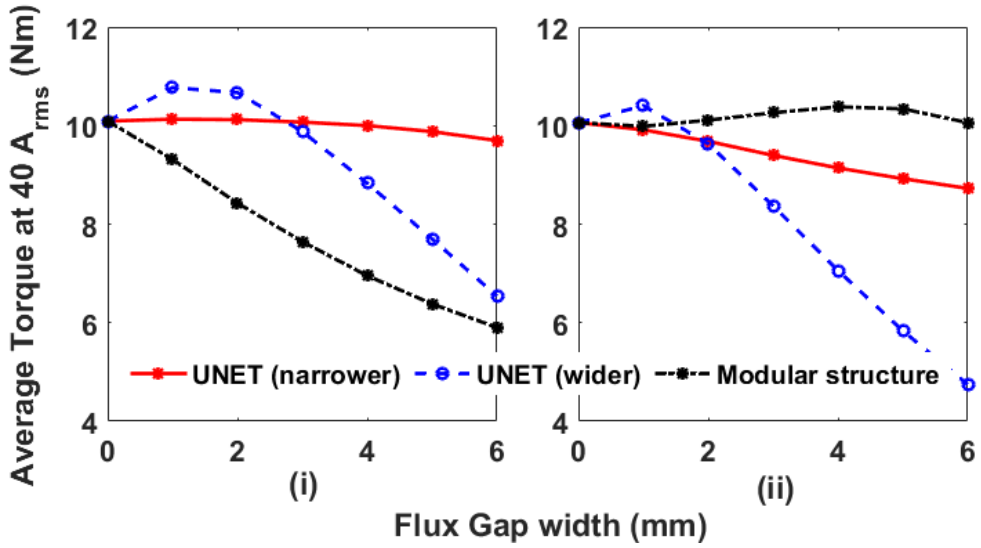

(a)

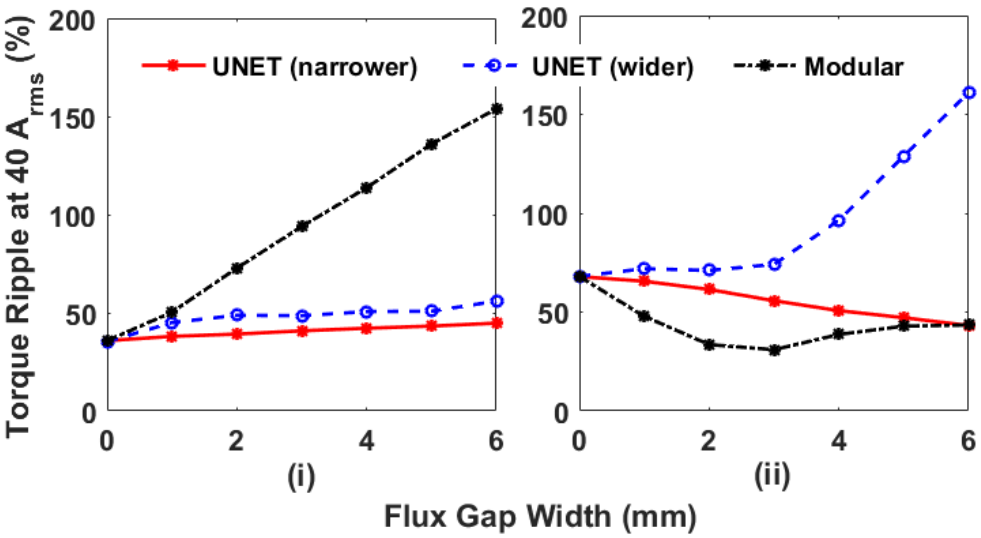

(b)

Fig. 3.23 (a) Average torque and (b) torque ripple comparison between modular and UNET CSRMs with (i) 12-slot/8-pole and (ii) 12-slot/14-pole. Appropriate conduction angles are employed.

3.5 EXPERIMENTAL VALIDATION

3.5.1 PROTOTYPES OF NON-MODULAR AND MODULAR SRMS

Prototypes of 12-slot/8-pole and 12-slot/14-pole non-modular and modular SRMs have been built to validate the predictions. Fig. I (c) and Fig. II (b) show the 12-slot stators with FG=0mm (no FGs) and 2mm, respectively. Fig. III (b) and Fig. IV (b) are the 8-pole and 14-pole rotors.

3.5.2 MEASUREMENT OF SELF- AND MUTUAL-INDUCTANCES

The self-inductance L_a and mutual-inductance M_{ab} were measured according to the method in [64]. The predicted and measured self- and mutual-inductances of both 12-slot/8-pole and 12-slot/14-pole non-modular and modular CSRMs are presented in Fig. 3.24 at 1A AC current. The measured results are generally higher than the predicted ones mainly due to the fact that the end-windings have not been taken into account in the predictions.

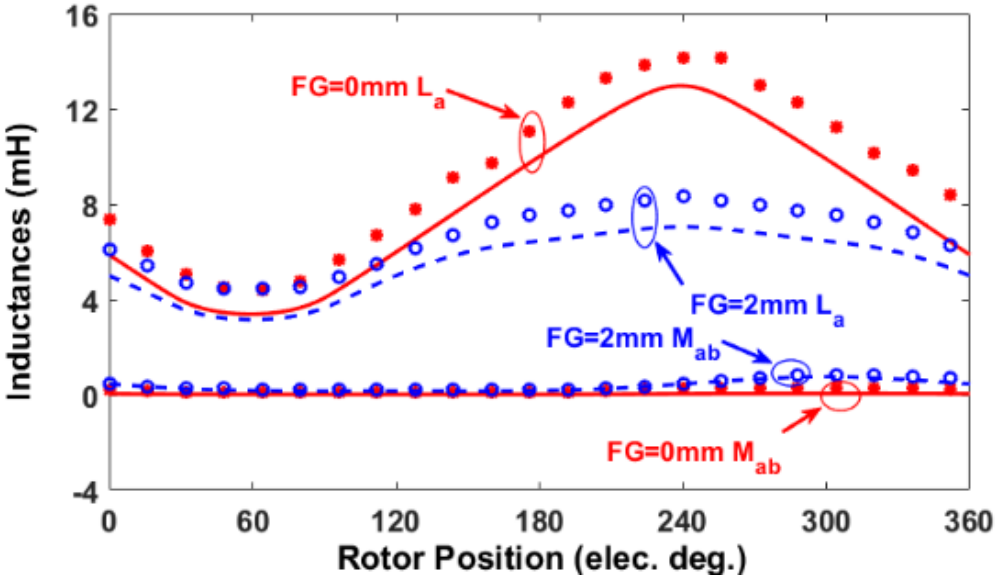

(a)

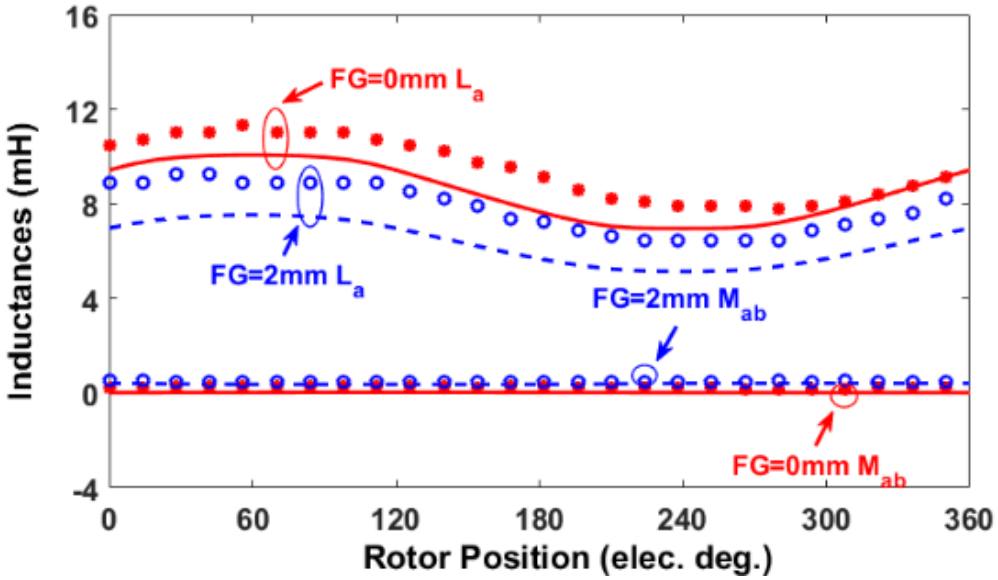

(b)

Fig. 3.24. Predicted and measured self- and mutual-inductances against rotor position at 1A AC current. (a) 12-slot/8-pole CSRMs with FG=0mm and 2mm. (b) 12-slot/14-pole CSRMs with FG=0mm and 2mm (lines: predicted results, and marks: measured results).

3.5.3 SELF- AND MUTUAL-TORQUES

In order to measure the static torque that produced by both the self- and mutual-inductances (self- and mutual-torques), the method of static torque measurement in Chapter 2 has been adopted.

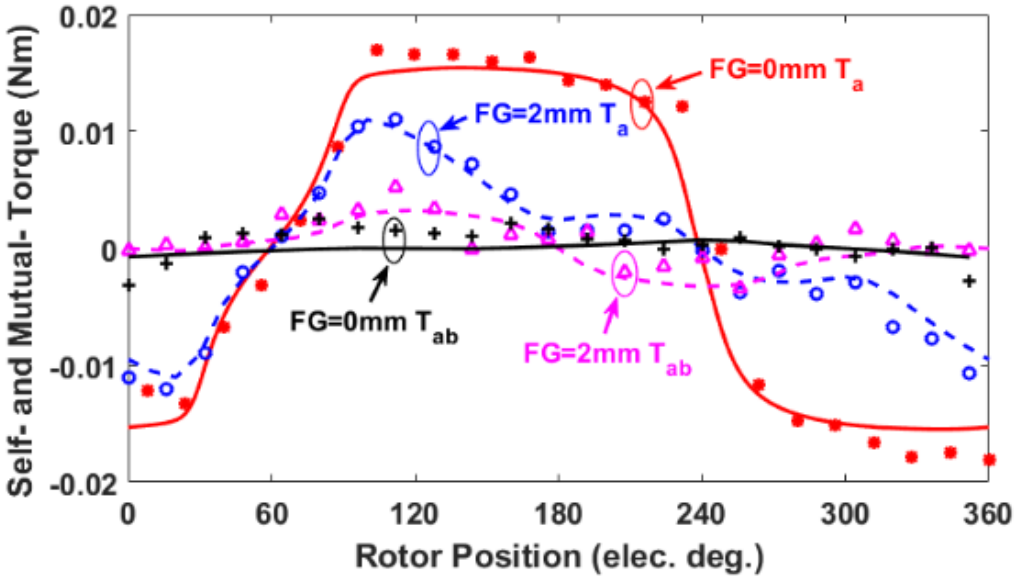

(a)

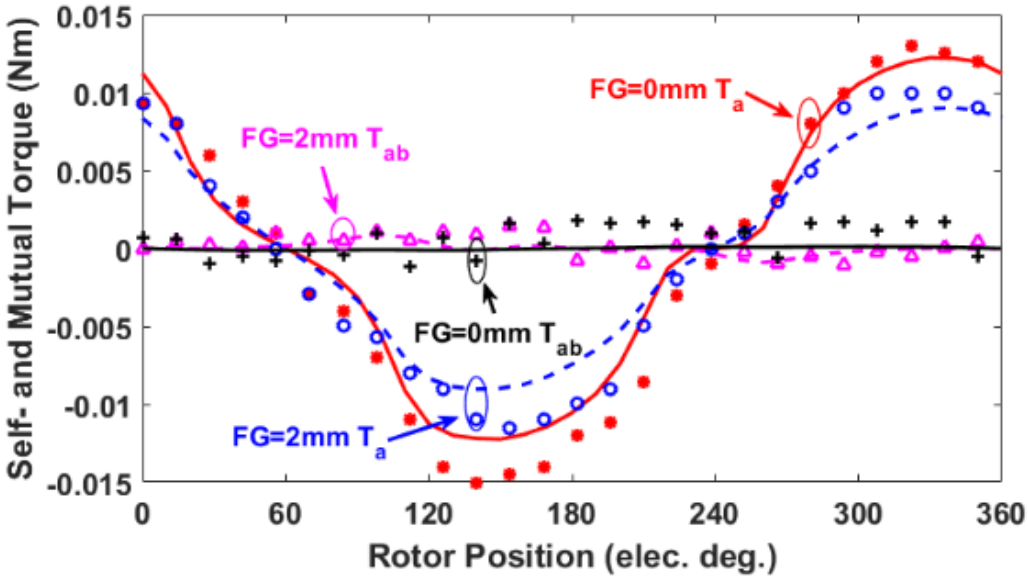

(b)

Fig. 3.25. Predicted and measured self- and mutual-torques against rotor position at 1A DC current. (a) 12-slot/8-pole CSRM with FG=0mm and 2mm. (b) 12-slot/14-pole CSRM with FG=0mm and 2mm (lines: predicted results, and marks: measured results).

By way of example, predicted and measured self-torques of the phase A, T_a, and mutual-torques between the phases A and B, T_{ab}, are shown in Fig. 3.25. It is worth noting that the mutual-torque T_{ab} is obtained by the torque produced by the phases A and B connected in series minus the sum of self-torques of the phases A and B. In order to minimize the influence of magnetic saturation and also to prevent the machine from overheating, 1A DC current is used for phase current supply during these tests.

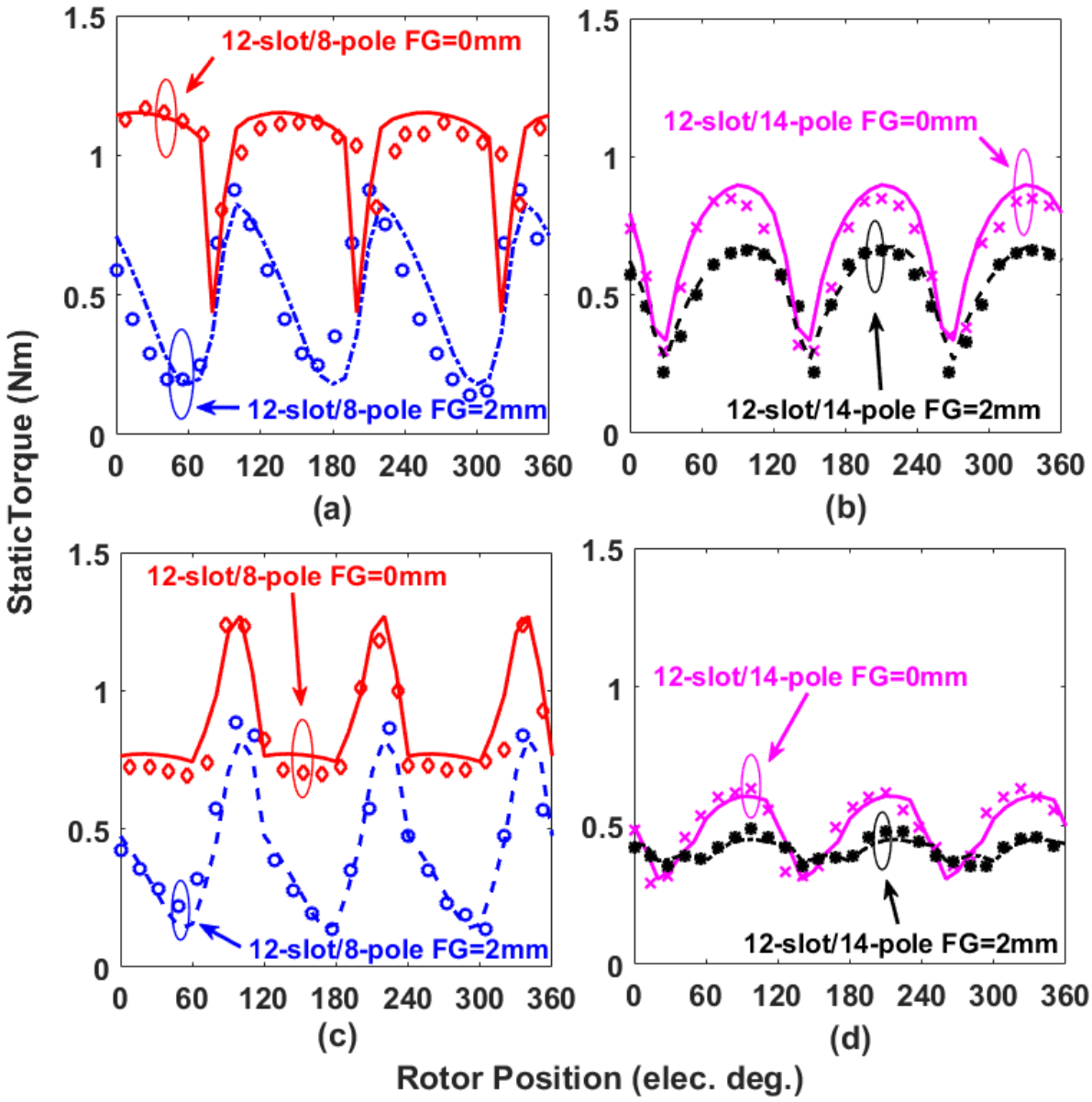

Fig. 3.26. Predicted and measured static on-load torques at 5A phase RMS current with different conduction angles, (a) and (b) unipolar 120° elec., (c) and (d) unipolar and bipolar 180° elec. for 12-slot/8-pole and 12-slot/14-pole CSRMs (lines: predicted results, and marks: measured results).

3.5.4 STATIC ON-LOAD TORQUE

Adopting the preferred conduction angles in TABLE 3.4, the static on-load torques of 12-slot/8-pole and 12-slot/14-pole CSRMs have also been measured at different rotor positions, as shown in Fig. 3.26. The phase RMS current was 5A for all the currents with different conduction angles. The aligned rotor position of the phase A can be tested by injecting current only into the phase A. This will cause the rotor to rotate to the aligned position of the phase A. In addition, the DC current can be injected into each phase at different rotor positions according to the current waveforms in order to obtain the torque waveforms shown in Fig. 3.26. Moreover, the values of average torque and torque ripple for both predicted and measured results are summarized in TABLE 3.10.

TABLE 3.10 COMPARISON OF TORQUE PERFORMANCE AT $5A_{RMS}$

Slot/pole number combination	FG (mm)	Average torque (Nm)		Torque ripple (%)	
		Predicted	Measured	Predicted	Measured
Unipolar 120° elec.					
12-slot/8-pole	0	1.05	1.04	68.48	34.59
	2	0.49	0.48	131.91	152.92
12-slot/14-pole	0	0.71	0.66	78.91	83.85
	2	0.54	0.52	75.40	84.85
Unipolar 180°/bipolar 180° elec.					
12-slot/8-pole	0	0.89	0.85	59.24	64.15
	2	0.42	0.43	162.46	172.26
12-slot/14-pole	0	0.49	0.50	61.24	68.82
	2	0.41	0.41	19.22	33.24

3.6 CONCLUSION

In this chapter, 3-phase modular and non-modular single layer CSRM and MCSRM with different slot/pole numbers (12-slot/8-pole, 12-slot/10-pole, 12-slot/14-pole, and 12-slot/16-pole) have been investigated. The optimal conduction angles have been established on the basis of non-modular machines and have been employed for electromagnetic torque investigation of the modular machines with different FG widths. It has been demonstrated that for this specific size of machine, the highest average torque at high current level can be achieved by the non-

modular 12-slot/8-pole SRMs and the modular 12-slot/14-pole SRMs. Moreover, the modular 12-slot/14-pole SRMs produce even higher average torque than non-modular 12-slot/8-pole SRMs at $40A_{rms}$ due to being less sensitive to magnetic saturation in the stator back iron. However, the lower torque ripple is obtained by the modular 12-slot/14-pole SRMs. In addition, regardless of the rotor pole numbers, the modular machines will tend to exhibit lower iron loss and radial force. Therefore, the modular SRMs have the potential of achieving lower levels of vibration and acoustic noise than the non-modular SRMs. The prototypes of 12-slot/8-pole and 12-slot/14-pole, with both non-modular and modular structures have been constructed and the predicted inductances and torques have been validated by measured results.

The rectangular wave excitation has been adopted to both non-modular and modular SRMs in Chapter 2 and Chapter 3. In following chapters, sinewave excitation will be adopted.

Chapter 4. SYNRMS WITH ALTERNATIVE WINDING CONFIGURATIONS AND SALIENT POLE ROTOR

In this chapter, the SRMs are supplied with sinewave currents so that a conventional 3-phase bridge converter can be employed. Such machines are in effect doubly salient synchronous reluctance machines (DSRMs) but with short-pitched and concentrated windings. In addition, this chapter comprehensively investigates the electromagnetic performance of 3-phase, 12-slot, 8-pole DSRMs with different winding configurations, i.e. double/single layer, short-pitched (non-overlapping concentrated) and fully-pitched (overlapping concentrated). Comparisons in terms of static and dynamic performances such as *d*- and *q*-axis inductances, on-load torque, torque-speed curve, efficiency map, etc. have been carried out using 2D FEA. It is demonstrated for the given size of machine considered, that for the same copper loss and without heavy magnetic saturation, both single and double layer mutually-coupled machines can produce higher on-load torque compared with conventional machines. Additionally, double layer mutually-coupled machine achieved the highest efficiency compared with other counterparts. When it comes to single layer machines, they are more suitable for middle speed applications and capable of producing higher average torque while lower torque ripple than their double layer counterparts at low phase current. Two prototype DSRMs, both single layer and double layer, are built to validate the predictions.

This chapter was published in [72].

4.1 INTRODUCTION

Without permanent magnets or field windings on the rotor, the SRMs have very simple and robust structures [3] [2] [4] [6]. However, due to the doubly salient structure, the SRMs can have abrupt change in radial force acting on the stator. In addition, the unipolar phase current waveforms of the SRMs (usually $120°$ elec. conduction for 3-phase SRMs) can have the abrupt change in phase current as well. As a result, the SRMs tend to exhibit higher levels of vibration and acoustic noise when compared with permanent magnet machines and induction machines [9] [10] [12] [13]. Moreover, the nonconventional power-converter used for conventional SRM drive system to some extent limits its foothold in the market. Similar to the SRMs, the SynRMs have magnet-free features but are supplied with sinewave currents. Hence, the off-the-shelf 3-phase standard inverter like that used in other synchronous machines can be used to drive the SynRMs [13] [63] [85]. Different from the SRMs, most SynRMs have flux barriers inside the rotor iron core and often employ distributed windings to achieve higher saliency ratio and hence higher reluctance torque [53] [85] [86]. However, the complicated rotor structure could not be manufactured as easy as that of the SRMs, leading to lower manufacturability and potentially higher manufacturing cost. In order to employ a standard 3-phase inverter for reducing the system cost and the doubly salient machine structure for simpler manufacturing, the SRMs have been supplied with sinewave currents which are in effect DSRMs but with short-pitched and concentrated windings.

Compare with the SRMs with conventional winding, lower vibration and acoustic noise levels can also be achieved by using the mutually-coupled windings [20], especially supplied with sinewave currents as demonstrated in [11], [63] and [68]. Moreover, it is well-established that, the double layer mutually-coupled DSRM (DLMC-DSRM) is less sensitive to magnetic saturation and consequently, on a like-for-like basis, produces higher average torque than double layer conventional DSRM (DLC-DSRM) at high phase current [21] with enhancement of the order around 77% up to $40A_{rms}$ [22]. However, the torque ripple of the DLMC-DSRM is relatively higher because of the nature of self- and mutual-inductance variations, and hence can potentially generate higher noise at low speed.

This issue can be mitigated by using the single layer fully-pitched DSRM (FP-DSRM) [22] [19]. However, its considerably longer end-windings result in an increased overall machine envelope and higher copper loss for a given phase current. To combine the merits of both the single layer FP-DSRM (high torque capability) and the DLMC-DSRM (short end-winding),

two short-pitched, single layer winding DSRMs have been proposed and compared with the double layer DSRMs and the FP-DSRM.

4.2 TOPOLOGIES AND WINDING CONFIGURATIONS

As previously mentioned, different winding configurations have significant influences on the electromagnetic performances of the DSRMs. To investigate this behaviour, 3-phase, 12-slot/8-pole DSRMs with two established short-pitched windings (DLC-DSRM and DLMC-DSRM) and one fully-pitched winding (FP-DSRM), as well as two proposed single-layer short-pitched windings (SLC-DSRM and SLMC-DSRM) have been considered. The leading machine dimensions and key design features are summarized in TABLE 4.1. Cross-sections through these machine designs are shown in Fig. 4.1, in which "-" represents a RETURN conductor while "+" represents a GO conductor. The machine dimensions have been optimized for the SLC-DSRM supplied by sinewave current. To simplify the comparison, all DSRMs have adopted the same dimensions. It is worth mentioning that the individual optimization of some DSRMs will slightly improve their output torque by less than 10% compared with the dimensions adopted in this chapter.

TABLE 4.1 MACHINE LEADING DIMENSIONS AND DESIGN FEATURES

Stator slot number	12	Active length (mm)	60
Rotor pole number	8	Turn number per phase	132
Stator outer radius (mm)	45	Coil packing factor	0.37
Airgap length (mm)	0.5	Rated RMS current (A)	10
Rotor outer radius (mm)	26.5	Current density (A_{rms}/mm^2)	5.68

It is worth mentioning that in this chapter, for all the static performance investigations such as average torque vs current or copper losses, iron losses, etc. the *ABC* frame has been used [6], [11]. However, in order to simplify the investigation of dynamic performances such as torque speed characteristics and efficiency map, the *dq*-axis frame has been employed and the *d*- and *q*-axes have been marked in Fig. 4.1 [87].

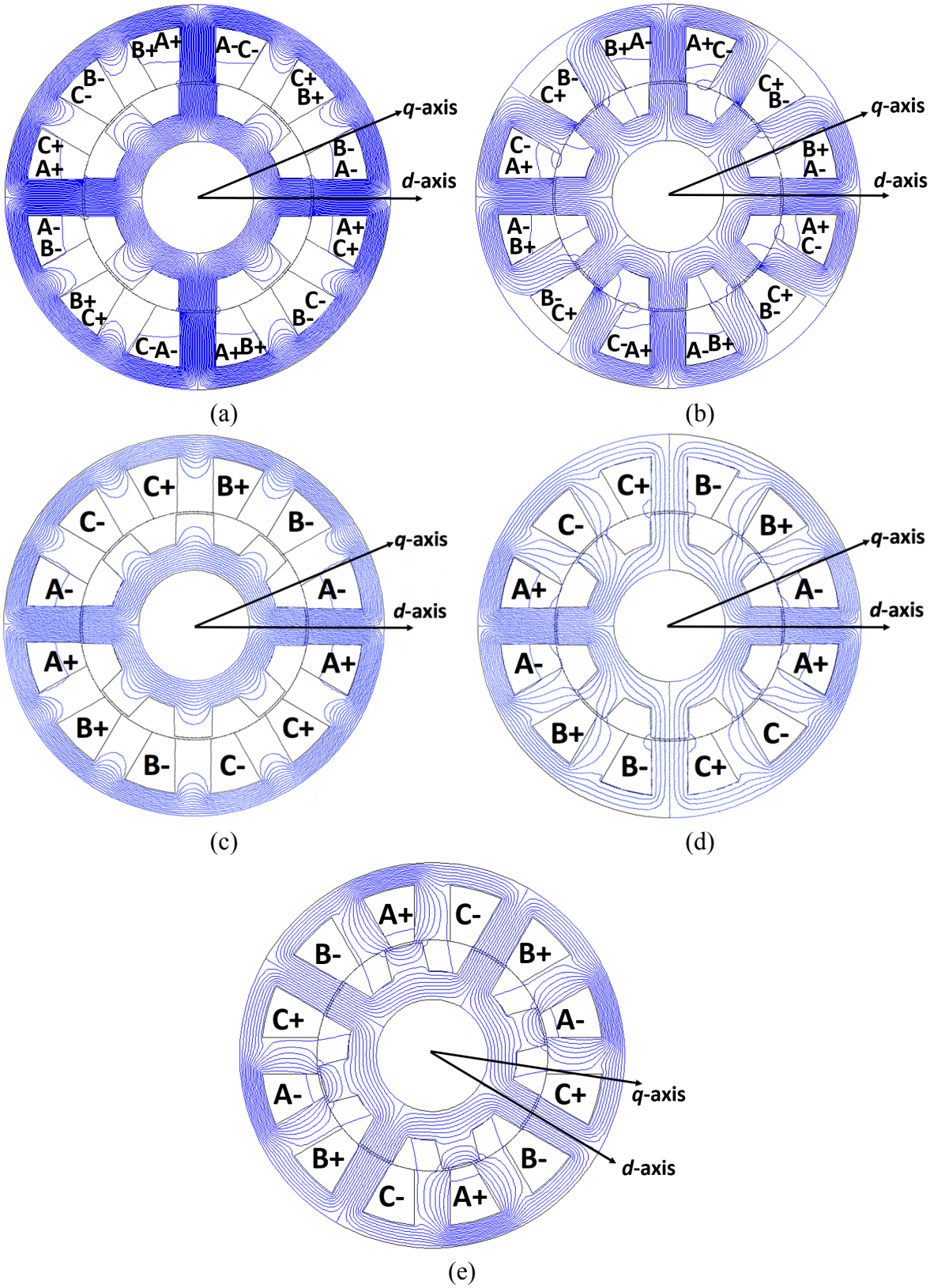

Fig. 4.1 Comparison of flux distributions when phase A is supplied by a 10A DC current. (a) DLC-DSRM, (b) DLMC-DSRM, (c) SLC-DSRM, (d) SLMC-DSRM, and (d) FP-DSRM. The rotors are at aligned position of the phase A.

4.3 STATIC PERFORMANCE INVESTIGATION FOR DSRMS

4.3.1 *D*- AND *Q*-AXIS INDUCTANCES

As the case for conventional SynRMs, the average electromagnetic torque of the DSRMs can be determined not only from the change in co-energy but also by the *d*- and *q*-axis inductances. Therefore, the well-established phasor diagram of the SynRM shown in Fig. 4.2 can be employed to analyse the DSRMs supplied with sinewave currents. This diagram illustrates the relationship between *d*- and *q*-axis currents and the stator phase current I_{ph}, as well as the relationship between *d*- and *q*-axis voltages and the phase voltage V_{ph} [50] [85]. In the phasor diagram, α corresponds to the phase advanced angle of I_{ph} with respect to the *d*-axis and, $\emptyset$ corresponds to the phase angle between I_{ph} and V_{ph}. It is worth mentioning that in this phasor diagram, the influence of resistance has been considered.

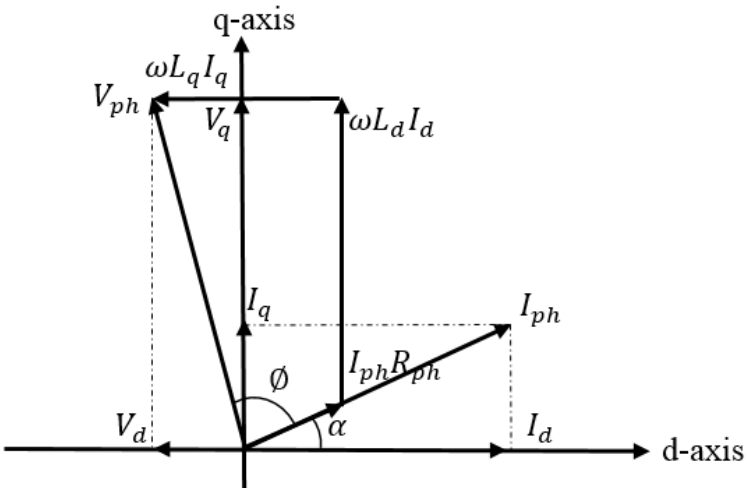

Fig. 4.2 Phasor diagram of the SynRM [50].

According to the phasor diagram, the *d*- and *q*-axis inductances L_d and L_q, with due account of the influence of cross-coupling, are given by:

$$L_d(i_d, i_q) = \frac{\psi_d(i_d, i_q)}{i_d} \tag{4.1}$$

$$L_q(i_d, i_q) = \frac{\psi_q(i_d, i_q)}{i_q} \tag{4.2}$$

The d- and q-axis voltages V_d and V_q can be obtained as

$$V_d = R_{ph} I_d - \omega \psi_q \tag{4.3}$$

$$V_q = R_{ph} I_q + \omega \psi_d \tag{4.4}$$

where ψ_d and ψ_q are the d- and q-axis stator flux linkages, respectively. i_d and i_q are the d- and q-axis stator currents, respectively. R_{ph} is the phase resistance and ω is the electrical angular velocity of the supply.

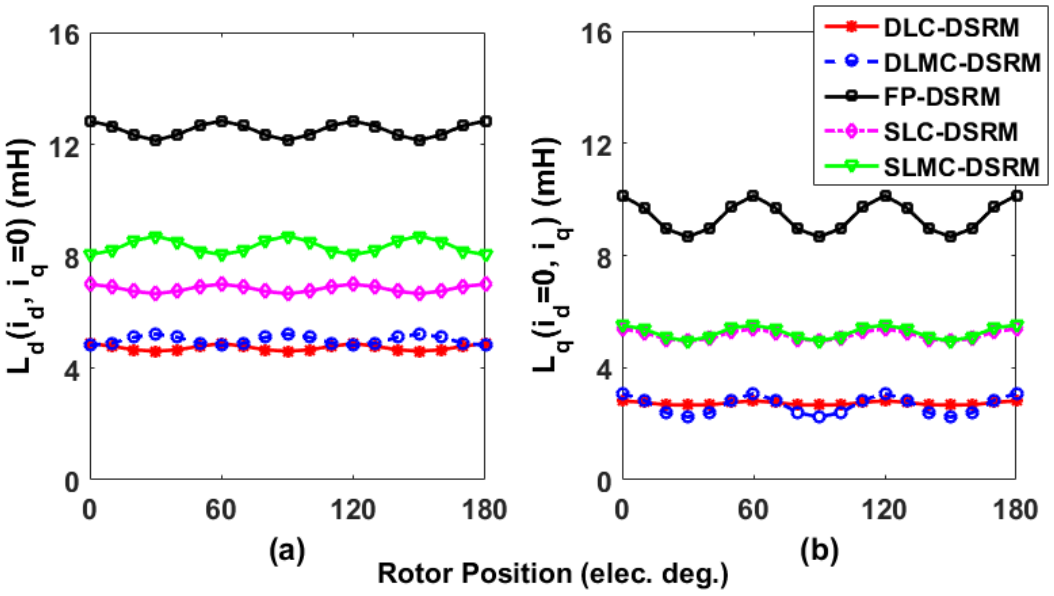

Fig. 4.3 Variation in (a) d-axis inductance $L_d(I_d, I_q = 0)$, and (b) q-axis inductance $L_q(I_d = 0, I_q)$ as a function of rotor position for a phase RMS current of 10A.

The variation in $L_d(I_d, I_q = 0)$ and $L_q(I_d = 0, I_q)$ with rotor position and phase RMS current for all the DSRMs have been calculated by 2D FEA. The resulting characteristics are shown in Fig. 4.3 and Fig. 4.4, respectively, from which it will be apparent that the highest d- and q-axis inductances are present in the FP-DSRM. Moreover, the d- and q-axis inductances of the single layer DSRMs are higher than those of their double layer counterparts. In terms of overload capability, Fig. 4.4 demonstrates that in all single layer DSRMs, the onset of discernible magnetic saturation occurs at lower currents than the corresponding double layer DSRM configurations (as indicated by the current at which the inductances begin to decline). This is again due to higher concentrated armature MMF, and hence a greater sensitivity to magnetic saturation than the corresponding double layer machines.

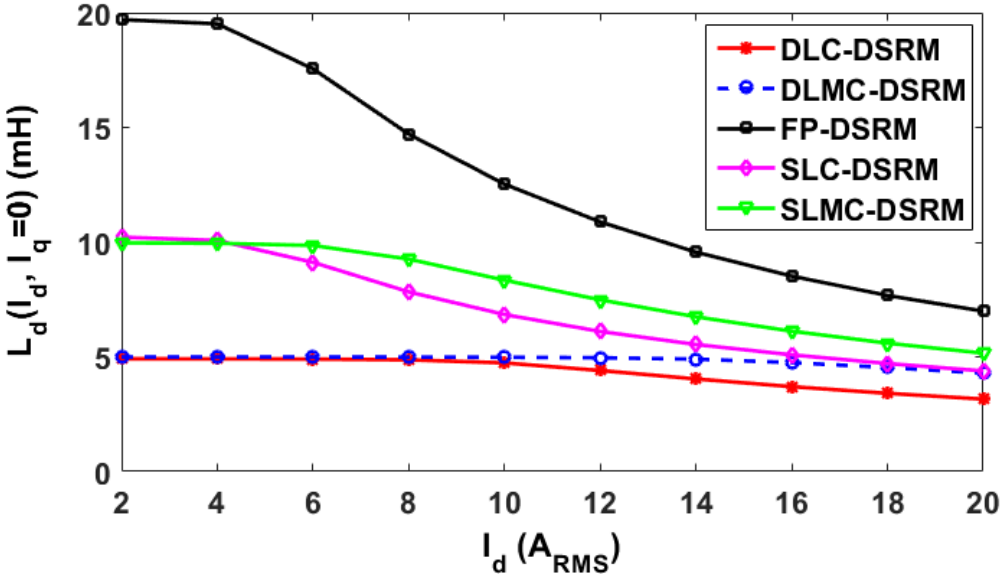

(a)

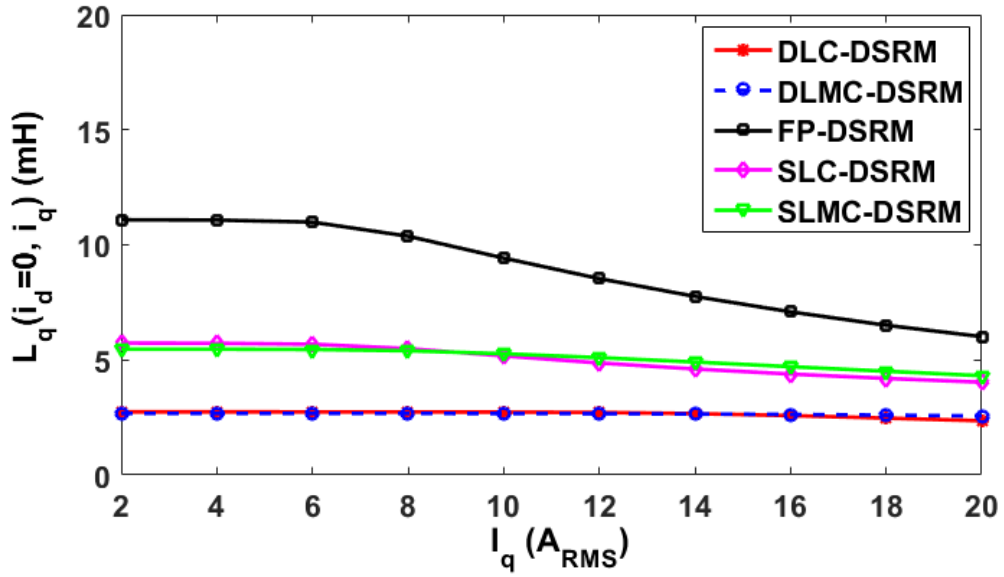

(b)

Fig. 4.4 Comparison of d- and q-axis inductances between the DSRMs as a function of phase RMS current. (a) d-axis inductance $L_d(I_d, I_q = 0)$, (b) q-axis inductance $L_q(I_d = 0, I_q)$.

It is worth noting that the difference between L_d and L_q can be used to determine the electromagnetic torque capability. In order to predict the torque, $(L_d\text{-}L_q)$ has been calculated at $\alpha = 45°$, with $I_d = I_q$, as shown in Fig. 4.5. As will be apparent, the difference between d- and q-axis inductances is greatest in the case of the FP-DSRM. Hence, for the particular size of stator and rotor core, the FP-DSRM will produce the highest torque in the absence of significant magnetic saturation. Similarly, the single layer DSRMs will produce higher torque

than the double layer DSRMs without saturation due to the higher *d*-*q* axis inductance difference.

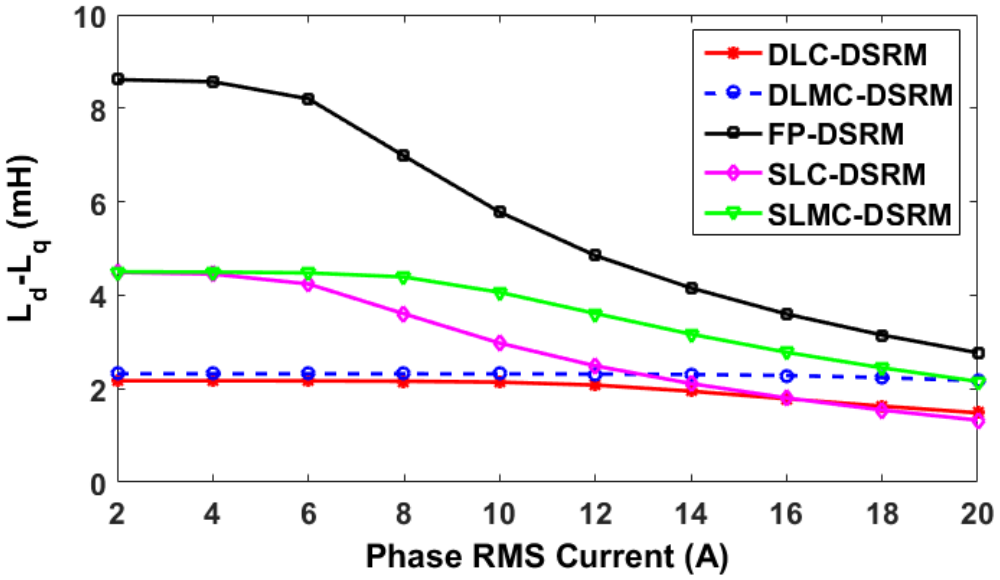

Fig. 4.5 Comparison of (L_d-L_q) between the DSRMs at $\alpha = 45°$.

4.3.2 AVERAGE TORQUE VS CURRENT PHASE ADVANCED ANGLE

Having established *d*- and *q*-axis inductances, the torque produced by a 3-phase synchronous reluctance machine can be calculated from [88]:

$$T = \frac{3}{2} \times p(L_d - L_q) I_d I_q \tag{4.5}$$

This expression can also be applied to the many variants of the DSRMs considered in this chapter when supplied with sinewave currents. Also, the *d*- and *q*-axis currents can be expressed in terms of the stator peak current yielding:

$$T = \frac{3}{4} \times p(L_d - L_q) {I_{pk}}^2 sin2\alpha \tag{4.6}$$

where p is pole-pair number, I_{pk} is stator peak current, and α is current phase advanced angle which influences the relationship between phase current i and rotor position θ, for instant of phase A $i_a = I_{rms} \sin(\theta - \alpha)$. It will be apparent from the expression in (4.6) that without magnetic saturation, the maximum average torque is achieved when $\alpha = 45°$. However, with

the onset of *d*-axis saturation, the maximum average torque will be obtained at values of α greater than 45° [50].

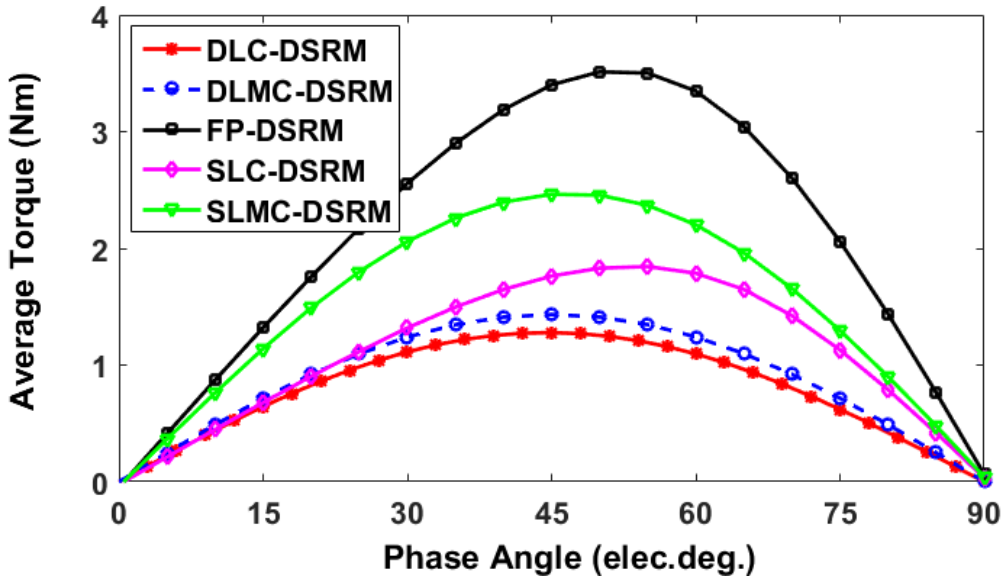

Fig. 4.6 Variation in average torque as a function of current phase angle α for a phase RMS current of 10A.

A comparison of average torque as a function of α between the different DSRMs configurations is shown in Fig. 4.6, a sinewave current of $10A_{rms}$ is applied in each case. As would be expected, under this excitation condition, the FP-DSRM produces the highest average torque. For the remaining topologies, the SLC-DSRM and SLMC-DSRM produce higher torque than their double layer counterparts. Additionally, the maximum average torques are generated at $\alpha = 45°$ for the DLC-DSRM, DLMC-DSRM and SLMC-DSRM at $10A_{rms}$. However, for the FP-DSRM and SLC-DSRM, the maximum average torques are achieved at 50° and 55°, respectively, behavior which is indicative of magnetic saturation even at this modest excitation level.

4.3.3 Average Torque and Torque Ripple as a Function of Phase RMS Current

The comparisons in terms of average torque and torque ripple coefficient against phase RMS current have been carried out, as shown in Fig. 4.7, in which the torque ripple coefficient is calculated according to (2.11).

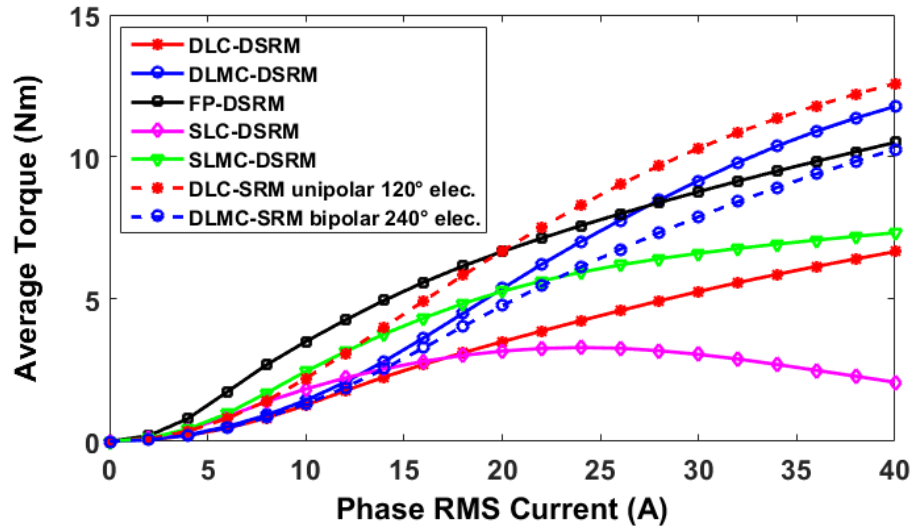

(a)

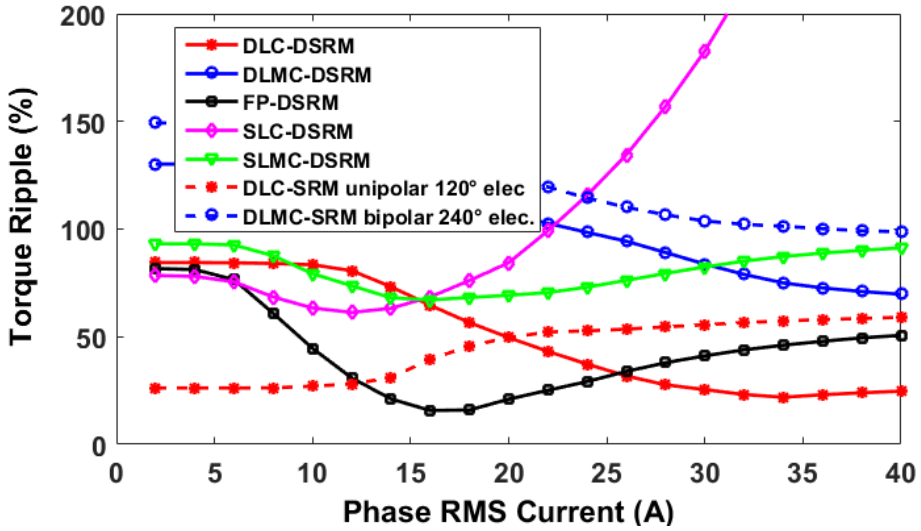

(b)

Fig. 4.7 Comparison of (a) average torque and (b) torque ripple coefficient against phase RMS current varying from 0A to 40A. (Solid lines stand for machines supplied with 3-phase sinewave currents. Performances of the DLC-DSRM and DLMC-DSRM also compare with that supplied with rectangular wave current with appropriate conduction angles according to TABLE 2.6.

It is found that at low current, the FP-DSRM produces higher average torque but lower torque ripple than the other DSRMs. Additionally, the SLMC-DSRM and SLC-DSRM generate higher average torque but lower torque ripple than their double layer counterparts, as expected. However, at high current, average torque of the DLMC-DSRM exceeds that of the FP-DSRM, because the FP-DSRM is more sensitive to magnetic saturation due to single layer winding structure. Similarly, at even higher phase current, both the SLC-DSRM and SLMC-DSRM produce less torque but potentially higher torque ripple than their relevant double layer counterparts. Therefore, it can be concluded that all the FP-DSRM, SLC-DSRM and SLMC-DSRM present superior performances at low current. However, the FP-DSRM has significant longer end-winding than both the SLC-DSRM and SLMC-DSRM, leading to much higher copper loss.

For completeness, the results for the SRMs supplied by rectangular wave current with the appropriate conduction angles according to TABLE 2.6 are compared with that obtained using sinewave currents, as shown in Fig. 4.7. Here, the DLC-SRM and DLMC-SRM have been selected as examples with the conduction angle of unipolar 120° elec. and bipolar 240° elec., respectively. It is found that the DLMC-SRM with sinewave excitation can produce higher average torque while with lower torque ripple. However, the DLC-SRM supplied by rectangular wave current can exhibit better performance, particularly at high phase current. However, it requires special converters, which is one of the main drawbacks of this machine type.

4.3.4 COPPER LOSS

In order to calculate the copper loss, the end-windings have been calculated in TABLE 2.7 for the machines with different winding configurations. TABLE 4.2 shows a comparison of copper loss between the DSRMs under rated condition for a coil temperature of 60°C (assume test temperature to be 60°C). The nature of the end-windings in a FP-DSRM dictates that for this relatively short axial length of stator core, the total mean length per turn is much higher than the corresponding double layer DSRMs, with consequent adverse implications for the phase resistance of the FP-DSRM. However, since the SLC-DSRM and SLMC-DSRM have similar short-pitched winding structures to their double layer counterparts, the penalty of resistance in these machines is much smaller.

However, as shown in TABLE 4.2, the torque per unit copper loss of the FP-DSRM is still competitive with the other DSRMs topologies. Indeed, in terms of torque per unit copper loss, there is a relatively narrow spread of values across the various machines. It is important to recognize that the aspect ratio of the stator core, i.e. length to diameter ratio, needs to be borne in mind when considering the relative merits of these topologies, since end-windings play a major role. Nevertheless, the SLC-DSRM and SLMC-DSRM, especially the latter, can achieve comparable torque against copper loss performance to the FP-DSRM but with much shorter end-winding and also smaller volume, especially at low average torque level as shown in TABLE 4.2. However, to achieve a high average torque, the copper loss of the FP-DSRM is much higher than that of the DLMC-DSRM. It is also worth noting that both the DLC-DSRM and SLC-DSRM have the worst torque against copper loss performance.

TABLE 4.2 COMPARISON OF COPPER LOSS WITH COIL TEMPERATURE OF 60℃ AT 10 A_{RMS}

Items	DLC-DSRM& DLMC-DSRM	FP-DSRM	SLC-DSRM& SLMC-DSRM
Mean length per turn (m)	0.15	0.24	0.17
Phase resistance (Ω)	0.61	0.95	0.66
Rated copper loss (W)	183	285	198
Average torque (Nm)	1.28&1.45	3.51	1.84&2.46
Average torque per unit copper loss (Nm/W)	0.00699&0.00792	0.01232	0.00929&0.01242

Comparisons of average torque and torque ripple against copper loss have been carried out, as shown in Fig. 4.8. To achieve a high average torque, e.g. 8Nm, the copper loss of the FP-DSRM is much higher than that of the DLMC-DSRM. Moreover, the output torques of other DSRMs can hardly achieve 8Nm although high current (copper loss) are supplied. However, to achieve a lower average torque, e.g. 3Nm, both the SLMC-DSRM and FP-DSRM produce lower copper loss than other DSRMs. It is also worth noting that both the DSRMs with conventional winding configurations have the worst torque against copper loss performance.

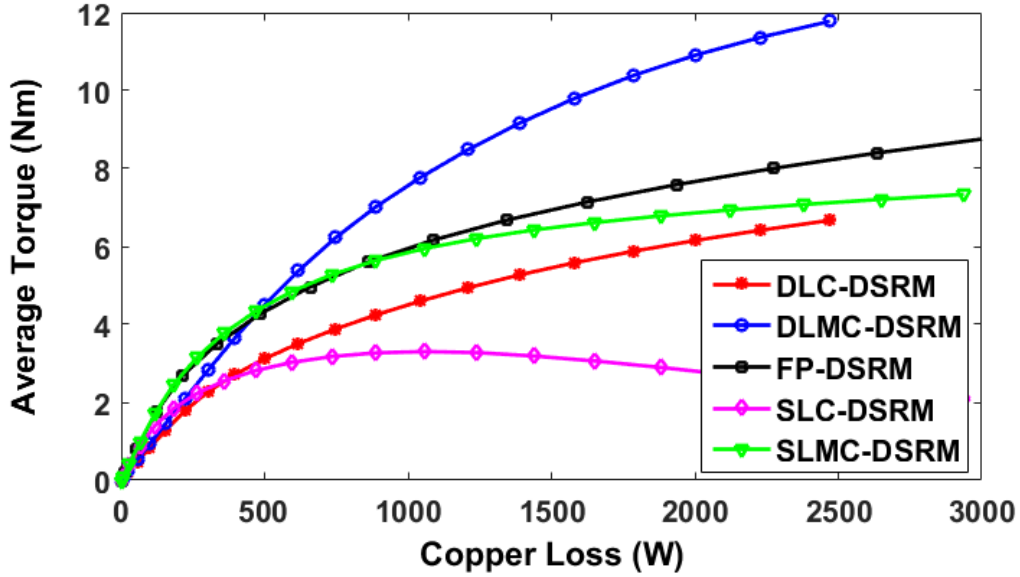

(a)

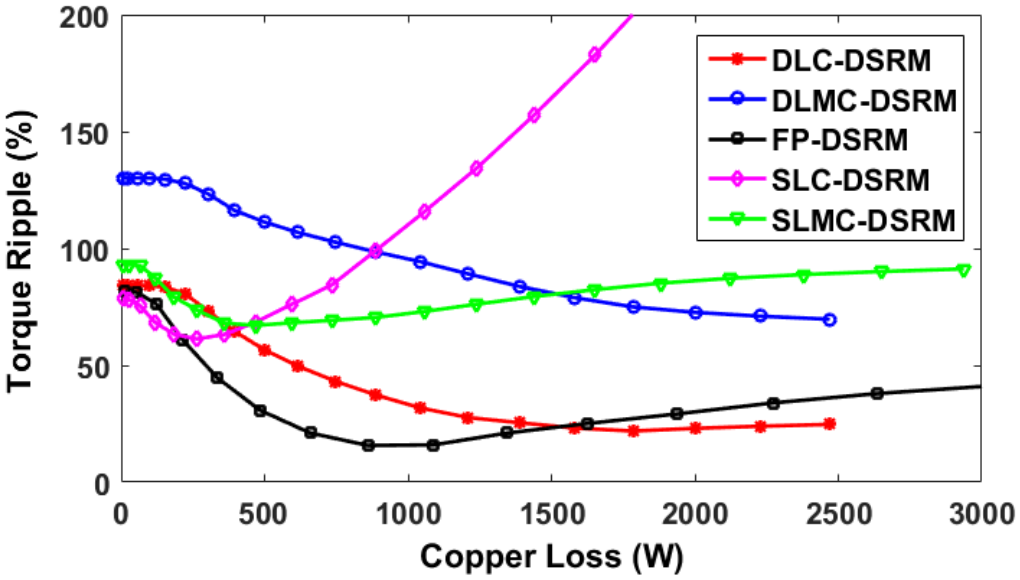

(b)

Fig. 4.8 Comparison of (a) average torque and (b) torque ripple against copper loss for phase RMS current changing from 0A to 40A.

4.3.5 IRON LOSS

The different winding arrangements will also influence the nature of the flux distribution within the DSRMs hence the magnitude of iron losses within stator and rotor iron cores. The calculation of iron losses in variable reluctance machines is very challenging, particularly in conventional SRMs operated with unipolar currents. In such machines, different regions of the

stator and/or rotor core can be exposed to localized flux density waveform that can be unipolar, asymmetric AC waveforms and contain significant minor-loop excursions [74] [78].

For the machine topologies considered in this chapter, the use of sinewave current simplifies the process for estimating iron loss, although many localized flux density are still likely to depart from sinusoidal.

In order to predict the iron loss, there are many methods presented in [78] [89]. In this chapter, the average iron loss density over one electrical cycle in a given region of the machine is estimated using (2.12) which is based on a simplified consideration of hysteresis and eddy current component of loss [6]. The total iron loss is obtained from a summation of the iron losses calculated in every individual FE mesh element of the stator and rotor. When applying (2.12), it is necessary to recognize that at a given rotor speed, the flux density variations in the stator and rotor are at different frequencies.

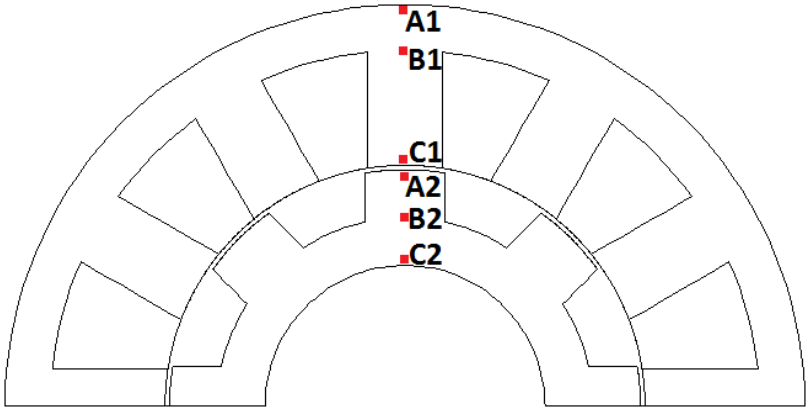

Fig. 4.9 Cross-section of 12-slot/8-pole DSRM. Point A1, B1, and C1 are used for stator flux density observation. Point A2, B2, and C2 are used for rotor flux density observation.

By way of illustration, a series of flux density loci at the series of six locations defined in Fig. 4.9 have been selected to determine the stator and rotor flux density frequencies. The resulting frequencies for the various machine topologies are summarized in TABLE 4.3. For all the topologies considered, the stator flux density frequencies f_0 are the same and it is given by $\frac{\Omega p}{60}$, where Ω is the mechanical rotor speed, and p is the pole-pair number. In addition, Fig. 4.10 shows the stator flux density loci of the DSRMs with different winding configurations.

In contrast, the rotor flux density frequencies are different in the various topologies as summarized in TABLE 4.3. For the DLC-DSRM and DLMC-DSRM, the effective rotor frequency is twice than that of their single layer counterparts. In addition, the rotor flux density

frequencies of both SLMC-DSRM and DLMC-DSRMs are twice than that of SLC-DSRM and SLMC-DSRM, respectively.

TABLE 4.3 FLUX DENSITY FREQUENCY

Machine types	Stator B_r/B_t frequency (Hz)	Rotor B_r/B_t frequency (Hz)
DLC-DSRM	f_0	$1.5f_0$
DLMC-DSRM	f_0	$3f_0$
FP-DSRM	f_0	$1.5f_0$
SLC-DSRM	f_0	$0.75f_0$
SLMC-DSRM	f_0	$1.5f_0$

The different rotor flux density frequencies dictate that the relative merits of the different machines in terms of their rotor iron losses cannot simply be gauged from the selected rotor flux density loci (hence not present in this chapter). Recourse to a full calculation of iron loss throughout the stator and rotor by the application of (2.12) over on repeating cycle in every element of the FE mode is required. To this end, the iron losses for the reference designs of all machine types being considered were calculated for sinewave current of $10A_{rms}$ at 400 rpm.

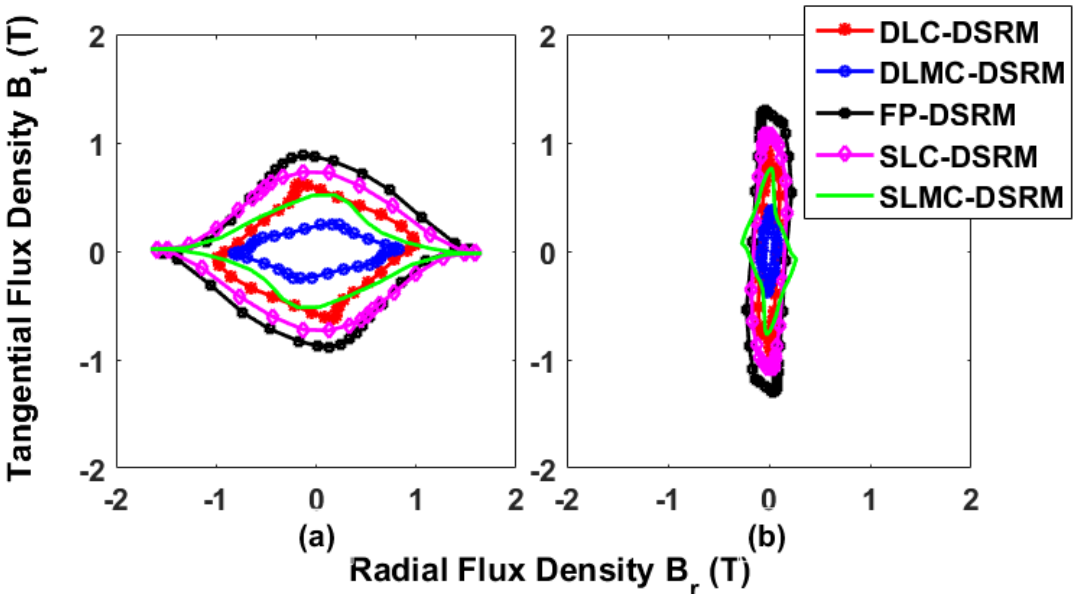

Fig. 4.10 Comparison of radial and circumferential stator flux densities of the DSRMs, at 400rpm, supplied by 10A phase RMS current. (a) Point A1, (b) point B1 in Fig. 2.16. B_t is the circumferential component while B_r is the radial component of flux density.

The resulting losses from this method are summarised in TABLE 4.4. It is found that the FP-DSRM has the highest stator iron loss while the DLMC-DSRM has the lowest stator iron loss at this operating condition. This is mainly due to the fact that all the DSRMs have the same stator flux density frequency while the FP-DSRM has the highest variation of both stator B_t and B_r, as shown in Fig. 4.10. Point C1 in the stator is not presented since the variation is only occurred in B_r. Despite the complicating factor of the different frequencies in the rotor, the same trend is observed for the rotor iron losses of FP-DSRM and DLMC-DSRM.

TABLE 4.4 IRON LOSS AT RATED CURRENT, 400 RPM

Machine types	Stator iron loss (W)	Rotor iron loss (W)	Total iron losses (W)
DLC-SRM	1.07	1.15	2.22
DLMC-SRM	0.57	0.24	0.81
FP-DSRM	2.24	2.45	4.69
SLC-DSRM	1.17	0.55	1.72
SLMC-DSRM	1.12	1.20	2.32

As is the case with all singly excited machines, the magnitude of the iron loss is increased markedly with the magnitude of the stator current. A comparison of iron losses as functions of phase RMS currents and rotor speeds is shown in Fig. 4.11. At rated speed and modest current (< 15A), the DLMC-DSRM has the lowest iron loss while the FP-DSRM has the highest iron loss. However, with increasing phase RMS current, the iron losses increase more slowly in the SLC-DSRM, DLC-DSRM and FP-DSRM, behaviour which can be attributed to the different means in which magnetic comes into play. At rated current, and with increasing rotor speed, the iron loss of the DLMC-DSRM is the lowest while the FP-DSRM being the highest.

However, as would be expected in these relatively small machines operating at modest speeds, the absolute levels of iron losses in all the machine topologies are very small in comparison with the copper losses shown previously in TABLE 4.2. Nevertheless, the relative magnitudes of the iron losses for the various topologies provide a valuable and, within reason, a scalable indicator of their relative performance in applications where iron losses is likely to be a substantially more important discriminator, e.g. larger and higher speed machines.

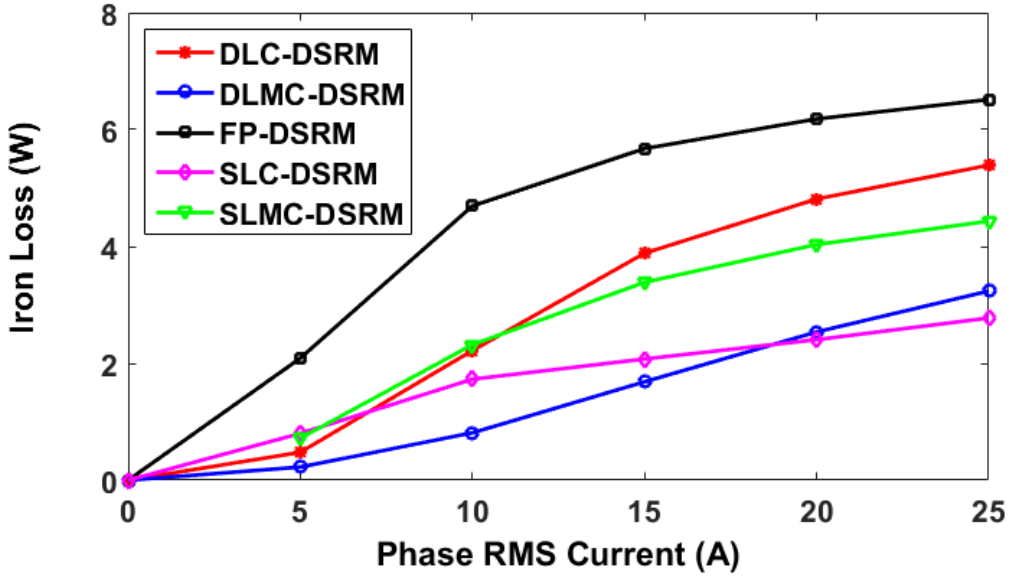

(a)

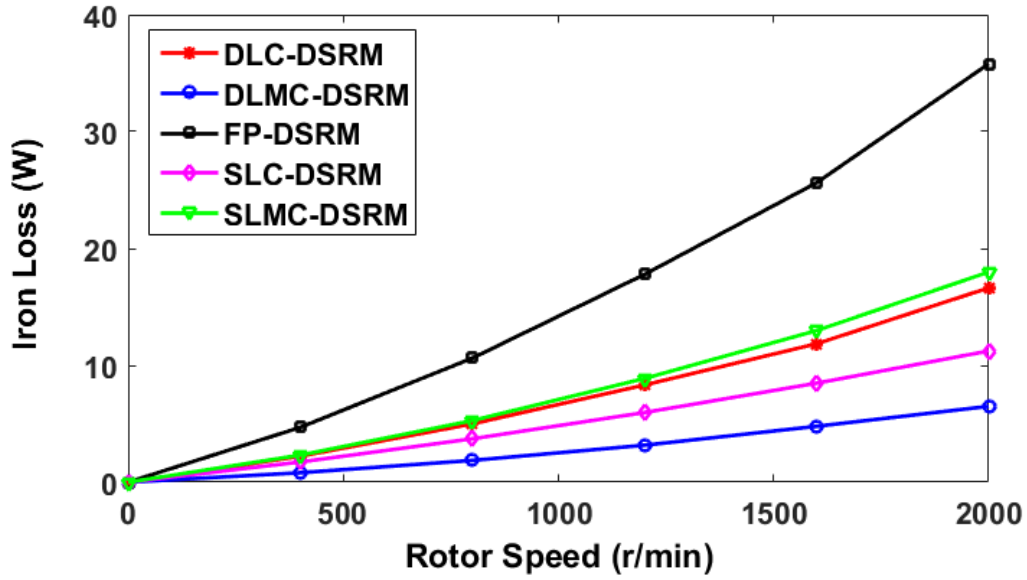

(b)

Fig. 4.11 Comparison of iron loss amongst DSRMs. (a) At rated speed with increasing phase RMS current, (b) at rated current with increasing rotor speed.

4.4 Comparison of Steady-State Performance

4.4.1 Torque Speed Characteristics

As already observed in Fig. 4.4, different winding structures lead to a range of different *d*- and *q*-axis inductances, which will in turn influence aspects of the machine dynamic performance, e.g. torque, power and power factor. In this analysis, the widely used circle

diagram approach is adopted to establish the torque speed characteristic of each design variant [90]. Under flux weakening control, the phase voltage and phase current limitation determines the maximum torque capability:

$$V_a = \sqrt{{V_d}^2 + {V_q}^2} \leq V_{max} \tag{4.7}$$

$$I_a = \sqrt{{I_d}^2 + {I_q}^2} \leq I_{max} \tag{4.8}$$

where V_a and I_a are the phase peak voltage and current, respectively.

Using the *d*- and *q*-axis inductances derived previously from (4.1) to (4.8), the torque speed curves shown in Fig. 4.12 (a) were obtained. In each case, the maximum current, I_{max}, is 14.14A ($10A_{rms}$) and the DC link voltage, V_{DC}, is 100V ($V_{max} = \frac{2}{\pi}V_{DC}$). The method employed to account for the influence of cross-coupling is the same to that has been proposed in [87].

It will be apparent from Fig. 4.12 that the FP-DSRM has the highest initial torque, but the lowest base speed, i.e. the speed at which the torque begins to reduce. It can also be observed that the DLC-DSRM and DLMC-DSRM have higher base speeds than their single layer counterparts. In order to validate the circle diagram approach used to derive these torque speed curves, the torque-speed curve for the SLMC-DSRM was calculated by the direct FE method (introduced in [87]). The Fig. 4.12 (a) shows a good agreement between the two methods.

A comparison of the variation in power factors with speed under the same current and voltage limitations ($10A_{rms}$ and 100V) is shown in Fig. 4.12 (b). Since the machines have different winding structures and hence different values of L_d and L_q, their power factors will also show some variations. With approximate end-winding structure and hence similar phase resistance, the DLC-DSRM and DLMC-DSRM have higher power factor than the SLC-DSRM and SLMC-DSRM at the same rotor speed, in large part because of their lower L_d and L_q.

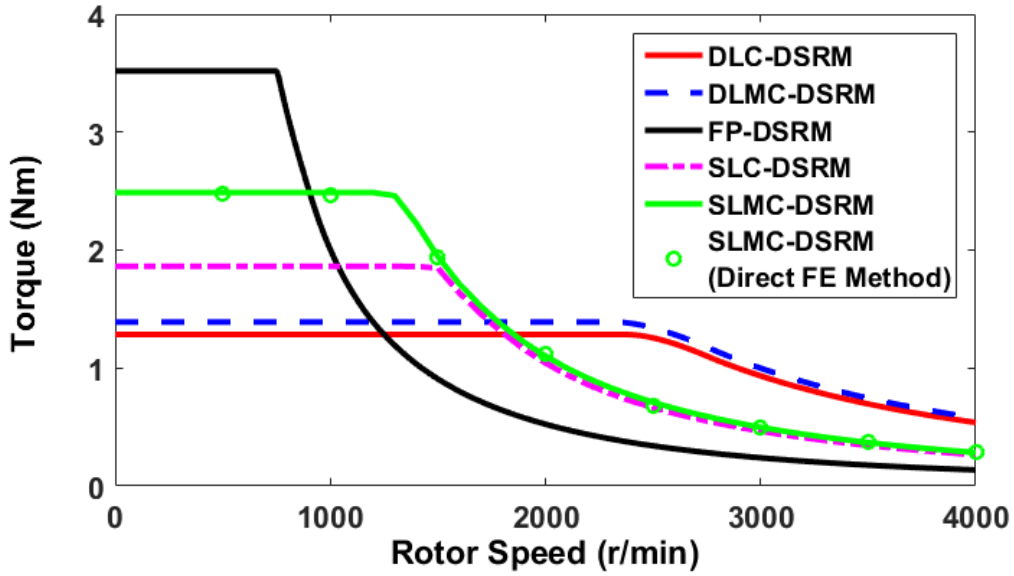

(a)

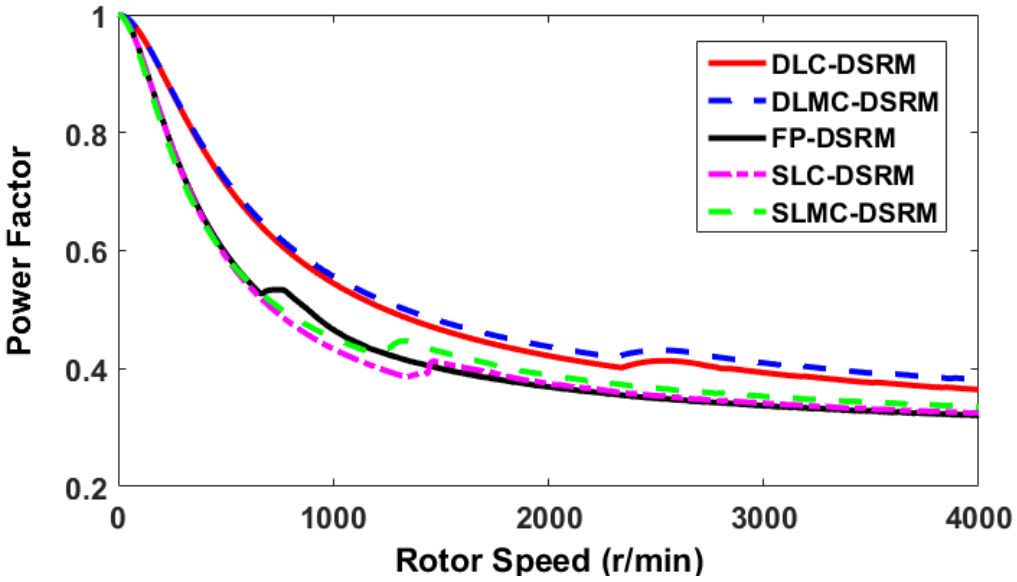

(b)

Fig. 4.12 Comparison of dynamic performance. $I_{max} = 14.14A$, and $V_{DC} = 100V$. (a) Torque-speed curves, (b) power factor-speed curves.

4.4.2 EFFICIENCY MAP

Efficiency maps for the various machines can be calculated from the torque speed characteristics and losses calculated previously using:

$$\eta = \frac{P_{out}}{P_{out} + P_{copper} + P_{iron} + P_{mech}} \times 100\% \tag{4.9}$$

where P_{out} is the output power which is given by $\frac{\omega T}{p}$, and P_{mech} is the mechanical loss which consists of aerodynamic windage and bearing losses. The mechanical loss is independent of the load but depends on the rotor speed, air-gap and the axial lengths. According to [91], mechanical losses were calculated to be 2.64W at 400 rpm for all the DSRMs of identical size. The mechanical losses will increase with rotor speed since the bearing loss and windage losses are proportional to Ω (rotor velocity) and Ω^3, respectively.

Efficiency maps for the double layer, single layer and fully-pitched machines are compared in Fig. 4.13, respectively (regions with efficiency below 50% are not shown). For this specific series of designs, a maximum efficiency of 76% is achieved by the DLMC-DSRM between 6000 and 8000 rpm. Of the remaining topologies, the DLC-DSRM also achieves its maximum efficiency towards the upper end of the speed range. In contrast, the SLC-DSRM and SLMC-DSRM achieve their maximum efficiencies (some 75%) over the speed range of 3000 to 4500 rpm. Finally, the FP-DSRM has a more modest efficiency of 66%, which is achieved at lower rotor speed of around 2000 rpm. It is important to caution that these general trends in efficiency are to some degree specific to the small size of these reference designs, in particular that copper loss tends to dominate over iron loss in small machines.

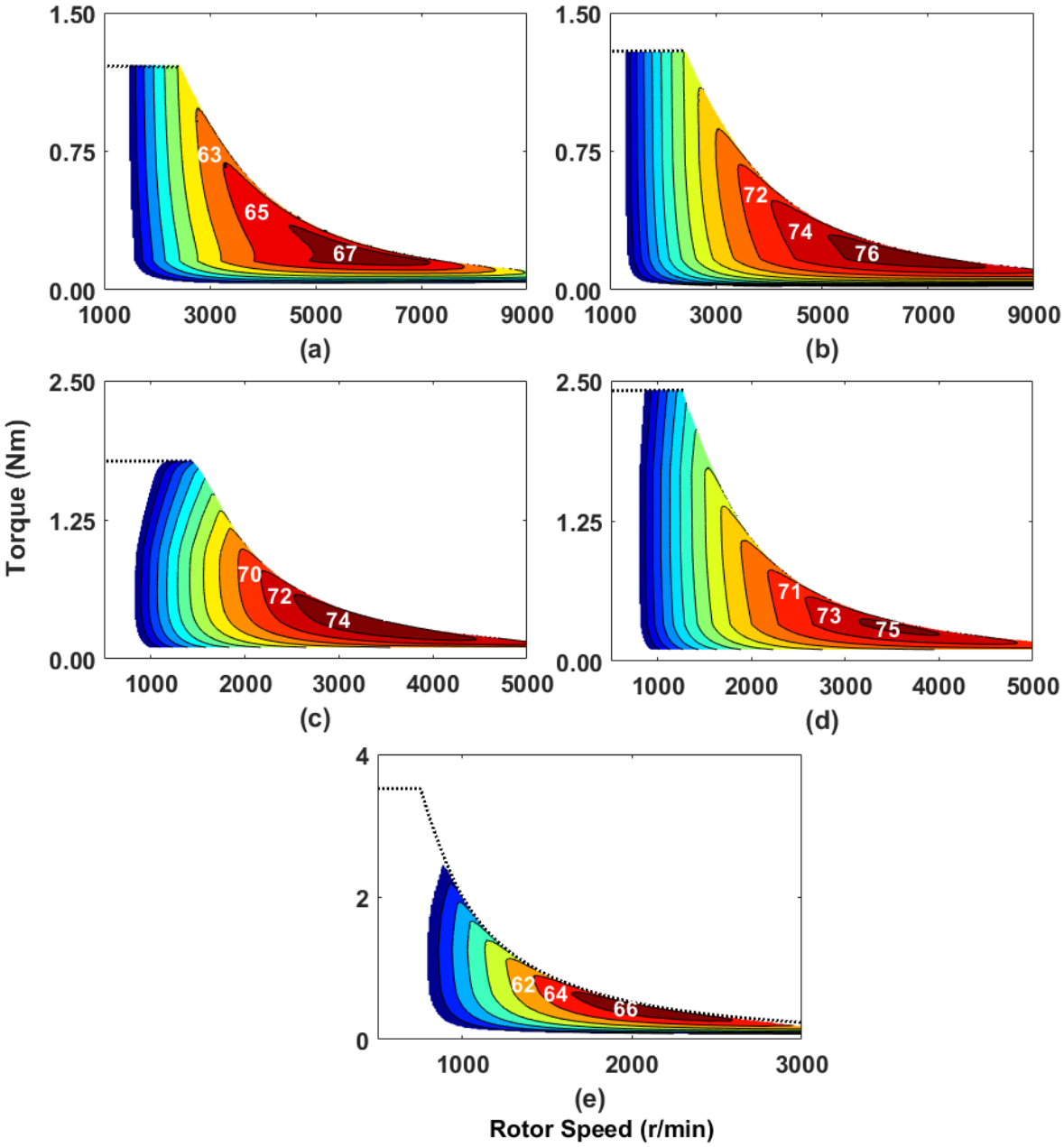

Fig. 4.13. Efficiency maps of the DSRMs when $I_{max} = 14.14A$, and $V_{DC} = 100V$. (Regions with efficiency below 50% are not shown) (a) DLC-SRM, (b) DLMC-DSRM, (c) SLC-DSRM, (d) SLMC-DSRM, and (e) FP-DSRM.

4.5 EXPERIMENTAL VALIDATION

4.5.1 PROTOTYPES OF DSRMS

In order to validate the torque capability of the double and single layer DSRMs, two machines with the design specifications shown previously in TABLE 4.1 were constructed. Fig. I (b) shows the wound stator of a 12-slot/8-pole DLC-DSRM and DLMC-DSRM while Fig. I (c) shows the stator for the SLC-DSRM and SLMC-DSRM. The conventional and mutually-coupled SRMs can be realized with the same stator core and coils through a simple reconnection of the individual coils as detailed in Fig. 4.1. The common rotor of all the single and double layer variants is shown in Fig. III (b).

4.5.2 MEASUREMENT OF STATIC TORQUE

The measured phase resistances are 1.48 Ω and 1.32 Ω for single and double layer DSRMs respectively. Moreover, the self-inductances at 1A DC phase current are shown in Fig. 4.14. The method of static torque measurement detailed in [80] was adopted for undertaking all torque measurements in this study. During the tests, three phases of the DSRMs are supplied with DC currents such as $I_A = I$, $I_B = -1/2I$ and $I_C = -1/2I$, where I is variable and controllable by the power supply. Fig. 4.15 shows the comparison of predicted and measured static torques at 10A DC current versus rotor angular positions (equivalent to current phase advanced angle when 3 phases are supplied with sinewave currents). Although the waveforms of static torque are not smooth and not sinusoidal due to torque ripple and measurement error, a good agreement can still be observed between the predicted and measured results.

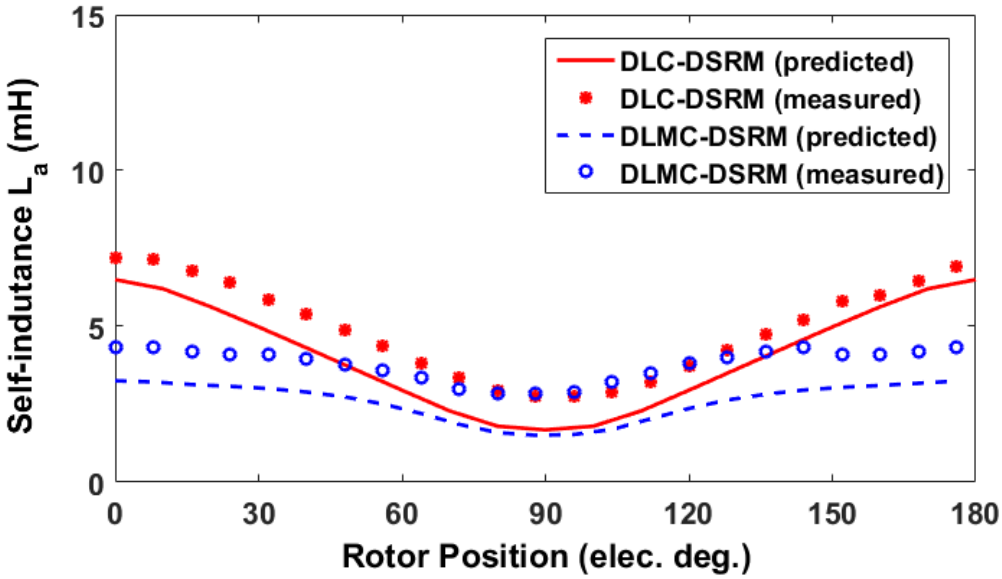

(a)

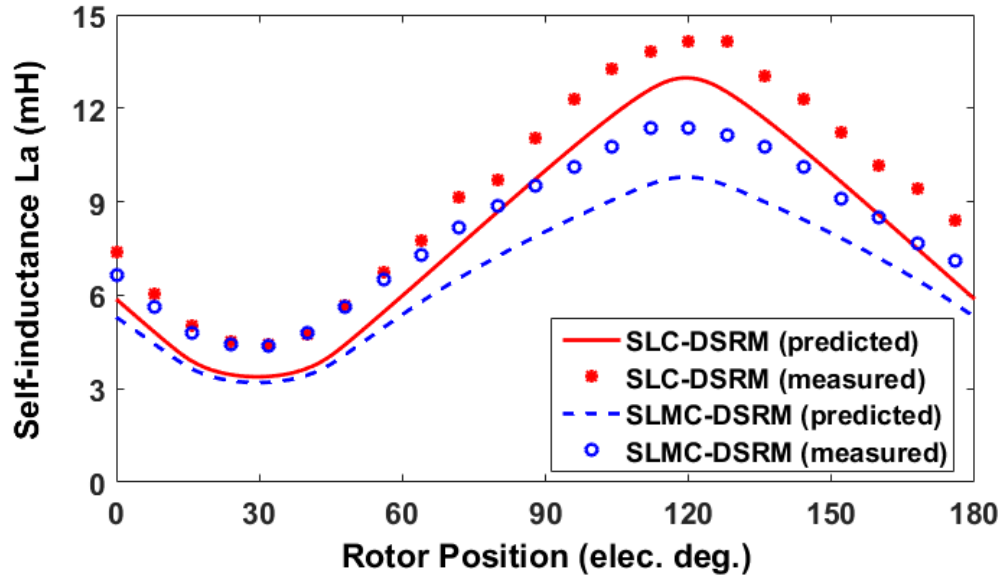

(b)

Fig. 4.14 Predicted and measured self-inductances versus rotor position at 1A DC phase peak current. (a) DLC-DSRM and DLMC-DSRM. (b) SLC-DSRM and SLMC-DSRM.

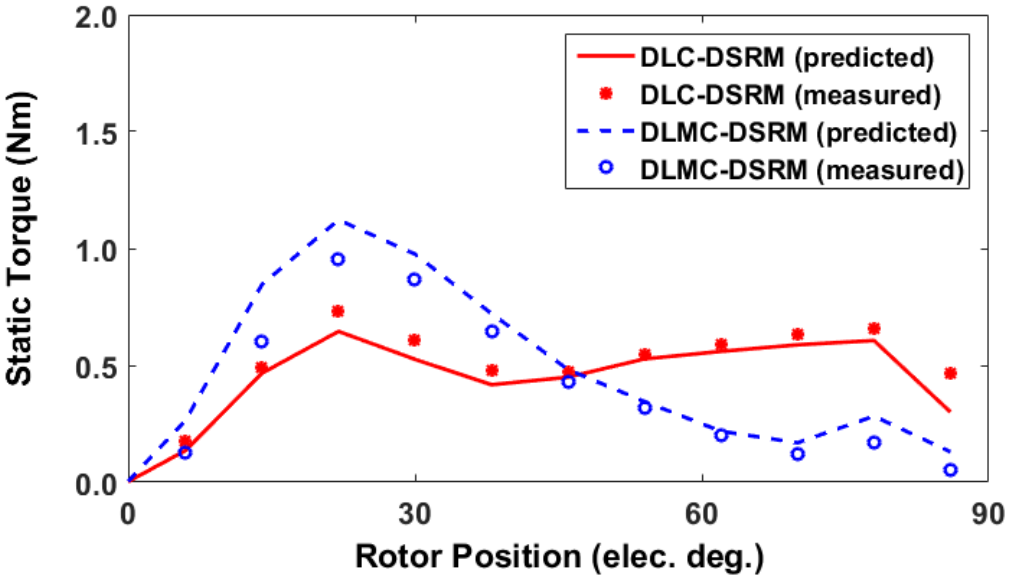

(a)

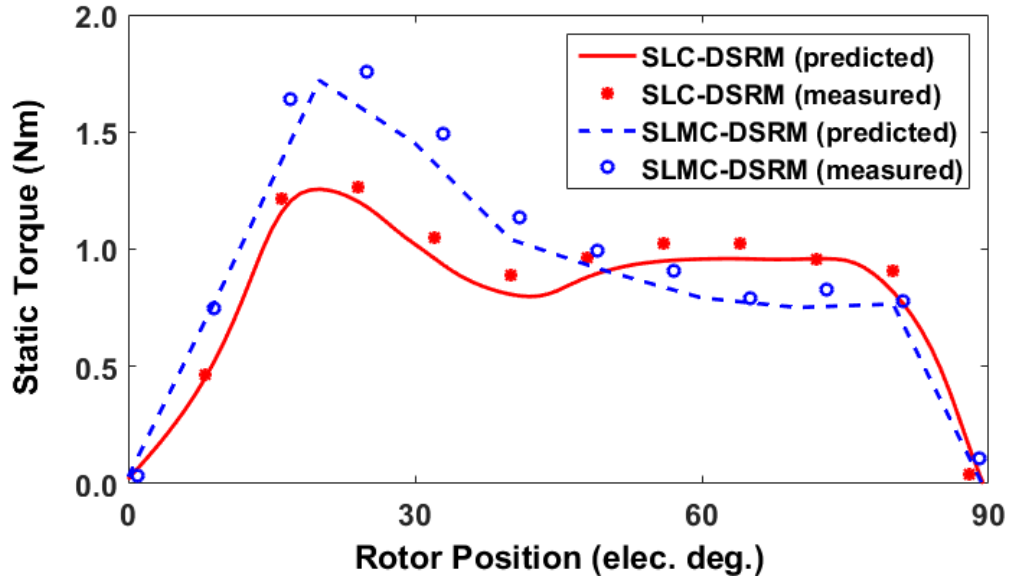

(b)

Fig. 4.15 Predicted and measured torques versus rotor position at 10A DC phase peak current. (a) DLC-DSRM and DLMC-DSRM. (b) SLC-DSRM and SLMC-DSRM.

Fig. 4.16 shows a comparison between the predicted and measured static torques for phase peak currents between 1A and 10A. In this series of torque measurements, the rotor was fixed in an angular position which corresponds to the maximum average torque (45 elec. deg. if magnetic saturation does not occur).

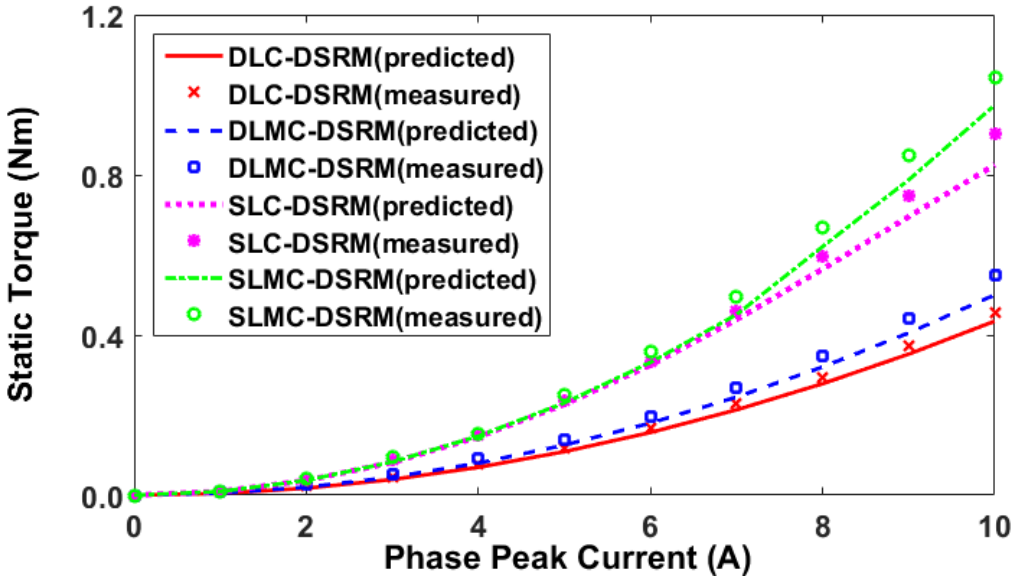

Fig. 4.16 Predicted and measured variations in static torque as a function of phase peak current.

4.5.3 DYNAMIC TESTS

Dynamic tests have been carried out according to the method established in [92]. The DC link voltage for all dynamic tests is 18V and the maximum phase peak current is 6A, which is limited by the load torque capacity of the DC machine. By way of example, tested current waveform of the phase A and PWM line voltage (between phases A and B) for one electrical period of the SLMC-DSRM are shown in Fig. 4.17.

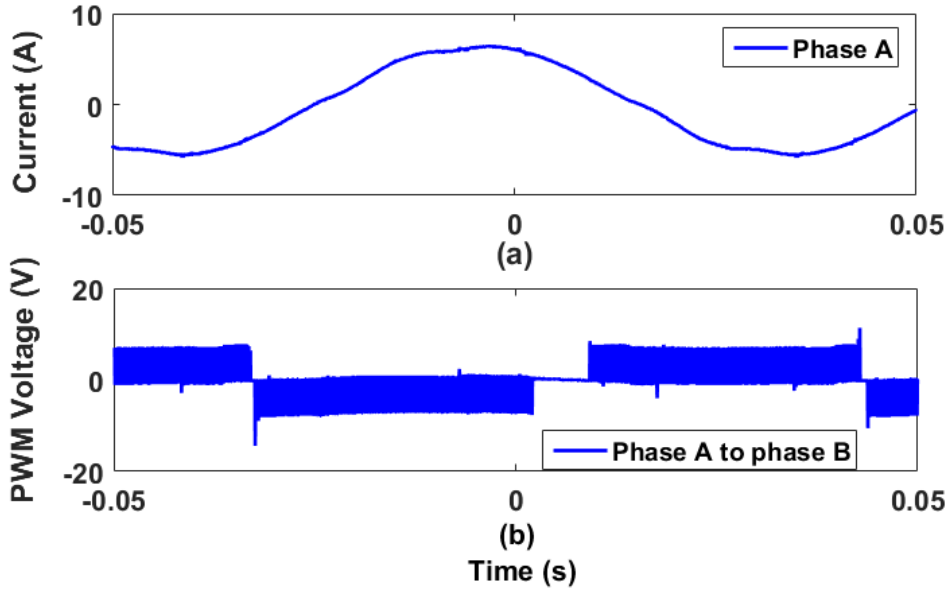

Fig. 4.17 Measured phase current and line voltage of the SLMC-DSRM. Switching frequency is 10kHz. (a) Phase A current, (b) PWM line voltage.

Fig. 4.18 and Fig. 4.19 show the comparison of predicted and measured torque-speed and efficiency-speed curves for both the single and double layer DSRMs. The measured results match well with the simulated ones. The difference is mainly due to the fact that the end-winding effect has not been taken into account in 2D FEA. The torque sensor accuracy and measuring error are other influencing factors that contribute to this discrepancy. It is also worth mentioning that the low efficiency is mainly due to the fact that for the prototype machines, smaller copper wires have been used to ease the winding process, leading to smaller slot filling factor and higher copper loss.

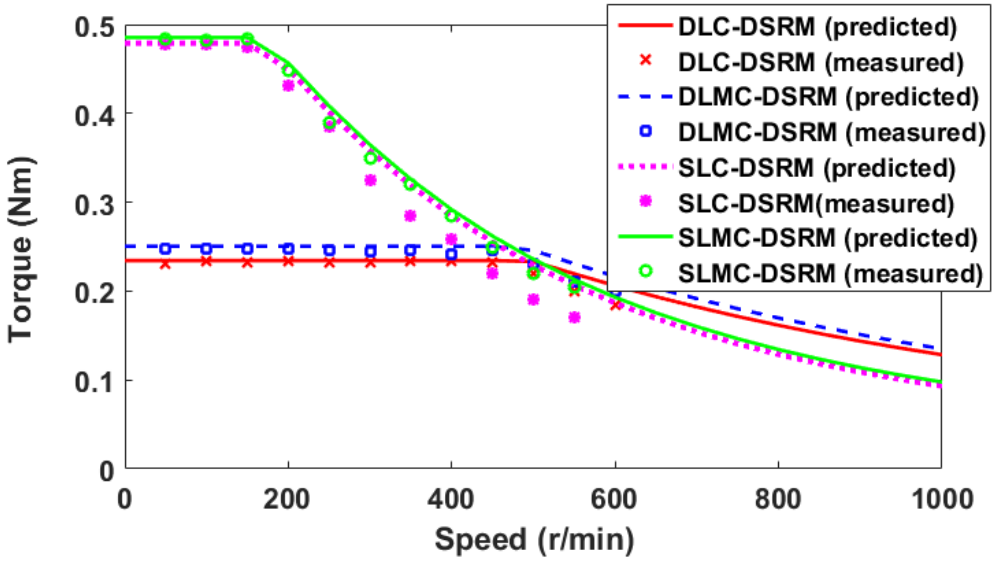

Fig. 4.18 Predicted and measured torque speed curves of double and single layer DSRMs. $I_{max} = 6A$, and $V_{DC} = 18V$.

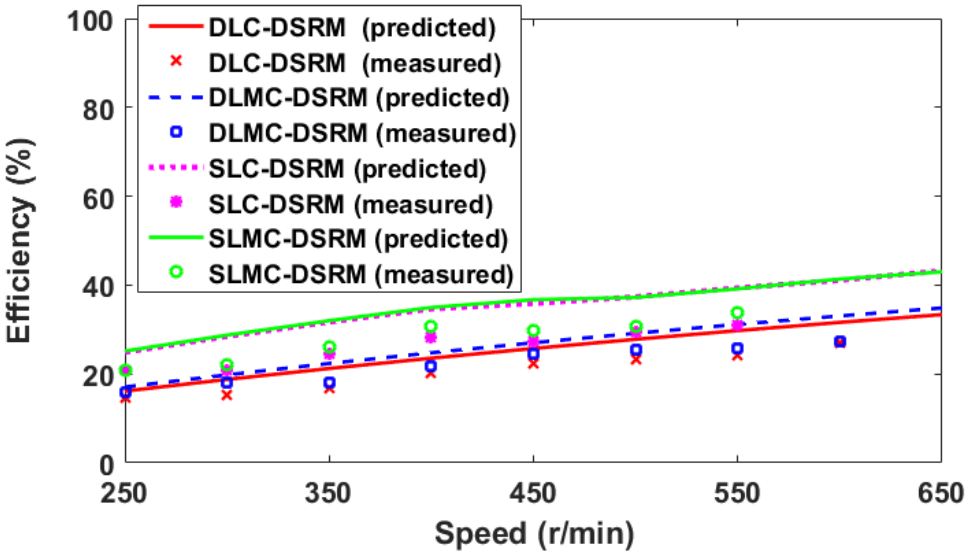

Fig. 4.19 Predicted and measured efficiency-speed curves. $I_{max} = 6A$, and $V_{DC} = 18V$.

4.6 CONCLUSION

The static and dynamic performances of the short-pitched double layer DSRMs (DLC-DSRM and DLMC-DSRM) and single layer DSRMs (SLC-DSRM and SLMC-DSRM), as well as one single layer fully-pitched DSRM (FP-DSRM), have been comprehensively investigated, principally through simulation and FE modelling, also experimental measurements of static torque and dynamic characteristics. It has been demonstrated, albeit within the context of relatively small machine dimensions, that at low phase current, the FP-DSRM produces lower copper loss per unit of average torque. However, due to the onset of magnetic saturation, performance of the FP-DSRM deteriorates markedly with increasing phase RMS current. Additionally, due to its inherently higher iron loss across the full speed range, the FP-DSRM achieves only modest performance at high speed. Due to its reduced propensity for magnetic saturation, the DLMC-DSRM performs well at high current level, producing higher average torque than the FP-DSRM for the same copper loss.

From a dynamic perspective, within the contest of this particular design study, the DLMC-DSRM yields the lowest iron loss and the highest peak efficiency. The SLC-DSRM and SLMC-DSRM produce higher average torque while with lower torque ripple than their double layer counterparts at low phase current. However, in common to the FP-DSRM design, both the SLC-DSRM and SLMC-DSRM are prone to the onset of significant magnetic saturation with increasing phase current, making them less attractive at high phase current than a DLMC-DSRM.

The SynRMs with double salient structure have been investigated in this chapter. In order to compare with the SynRMs with conventional synchronous reluctance rotors, the SynRMs with different rotor topologies will be studied in next chapter.

Chapter 5. INFLUENCE OF ROTOR TOPOLOGIES ON THE PERFORMANCES OF SYNRMS WITH ALTERNATIVE WINDING CONFIGURATIONS AND SLOT/POLE NUMBER COMBINATIONS

This chapter investigates the influence of rotor topologies and winding configurations on the electromagnetic performance of 3-phase SynRMs with different slot/pole number combinations, e.g. 12-slot/4-pole and 12-slot/8-pole. Transversally laminated synchronous reluctance rotors with both round and angled flux barriers have been considered, as well as the doubly salient rotor as that used in the SRMs and investigated in previous chapters. Both non-overlapping and overlapping concentrated winding configurations are accounted for, i.e., single layer and double layer conventional and mutually-coupled windings, as well as fully-pitched winding. The machine performance in terms of *d*- and *q*-axis inductances, on-load torque, copper loss, and iron loss have been investigated using 2D FEA. With appropriate rotor topology, the 12-slot/4-pole and 12-slot/8-pole machines with fully-pitched and double layer mutually-coupled windings can achieve similar torque capacity, which are higher than the machines with other winding configurations. In addition, the SynRM with round flux barriers can have lower iron loss than the DSRM under different working conditions. The prototypes of 12-slot/8-pole single layer and double layer DSRMs built in previous chapters have been used to validate the predictions in terms of inductances and torques.

This chapter was published in [93].

5.1 INTRODUCTION

Compared with permanent magnet machines and induction machines, both the synchronous reluctance machines (SynRM) and the switched reluctance machines (SRMs) are becoming increasingly attractive in various applications ranging from domestic appliances to electrical vehicles and hybrid electrical vehicles (EVs and HEVs).

The classic SynRMs often employ the distributed stator windings. For the DSRMs, both the short-pitched windings and the FP windings can be employed and this has been well investigated in literature [64], [72]. It has been found that the DSRM equipped with double layer mutually-coupled (DLMC) winding, which is also a short-pitched winding, is less sensitive to magnetic saturation than the ones equipped with the double layer conventional (DLC) windings and hence, produce higher average torque at high phase current [72]. However, the torque ripple coefficient of the DSRM equipped with the DLMC windings is relatively higher due to its nature of self- and mutual-inductances [21]. The FP winding DSRM can generate lower torque ripple but its long end-winding will result in higher copper loss for a given phase current. In order to take advantage of both the FP windings (higher torque capability) and the short-pitched windings (shorter end-winding), single layer windings (SLC and SLMC) DSRMs have been proposed in [72]. They can have higher torque capability than the double layer windings (DLC and DLMC) counterparts but lower copper loss than that of the FP windings.

Although the rotor of the DSRM is simpler and easier for manufacturing than that of the SynRM, the doubly salient rotor structure will result in high levels of vibration and acoustic noise [94] [95]. In contrast, most SynRMs have non-salient rotors (from the perspective of mechanical construction) with various topologies in order to increase the saliency ratio and also the difference between *d*- and *q*-axis inductances, and hence to increase the torque capability [50] [55]. It is well established in literature that the SynRMs are generally designed with transversally laminated rotor [53] [60]. Although the axially laminated rotor has advantages such as increased saliency ratio, hence improved power density and power factor [49] [54], it is very complex for industrial manufacturing. Therefore, the transversally laminated rotor has been selected for investigation in this chapter. By way of example, rotors with 4 poles are illustrated and they generally have two shapes, e.g. round flux barrier (RFB) and angled flux barrier (AFB) [53] [85] [86]. The latter is also used for some permanent magnet assisted SynRMs as shown in [96] [97]. It has been found in [54] that with the distributed

windings, the three-layer flux barriers SynRM can produce similar average torque but lower torque ripple than other number of flux barrier layers. In addition, the influence of slot numbers on the average torque is very minor but lower torque ripple can be produced with higher slot numbers. Hence, the three-layer flux barriers in the rotor will be adopted for the 12-slot/4-pole and 12-slot/8-pole machines in this chapter.

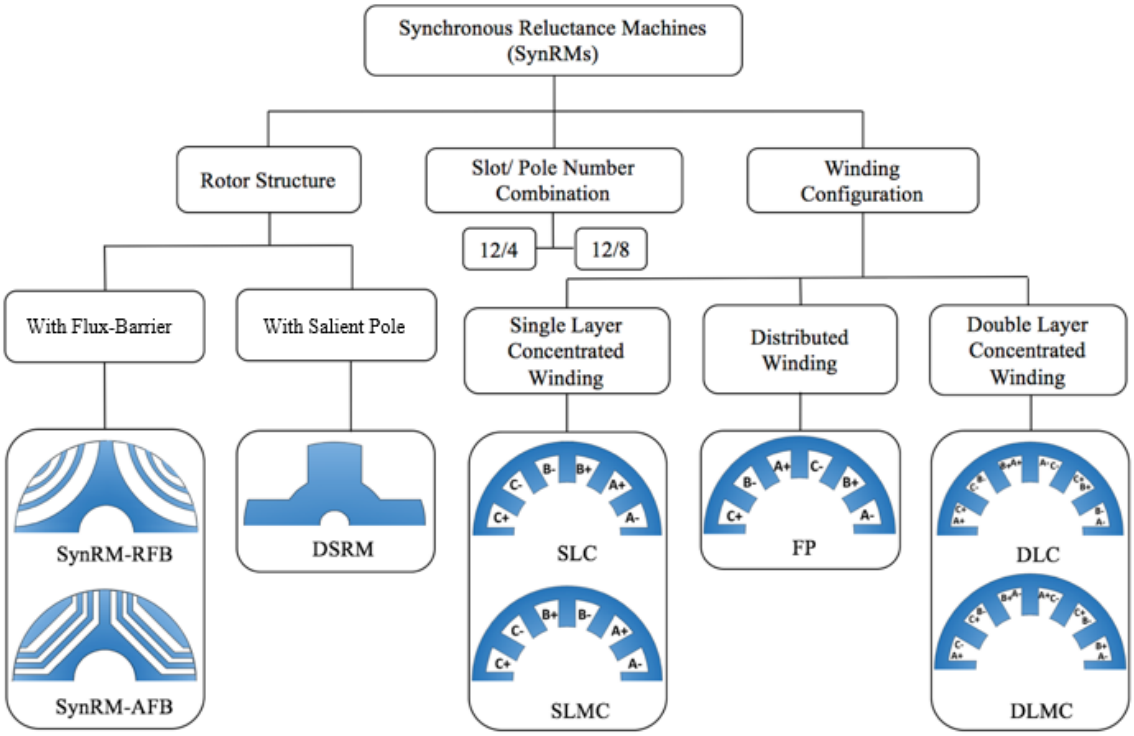

Fig. 5.1 Investigated reluctance machines in this chapter with different winding configurations and rotor topologies.

For clarity, a diagram including rotor topologies, slot/pole number combinations and winding configurations for all the investigated reluctance machines in this chapter is shown in Fig. 5.1. The three rotor topologies: SynRM-RFB, SynRM-AFB and DSRM will be investigated for both the 12-slot/4-pole and 12-slot/8-pole combinations. In addition, the double and single layer conventional windings (DLC and SLC), the double and single layer mutually-coupled windings (DLMC and SLMC), as well as the FP winding will be employed and are illustrated in Fig. 5.1. By way of example, the *d*- and *q*-axis inductances and power factors will be investigated on the 12-slot/8-pole machines with different windings and rotor topologies. For the performance investigation throughout this chapter, appropriate rotor structure will be identified based on torque comparison at both low and high current levels for

both the 12-slot/4-pole and 12-slot/8-pole machines. Then, comparison in terms of average torque, torque ripple, copper loss and iron loss will be carried out by 2D FEA between different slot/pole number combinations and winding configurations for the machines with appropriate rotor topologies.

5.2 FEATURES OF SYNRMS

5.2.1 DIFFERENT ROTOR TOPOLOGIES AND WINDING CONFIGURATIONS

For fairer comparison throughout this chapter, machines with different windings and rotor topologies have been optimized separately, and the optimization objective is to achieve the highest torque for constant copper loss (only DC losses have been considered, the end-winding has also been included in copper loss calculations). It is worth mentioning that for the concentrated windings, only the single layer windings have been selected for optimization mainly because they can generally produce higher average torque than their double layer counterparts. Hence, the dimensions of stator core are kept the same for all the winding configurations. However, the stator core has been optimized separately for machines with different rotor structure. The main dimensions of all investigated machines are kept the same as shown in TABLE 5.1. The rib width is 0.3 mm for all the SynRMs. However, the stator inner radii for the 12-slot/8-pole SynRM-RFB, SynRM-AFB, and DSRM are optimized as 27 mm, 27 mm and 28.4 mm, and the shaft outer radii are 13 mm, 9 mm and 11.6 mm, respectively.

TABLE 5.1 GENERAL DIMENSIONS AND DESIGN PARAMETERS OF SYNRMS

Stator slot number	12	Active length (mm)	60
Rotor pole number	4/8	Number of turns per phase	132
Stator outer radius (mm)	45	Slot area (mm^2)	116
Airgap length (mm)	0.5	Current density (A_{rms}/mm^2)	5.68

As mentioned previously, the SynRMs with three-layer flux barriers in the rotor have been selected for investigation in this chapter. By way of example, the flux distribution of the optimized 12-slot/8-pole SynRMs with both round and angled flux barrier rotors, as well as the DSRM with SLC winding configuration, are shown in Fig. 5.2. The phase A is supplied with a 10A DC current and the rotor pole is aligned with the phase A. It can be found that there is

no flux through the phase B and the phase C for the conventional concentrated windings as shown in Fig. 5.2.

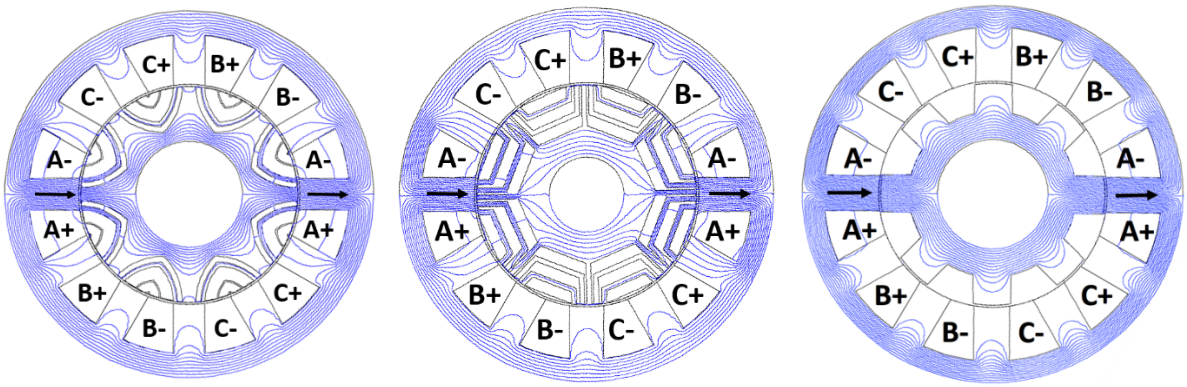

(a) (b) (c)

Fig. 5.2 Flux line distributions of the 12-slot/8-pole reluctance machines with different rotor topologies and SLC winding. The rotor pole is at the aligned position with the phase A, which is supplied with a 10A DC current. (a) SynRM with RFBs, (b) SynRM with AFBs, (c) DSRM.

The material M330-35A is used for the prototype machines, which has a yield stress of 300MPa and a material density of $7650kg/m^3$. By using 2D FEA, the maximum speed of 19000 rpm and mechanical stress of 295MPa for the 8-pole SynRM rotor with AFBs have been obtained. However, the 8-pole SynRM rotor with RFBs and the DSRM rotor can achieve much higher speed, i.e. 26000 rpm and 47000 rpm, respectively. Fig. 5.3 shows the comparison of the mechanical stress σ and the radial displacement u between different rotors at 19000 rpm. It is found that at this speed, the displacements of the rotor into the air-gap are lower than 1.84% of the airgap length (0.5mm). This means that the rotor will not rub the stator inner surface at this operating speed.

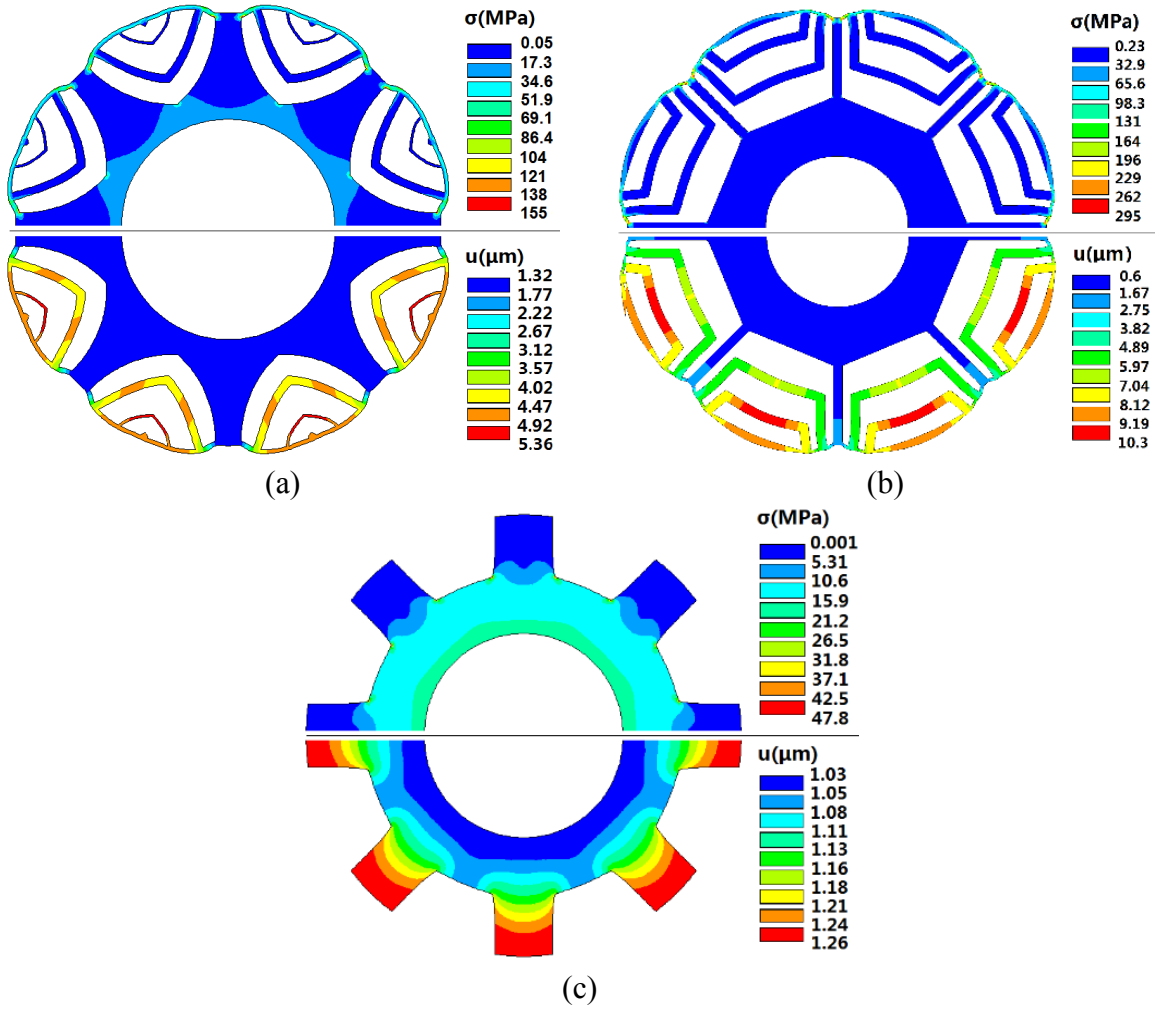

Fig. 5.3 Mechanical stress σ and radial displacement u comparison between different 8-pole rotors at 19000 rpm. (a) SynRM with RFBs, (b) SynRM with AFBs, (c) DSRM.

5.2.2 Influence of Rotor Topologies and Winding Configurations on D- and Q-Axis Inductances and Power Factors

Due to different magnetic polarities (different windings), different airgap magnetic fields have been generated, leading to different d- and q-axis inductances. The phasor diagram of the SynRMs is applicable to the DSRMs as well, the d- and q-axis inductances L_d and L_q which account for the cross-couplings are described by (4.1) and (4.2), respectively.

By way of example, the 12-slot/8-pole machines have been selected to investigate the influence of rotor topologies and winding configurations on the d- and q-axis inductances. TABLE 5.2 compares L_d and L_q of the 12-slot/8-pole machine topologies with different rotor

topologies and winding configurations. It can be found that the machines with the FP winding have the highest L_d and L_q at $10A_{rms}$ than others, regardless of rotor topologies. This will become an important factor that limits the constant power speed range. Additionally, the single layer winding machines have higher L_d and L_q than their double layer counterparts. The saliency ratio ($\zeta = \frac{L_d}{L_q}$) in TABLE 5.3 shows that the machines with the DLMC winding have the highest ζ, regardless of the rotor structures. Therefore, due to their highest saliency ratio, it can be predicted that the 12-slot/8-pole machines with the DLMC winding could have better performance than others. Furthermore, the power factors (see TABLE 5.3) can be obtained according to the phasor diagram of the SynRMs. It can be found that the SynRM-RFB can have the highest saliency ratio and power factors, regardless of winding configurations. Moreover, the power factors of the machines with double layer windings are higher than that of the machines with single layer windings. The machines with FP winding have the lowest power factors.

TABLE 5.2 COMPARISON OF *D*- AND *Q*-AXIS INDUCTNACES BETWEEN DIFFERENT 12-SLOT/8-POLE MACHINES AT $10A_{rms}$ ($I_d = I_q$)

	L_{d} (mH)			L_{q}(mH)		
	SynRM-RFB	SynRM-AFB	DSRM	SynRM-RFB	SynRM-AFB	DSRM
SLC	6.9	7.3	7.7	3.9	4.5	4.7
SLMC	7.1	7.7	9.0	3.9	4.5	4.9
FP	11.9	9.9	14.1	7.8	8.7	8.4
DLC	3.5	3.2	4.8	2.4	2.8	2.7
DLMC	4.4	5.4	5.0	2.1	2.6	2.6

It is established that the electromagnetic torque performance of the DSRMs can be determined by the difference between L_d and L_q, and rotor pole pair numbers. With the same pole pair number, the machine with higher inductance difference can generate higher average torque. Accordingly, $(L_d - L_q)$ of the 12-slot/8-pole machines have been calculated for different rotor topologies and winding configurations, as shown in Fig. 5.4, Fig. 5.5, and Fig. 5.6. In addition, $(\frac{\mathrm{L_d}}{\mathrm{L_q}} - 1)$ of the DSRMs has been shown in Fig. 5.6, which is directly proportional to the power factor without consideration of the phase resistance. It is apparent that at low current, the highest $(L_d - L_q)$ of the SynRM-RFB and the DSRM are achieved by

using the FP winding. However, for the SynRM-AFB, this can be obtained by using the SLMC winding. Therefore, at low current, the 12-slot/8-pole FP-SynRM RFB and FP-DSRM can be predicted to produce higher torque than other 12-slot/8-pole SynRM-RFBs and DSRMs, respectively. However, at high current, the DLMC winding produces the highest ($L_d - L_q$), regardless of rotor topologies. Hence, it could be predicted that all the three 12-slot/8-pole machine topologies can achieve their best torque performances at high current level when the DLMC winding configuration is employed. Moreover, the 12-slot/8-pole DLMC-DSRM could potentially generate higher torque than the 12-slot/8-pole DLMC-SynRMs due to slightly higher ($L_d - L_q$).

TABLE 5.3 COMPARISON OF SALIENCY RATIO $\frac{L_D}{L_Q}$ AND POWER FACTOR FOR DIFFERENT 12-SLOT/ 8-POLE MACHINES AT $10A_{rms}$ ($I_d = I_q$)

	SynRM-RFB		SynRM-AFB		DSRM	
	L_d/L_q	Power Factor	L_d/L_q	Power Factor	L_d/L_q	Power Factor
SLC	1.787	0.676	1.639	0.638	1.635	0.621
SLMC	1.847	0.679	1.713	0.637	1.834	0.620
FP	1.523	0.576	1.135	0.508	1.680	0.567
DLC	1.459	0.778	1.122	0.741	1.787	0.745
DLMC	2.106	0.796	2.096	0.752	1.895	0.750

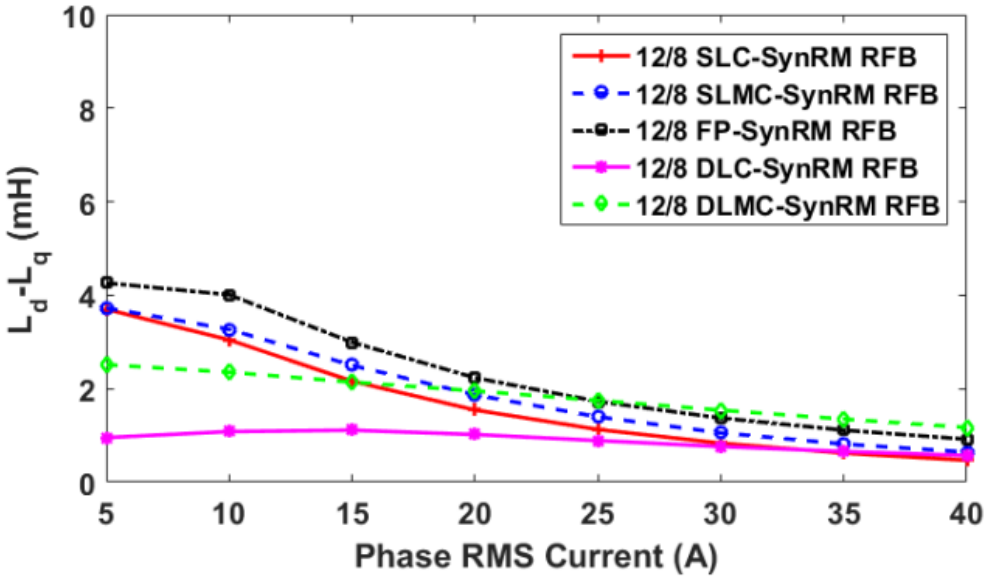

(a)

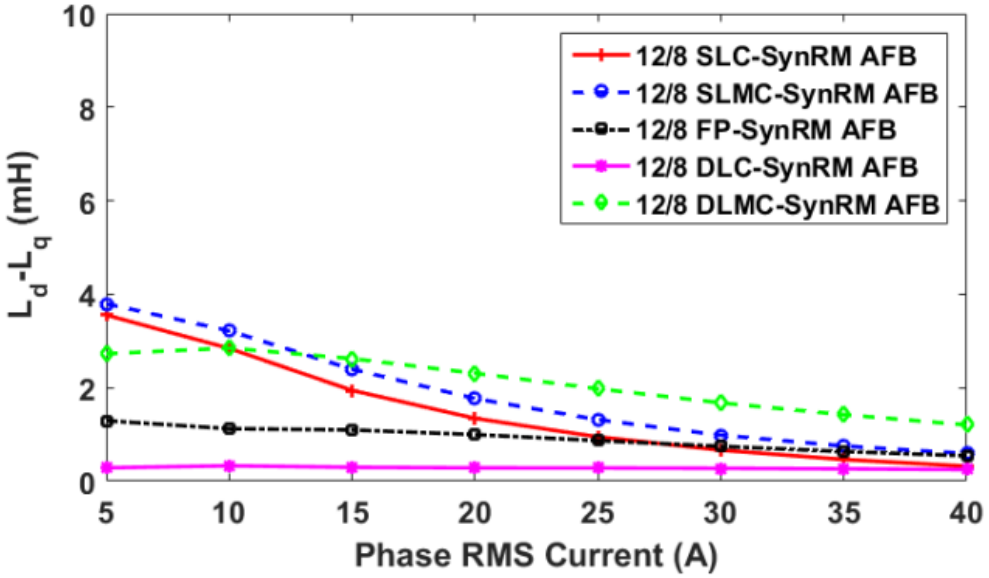

(b)

Fig. 5.4 Comparison of $(L_d - L_q)$ against phase RMS current between 12-slot/8-pole SynRMs with (a) RFBs, and (b) AFBs. The machines are supplied with 3-phase sinewave currents with $I_d = I_q$.

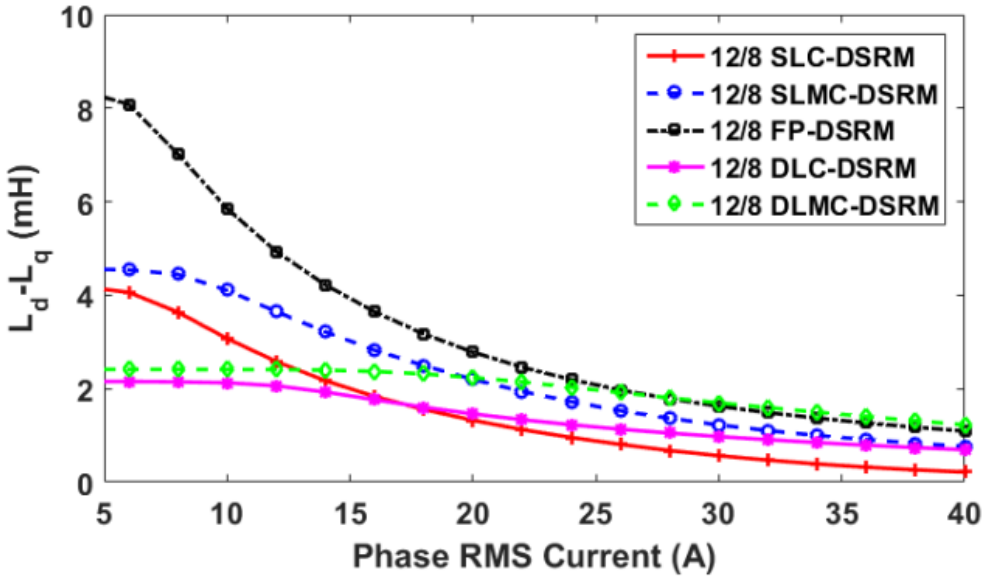

Fig. 5.5 The $(L_d - L_q)$ against phase RMS current between 12-slot/8-pole DSRMs. The machines are supplied with 3-phase sinewave currents with $I_d = I_q$.

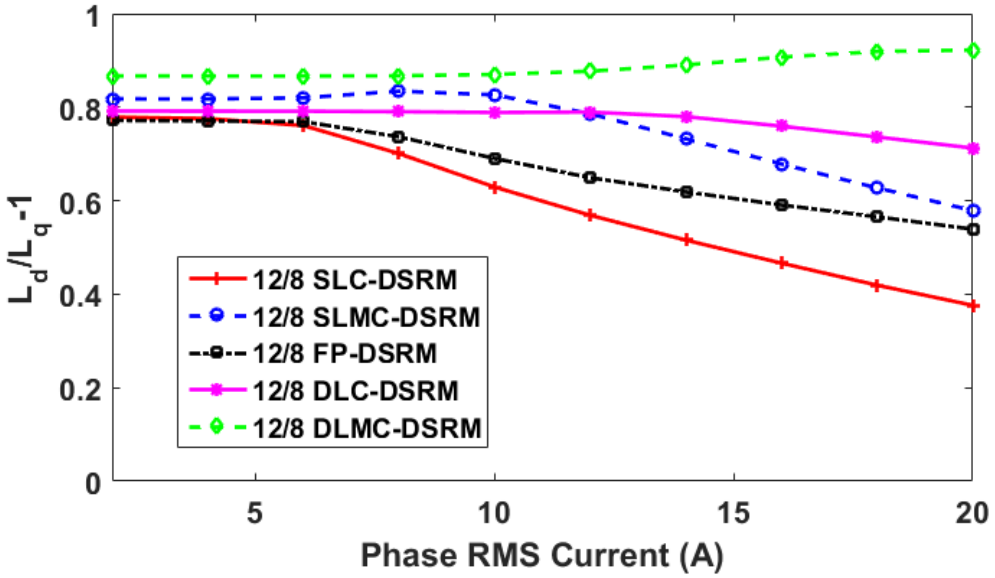

Fig. 5.6 The $(\frac{L_d}{L_q} - 1)$ against phase RMS current between 12-slot/8-pole DSRMs. The machines are supplied with 3-phase sinewave currents with $I_d = I_q$.

5.3 TORQUE PERFORMANCES FOR DIFFERENT WINDINGS, ROTOR TOPOLOGIES AND POLE NUMBERS

5.3.1 INFLUENCE OF ROTOR TOPOLOGIES ON TORQUE PERFORMANCES FOR BOTH THE 12-SLOT/4-POLE AND 12-SLOT/8-POLE MACHINES

According to the *d*- and *q*-axis inductances, the electromagnetic torque of a 3-phase reluctance machine can be calculated by (4.5) and (4.6). For completeness, the average torques at different current levels of all the 12-slot/4-pole and 12-slot/8-pole machines have been obtained by 2D FEA, as shown in Fig. 5.7 and Fig. 5.8, respectively. The torque ripple coefficient is calculated according to (2.11). It is worth noting that with different pole numbers and winding configurations, the reluctance will be different due to different winding factors and airgap permeances. For different slot/rotor pole number combinations, the winding factor has an important influence on the torque generation. By way of example, with SLC and SLMC winding configurations, the winding factors have been calculated as 0.5 for 12-slot/4-pole but 0.866 for 12-slot/8-pole machines. Hence, the average torque of the 12-slot/8-pole SLC-DSRM and SLMC-DSRM can be predicted to be higher than that of the 12-slot/4-pole SLC-DSRM and SLMC-DSRM. Hence, their influence on torque performances will be investigated separately in the following sections.

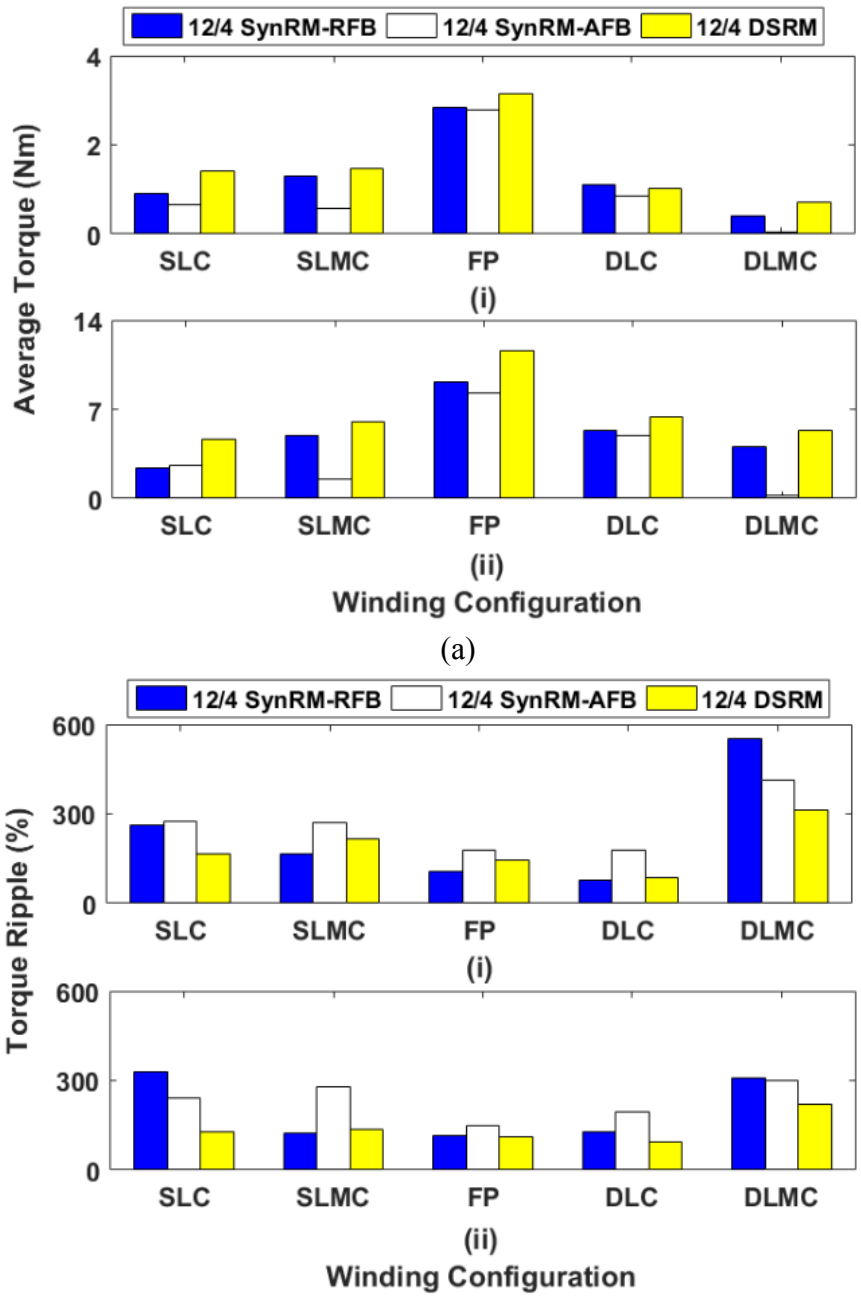

Fig. 5.7 (a) Average torque and (b) torque ripple coefficient of the 12-slot/4-pole SynRMs and DSRMs with different winding configurations at (i) 10 Arms and (ii) 40 Arms.

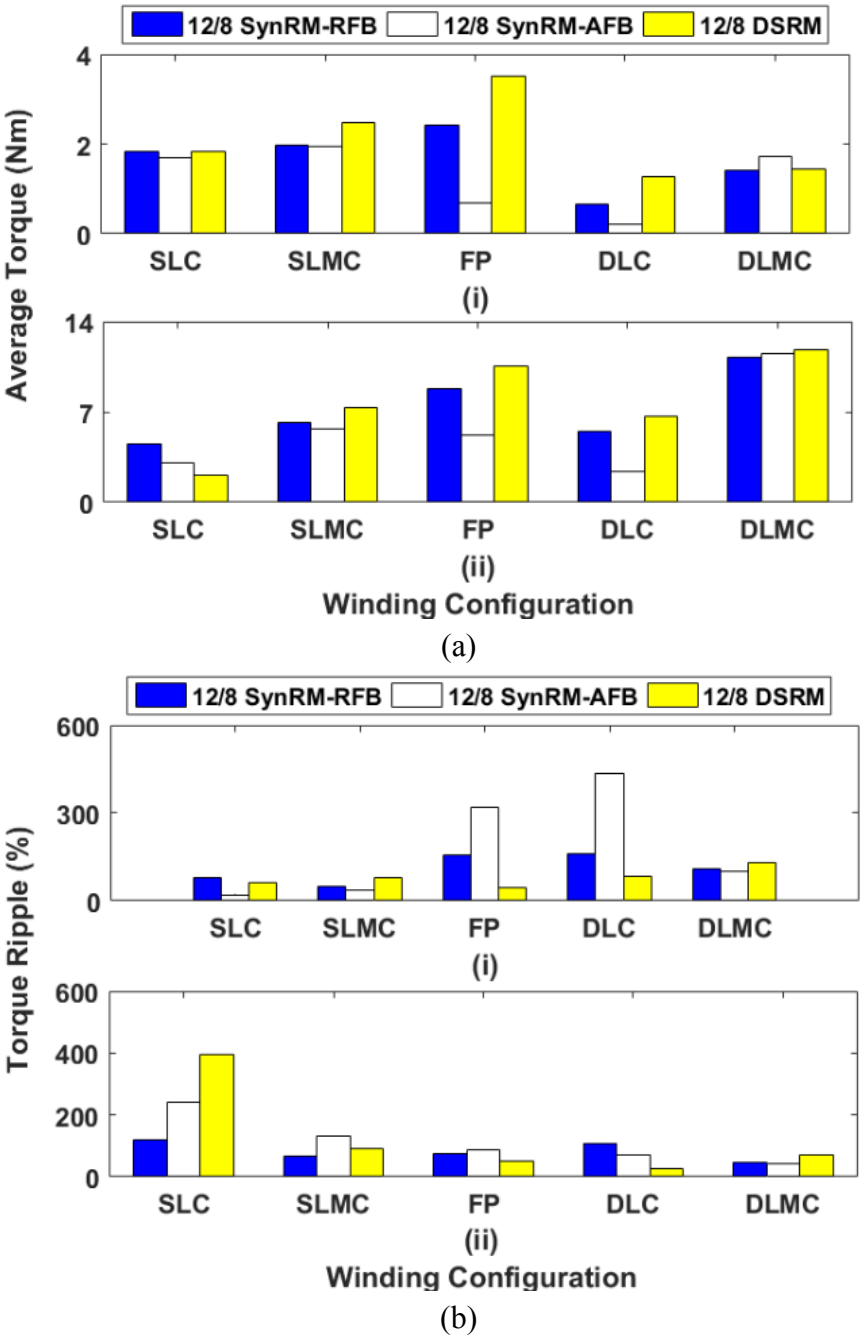

Fig. 5.8 (a) Average torque and (b) torque ripple coefficient of the 12-slot/8-pole SynRMs and DSRMs with different winding configurations at (i) 10 Arms and (ii) 40 Arms.

It can be found that for the SynRMs, the RFB rotor can produce higher average torque than the AFB rotor due to 20% higher average ratio of flux barrier thickness to the combined thickness of lamination and flux barriers, hence higher $\frac{L_d}{L_q}$ [50]. This is true for almost all winding configurations and for both low and high current levels (except the 12-slot/4-pole SLC winding at high current and the 12-slot/8-pole DLMC winding). However, the 12-slot/4-pole and 12-slot/8-pole DSRMs can produce similar or even higher average torque than the SynRMs

at both low and high current levels, regardless of winding configurations. The SynRMs with AFB rotor produce higher torque ripple than the DSRMs and the SynRMs with RFB rotor for most winding configurations. However, with similar average torque, the AFB rotor can produce lower torque ripple at 12% for the 12-slot/8-pole SLC winding at low current.

Accordingly, the appropriate rotor topologies to obtain the maximum average torque for both the 12-slot/4-pole and 12-slot/8-pole machines with different winding configurations have been summarized in TABLE 5.4. For clarity, only the most appropriate rotor topologies have been selected for further investigations.

TABLE 5.4 APPROPRIATE ROTOR TOPOLOGIES TO OBTAIN THE MAXIMUM AVERAGE TORQUE

Slot/pole number combinations	Winding configurations				
	SLC	SLMC	FP	DLC	DLMC
12-slot/4-pole	DSRM	DSRM	DSRM	SynRM-RFB &DSRM	DSRM
12-slot/8-pole	SynRM-RFB &DSRM	DSRM	DSRM	DSRM	SynRM-AFB &DSRM

5.3.2 INFLUENCE OF SLOT/POLE NUMBER COMBINATIONS ON TORQUE PERFORMANCE WITH APPROPRIATE ROTOR TOPOLOGIES

With the appropriate rotor topologies such as the ones shown in TABLE 5.4, the influence of slot/pole number combinations on torque-speed characteristics under $I_{max} = 14.14A$ and $V_{DC} = 100V$ is shown in Fig. 5.9.

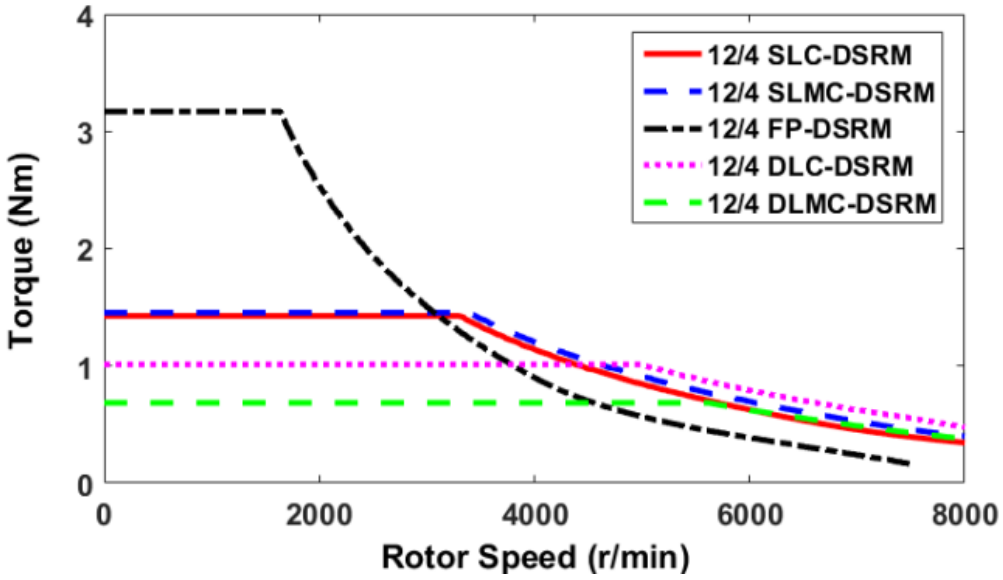

(a)

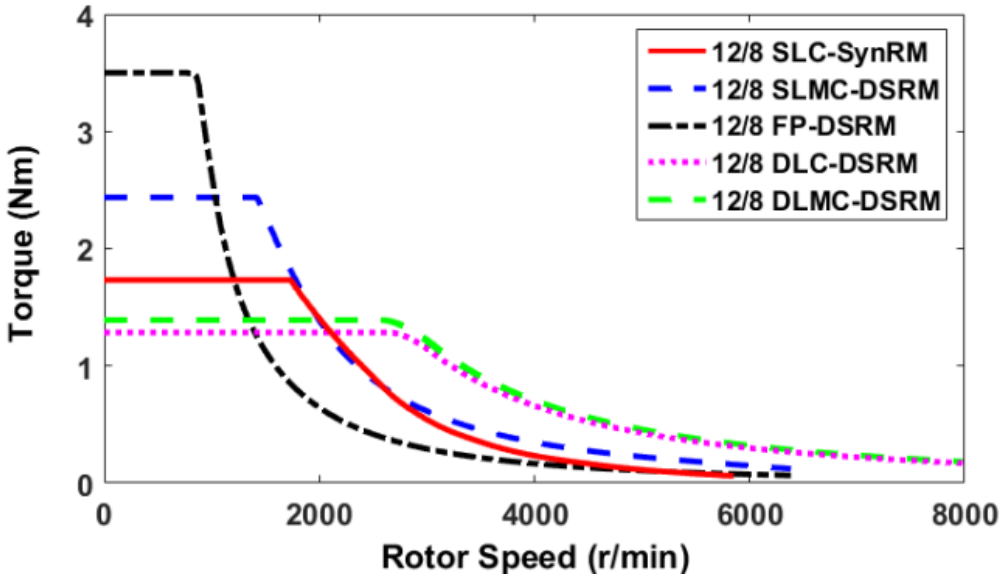

(b)

Fig. 5.9 Torque-speed curves between (a) 12-slot/4-pole and (b) 12-slot/8-pole machines with different windings. $I_{max} = 14.14A$ and $V_{DC} = 100V$.

It can be found in Fig. 5.9 that both the 12-slot/4-pole and 12-slot/8-pole machines with the FP windings and the salient rotors can achieve their best initial torques at $10A_{rms}$. However, the 12-slot/4-pole machines can have wider constant torque range than the 12-slot/8-pole machines. In addition, it is also found that the double layer machines can have higher base speed than other machines. However, the FP machines have the highest initial torque but the lowest base speed under the limit of $I_{max} = 14.14$A and $V_{DC} = 100$V. It is worth mentioning

that the 4-pole machines would produce less iron losses due to lower electrical frequency than the 8-pole machines. This will be investigated in the following section.

5.4 INFLUENCE OF MACHINE TOPOLOGIES ON COPPER LOSS AND IRON LOSS

It is well-established that the copper loss (proportional to current squared) could be the dominant loss for high torque low speed applications, while the iron loss could be the dominant loss for high speed applications, where the iron losses are determined by the iron core flux density and also the electrical frequency. Therefore, the aforementioned influence of winding and rotor topologies on torque performance will also be reflected into the machine losses.

5.4.1 COPPER LOSS

Due to different end-windings, the winding configurations will have significant influence on the copper loss characteristics. However, if phase current is unchanged then the different rotor pole numbers and rotor topologies will have no influence on copper loss for the same sized machines. Due to longer end-windings, the FP machines will generally produce higher copper loss than other machines, regardless of current levels. At $10A_{rms}$, the copper loss of the FP (246W) can be around 1.5 times higher than that of the single layer (171W) and double layer (159W) winding machines.

Although the FP machines generate higher copper loss than the single and double layer winding machines, the average torque against copper loss characteristics could be more important for investigation because the FP machines could generate higher average torque as well, as investigated previously. With appropriate rotor topologies, both average torque and torque ripple against copper loss for machines with different slot/pole number combinations and winding configurations have been obtained, as shown in Fig. 5.10 and Fig. 5.11. At lower torque level, e.g. 4Nm, both the 12-slot/4-pole and 12-slot/8-pole FP-DSRM will produce lower copper loss. At high torque level, e.g. 6Nm, the 12-slot/4-pole machine with the FP winding still have the best torque against copper loss performance than others. However, for the 12-slot/8-pole machines, the copper loss of the DLMC winding is much lower than that of the 12-slot/8-pole FP winding machine at 10Nm. Moreover, the 12-slot/8-pole DLMC machine exhibits even higher average torque at high current. This is due to the fact that the machines with the DLMC windings have lower MMF concentration in the stator yoke, hence are less

sensitive to the magnetic saturation. Nevertheless, they exhibit higher torque ripple than the FP winding machines due to their nature of self- and mutual-inductances as mentioned previously. It is also found that with appropriate winding configurations, the torque capability of the 12-slot/4-pole machines is similar to that of the 12-slot/8-pole machines. Overall, it can be concluded that with the FP windings, both the 12-slot/4-pole and 12-slot/8-pole machines can have better torque against copper loss characteristics without heavy magnetic saturation. However, the 12-slot/8-pole DLMC machines can have better performance at high current level (high copper loss).

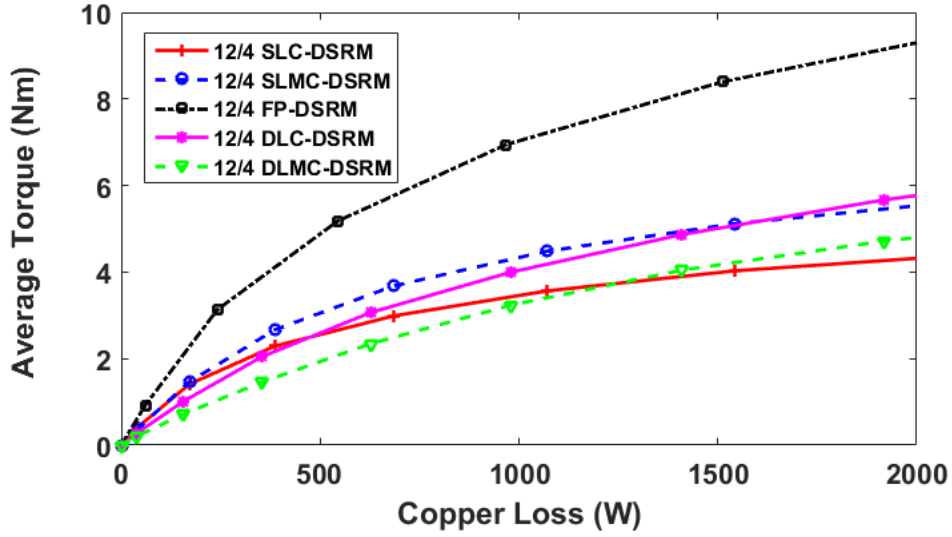

(a)

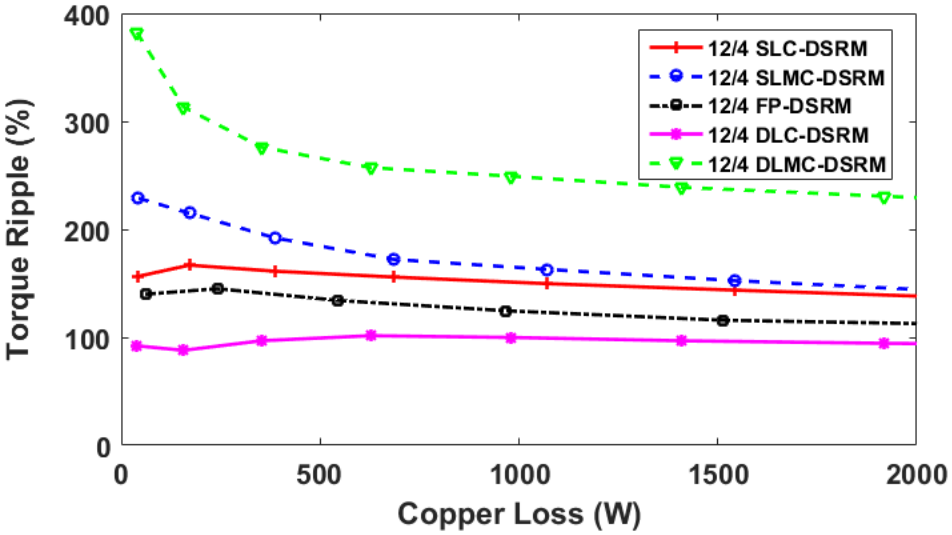

(b)

Fig. 5.10 Influence of winding configurations on torque performance against copper loss of 12-slot/4-pole machines. (a) Average torque against copper loss, (b) torque ripple against copper loss.

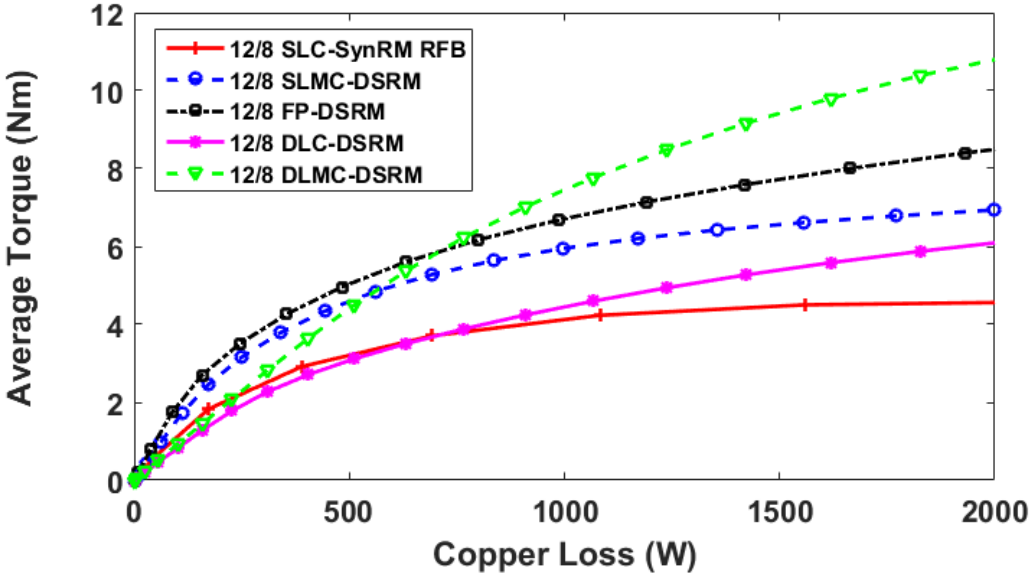

(a)

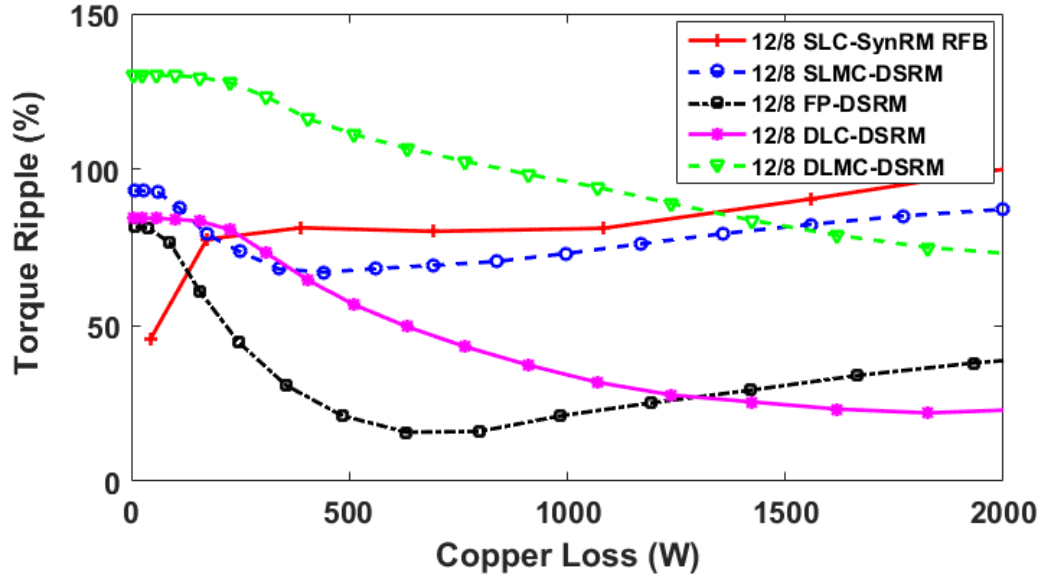

(b)

Fig. 5.11 Influence of winding configurations on torque performance against copper loss of 12-slot/8-pole machines. (a) Average torque against copper loss, (b) torque ripple against copper loss.

5.4.2 IRON LOSS

Different from copper loss, the iron loss can be influenced not only by the winding configurations, but also by the slot/pole number combinations and rotor topologies. Considering the torque performance, the FP and SLMC windings are selected for the 12-slot/4-pole machines, whilst the FP and DLMC windings are selected for the 12-slot/8-pole machines. Moreover, both the DSRM and SynRM rotors are selected for iron loss investigation. The iron loss density over one electrical cycle is comprised of hysteresis loss and eddy-current loss, which can be calculated using (2.12).

The total iron loss is obtained by the summation of the iron losses calculated in every individual FE mesh element in both the stator and the rotor. According to (2.12), it is necessary to investigate the radial and tangential flux densities (B_r and B_t) frequencies and their variations for both the stator and the rotor, as shown in TABLE 5.5. It is worth noting that the rotor topology does not have any influence on the flux density frequencies.

TABLE 5.5 FLUX DENSITY FREQUENCIES OF STATOR AND ROTOR

Slot/pole number combination	Winding configuration	Stator B_r/B_t frequency (Hz)	Rotor B_r/B_t frequency (Hz)
12-slot/4-pole	FP	13.3	80
	SLMC	13.3	40
12-slot/8-pole	FP	26.6	40
	DLMC	26.6	80

It can be found that the stator flux density frequency is only influenced by the slot/pole number combination and it is equal to $p\Omega/60$, where Ω is the mechanical rotor speed, and p is the pole-pair number. This means that the stator flux density has 1 period in every electrical cycle. Nevertheless, the rotor flux density will present different frequencies due to different winding configurations and rotor pole numbers.

By way of example, the 12-slot/8-pole FP and 12-slot/8-pole DLMC machines have been shown in TABLE 5.6 for investigation on the stator and rotor iron losses at 10 A_{rms}, 400 rpm. It can be found that, with the same stator and rotor flux density frequencies, the SynRM-AFB generates higher stator and rotor iron losses than the DSRM with 12-slot/8-pole DLMC windings due to higher variations in B_r and B_t. However, the SynRM-RFB will generate lower

stator and rotor iron losses than the DSRM with 12-slot/8-pole FP windings due to lower variations in B_r and B_t.

TABLE 5.6 IRON LOSS OF 12-SLOT/8-POLE MACHINES AT $10A_{RMS}$ AND 400 RPM

Machines	Iron loss (W)		
	Stator	Rotor	Total
12-slot/8-pole FP-SynRM RFB	1.79	1.86	3.65
12-slot/8-pole FP-DSRM	2.24	2.45	4.69
12-slot/8-pole DLMC-SynRM AFB	0.59	1.03	1.63
12-slot/8-pole DLMC-DSRM	0.57	0.24	0.81

According to the torque capability, two rotor topologies have been selected for the 12-slot/4-pole and 12-slot/8-pole machines with appropriate winding configurations. For completeness, the influences of phase RMS current and speed on total iron loss have been calculated, as shown in Fig. 5.12 and Fig. 5.13 for 12-slot/4-pole and 12-slot/8-pole machines, respectively. It can be found that for the 12-slot/4-pole machines, the SynRM-RFB with FP winding can produce the lowest iron losses for the full speed and current ranges. However, for the 12-slot/8-pole machines, the DSRM with DLMC winding produces the lowest iron losses for the full speed and current ranges. Moreover, it is found that the 12-slot/8-pole machines have higher iron loss than the 12-slot/4-pole machines with the same rotor topologies and windings at variable current levels and speeds, as expected.

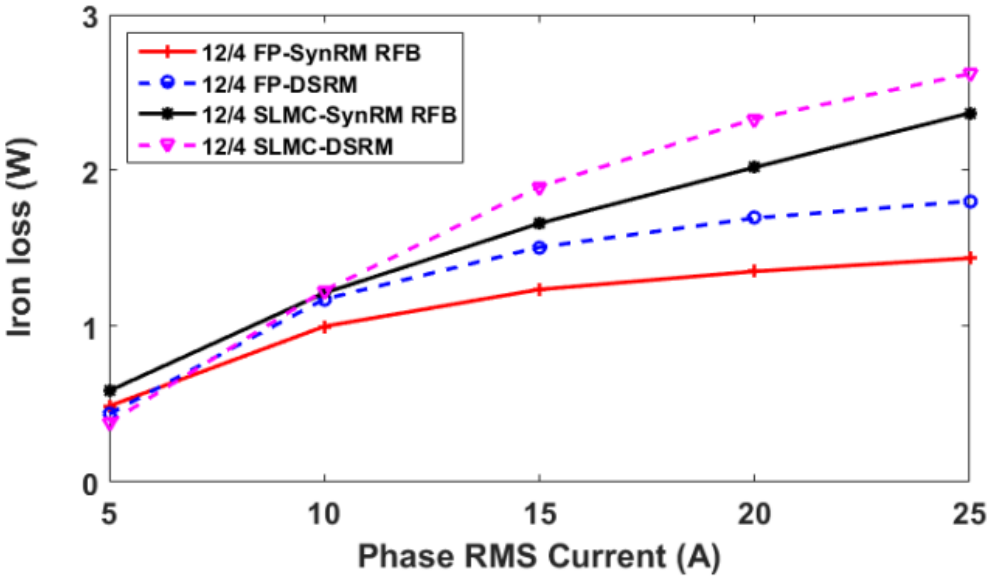

(a)

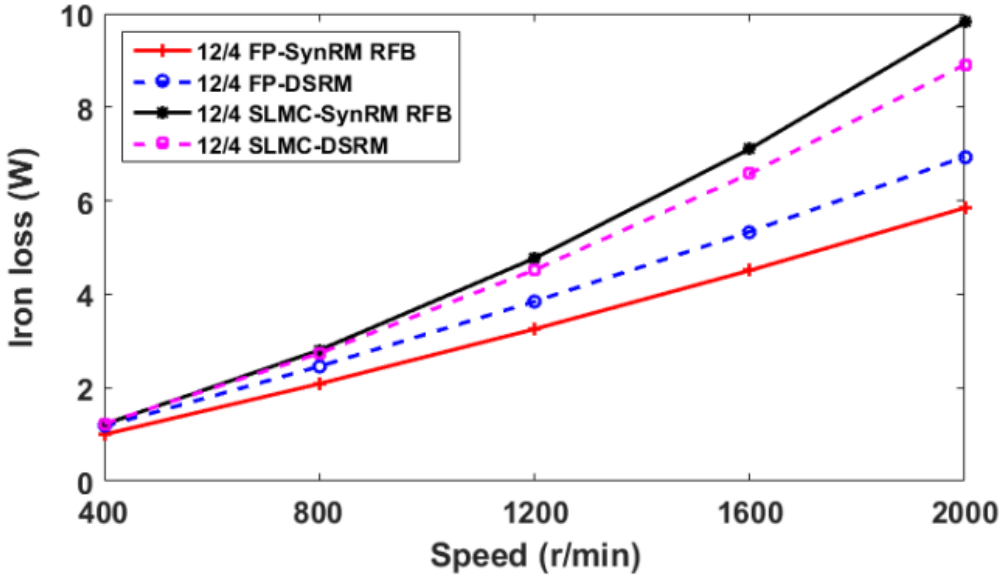

(b)

Fig. 5.12 Iron loss of selected 12-slot/4-pole machines under different operating conditions. (a) At 400 rpm with increasing phase RMS current, (b) at 10Arms with increasing speed.

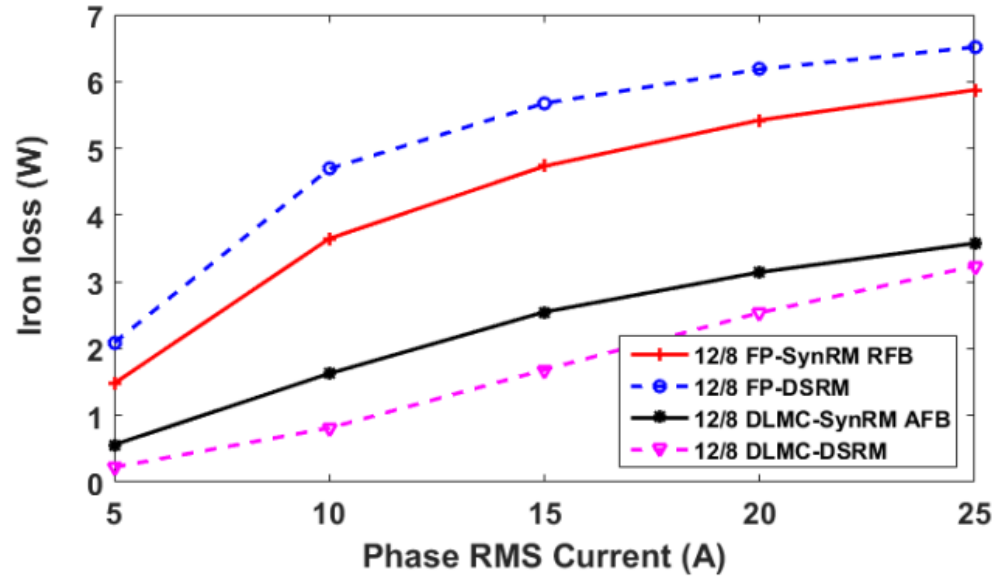

(a)

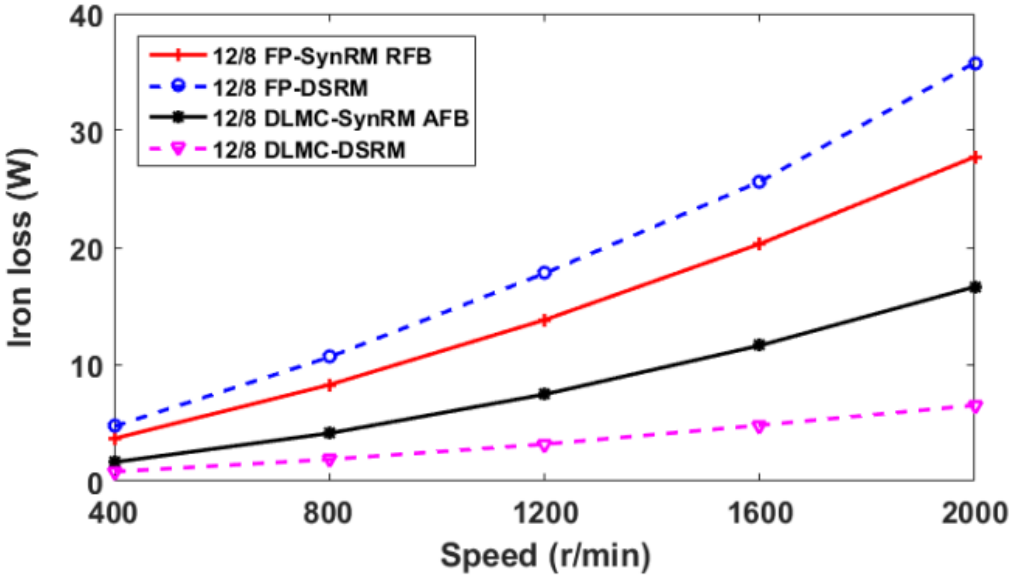

(b)

Fig. 5.13 Iron loss of selected 12-slot/8-pole machines under different operating conditions. (a) At 400 rpm with increasing phase RMS current, (b) at 10Arms with increasing speed.

5.5 Experimental Validation

In order to validate the predictions, both the 12-slot/8-pole single layer DSRMs and the 12-slot/8-pole double layer DSRMs that have been built in Chapter 4 are employed in this chapter, and the inductances and static torques have been measured as detailed in the following sections. The FP winding has not been built due to its significantly longer end-winding than other

winding configurations, leading to higher copper loss. In addition, it has relatively lower power factor.

The self- and mutual-inductances of the 12-slot/8-pole DSRMs with different windings are measured against rotor positions at 1A DC current as shown in Fig. 5.14. The measured phase resistances of the single and double layer DSRMs are 1.48Ω and 1.32 Ω, respectively. The method of static torque measurement in [80] has been adopted for undertaking the torque measurements in this chapter. In order to measure the static torque, three phases of the DSRMs are supplied with DC currents such as $I_A = I$, $I_B = I_C = -1/2I$, where I is variable and controllable by the power supply. The static torques against rotor positions for variable currents have been measured, as shown in Fig. 5.15 and Fig. 5.16. It can be found that the measured results are in good agreement with the predicted results.

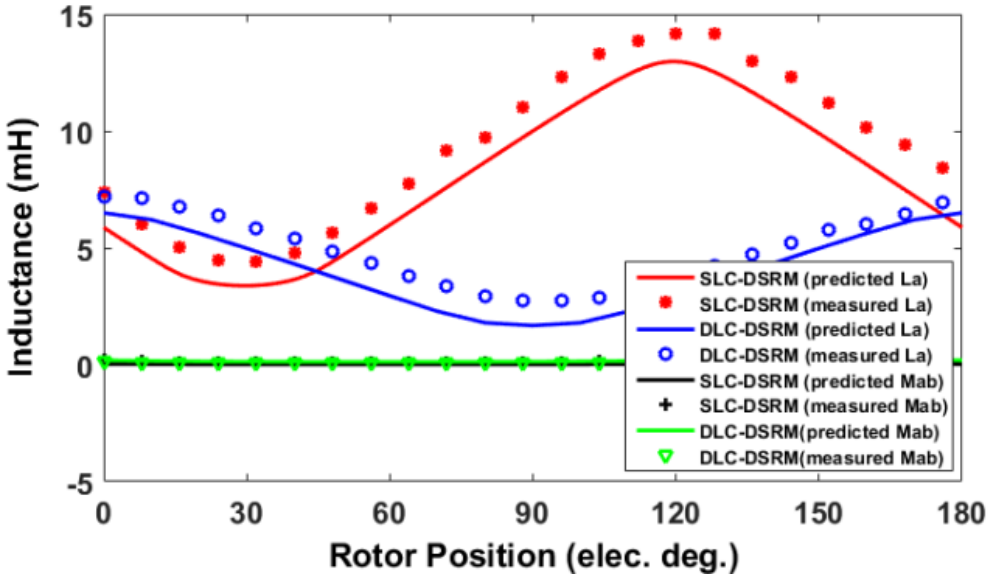

(a)

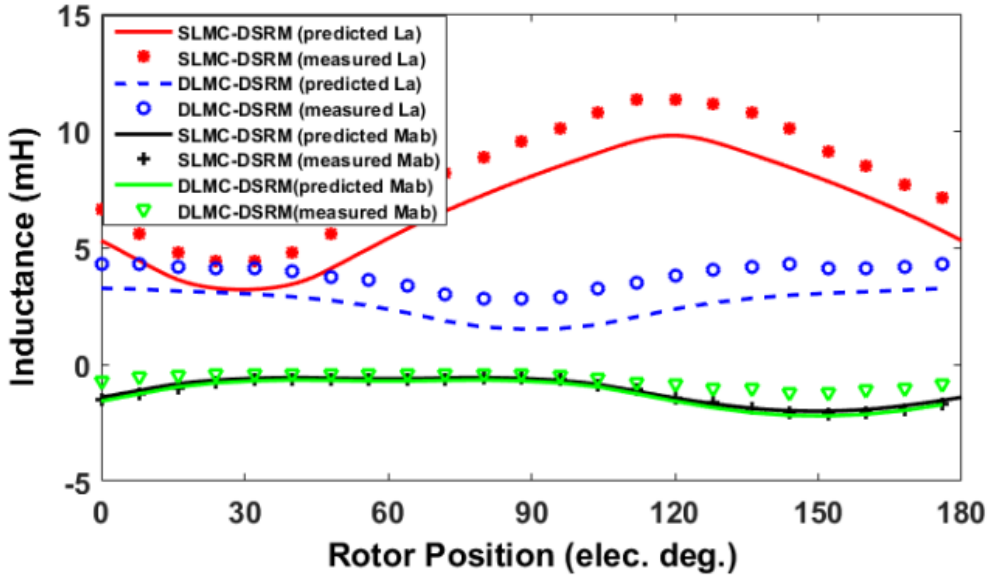

(b)

Fig. 5.14 Measurement of self- and mutual-inductances of 12-slot/8-pole DSRMs with different windings at 1A DC current. (a) Conventional winding DSRMs, (b) mutually-coupled winding DSRMs.

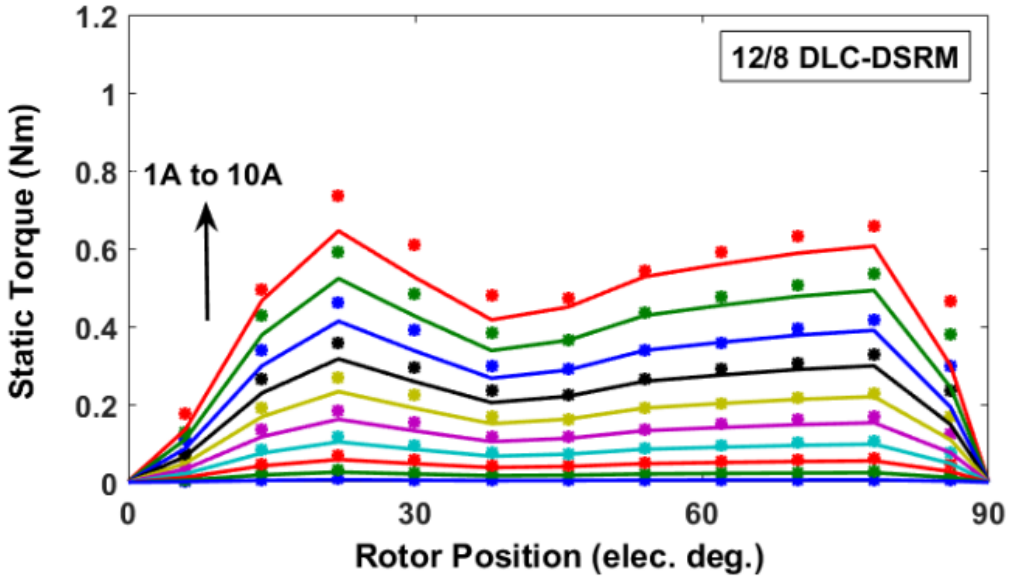

(a)

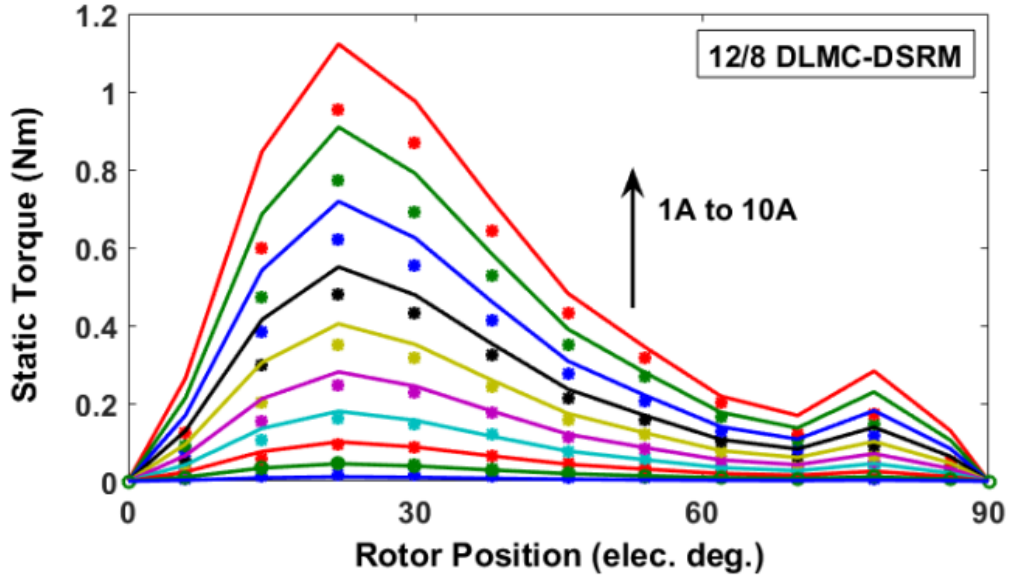

(b)

Fig. 5.15 Static torque against rotor position for variable currents (solid line: predicted results, dot: measured results). (a) 12-slot/8-pole DLC-DSRM, (b) 12-slot/8-pole DLMC-DSRM.

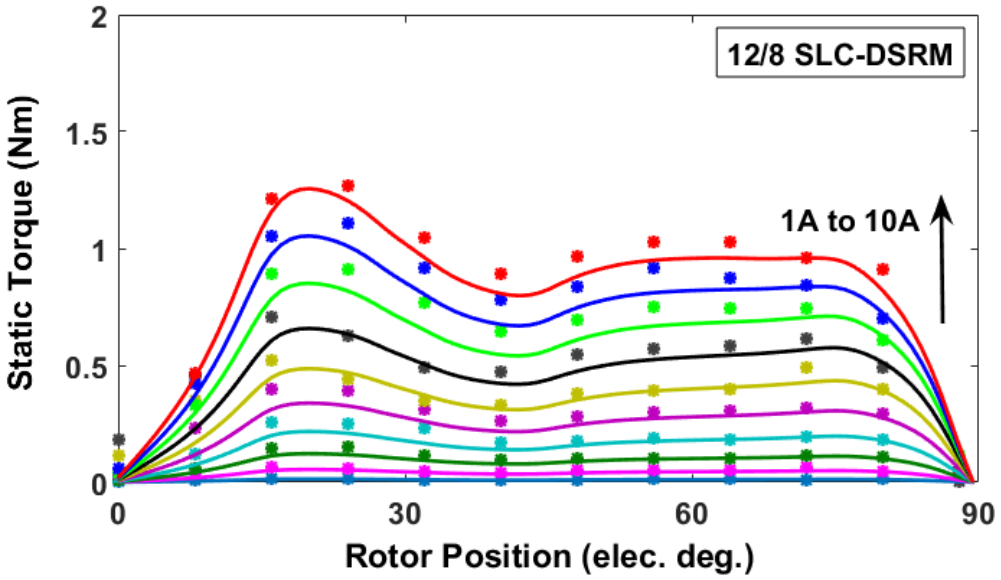

(a)

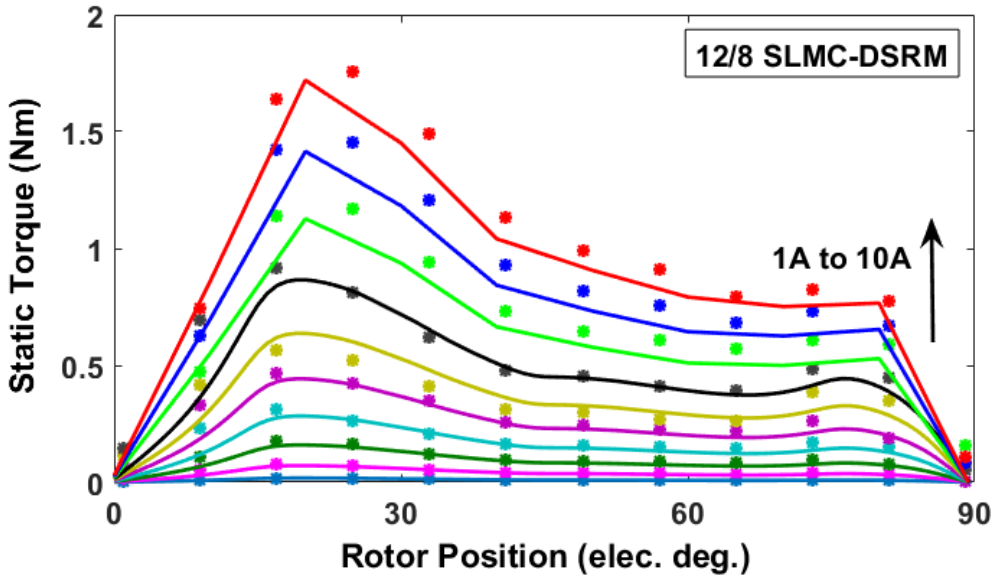

(b)

Fig. 5.16. Static torque against rotor position for variable currents (solid line: predicted results, dot: measured results). (a) 12-slot/8-pole SLC-DSRM, (b) 12-slot/8-pole SLMC-DSRM.

Furthermore, the machine efficiency has been obtained for both the 12-slot/8-pole single and double layer DSRMs as shown in TABLE 5.7 where the DC link voltage is 18V and the maximum phase peak current is 6A, which is limited by the load-torque capacity of the used DC machine. The low efficiency is mainly due to the fact that for the prototype machines, smaller copper wires have been used to ease the winding process, leading to smaller slot filling factor and higher copper loss. The difference between predicted and measured results is mainly because the end-winding effect has not been taken into account in the 2D FEA. In addition, the

torque-sensor accuracy and measuring error can be the other factors that contribute to this discrepancy.

TABLE 5.7 MACHINE EFFICIENCY (%) OF 12-SLOT/8-POLE SINGLE AND DOUBLE LAYER DSRMS AT $10A_{RMS}$ AND 400 RPM

Speed (rpm)	DLC-DSRM		DLMC-DSRM		SLC-DSRM		SLMC-DSRM	
	Predicted	Measured	Predicted	Measured	Predicted	Measured	Predicted	Measured
350	21.24	16.86	22.37	17.97	31.71	24.67	32	26.2
400	23.56	20.30	24.77	21.83	34.67	28.31	34.98	30.56
450	25.74	22.34	27.03	24.55	35.89	27.19	36.73	29.85
500	27.81	23.43	29.16	25.57	37.36	30.61	37.22	30.84
550	29.76	24.24	31.17	25.64	39.35	31.02	39.18	33.83
600	31.61	26.9	33.06	27.37	41.11	--	41.36	--

5.6 CONCLUSION

Three rotor topologies (SynRM-RFB, SynRM-AFB, and DSRM), five winding configurations (SLC, SLMC, FP, DLC, DLMC) and two slot/pole number combinations (12-slot/4-pole and 12-slot/8-pole) are employed for investigation on the synchronous reluctance machines. The results have revealed that the 12-slot/8-pole SynRM-RFB can produce the highest power factors regardless of winding configurations. In addition, the power factors of the double layer windings are higher than both the single layer and FP windings. The appropriate rotor topologies have been identified for each winding configuration and slot/pole number combination, according to the torque performance at different current levels. With appropriate rotor topology, the influence of slot/pole number combinations on average torque and torque ripple for different phase currents have been investigated. It has been found that the 12-slot/4-pole and 12-slot/8-pole machines have similar torque capability (12Nm at $40A_{rms}$) when the appropriate winding configurations are employed. By way of example, the FP winding is the most appropriate winding configuration for the 12-slot/4-pole machines, while the DLMC winding is the best for the 12-slot/8-pole machines.

Regarding the copper loss, the FP winding presents the best average torque against copper loss characteristics at low current for both the 12-slot/4-pole and 12-slot/8-pole machines. However, the 12-slot/8-pole machines with the DLMC winding achieve better average torque

against copper loss at high current due to their shorter end-windings. The investigation on iron loss shows that lower iron loss can be achieved by the SynRM-RFB rotor topology when compared with the DSRM. Moreover, the FP and DLMC windings can produce lower iron loss than other windings for the 12-slot/4-pole and 12-slot/8-pole machines, respectively.

Different winding configurations and machine topologies have been investigated by 2D FEA. In order to achieve better understanding of the nature of the DSRMs, analytical modelling will be adopted in next chapter to investigate the contribution of airgap field harmonics to torque production for the DSRMs with alternative winding configurations.

Chapter 6. QUANTITATIVE ANALYSIS OF CONTRIBUTION OF AIRGAP FIELD HARMONICS TO TORQUE PRODUCTION IN SYNRMS WITH ALTERNATIVE WINDING CONFIGURATIONS AND SALIENT POLE ROTOR

Previous chapters proposed some novel DSRMs for performance improvement, this chapter will adopt some simple analytical modelling to investigate the contribution of airgap field harmonics to the torque production in some 3-phase, 12-slot/8-pole DSRMs that has been investigated in previous chapters with both conventional and mutually-coupled winding configurations. The airgap flux density has been calculated based on the analytically obtained MMF and doubly salient airgap permeance for both the double layer and single layer DSRMs with different winding configurations. Then the contribution of different airgap field harmonics to average torque and torque ripple can be investigated and validated by 2D FEA. It has been found that in the DSRM, the 10th order harmonic in the double layer conventional (DLC), the 4th order harmonic in the double layer mutually-coupled (DLMC), the 7th order harmonic in the single layer conventional (SLC) and the 10th order harmonic in the single layer mutually-coupled (SLMC) have the highest contribution to positive average torque and positive influence on torque ripple reduction. However, the 2nd order harmonic in the DLC, the 8th order harmonic in the DLMC, the 5th order harmonic in the SLC and the 2nd order harmonic in the SLMC machines mainly reduce the average torque.

This chapter was published in [98].

6.1 INTRODUCTION

As mentioned in previous chapters, the SRMs can adopt the sinewave excitation which are in effect the DSRMs, for the sake of utilizing the standard 3-phase inverter in order to reduce the system cost and to employ the doubly salient machine structure for simpler manufacturing.

Similar to the SRMs, both the concentrated and distributed windings can be applied for the DSRMs, which have significant influence on the electromagnetic performance. It is well-established that the SRM with double layer conventional winding configuration (DLC) obtains its best electromagnetic performance when it adopts the conventional square wave unipolar current with 120 elec. deg. conduction [70]. However, the DSRM with DLC cannot have a good performance with sinewave excitation since only self-inductances can contribute to the electromagnetic torque. Different from the DLC, the machine with double layer mutually-coupled winding (DLMC) can have both self- and mutual-inductances since the flux in one phase also links to other phases [6] [20] [70]. In addition, the DLMC is less sensitive to magnetic saturation due to the less concentrated MMF in the stator iron core. As a result, it has been found that the DLMC can achieve better overload torque capability [11]. Moreover, it is evident in [11] [15] that the vibration and acoustic noise can be reduced with the DLMC. However, the torque ripple of this machine is higher than that with the DLC due to the nature of self- and mutual-inductances.

With sinewave excitation, higher average torque while with lower torque ripple can be achieved by both single layer conventional (SLC) and single layer mutually-coupled (SLMC) machines at low current level, in which the winding configurations are similar to their double layer counterparts [72]. However, similar to the single layer winding structure in the well-established fully-pitched winding machine, the two single layer machines are more sensitive to magnetic saturation, making them less attractive at high phase current than the double layer machines.

In this chapter, in order to investigate the machine mechanism between different winding configurations, both the double or single layer machines have been selected for quantitative analysis of the airgap field harmonics and their contribution to the torque performances (average torque and torque ripple). Some simple analytical models have been developed based on the airgap permeance and armature winding MMFs. In order to evaluate the slotting effect on the airgap permeance and hence on the airgap field, two main methods can be adopted, which have been well established in literature. One is to evaluate a relative permenace function

on the basis of the conformal transformation (considered in this chapter), the other approach is to use the subdomain models, which might be relatively more accurate, but more complicated to use as well [99] [100] [101] [102]. In addition, the analytical models of the airgap flux density have been developed according to the MMF-permeance theory reported in [103] [104] [105] [106]. It is worth mentioning that in order to simplify the analyses, the permeability of the stator and the rotor iron cores has been assumed to be infinite. As a result, the magnetic saturation is not considered. In addition, the analytical model will be 2D, and hence the end effect is neglected as well.

6.2 INFLUENCE OF WINDING CONFIGURATIONS ON MMF

6.2.1 WINDING CONFIGURATIONS OF DOUBLE AND SINGLE LAYER DSRMS

In this chapter, the 3-phase 12-slot/8-pole DSRMs employ both the double/single layer, conventional/mutually-coupled winding configurations. To simplify the analysis, all the machines have the same dimensions and their design parameters are shown in TABLE 6.1. The flux paths of the double layer conventional and mutually-coupled (DLC and DLMC) DSRMs, as well as the single layer conventional and mutually-coupled (SLC and SLMC) DSRMs are shown in Fig. 6.1.

TABLE 6.1 MACHINE DIMENSIONS AND DESIGN PARAMETERS

Stator slot number	12	Active length (mm)	60
Rotor pole number	8	Stator slot opening coefficient β_s	0.49
Stator outer radius (mm)	45	Rotor slot opening coefficient β_r	0.57
Stator inner radius	29.3	Turn number per phase	132
Airgap length (mm)	0.5	Rated RMS current (A)	10
Rotor outer radius (mm)	28.8	Current density (A_{rms}/mm^2)	5.68
Rotor inner radius (mm)	9.3		

When the phase A is supplied with a DC current, it can be found in Fig. 6.1 (a) and (c) that there is almost no mutual-flux in the DLC and SLC. However, the flux of phase A is also linked with other phases in the DLMC and SLMC, as shown in Fig. 6.1 (b) and (d), respectively. In addition, the number of flux paths of the phase A in mutually-coupled winding machines is doubled than that in the conventional winding machines, regardless of double or single layer winding structure. This is also reflected in the coil magnetic polarities of the phase A that the DLC is SNSN while it is SSSS for the DLMC. As a result, the MMF waveform of the phase A of the DLC should be different from that of the DLMC as will be detailed later in this chapter.

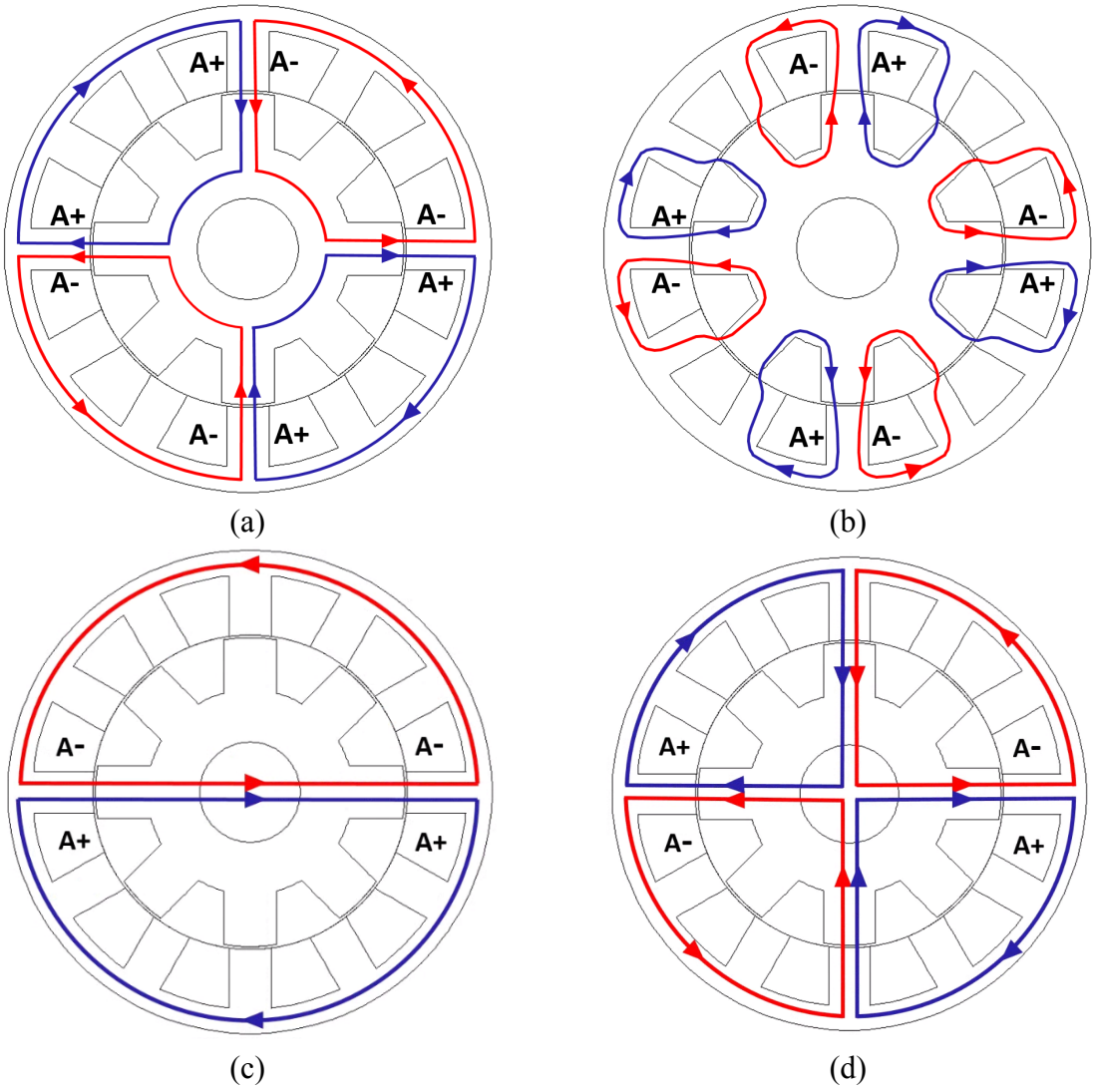

Fig. 6.1 Flux paths in (a) DLC, (b) DLMC, (c) SLC, and (d) SLMC when the phase A is supplied with a DC current.

The single layer winding machines have similar winding arrangement to double layer ones but with single layer winding structure. Hence, it can be found in TABLE 6.2 that the SLC and

SLMC have similar coil magnetic polarities as the DLC and DLMC, respectively. However, the periodicity of the magnetic polarities in the double layer machines is doubled than that in the single layer machines due to the fact that the number of flux paths is doubled than that of the single layer machines, as shown in Fig. 6.1.

TABLE 6.2 COIL MAGNETIC POLARITIES OF DSRMS WITH DIFFERENT WINDING CONFIGURATIONS

Winding configurations	Coil magnetic polarities
DLC	SNSNSNSNSNSN
DLMC	SSSSSSSSSSSS
SLC	NSNSNS
SLMC	NNNNNN

Additionally, it is worth noting that the number of coils per phase of the double layer machines is doubled when compared with that of the single layer ones. However, the double layer machines have half number of turns per coil compared with the single layer ones, so they have the same number of turns per phase. By way of example, with 4 coils per phase, the double layer machines have 33 turns per coil to achieve 132 series turns per phase. However, the single layer ones have 2 coils per phase and 66 turns per coil. Therefore, at the same current, the amplitude of single phase MMF of the single layer machines is doubled than that of the double layer ones, regardless of the winding configurations. This means that the single layer winding might generate more torque but it could be more prone to magnetic saturation as well.

6.2.2 ANALYSIS OF SINGLE-PHASE MMF FOR DIFFERENT WINDING CONFIGURATIONS

According to the winding configurations and coil magnetic polarities, the single-phase MMF of both the double and single layer configurations can be calculated. It is worth noting that the waveforms of the single-phase MMF of the double layer winding configurations are similar to that of their single layer counterparts, while their amplitudes (influenced by number of turns per coil) and periodicities (influenced by the periodicity of the coil magnetic polarities) are different. In order to avoid the duplication, only the DLC and DLMC have been selected

for the MMF analytical modelling in this section. However, the SLC and SLMC have been shown in the appendix.

6.2.2.1 CONVENTIONAL WINDING CONFIGURATIONS (DLC)

With 4 coils per phase, the coil magnetic polarities of the phase A of the DLC are SNSN. Therefore, the phase A winding has 2 pole pairs, and its MMF against angular position θ, at t=0, can be calculated over half of a mechanical period, i.e. $[0, \pi]$:

$$MMF_a(\theta, t=0) = \begin{cases} H & 0 \le \theta < \frac{1}{2}\theta_s - \frac{1}{2}\beta_s\theta_s \\ -\frac{2H}{\beta_s\theta_s}\left(\theta - \frac{1}{2}\theta_s\right) & \frac{1}{2}\theta_s - \frac{1}{2}\beta_s\theta_s \le \theta < \frac{1}{2}\theta_s \\ 0 & \frac{1}{2}\theta_s \le \theta < \frac{5}{2}\theta_s \\ -\frac{2H}{\beta_s\theta_s}\left(\theta - \frac{5}{2}\theta_s\right) & \frac{5}{2}\theta_s \le \theta < \frac{5}{2}\theta_s + \frac{1}{2}\beta_s\theta_s \\ -H & \frac{5}{2}\theta_s + \frac{1}{2}\beta_s\theta_s \le \theta < \frac{7}{2}\theta_s - \frac{1}{2}\beta_s\theta_s \\ \frac{2H}{\beta_s\theta_s}\left(\theta - \frac{7}{2}\theta_s\right) & \frac{7}{2}\theta_s - \frac{1}{2}\beta_s\theta_s \le \theta < \frac{7}{2}\theta_s \\ 0 & \frac{7}{2}\theta_s \le \theta < \frac{11}{2}\theta_s \\ \frac{2H}{\beta_s\theta_s}\left(\theta - \frac{11}{2}\theta_s\right) & \frac{11}{2}\theta_s \le \theta < \frac{11}{2}\theta_s + \frac{1}{2}\beta_s\theta_s \\ H & \frac{11}{2}\theta_s + \frac{1}{2}\beta_s\theta_s \le \theta < 6\theta_s \end{cases} \quad (6.1)$$

where $H = N_c I_{ph}$ is the MMF per coil ($N_c = 33$ for the double layer machines while $N_c = 66$ for the single layer machines). The DC phase current is used for the single-phase MMF modelling, while for the three-phase MMF modelling it is the phase peak current. θ_s is the stator pole pitch (30 mech. deg. for the 12-slot/8-pole machines), $\beta_s\theta_s$ is the stator slot opening which can be found in TABLE 6.1, and θ is the angular position in mech. deg. Accordingly, (6.1) can be expanded into Fourier series over $[0, 2\pi]$ as

$$MMF_a(\theta, t=0) = \frac{2N_c I_{ph}}{\pi\beta_s\theta_s} \sum_{k=1}^{\infty} \frac{1}{k^2} C_{a,k} \cos(k\theta) \quad (6.2)$$

where the coefficient $C_{a,k}$ is shown in TABLE 6.3. It can be found that the single-phase MMF of the DLC contains harmonic orders of 2, 6, 10, …, (4k-2), where k=1, 2, 3, … Accordingly, the magnitude of each harmonic in the single-phase MMF can be obtained.

TABLE 6.3 COEFFICIENT $C_{a,k}$ IN SINGLE-PHASE MMF OF THE DLC

$C_{a,k}$	n
$4\sin(\frac{1}{2}n\beta_s\theta_s) - 4\sqrt{3}\left[\cos\left(\frac{n\beta_s\theta_s}{2}\right) - 1\right]$	$2 + 24(k-1)$
$8\sin(\frac{1}{2}n\beta_s\theta_s)$	$6 + 24(k-1)$
$4\sin(\frac{1}{2}n\beta_s\theta_s) + 4\sqrt{3}\left[\cos\left(\frac{n\beta_s\theta_s}{2}\right) - 1\right]$	$10 + 24(k-1)$
$-4\sin(\frac{1}{2}n\beta_s\theta_s) + 4\sqrt{3}\left[\cos\left(\frac{n\beta_s\theta_s}{2}\right) - 1\right]$	$14 + 24(k-1)$
$-8\sin(\frac{1}{2}n\beta_s\theta_s)$	$18 + 24(k-1)$
$-4\sin(\frac{1}{2}n\beta_s\theta_s) - 4\sqrt{3}\left[\cos\left(\frac{n\beta_s\theta_s}{2}\right) - 1\right]$	$22 + 24(k-1)$

6.2.2.2 MUTUALLY-COUPLED WINDING CONFIGURATIONS (DLMC)

If the mutually-coupled winding is employed, the flux path is different from that of the DLC. It can be seen from Fig. 6.1(b) that the number of flux paths is doubled in the DLMC. In addition, its coil magnetic polarities, such as for the phase A, are SSSS. As a result, the periodicity of the single-phase MMF of the DLMC is 4 over one mechanical period ($[0, 2\pi]$), and the phase A MMF against the angular position θ, at t=0, is calculated over $\left[0, \frac{1}{2}\pi\right]$.

$$MMF_a(\theta, t=0) = \begin{cases} \frac{H}{2} - \delta_0 & 0 \le \theta < \frac{1}{2}\theta_s - \frac{1}{2}\beta_s\theta_s \\ -\frac{2H}{\beta_s\theta_s}\left(\theta - \frac{1}{2}\theta_s + \frac{1}{4}\beta_s\theta_s\right) - \delta_0 & \frac{1}{2}\theta_s - \frac{1}{2}\beta_s\theta_s \le \theta < \frac{1}{2}\theta_s \\ -\frac{H}{2} - \delta_0 & \frac{1}{2}\theta_s \le \theta < \frac{5}{2}\theta_s \\ \frac{2H}{\beta_s\theta_s}\left(\theta - \frac{5}{2}\theta_s - \frac{1}{4}\beta_s\theta_s\right) - \delta_0 & \frac{5}{2}\theta_s \le \theta < \frac{5}{2}\theta_s + \frac{1}{2}\beta_s\theta_s \\ \frac{H}{2} - \delta_0 & \frac{5}{2}\theta_s + \frac{1}{2}\beta_s\theta_s \le \theta < 3\theta_s \end{cases} \quad (6.3)$$

where

$$\delta_0 = \frac{1}{T}\int_0^{2\pi} MMF_a(\theta, \delta_0 = 0)d\theta = -\frac{H}{6}(\beta_s + 1) \tag{6.4}$$

δ_0 is referred to the DC component which is considered for the mutual flux path through other phases (when the phase A is excited). Accordingly, (6.3) can be expanded into Fourier series over $[0, 2\pi]$ as

$$MMF_a(\theta, t = 0) = \frac{2N_c I_{ph}}{\pi\beta_s\theta_s}\sum_{k=1}^{\infty}\frac{1}{k^2}M_{a,k}\cos(k\theta) \tag{6.5}$$

where the coefficient $M_{a,k}$ is shown in TABLE 6.4. Therefore, the single-phase MMF of the DLMC contains harmonic orders of 4, 8, 12, …, (4k), where k=1, 2, 3, … It is apparent that the harmonic orders in MMF are different from the DLC due to different magnetic polarities.

TABLE 6.4 COEFFICIENT $M_{a,k}$ IN SINGLE-PHASE MMF OF THE DLMC

$M_{a,k}$	n
$4\sqrt{3}\sin(\frac{1}{2}n\beta_s\theta_s) + 4\left[\cos\left(\frac{n\beta_s\theta_s}{2}\right) - 1\right]$	$4 + 24(k-1)$
$4\sqrt{3}\sin(\frac{1}{2}n\beta_s\theta_s) - 4\left[\cos\left(\frac{n\beta_s\theta_s}{2}\right) - 1\right]$	$8 + 24(k-1)$
$-8\left[\cos\left(\frac{n\beta_s\theta_s}{2}\right) - 1\right]$	$12 + 24(k-1)$
$-4\sqrt{3}\sin(\frac{1}{2}n\beta_s\theta_s) - 4\left[\cos\left(\frac{n\beta_s\theta_s}{2}\right) - 1\right]$	$16 + 24(k-1)$
$-4\sqrt{3}\sin(\frac{1}{2}n\beta_s\theta_s) + 4\left[\cos\left(\frac{n\beta_s\theta_s}{2}\right) - 1\right]$	$20 + 24(k-1)$
$8\left[\cos\left(\frac{n\beta_s\theta_s}{2}\right) - 1\right]$	$24 + 24(k-1)$

The single-phase MMFs of both the SLC and SLMC can be obtained in similar way, as shown in the appendix. According to these Fourier series expressions, the single-phase MMFs of both the double and single layer machines are illustrated in Fig. 6.2 (a) and (b), respectively. Fig. 6.3 shows their spectra. It can be found that the MMF amplitudes of both the double layer DSRMs are lower than that of the single layer ones, but the periodicity is doubled. This is due to the fact that the single layer DSRMs have doubled number of turns per coil but halved

periodicity in the coil magnetic polarities, as mentioned previously. In addition, with the conventional winding configurations, the harmonic orders of the SLC are 1, 3, 5, …, (2*k*-1), where *k*=1, 2, 3, ..., while with the mutually-coupled winding configurations, the harmonic orders of the SLMC are 2, 4, 6, …, 2*k*, where *k*=1, 2, 3, ... Hence, the harmonic orders of the double layer DSRMs are doubled than those of the single layer ones, regardless of the winding configurations. Furthermore, it can be found that the phase A MMF is not zero at the angular position of other phases, e.g. 120 mech. deg., for phase B or C, in both the double and single layer mutually-coupled machines. This is due to the mutual flux between phases as explained previously.

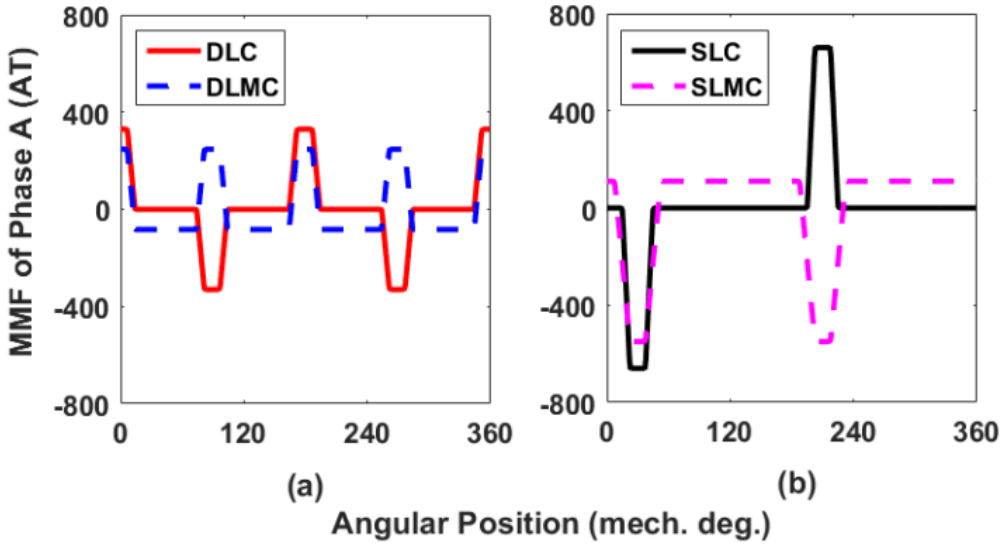

Fig. 6.2 Comparison of the single phase MMFs between the 12-slot/8-pole DSRMs. (a) Double layer, and (b) single layer machines. Phase A is supplied with a 10A DC current.

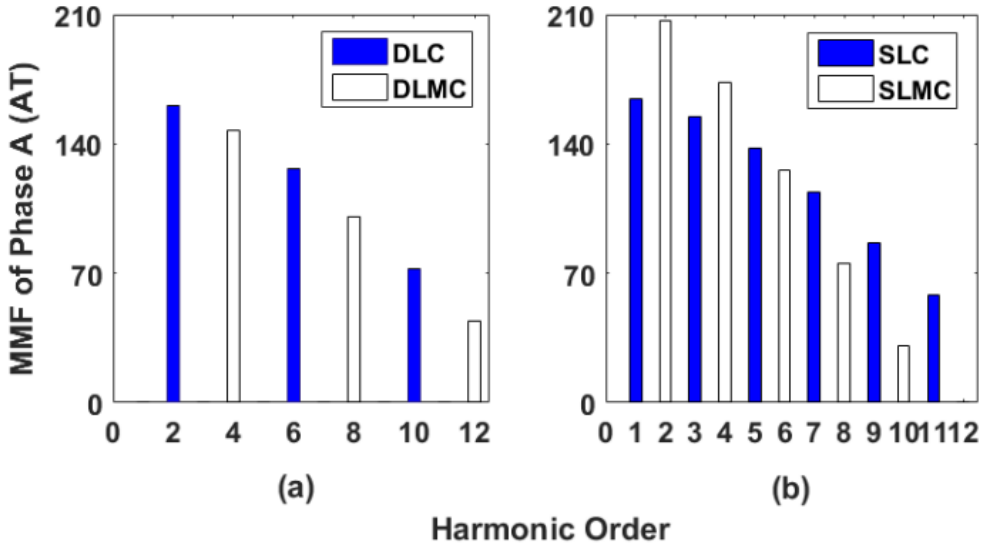

Fig. 6.3 Spectra of the single phase MMFs. (a) Double layer, and (b) single layer machines. Phase A is supplied with a 10A DC current.

6.2.3 3-PHASE MMF SUPPLIED WITH SINEWAVE CURRENTS

Supplied with 3-phase sinewave currents as shown in (6.6), the 3-phase MMF can be calculated at different rotor positions.

$$\begin{cases} i_a = \sqrt{2} I_{rms} \sin(\omega t) \\ i_b = \sqrt{2} I_{rms} \sin(\omega t - \frac{2\pi}{3}) \\ i_c = \sqrt{2} I_{rms} \sin(\omega t + \frac{2\pi}{3}) \end{cases} \tag{6.6}$$

For the DLC-DSRM, the 3-phase MMF is given by

$$MMF_{abc}(\theta, t) = \frac{3\sqrt{2} N_c I_{rms}}{\pi \beta_s \theta_s} \sum_{k=1}^{\infty} \frac{1}{k^2} C_{a,k} \sin \beta_C \tag{6.7}$$

where

$$\beta_C = \begin{cases} n\theta + \omega t & n = 2 + 12(k-1) \\ 0 & n = 6 + 12(k-1) \\ -n\theta + \omega t & n = 10 + 12(k-1) \end{cases} \tag{6.8}$$

Similarly, the 3-phase MMF of the DLMC-DSRM is given by

$$MMF_{abc}(\theta,t)=\frac{3\sqrt{2}N_cI_{rms}}{\pi\beta_s\theta_s}\sum_{k=1}^{\infty}\frac{1}{k^2}M_{a,k}\sin\beta_M \tag{6.9}$$

where

$$\beta_M=\begin{cases}-n\theta+\omega t & n=4+12(k-1)\\ n\theta+\omega t & n=8+12(k-1)\\ 0 & n=12+12(k-1)\end{cases} \tag{6.10}$$

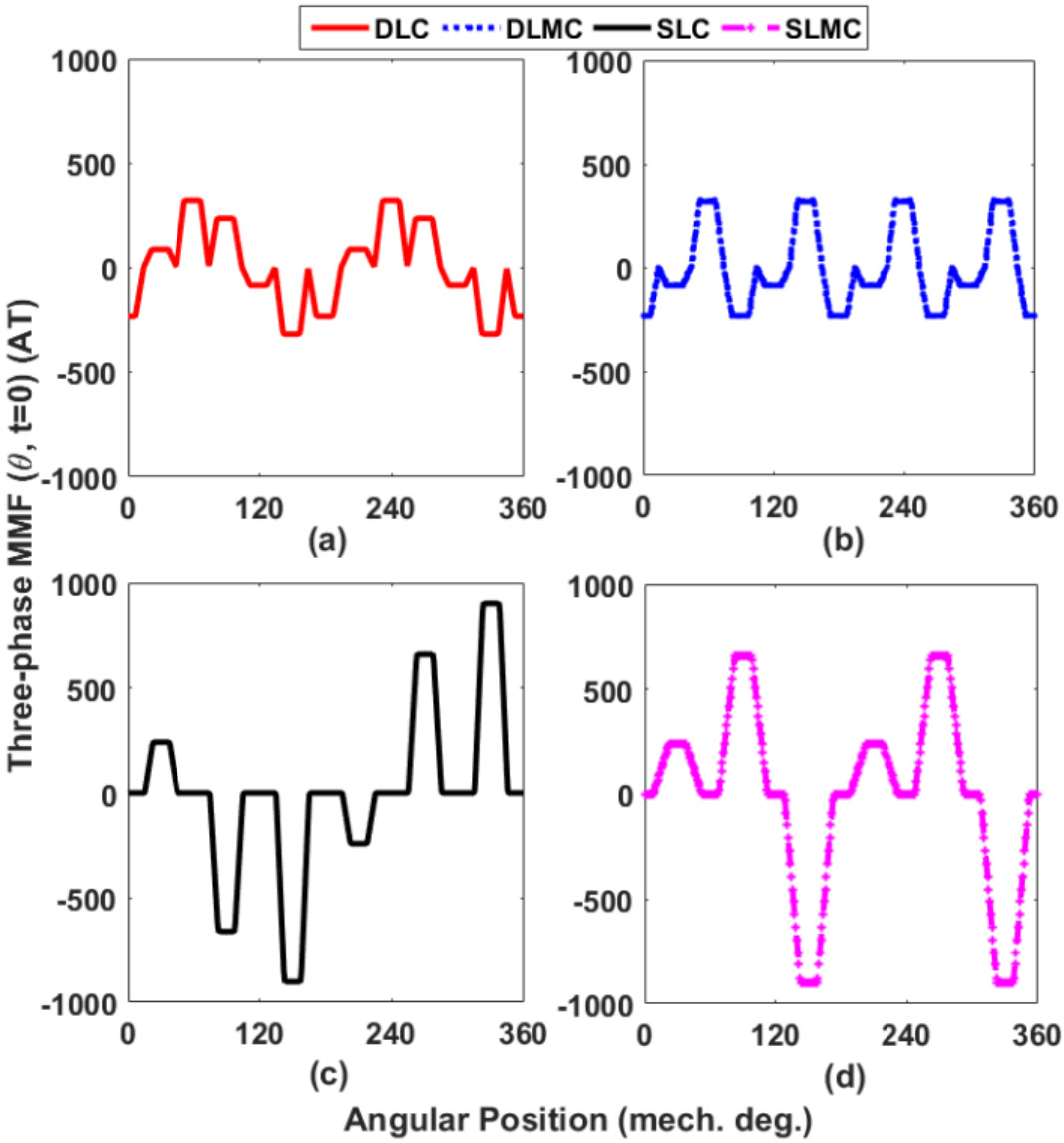

Fig. 6.4 Comparison of the 3-phase MMFs between the 12-slot/8-pole DSRMs at $10A_{rms}$. (a) DLC, (b) DLMC, (c) SLC, and (d) SLMC.

The 3-phase MMF of the single layer machines are shown in the appendix. It can be found from (6.7) to (6.10) that the 10th order harmonic of the DLC and the 4th order harmonic of the DLMC are forward rotating (positive rotating speed). However, the 2nd order harmonic of the DLC and the 8th order harmonic of the DLMC are backward rotating (negative rotating speed). By way of example, it can be found from (6.8) that the rotating speed of the 2nd order harmonic in the DLC is $-\frac{\omega}{n}$, where k=1. Moreover, there are no triplen harmonics in the 3-phase MMF, as for other conventional 3-phase machines with neutral point. Fig. 6.4 shows the comparison of the 3-phase MMFs at t=0 between the DSRMs with both the double and single layer windings and Fig. 6.5 shows their spectra.

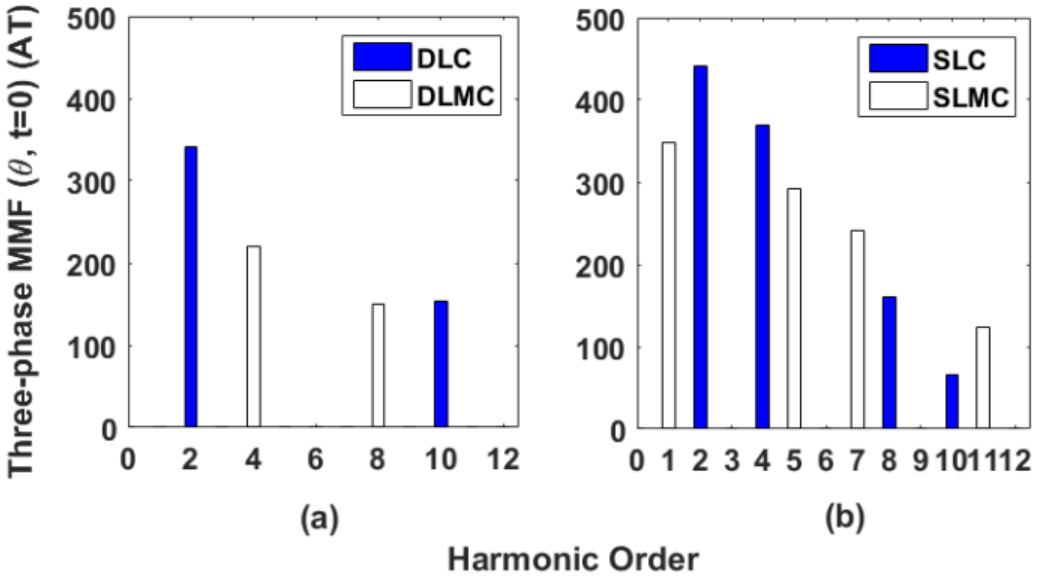

Fig. 6.5 Spectra of the 3-phase MMFs between the 12-slot/8-pole DSRMs at $10A_{rms}$. (a) Double layer, and (b) single layer machines.

6.3 Analysis of Airgap Flux Density

6.3.1 Airgap Permeance

In order to investigate the slotting effect on the air-gap flux density, the doubly slotted airgap is divided into three regions, e.g. the stator slots, the air-gap, and the rotor slots, as shown in Fig. 6.6. As a result, the resultant airgap permeance can be written by (6.11).

$$\Lambda_{resultant}(\theta,t)=\frac{1}{\delta_s(\theta)+\delta_r(\theta,t)+l_g} \tag{6.11}$$

where δ_s and δ_r are additional airgaps due to the stator and rotor slotting effect, respectively, and l_g is the airgap length. In addition, R_{s1} and R_{s2} are the radii of flux path lengths in the stator slot openings, and R_{r1} and R_{r2} are the radii of flux path lengths in the rotor slot openings. The resultant flux path in the stator and rotor slot openings have been derived in [105] and the additional airgap due to the stator and rotor slot openings over $[0,\theta_s]$ and $[0,\theta_r]$ are given by (6.12) and (6.13).

$$\delta_s(\theta)=\begin{cases}0 & 0\le\theta<\frac{1}{2}\theta_s-\frac{1}{2}\beta_s\theta_s\\ \frac{\pi R_{si}}{2}\frac{\sin(\frac{\theta}{2}-\frac{1}{4}\theta_s+\frac{\beta_s\theta_s}{4})\sin(\frac{\beta_s\theta_s}{4}-\frac{\theta}{2}+\frac{1}{4}\theta_s)}{\sin(\frac{\beta_s\theta_s}{4})\cos(\frac{\theta_s}{4}-\frac{\theta}{2})} & \frac{1}{2}\theta_s-\frac{1}{2}\beta_s\theta_s\le\theta<\frac{1}{2}\theta_s+\frac{1}{2}\beta_s\theta_s\\ 0 & \frac{1}{2}\theta_s+\frac{1}{2}\beta_s\theta_s\le\theta<\theta_s\end{cases} \tag{6.12}$$

$$\delta_r(\theta,t=0)=\begin{cases}0 & 0\le\theta<\frac{1}{2}\theta_r-\frac{1}{2}\beta_r\theta_r\\ \frac{\pi R_{ro}}{2}\frac{\sin(\frac{\theta}{2}-\frac{1}{4}\theta_r+\frac{\beta_r\theta_r}{4})\sin(\frac{\beta_r\theta_r}{4}-\frac{\theta}{2}+\frac{1}{4}\theta_r)}{\sin(\frac{\beta_r\theta_r}{4})\cos(\frac{\theta_r}{4}-\frac{\theta}{2})} & \frac{1}{2}\theta_r-\frac{1}{2}\beta_r\theta_r\le\theta<\frac{1}{2}\theta_r+\frac{1}{2}\beta_r\theta_r\\ 0 & \frac{1}{2}\theta_r+\frac{1}{2}\beta_r\theta_r\le\theta<\theta_r\end{cases} \tag{6.13}$$

where R_{si} is the stator inner radius, R_{ro} is the rotor outer radius, θ_r is the rotor pole pitch (45 mech. deg. for the 12-slot/8-pole machines), β_r is the rotor slot opening coefficient which can be found in TABLE 6.1, and θ is the angular position in mech. deg.. Expanding (6.12) and (6.13) using Fourier series analysis over $[0,2\pi]$ gives

$$\begin{aligned}\delta_s(\theta)=&\frac{R_{si}(\pi\beta_s)^2}{72}\\ &+\sum_{k=1}^{+\infty}\left\{-\frac{R_{si}}{24k^2}\left[1+\cos(2\pi k\beta_s)-\frac{1}{\pi k\beta_s}\sin(2\pi k\beta_s)\right]\right\}\cos[6k(2\theta\\ &-\theta_s+\beta_s\theta_s)]\\ &+\sum_{k=1}^{+\infty}\left\{\frac{R_{si}}{24k^2}\left[\frac{1}{\pi k\beta_s}[1-\cos(2\pi k\beta_s)]-\sin(2\pi k\beta_s)\right]\right\}\sin[6k(2\theta\\ &-\theta_s+\beta_s\theta_s)]\end{aligned} \tag{6.14}$$

$$\delta_r(\theta,t) = \frac{R_{ro}(\pi\beta_r)^2}{48} + \sum_{k=1}^{+\infty}\left\{-\frac{R_{ro}}{16k^2}\left[1+\cos(2\pi k\beta_r)-\frac{1}{\pi k\beta_r}\sin(2\pi k\beta_r)\right]\right\}\cos[4k(2\theta - \theta_r + \beta_r\theta_r - 2t)] + \sum_{k=1}^{+\infty}\left\{\frac{R_{ro}}{16k^2}\left[\frac{1}{\pi k\beta_r}[1-\cos(2\pi k\beta_r)]-\sin(2\pi k\beta_r)\right]\right\}\sin[4k(2\theta - \theta_r + \beta_r\theta_r - 2t)] \tag{6.15}$$

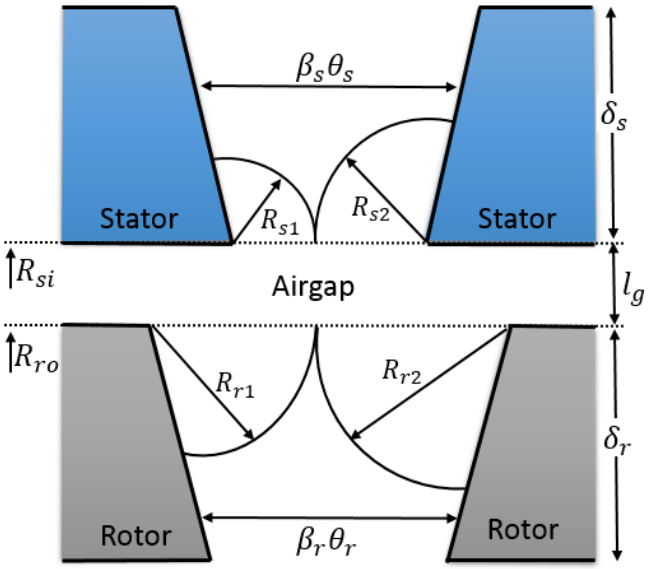

Fig. 6.6 Diagram for illustration of reciprocal of resultant airgap permeance with idealized flux path in slot openings.

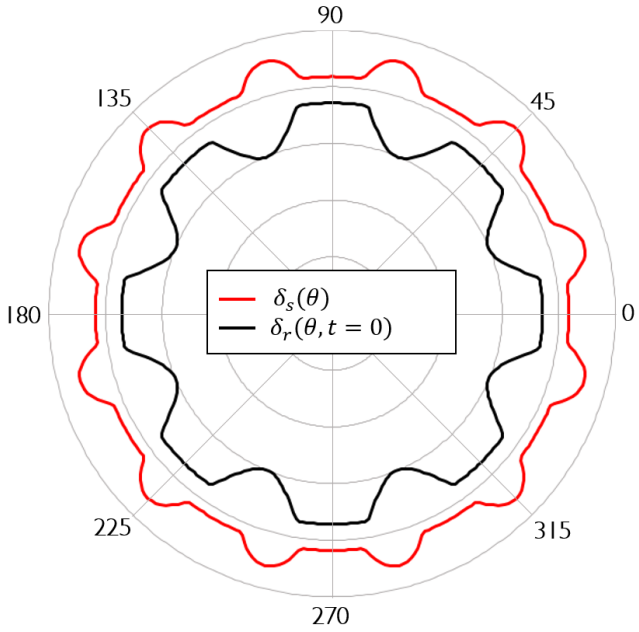

Fig. 6.7 Additional airgap δ due to stator and rotor slotting effect.

Accordingly, the additional airgaps due to the stator and rotor slotting effects and their spectra have been illustrated in Fig. 6.7 and Fig. 6.8, respectively. Besides the DC component (1mm), it is apparent that with a slot number of 12, the harmonic orders of the stator side airgap are 12k, where k=1, 2, 3, … Similarly, the harmonic orders of the rotor side airgap for a 8-pole machine are 8k, where k=1, 2, 3,… Substituting (6.14) and (6.15) into (6.11), the resultant airgap permeance can be obtained as shown in Fig. 6.9. It can be found that the periodicity of the resultant airgap permeance in one mechanical period is 4, also, it is indeed the greatest common divisor of the slot and pole numbers. The harmonic orders of the resultant airgap permeance are 4k where k=1, 2, 3, …, as shown in Fig. 6.9 (b).

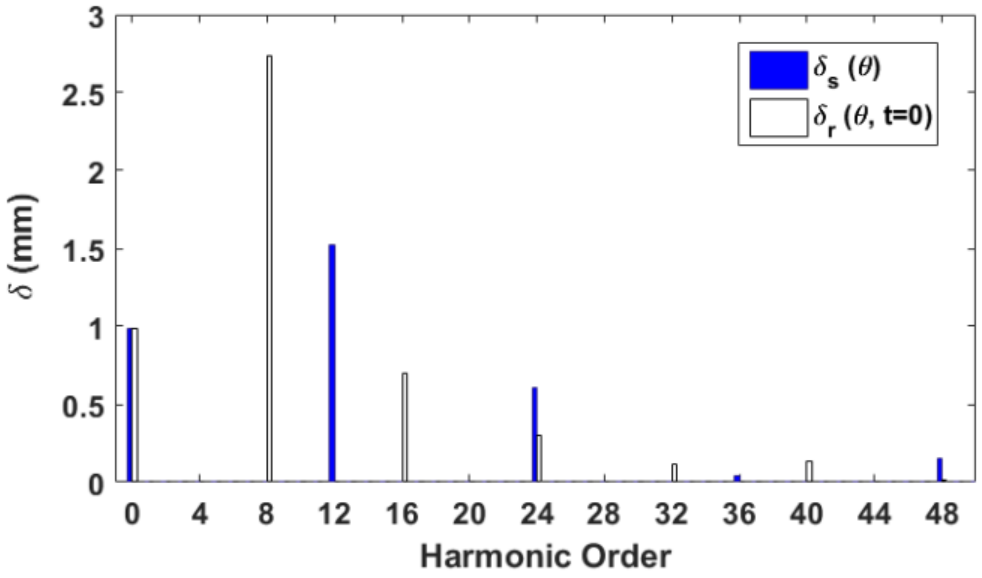

Fig. 6.8 Spectra of the additional airgap δ due to the stator and rotor slotting effect.

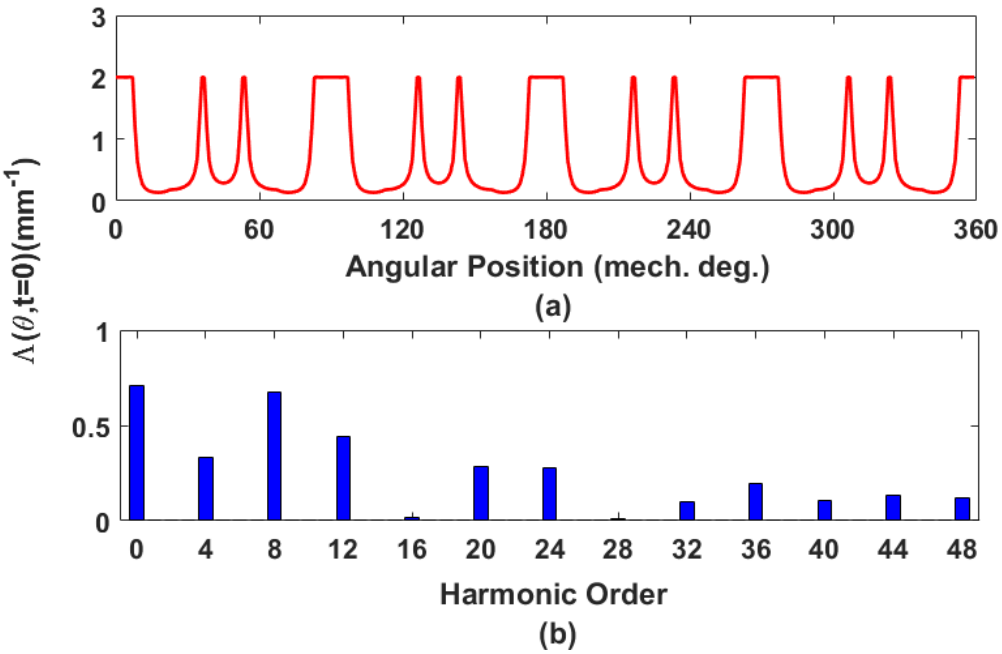

Fig. 6.9 Airgap permeance of the 12-slot/8-pole DSRMs. (a) Airgap permeance $\Lambda\ (\theta, t = 0)$, and (b) spectra.

6.3.2 AIRGAP FLUX DENSITY

With the assumption of infinite permeability in the stator and rotor iron cores, the radial airgap flux density can be defined as

$$B_r\,(\theta,t) = \mu_0 MMF(\theta,t)\Lambda\,(\theta,t) \tag{6.16}$$

where μ_0 is the permeability of free space and Λ is the airgap permeance. It is worth mentioning that the analytical model of MMF in section 6.2 only considers the excitation of the armature coils. Hence, only the stator scalar magnetic potential is defined but the rotor scalar magnetic potential is assumed to be zero. Indeed, this approach can be used for a non-salient rotor case. However, due to the doubly salient structure in the DSRMs, the MMF has to be modified in order to take the non-zero rotor scalar magnetic potential into account. According to Gauss's law for magnetism which states that $div\vec{B} = 0$, a coefficient q_c can be defined according to [105] as

$$q_c(t) = -\frac{\int_0^{2\pi} MMF_a(\theta)\Lambda\,(\theta,t)\,d\theta}{\int_0^{2\pi} \Lambda\,(\theta,t)\,d\theta} \tag{6.17}$$

Hence, the MMF can be modified by adding the coefficient q_c:

$$MMF_{modified,a}(\theta,t) = MMF_a(\theta,t) + q_c(t) \tag{6.18}$$

In addition, the coefficient q_c is calculated as zero for conventional winding machines, regardless of the single or double layer winding structure. This is because that their DC component of $MMF_a(\theta)\Lambda\,(\theta,t)$ equals zero, which is directly proportional to $\int_0^{2\pi} MMF_a(\theta)\Lambda\,(\theta,t)\,d\theta$. Hence, the MMF of the conventional DSRMs can still be calculated using the analytical modelling in section 6.2. However, this is not the case for the mutually-coupled DSRMs, as will be detailed in the following sections. Hence, it can be concluded that the coefficient q_c is only presented in the machine with mutually-coupled winding configurations due to their unipolar MMF waveforms.

6.3.2.1 SINGLE-PHASE AIRGAP FLUX DENSITY

With the modified MMF, the airgap flux density can be obtained according to (6.16). The comparison of the single-phase airgap flux densities of the DLC and DLMC between 2D FEA and analytical modelling is shown in Fig. 6.10 (a) and (b), respectively. The phase A is supplied with a 10A DC current. Fig. 6.11 shows the spectra. It is apparent that the analytical results match well with the FE results for both the DLC and DLMC. Due to the doubled effective rotor pole number, the DLMC presents doubled periodicity than that of the DLC in the single-phase airgap flux density. It can be found that the harmonic orders of the DLC are 2, 6, 10, …, ($4k$-2), while they are 4, 8, 12, …, $4k$ for the DLMC, where k=1, 2, 3, … Moreover, the harmonic orders of the single-phase airgap flux density are the same as that of the single-phase MMF which have been calculated in TABLE 6.3 and TABLE 6.4.

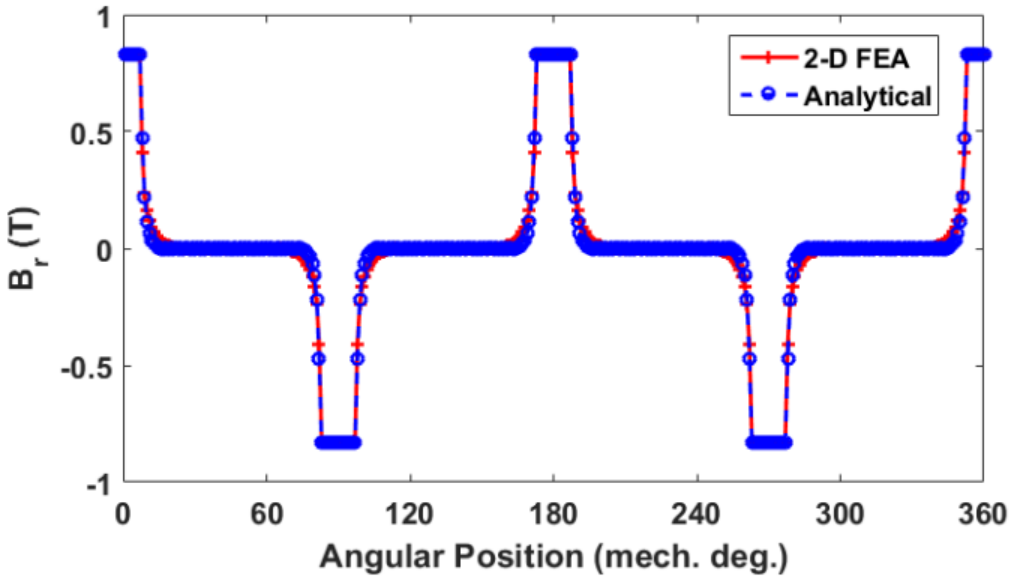

(a)

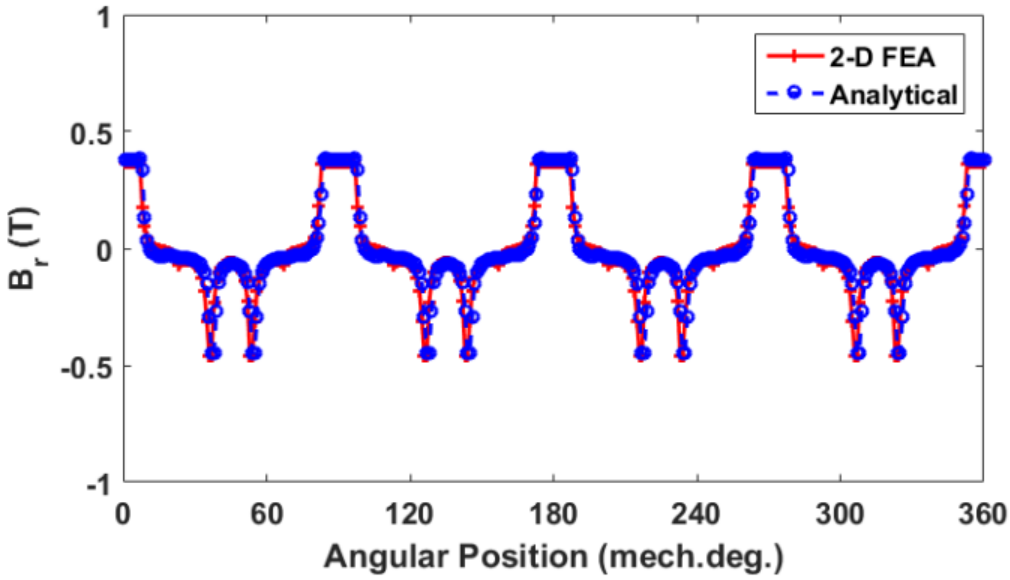

(b)

Fig. 6.10 Comparison of the single-phase airgap flux density B_r between 2D FEA and analytical modelling. Phase A is supplied with a 10A DC current. (a) DLC, and (b) DLMC.

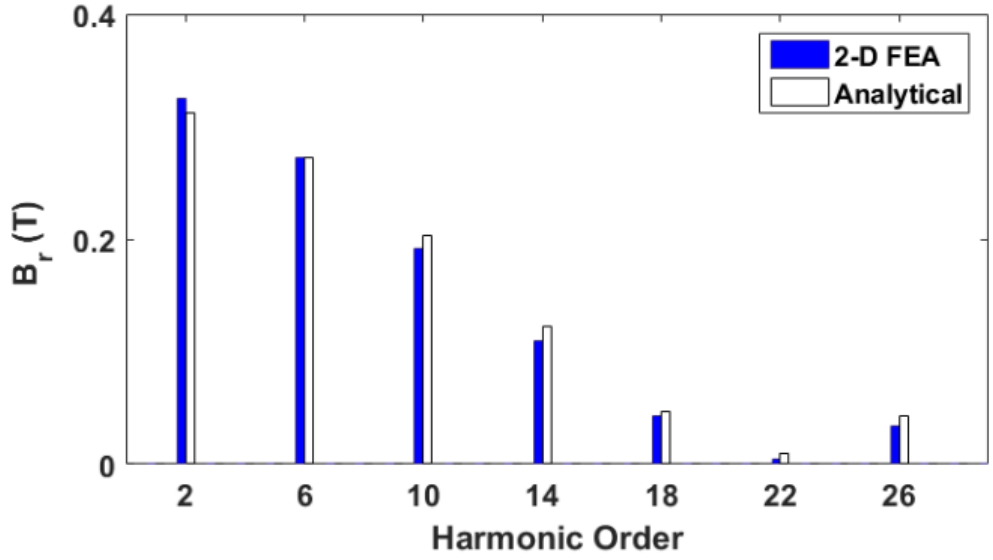

(a)

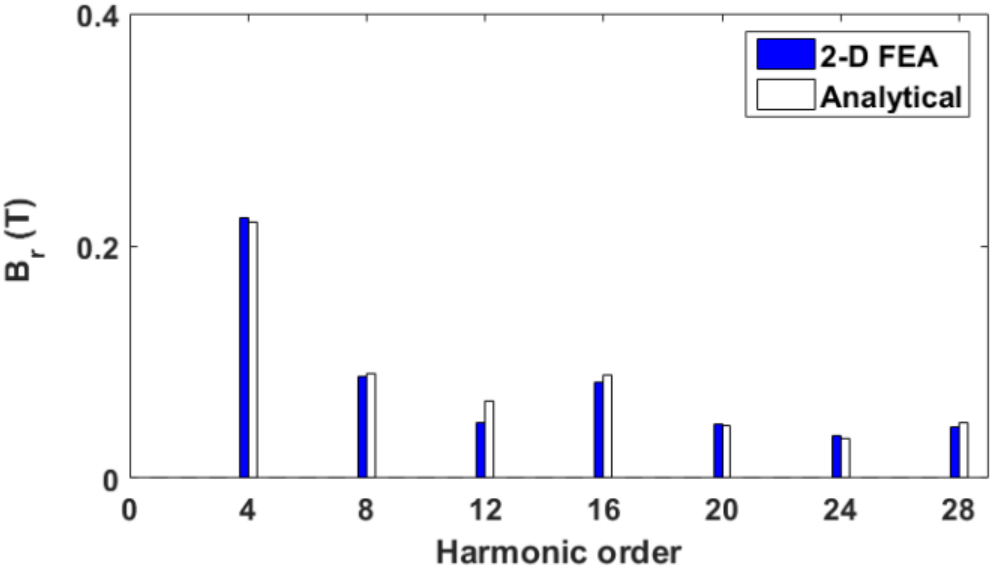

(b)

Fig. 6.11 Spectra of the single-phase airgap flux density B_r between 2D FEA and analytical modelling. Phase A is supplied with a 10A DC current. (a) DLC, and (b) DLMC.

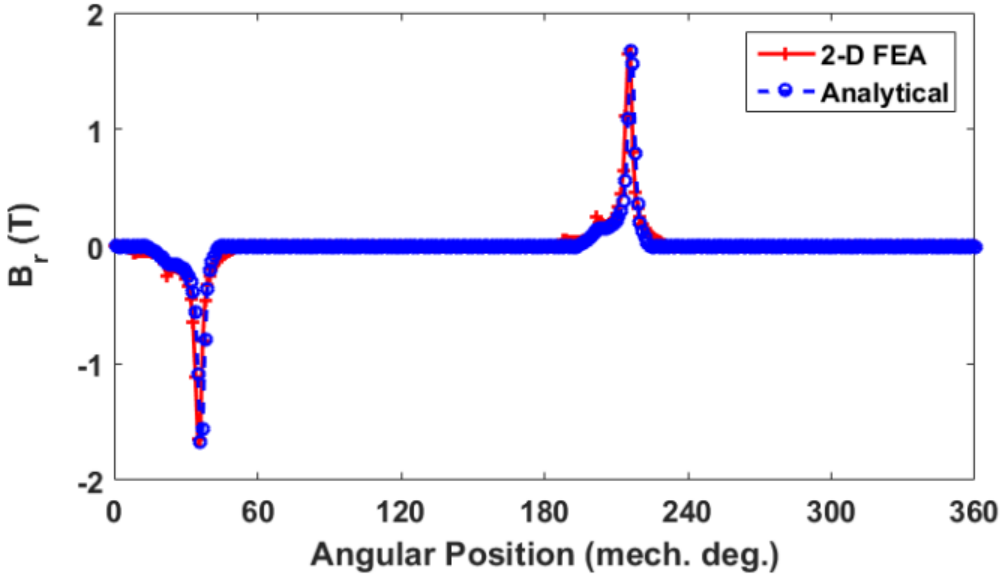

(a)

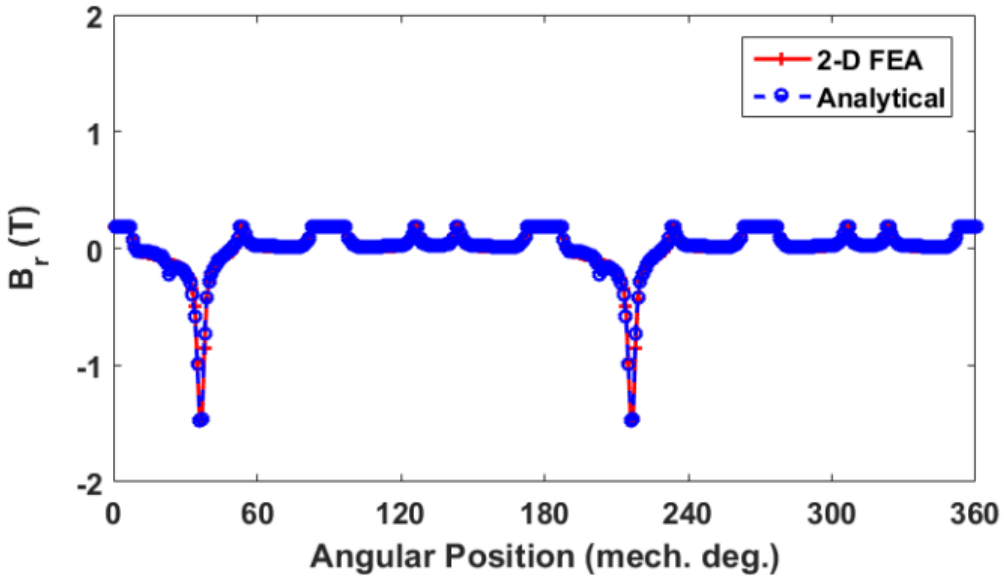

(b)

Fig. 6.12 Comparison of the single-phase airgap flux density B_r between 2D FEA and analytical modelling. Phase A is supplied with a 10A DC current. (a) SLC, and (b) SLMC.

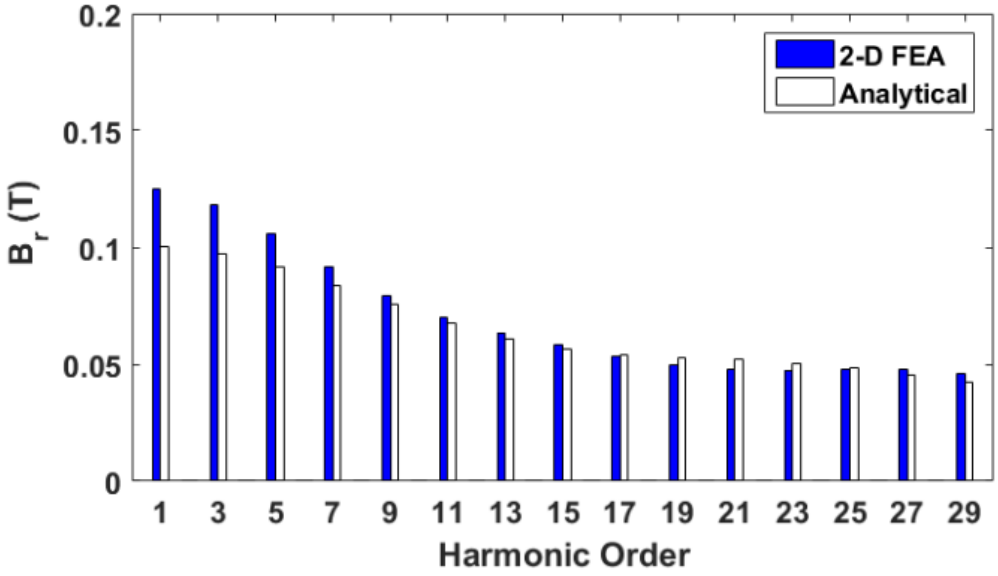

(a)

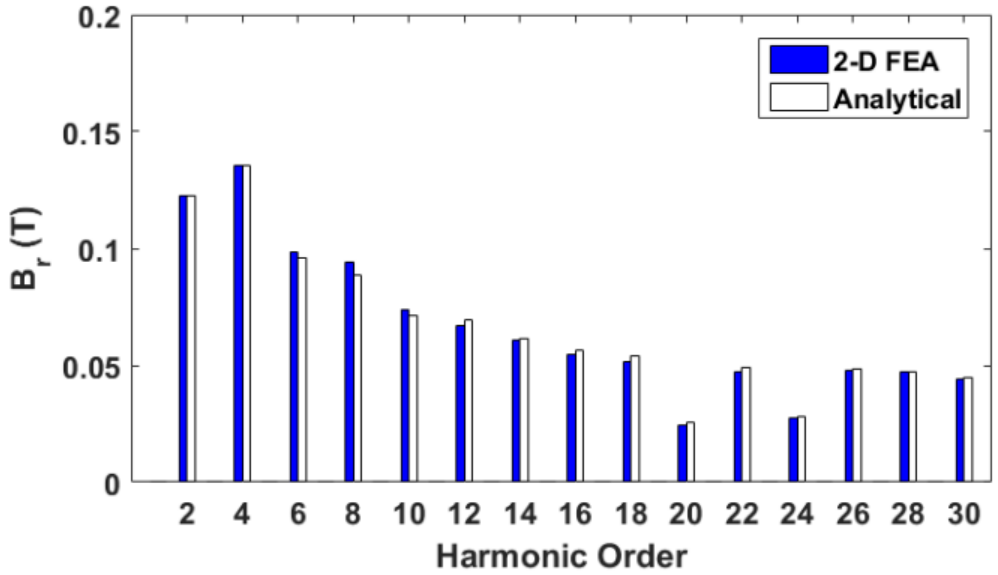

(b)

Fig. 6.13 Spectra of the single-phase airgap flux density B_r between 2D FEA and analytical modelling. Phase A is supplied with a 10A DC current. (a) SLC, and (b) SLMC.

6.3.2.2 3-PHASE AIRGAP FLUX DENSITY

The 3-phase airgap flux density can be obtained by the same approach as for the single-phase airgap flux density. Fig. 6.14 and Fig. 6.15 compare the 2D FEA and analytical 3-phase airgap flux densities and their spectra for the double layer DSRMs. The phase current is $10A_{rms}$. For completeness, the 3-phase airgap flux density and the spectra of the single layer DSRMs are shown in Fig. 6.16 and Fig. 6.17. It can be found that the 3-phase airgap flux

densities have the same harmonic orders as the single-phase airgap flux density for both the double and single layer DSRMs. It is worth noting that the harmonics in the 3-phase airgap flux density contribute directly (whether positively or negatively) to the on-load torque, which will be detailed later.

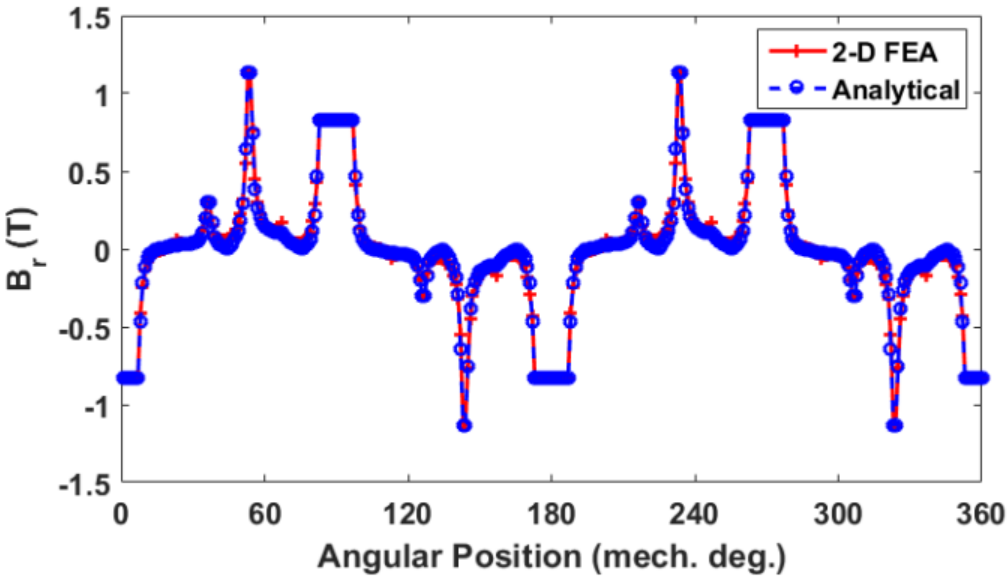

(a)

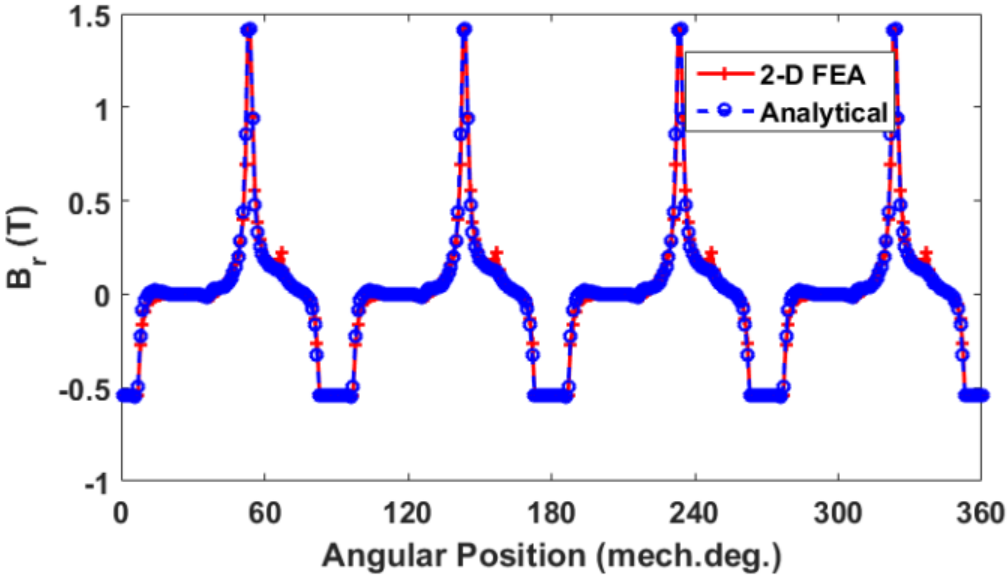

(b)

Fig. 6.14 Comparison of the 3-phase airgap flux density B_r between 2D FEA and analytical modelling at $10A_{rms}$. (a) DLC, and (b) DLMC.

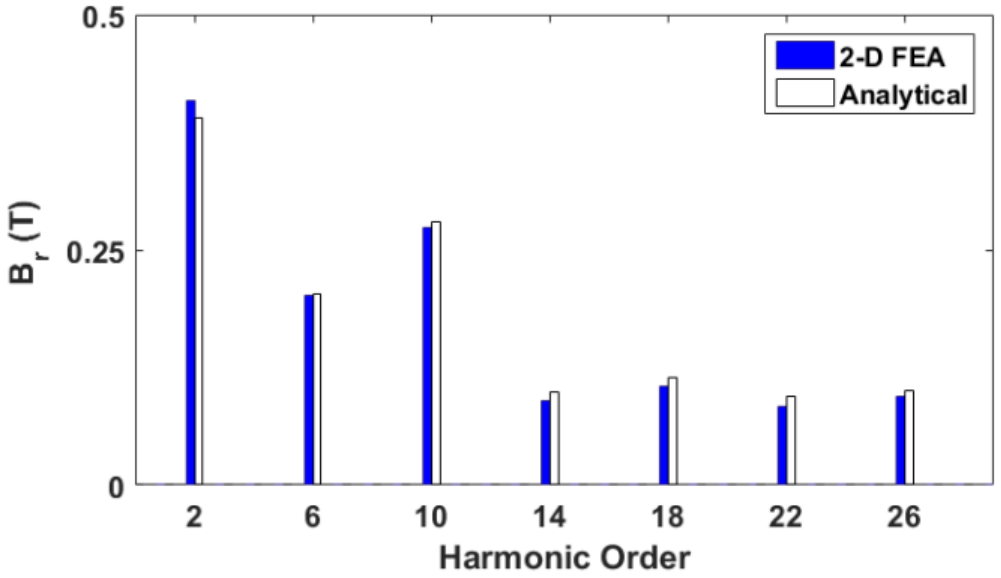

(a)

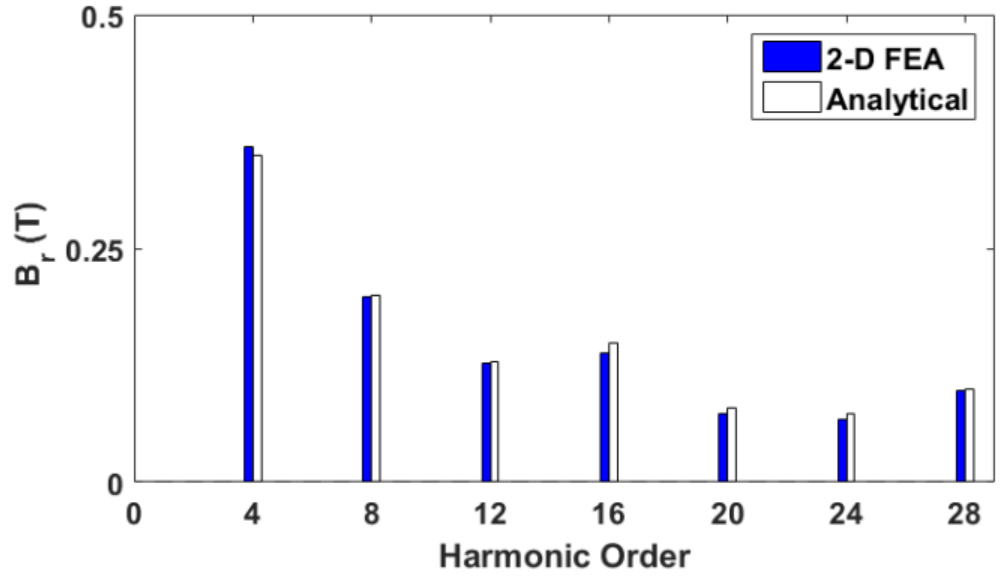

(b)

Fig. 6.15 Spectra of the 3-phase airgap flux density B_r between 2D FEA and analytical modelling at $10A_{rms}$. (a) DLC, and (b) DLMC.

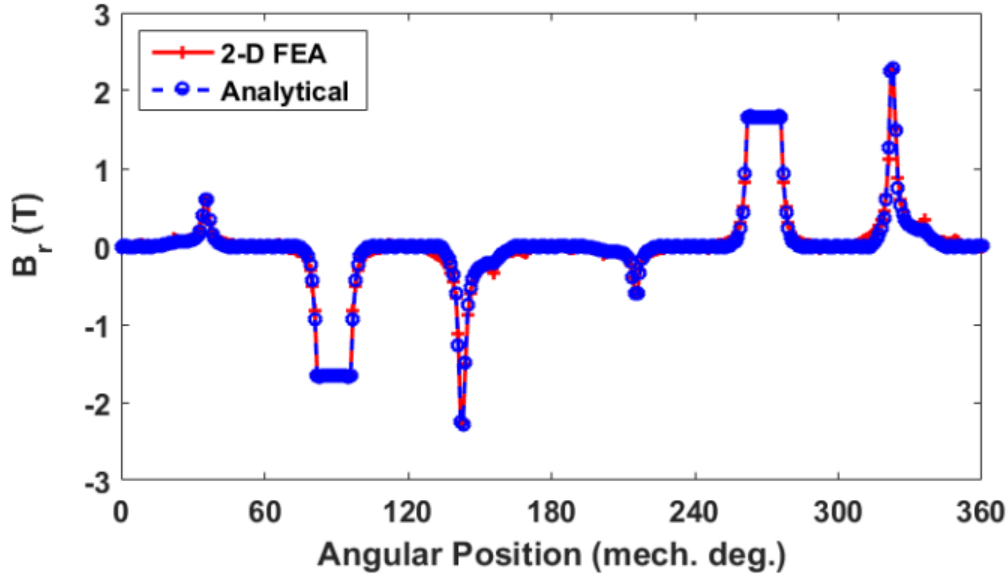

(a)

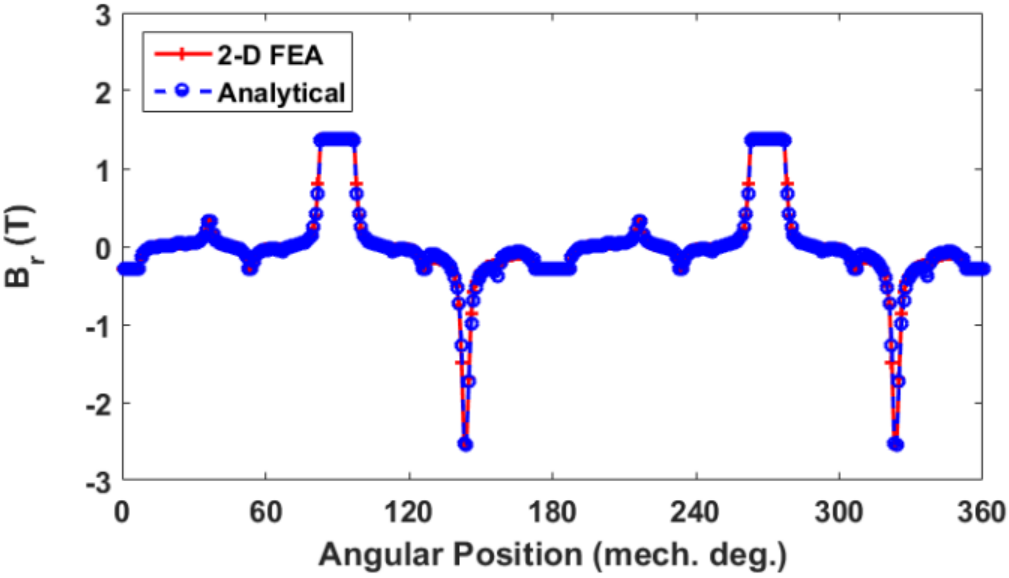

(b)

Fig. 6.16 Comparison of the 3-phase airgap flux density B_r between 2D FEA and analytical modelling at $10A_{rms}$. (a) SLC, and (b) SLMC.

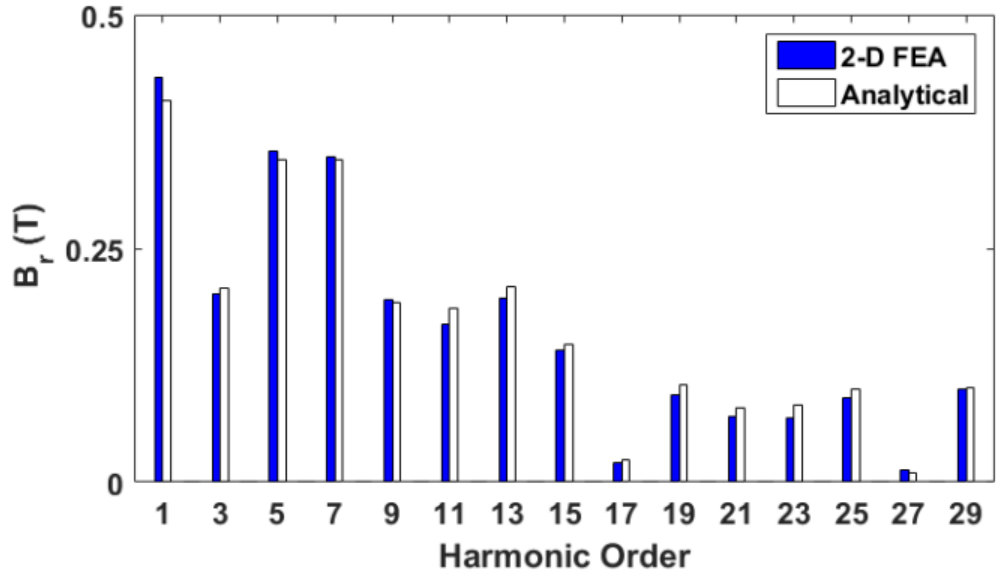

(a)

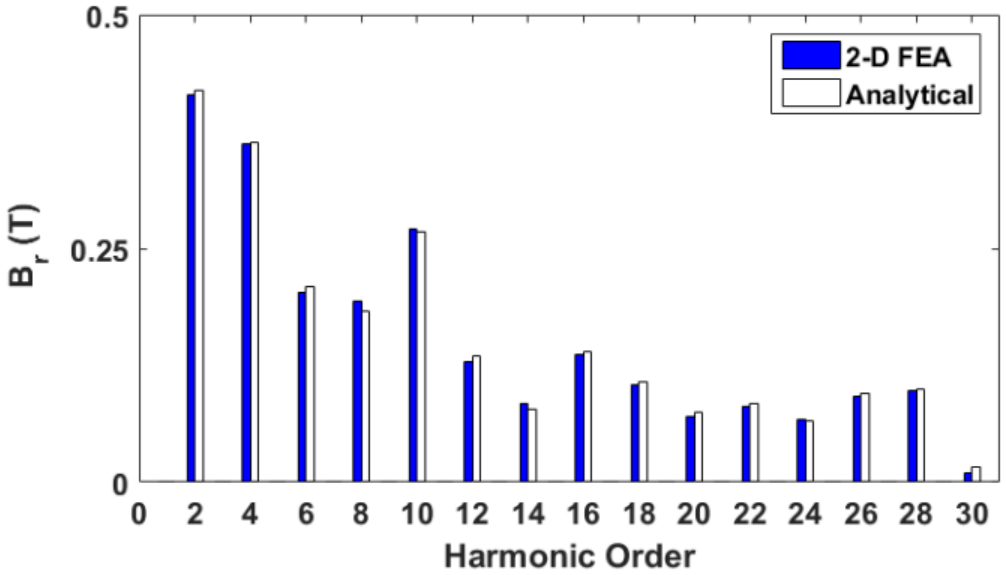

(b)

Fig. 6.17 Spectra of the 3-phase airgap flux density B_r between 2D FEA and analytical modelling at $10A_{rms}$. (a) SLC, and (b) SLMC.

6.4 CONTRIBUTION OF AIRGAP FLUX DENSITY HARMONICS TO ON-LOAD TORQUE

In this chapter, the Maxwell stress tensor is used to investigate the contribution of the airgap flux density harmonics to on-load torque, which can be expressed as

$$T(t) = \frac{L}{\mu_0}\int_0^{2\pi} r^2 B_r B_t \, d\theta \tag{6.19}$$

where r is the airgap radius, L is the active length, and θ is the rotor position in mechanical degree. The radial and tangential airgap flux densities B_r and B_t can be expressed using Fourier series analysis as

$$\begin{cases} B_r(\theta,t) = \sum_{i}^{+\infty} B_{ri}\cos[i\theta - \theta_{ri}(t)] \\ B_t(\theta,t) = \sum_{j}^{+\infty} B_{tj}\cos[j\theta - \theta_{tj}(t)] \end{cases} \tag{6.20}$$

where B_{ri} and B_{tj} are the i^{th} and j^{th} order harmonics of B_r and B_t, respectively. In addition, θ_{ri} and θ_{tj} are the corresponding phases of each harmonic. Substituting (6.20) into (6.19), the instantaneous torque $T_{i,j}(t)$ generated by the i^{th} radial and j^{th} tangential airgap flux density harmonics can be given by

$$T_{i,j}(t) = \frac{Lr^2}{\mu_0}\int_0^{2\pi}\left\{\sum_{i}^{+\infty}\sum_{j}^{+\infty} B_{ri}B_{tj}\cos[i\theta - \theta_{ri}(t)]\cos[j\theta - \theta_{tj}(t)]\right\} d\theta \tag{6.21}$$

It is found that the instantaneous torque $T_{i,j}(t)$ can only be produced when $i = j$. It refers to the fact that only the same harmonic order of the radial and tangential airgap flux densities can contribute to the torque. It is worth mentioning that only the radial airgap flux density is calculated by analytical modelling in this chapter, and the accuracy of MMF modelling can be validated by the comparison between analytical and 2D FEA radial airgap flux densities. The tangential airgap flux density is obtained by 2D FEA directly. Although the latter can also be calculated by analytical means such as subdomain methods in [100] or conformal mapping

using complex airgap permeance model in [107], these methods are quite complicated to implement due to the doubly salient structure of the investigated machines and hence are not the main focus of this chapter. Accordingly, the instantaneous torque can be rewritten as

$$T(t) = \sum_{i}^{+\infty} T_i(t) = \frac{\pi L r^2}{\mu_0} \sum_{i}^{+\infty} B_{ri} B_{ti} \cos[\theta_{ri}(t) - \theta_{ti}(t)] \tag{6.22}$$

Based on (6.22), the on-load torque can be obtained by summing the instantaneous torque $T_i(t)$. In addition, the positive or negative contribution to average torque can be calculated when instantaneous $T_i(t)$ and $T(t)$ are averaged. By way of example, $T_i(t)$ of the DLC and DLMC have been shown in Fig. 6.18, which account up to the 50th order harmonic in the airgap flux density. In addition, the resultant torque calculated by (6.22) has been compared with that obtained by direct 2D FEA and a good agreement can be observed.

In order to investigate the contribution of each harmonic in the airgap flux density to the on-load torque, the two most dominant harmonics in the radial airgap flux density (as shown in Fig. 6.15 and Fig. 6.17) have been selected. For example, the 2nd and 10th order harmonics are the two most dominant harmonics for the DLC as shown in Fig. 6.15, while the 4th and 8th order harmonics are selected for the DLMC. It is apparent in Fig. 6.18 that the 10th order harmonic in the airgap flux density of the DLC produces positive torque. However, the 2nd order harmonic produces negative torque. For the DLMC, the 4th and 8th order harmonics produce positive and negative torques, respectively. Similarly, the on-load torque produced by the two most dominant harmonics in the radial airgap flux density of the SLC and SLMC has been shown in Fig. 6.19 (a) and (b), respectively.

When looking at the rotating speed of the MMF shown in (6.8) and (6.10), the 10th order harmonic in the DLC and the 4th order harmonic in the DLMC have positive rotating speed. However, the 2nd order harmonic in the DLC and the 8th order harmonic in the DLMC have negative rotating speed. As a result, it can be concluded that the dominant MMF harmonics with positive rotating speed (forward rotating) will produce positive torque. However, the dominant MMF harmonics with backward rotating will produce negative torque. The dominant harmonic orders in MMF account for up to the 12th order harmonics in both single and double layer machines. Also, it is worth mentioning that the dominant harmonics are the ones that contribute more than 5% of the resultant average torque.

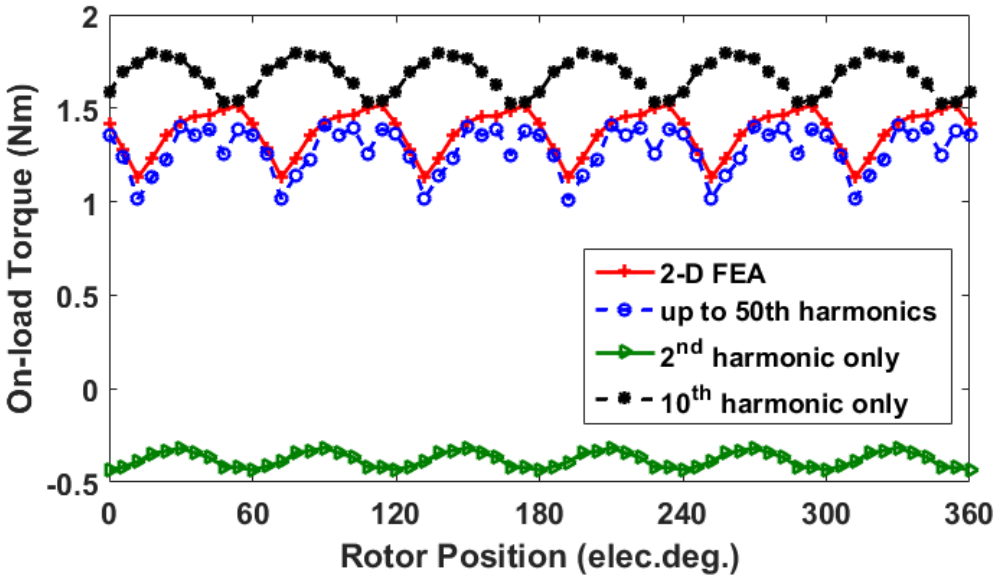

(a)

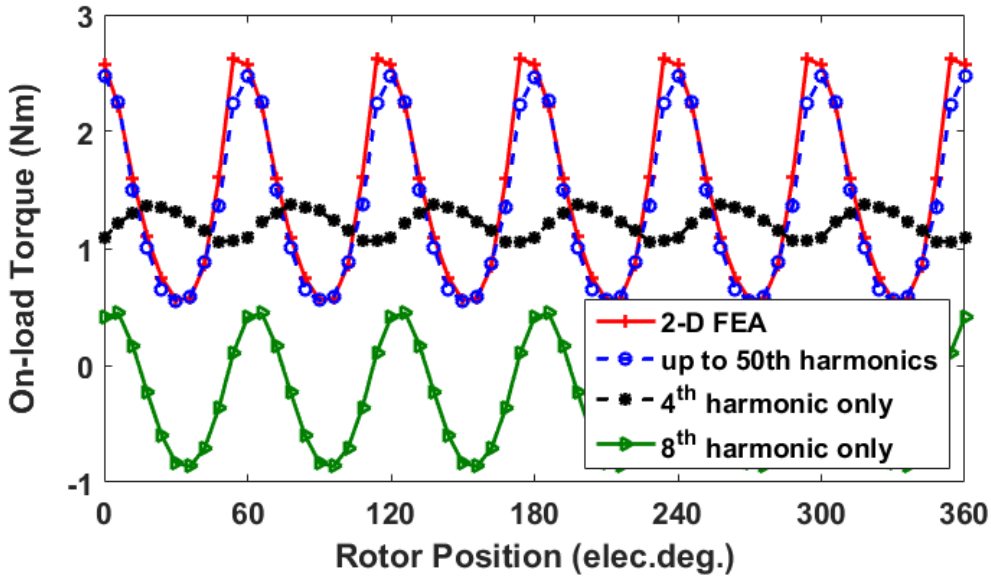

(b)

Fig. 6.18 Comparison of torques at $10A_{rms}$. (a) DLC, and (b) DLMC.

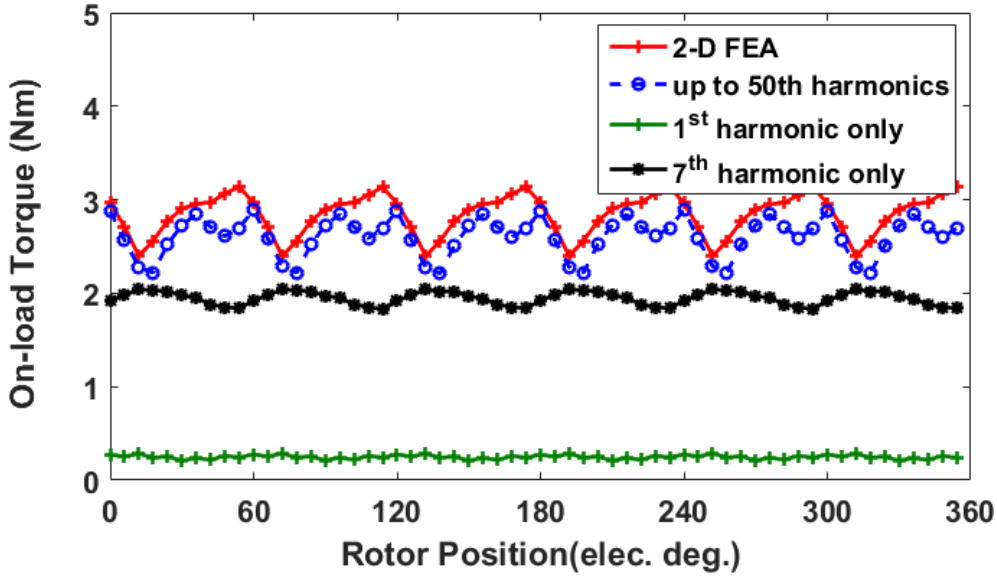

(a)

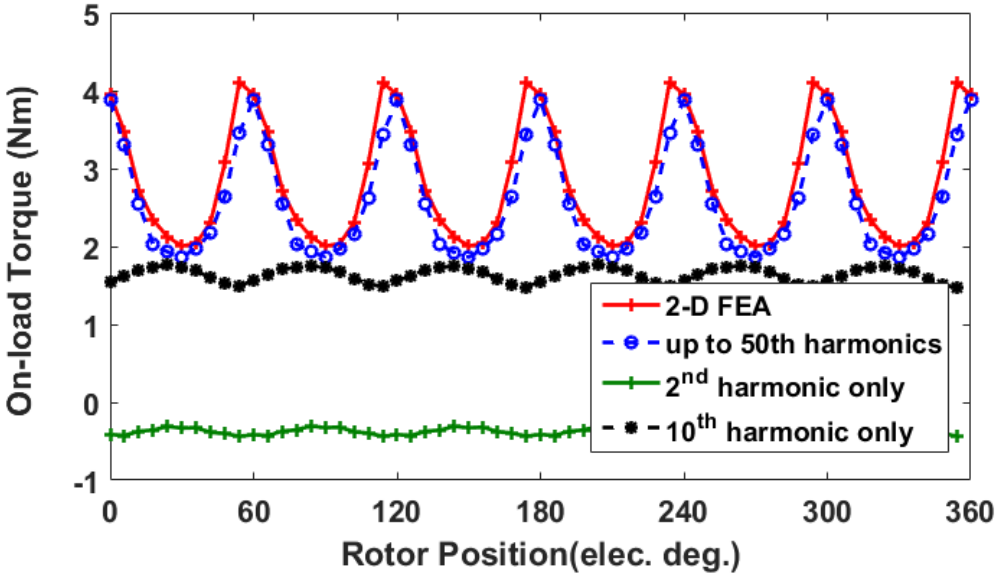

(b)

Fig. 6.19 Comparison of torques at $10A_{rms}$. (a) SLC, and (b) SLMC.

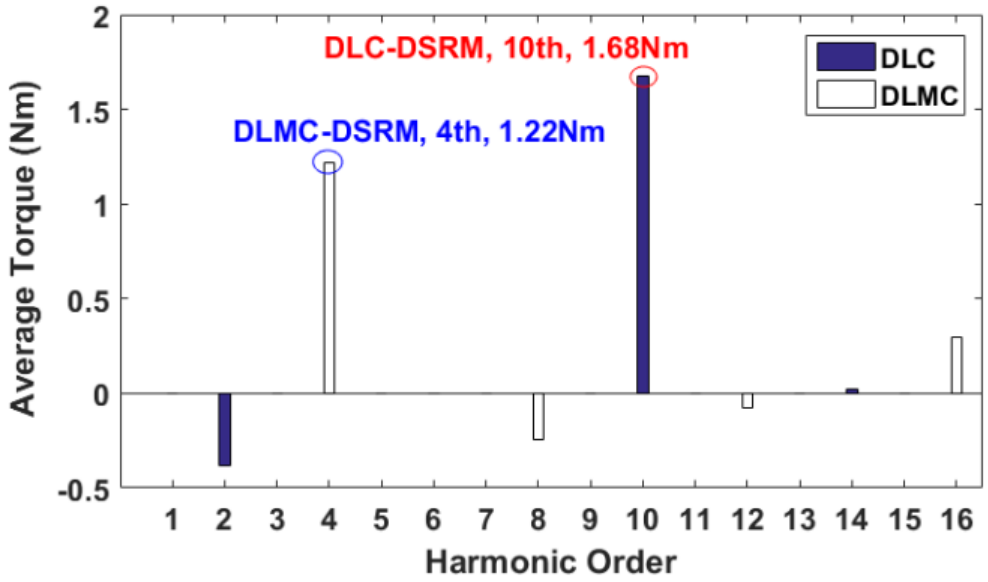

(a)

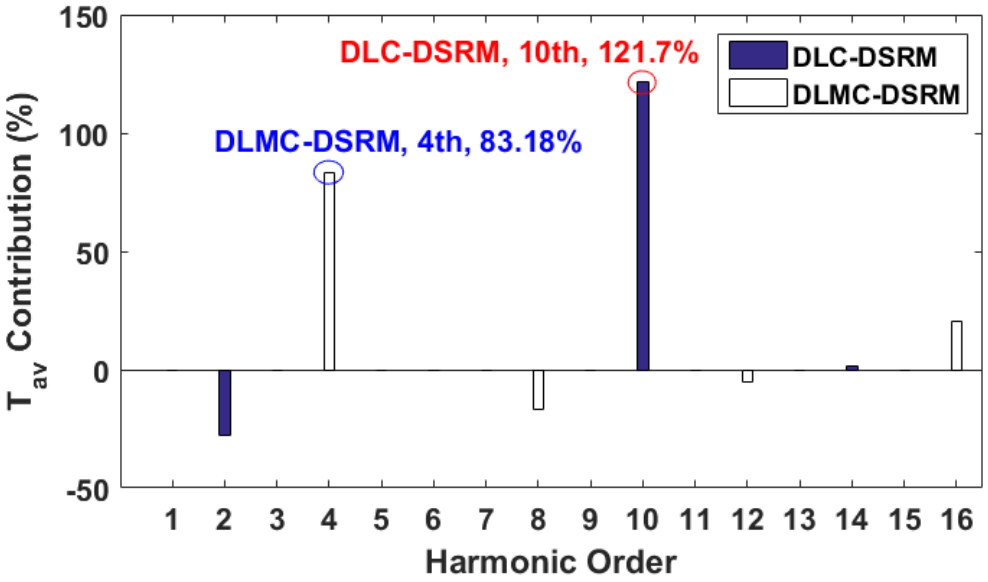

(b)

Fig. 6.20 (a) Average torque and (b) contribution to average torque by airgap flux density harmonics for the DLC and DLMC at $10A_{rms}$.

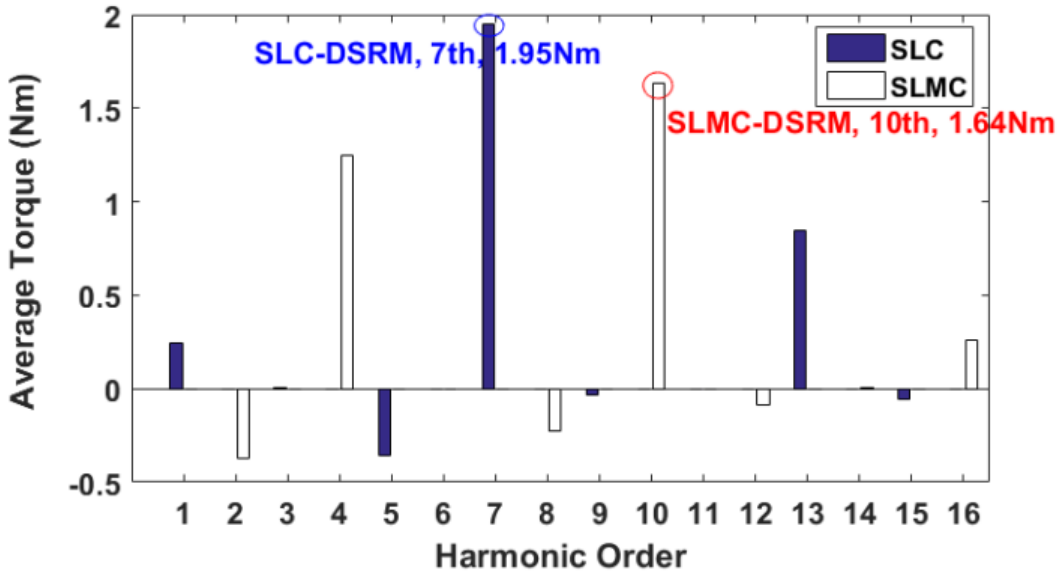

(a)

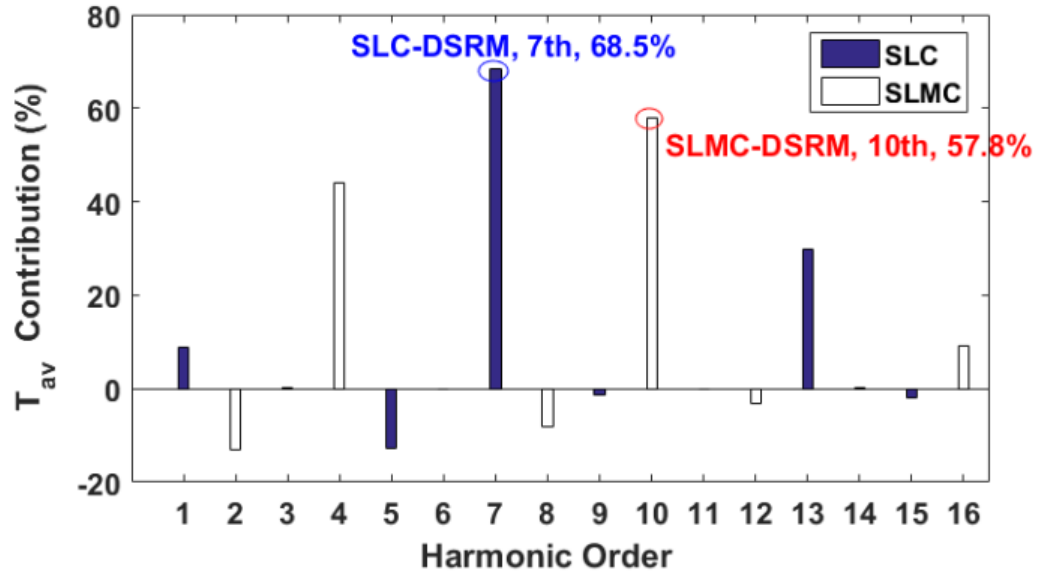

(b)

Fig. 6.21 (a) Average torque and (b) contribution to average torque by airgap flux density harmonics for the SLC and SLMC at $10A_{rms}$.

The instantaneous torque generated by the i^{th} order airgap flux density harmonics, where $i \leq 50$ has also been calculated. Moreover, the average torque produced by different airgap flux density harmonics of both the double and single layer DSRMs has been obtained as shown in Fig. 6.20 and Fig. 6.21, respectively. For clarity, the contribution of the airgap flux density harmonics to the average torque (>5%) and the torque ripple has been summarized in TABLE 6.5.

In order to obtain the contribution of the i^{th} order harmonic to the torque ripple, the peak to peak value of resultant torque ($\Delta T_{result(without\ i^{th})}$) has been firstly calculated without the i^{th} order harmonic in the airgap field. Then, the contribution of the i^{th} order harmonic to torque ripple can be given by

$$T_{rc} = \frac{\Delta T_{result} - \Delta T_{result(without\ i^{th})}}{\Delta T_{result}} \times 100\% \tag{6.23}$$

where ΔT_{result} is the difference between the maximum and minimum resultant torque.

TABLE 6.5 CONTRIBUTION OF AIRGAP FIELD HARMONICS TO AVERAGE TORQUE AND TORQUE RIPPE

Winding configuration	Harmonic order	Contribution to average torque (%)	Contribution to torque ripple (%)
DLC	2	-27.5	-3.02
	10	121.7	-45.73
DLMC	4	83.2	-11.93
	8	-16.9	53.19
	12	-5.4	23.71
	16	20.2	0.24
	24	7.4	2.53
SLC	1	8.7	2.16
	5	-12.6	-18.73
	7	68.5	-15.27
	13	29.7	-20.75
SLMC	2	-13.2	-4.36
	4	44.1	-9.41
	8	-8.1	39.16
	10	57.8	-8.36
	16	9.12	0.78

It is found that the 10th order harmonic in the airgap flux density has the highest contribution (121.7%) to the average torque and contributes -45.73% to the torque ripple in the DLC. However, the 2nd order harmonic contributes -27.5% to the average torque. This means that the 10th order harmonic not only contributes to positive average torque but also has positive

influence on the mitigation of the torque ripple. However, the 2nd order harmonic has negative influence on the average torque.

For the DLMC, the 4th order harmonic has the highest contribution (83.18%) to the average torque and while the 8th and 12th order harmonics generate negative average torque. For the single layer machines, the 7th order harmonic in the SLC has the highest contribution (68.5%) to the average torque while the 10th order harmonic in the SLMC contributes the most to the average torque (57.8%). Furthermore, it can be found that the harmonic order which has the most significant contribution to positive average torque can also reduce the resultant torque ripple, regardless of the winding configurations.

6.5 CONCLUSION

By using simple analytical modelling for 3-phase, 12-slot/8-pole DSRMs, this chapter achieves a better understanding of the different torque production mechanisms between single/double layer, conventional/mutually-coupled winding configurations. According to the MMF model, it is found that the working harmonic orders of the mutually-coupled windings are doubled compared with that of the conventional windings. In addition, the harmonic orders of the double layer machines are also doubled compared with that of the single layer ones.

It is also found that the dominant MMF harmonics with positive rotating speed (forward rotating) produce positive torque. However, the dominant MMF harmonics with backward rotating produce negative torque. TABLE 6.6 summarizes the harmonic orders in MMF_a and airgap flux density, as well as the dominant harmonics which contribute to positive (T_{AV}+) and negative (T_{AV}-) average torque. Based on the results, the future work would be the torque capability enhancement by reducing the MMF harmonics which contribute to negative torque through advanced control strategies such as harmonic current injection.

TABLE 6.6 SUMMARY OF HARMONIC ORDERS IN MMF AND AIRGAP FLUX DENSITY, AND THEIR CONTRIBUTION TO AVERAGE TORQUE

Winding configuration	MMF_a	Airgap flux density	$T_{AV}+$	$T_{AV}-$
DLC	$4k$-2	$4k$-2	10	2
DLMC	$4k$	$4k$	4	8
SLC	$2k$-1	$2k$-1	7	5
SLMC	$2k$	$2k$	10	2

Chapter 7. CONCLUSION AND FUTURE WORK

7.1 CONCLUSION

In this thesis, electromagnetic performances of the 3-phase reluctance machines, both switched reluctance and synchronous reluctance machines (SRMs and SynRMs), have been investigated. These machines can have different winding configurations (double/single layer conventional and mutually-coupled, as well as fully-pitched) and also machine topologies (modular and non-modular stators). They can also be supplied with different excitation methods (rectangular wave and sinewave). A general conclusion can be given in detail based on the findings in each chapter.

In order to improve the machine performance, two novel 12-slot/8-pole machines with single layer conventional and single layer mutually-coupled winding configurations have been proposed on the basis of double layer conventional and mutually-coupled machines, respectively. With rectangular wave excitation, the proposed single layer SRMs can have better torque performance than their double layer counterparts without heavy magnetic saturation. In addition, the influence of unipolar and bipolar rectangular wave excitations with different conduction angles on the machine performances has been investigated and compared among different SRMs. As a result, the most appropriate conduction angle has been obtained for machines with different winding configurations at variable current levels. By way of example, the single layer conventional SRM can achieve its highest average torque with unipolar 120° elec. conduction at low current level. However, at high current level, the higher average torque is obtained by unipolar 180° elec. conduction. While bipolar 180° elec. conduction is the most appropriate one for single layer mutually-coupled SRM to generate a higher average torque and higher efficiency while with lower torque ripple.

Adopted by these two windings (single layer conventional and mutually-coupled), several novel modular SRMs have been proposed with different slot/pole number combinations and flux gap widths, in order to achieve further improvement of the machine performance, simpler manufacturing process and better fault tolerant capability. Compare with non-modular 12-slot/8-pole SRMs, the modular SRMs with higher rotor pole number than stator slot number (e.g. 12-slot/14-pole) can achieve similar average torque at the same copper loss (phase current) but with lower torque ripple, lower iron loss, and lower radial force, hence, it has the potential to generate lower vibration and acoustic noise.

The investigation has also been done with sinewave excitation, employing different winding configurations, slot/pole number combinations and rotor topologies. For 12-slot/8-

pole doubly salient synchronous reluctance machines (DSRMs), the best torque performance can be obtained by the fully-pitched winding, at low current. In addition, the single layer conventional and mutually-coupled DSRMs produce higher average torque while with lower torque ripple than their double layer counterparts, respectively. However, due to the onset of magnetic saturation, the performance of fully-pitched and single layer DSRMs deteriorates markedly with increasing phase RMS current, making them less attractive at high phase current. While with less sensitivity to magnetic saturation, the double layer mutually-coupled DSRM performs well at high current level, producing higher average torque than other machines. Moreover, the highest peak efficiency is obtained by double layer mutually-coupled DSRM. In addition, both the double layer DSRMs achieve their highest efficiency between 6000 and 8000rpm. The single layer DSRMs are suitable for middle speed applications over the range of 3000 to 4500 rpm. Fully-pitched DSRM obtains a more modest efficiency at lower speed around 2000rpm.

When compared with the SynRMs with angled and round flux barriers inside the rotor, and employed by both the 12-slot/8-pole and 12-slot/4-pole, it is found that the 12-slot/8-pole SynRMs with round flux barriers can produce the highest power factors, regardless of winding configurations. In addition, the power factors of double layer windings are higher than that of other winding configurations. Accordingly, appropriate rotor topologies can be selected for specific windings and slot/pole number combinations, according to the torque performance at different current levels. Moreover, with appropriate rotor topology, it has been found that the fully-pitched winding is the most appropriate for the 12-slot/4-pole machines, while the double layer mutually-coupled winding is the best for the 12-slot/8-pole machines.

Furthermore, analytical modelling has been developed to distinguish the single/double layer conventional and mutually-coupled winding configurations and to achieve a better understanding of the nature of the DSRMs. According to the MMF model, it is found that the working harmonic orders of mutually-coupled windings are doubled than that of the conventional windings. In addition, the harmonic orders of the double layer machines are doubled than that of the single layer ones. As a result, the contribution of airgap field harmonics to average torque and torque ripple has been obtained. It is found that the dominant MMF harmonics with positive rotating speed (forward rotating) produce positive torque. However, the dominant MMF harmonics with backward rotating produce negative torque.

7.2 FUTURE WORK

Several research works have been done for the novel DSRMs in this thesis. However, for completeness, there are still some works to be done in the future, which include but not limit to:

- The influence of machine topologies with double/single layer conventional and mutually-coupled winding configurations on unbalance magnetic force at the presence of rotor eccentricity.
- External rotor DSRMs with different winding configurations and excitation methods.
- Investigation of vibration and acoustic noise on modular SRMs with different winding configurations and conduction angles.
- Thermal analysis of modular SRMs with different winding configurations, slot/pole combinations and conduction angles.
- Investigation of novel DSRMs with DC field excitation for higher torque density.
- Torque capability enhancement by reducing the MMF harmonics which contribute to negative torque through advanced control strategies such as harmonic current injections.

REFERENCES

[1] R. Jarvis, "Davidson's Locomotive: how did he do it?," *Engineering Science & Education Journal,* vol. 5, no. 6, pp. 281-288, 1996.

[2] P. J. Lawrenson, J. M. Stephenson, P. T. Blenkinsop, J. Corda and N. N. Fulton, "Variable-speed switched reluctance motors," *IEE Proc. B- Elec. Power Appl.,* vol. 127, no. 4, pp. 253-265, Jul. 1980.

[3] T. J. E. Miller, "Optimal design of switched reluctance motors," *IEEE Trans. Ind. Electron.,* vol. 49, no. 1, pp. 15-27, Feb. 2002.

[4] H. Lin, T. S. Low and S. X. Chen, "Investigation on magnetic saturation in switched reluctance motor using 2D hybrid finite element method," *IEEE Trans. Magn.,* vol. 32, no. 5, pp. 4317-4319, Sep. 1996.

[5] P. J. Lawrenson, "Development and application of reluctance motors," *Proc. Electron. Power,* vol. 11, no. 6, pp. 195-198, Jun. 1965.

[6] G. J. Li, J. Ojeda, E. Hoang, M. Lecrivain and M. Gabsi, "Comparative studies between classical and mutually coupled switched reluctance motors using thermal-electromagnetic analysis for driving cycles," *IEEE Trans. Magn.,* vol. 47, no. 4, pp. 839-847, Apr. 2011.

[7] F. L. M. d. Santos, J. Anthonis, F. Naclerio, J. J. C. Gyselinck, H. V. d. Auweraer and L. C. S. Goes, "Multiphysics NVH modeling: simulation of a switched reluctance motor for an electric vehicle," *IEEE Trans. Ind. Electron.,* vol. 61, no. 1, pp. 469-476, Jan. 2014.

[8] D. A. Torrey, X. M. Niu and E. J. Unkauf, "Analytical modelling of variable-reluctance machine magnetisation characteristics," *IEE Proc. Elec. Power Appl.,* vol. 142, no. 1, pp. 14-22, Jan. 1995.

[9] D. E. Cameron, J. H. Lang and S. D. Umans, "The origin and reduction of acoustic noise in doubly salient variable-reluctance motors," *IEEE Trans. Ind. Appl.,* vol. 28, pp. 1250-1255, Nov./Dec. 1992.

[10] C. Wei, P. Pillay, Z. J. Tang and A. M. Omekanda , “Low-vibration design of switched reluctance motors for automotive applications using modal analysis,” *IEEE Trans. Ind. Appl.,* vol. 39, no. 4, pp. 971-977, Jul./ Aug. 2003.

[11] X. B. Liang, G. J. Li, J. Ojeda, M. Gabsi and Z. X. Ren, “Comparative study of classical and mutually coupled switched reluctance motors using multiphysics finite-element modeling,” *IEEE Trans. Ind. Electron.,* vol. 61, no. 9, pp. 5066-5074, Oct. 2013.

[12] S. A. Long, Z. Q. Zhu and D. Howe, “Effectiveness of active noise and vibration cancellation for switched reluctance machines operating under alternative control strategies,” *IEEE Trans. Energy Convers.,* vol. 20, no. 4, pp. 792-801, Dec. 2005.

[13] D. A. Staton, W. L. Soong and T. J. E. Miler, “Unified theory of torque production in switched reluctance and synchronous reluctance motors,” *IEEE Trans. Ind. Appl.,* vol. 31, no. 2, pp. 329-337, Mar./Apr. 1995.

[14] H. Y. Yang, Y. C. Lim and H. C. Kim, “Acoustic noise/ vibration reduction of a single-phase SRM using skewed stator and rotor,” *IEEE Trans. Ind. Electron.,* vol. 60, no. 10, pp. 4292-4300, Oct. 2013.

[15] J. W. Ahn, S. J. Park and D. H. Lee, “Hybrid excitation of SRM for reduction of vibration and acoustic noise,” *IEEE Trans. Ind. Electron.,* vol. 51, no. 2, pp. 374-380, Apr. 2004.

[16] C. Y. Wu and C. Pollock, “Analysis and reduction of vibration and acoustic noise in the switched reluctance drive,” *IEEE Trans. Ind. Appl.,* vol. 31, no. 1, pp. 91-98, Jan./Feb. 1995.

[17] X. Ojeda, X. Mininger, H. B. Ahmed, M. Gabsi and M. Lecrivain, “Piezoelectric actuator design and placement for switched reluctance motors active dampling,” *IEEE Trans. Energy Convers.,* vol. 24, no. 2, pp. 305-313, Jun. 2009.

[18] X. Mininger, N. Galopin, X. Ojeda, F. Bouillault and M. Gabsi, “Modeling of magnetoelastic and piezoelectric coupling: Application to SRM noise damping,” *IEEE Trans. Magn.,* vol. 45, no. 3, pp. 1218-1221, Mar. 2009.

[19] B. C. Mecrow, “Fully pitched-winding switched reluctance and stepping-motor arrangements,” *IEE Proc. B- Elec. Power Appl.,* vol. 40, no. 1, pp. 61-70, Jan. 1993.

[20] J. W. Ahn, S. G. Oh, J. W. Moon and Y. M. Hwang, “A three-phase switched reluctance motor with two-phase excitation,” *IEEE Trans. Ind. Appl.,* vol. 35, no. 5, pp. 1067-1075, Sep./Oct. 1999.

[21] G. J. Li, J. Ojeda, S. Hlioui, E. Hoang, M. Lecrivain and M. Gabsi, "Modification in rotor pole geometry of mutually coupled switched reluctance machine for torque ripple mitigating," *IEEE Trans. Magn.,* vol. 48, no. 6, pp. 2025-2034, Jun. 2012.

[22] X. Y. Ma, G. J. Li, G. Jewell and Z. Q. Zhu, "Comparative study of short-pitched and fully-pitched SRMs supplied by sine wave currents," in *ICIT15*, Sevilla, Spain, Mar. 17-19, 2015.

[23] T. J. E. Miller, Brushless permanent-magnet and reluctance motor drives, New York: Oxford university press, 1989.

[24] P. C. Desai, M. Krishnamurthy, N. Schofield and A. Emadi, "Novel switched reluctance machine configuration with higher number of rotor pole than stator poles: concept to implementation," *IEEE Trans. Ind. Electron.,* vol. 57, no. 2, pp. 649-659, Oct. 2009.

[25] G. E. Horst, "Redundant switched reluctance motor". U. S. Patent 5 239 217, 24 Aug. 1993.

[26] R. R. Kalpathi, N. Liu, S. E. Blackburn and S. F. Kolomeitsev, "Method and apparatus of reducing acoustic noise in switched reluctance electric motor". U. S. Patent 5 973 462, 26 Oct. 1999.

[27] T. Heese and M. Heidrich, "Reluctance motor electric machine". U. S. Patent 6 194 805, 27 Feb. 2001.

[28] T. J. E. Miller, "Switched reluctance motors and their control," Oxford, Magna phsics publishing and clarendon press, 1999, pp. 25-44.

[29] X. Deng, B. Mecrow, R. Martin and S. Gadoue, "Effects of winding connection on performance of a six-phase switched reluctance machine," *IEEE Trans. Energy Convers.,* vol. 33, no. 1, pp. 166-178, Mar. 2018.

[30] X. Chen, J. Wang, V. I. Patel and P. Lazari, "A nine-phase 18-slot 14-pole interior permanent magnet machine with low space harmonics for electric vehicle applications," *IEEE Trans. Energy Convers.,* vol. 31, no. 3, pp. 860-871, Sept. 2016.

[31] B. Qu, J. Song, T. Liang and H. Zhang, "Mutual coupling and its effect on torque waveform of even number phase switched reluctance motor," in *ICEMS*, Wuhan, China, Oct. 17-20, 2008.

[32] S. Han, C. Liu, L. Zhang, G. Jun and S. Dai, “Mutual coupling and its effect on current and torque of six phases switched reluctance motor,” in *11th Int. Conf. EVER*, Monte Carlo, Monaco, Apr. 6-8, 2016.

[33] C. Lee, R. Krishnan and N. S. Lobo, “Novel two-phase switched reluctance machine using common-pole E-core structure: concept, analysis, and experimental verification,” *IEEE Trans. Ind. Appl.,* vol. 45, no. 2, pp. 703-711, Mar./Apr. 2009.

[34] M. Tanujaya, D. H. Lee and J. W. Ahn, “Characteristic analysis of a novel 6/5 C-core type three-phase switched reluctance motor,” in *ICEMS*, Beijing, China, Aug. 20-23, 2011.

[35] H. Eskandari and M. Mirsalim, “An improved 9/12 two phase E-core switched reluctance machine,” *IEEE Trans. Energy Convers.,* vol. 28, no. 4, pp. 951-958, Dec. 2013.

[36] C. Lee and R. Krishnan, “New design of a two-phase E-core switched reluctance machine by optimizing the magnetic structure for a specific application: concept, design, and analysis,” *IEEE Trans. Ind. Appl.,* vol. 45, no. 5, pp. 1804-1814, Sep./Oct. 2009.

[37] W. Ding, S. Yang and Y. Hu, “Development and investigation on segmented-stator hybrid-excitation switched reluctance machines with different rotor pole numbers,” *IEEE Trans. Ind. Electron.,* vol. 65, no. 5, pp. 3784-3794, May 2018.

[38] S. H. Mao and M. C. Tsai, “A novel switched reluctance motor with C-core stators,” *IEEE Trans. Magn.,* vol. 41, no. 12, pp. 4413-4420, Dec. 2005.

[39] W. Ding, Y. Hu and L. Wu, “Analysis and development of novel three-phase hybrid magnetic paths swtiched reluctance motors using modular and segmental structures for EV applications,” *IEEE Trans. Mechatron.,* vol. 20, no. 5, pp. 2437-2451, Oct. 2015.

[40] W. Ding, Y. Hu, T. Wang and S. Yang, “Comprehensive research of modular E-core stator hybrid-flux switched reluctance motors with segmented and nonsegmented rotors,” *IEEE Trans. Energy Convers.,* vol. 32, no. 1, pp. 382-393, Mar. 2017.

[41] P. J. Lawrenson and S. K. Gupta, “Developments in the performance and theory of segmental-rotor reluctance motors,” *Proc. IEE,* vol. 114, no. 5, pp. 645-653, May 1967.

[42] J. D. Widmer and B. C. Mecrow, “Optimized segmental rotor switched reluctance machines with a greater number of rotor segments than stator slots,” *IEEE Trans. Ind. Appl.,* vol. 49, no. 4, pp. 1491-1498, Jul./Aug. 2013.

[43] R. Vandana and B. G. Fernandes, “Design methodology for high-performance segmented rotor switched reluctance motors,” *IEEE Trans. Energy Convers.,* vol. 30, no. 1, pp. 11-21, Mar. 2015.

[44] A. Labak and N. C. Kar, “Outer rotor switched reluctance motor design for in-wheel drive of electric bus applications,” in *ICEM*, Marseille, France, Sep. 2-5, 2012.

[45] M. D. Hennen and R. W. D. Doncker, “Comparison of outer- and inner-rotor switched reluctance machines,” in *7th PEDS*, Bangkok, Thailand, Nov. 27-30, 2007.

[46] H. Chen and J. J. Gu, “Switched reluctance motor drive with external rotor for fan in air conditioner,” *IEEE/ASME Trans. Mechatron.,* vol. 18, no. 5, pp. 1448 - 1458, Oct. 2013.

[47] H. Karim, N. Arbab, H. Torkaman and E. Afjei, “Performance analysis of an external rotor switched reluctance generator with minimum mutual flux,” in *POWERENG*, Malaga, Spain, May 11-13, 2011.

[48] J. Lin, N. Schofield and A. Emadi, “External-rotor 6-10 switched reluctance motor for an electric bicycle,” in *IECON*, Vienna, Austria, Nov. 10-13, 2013.

[49] J. Kolehmainen, “Synchronous reluctance motor with form blocked rotor,” *IEEE Trans. Energy Convers.,* vol. 25, no. 2, pp. 450-456, Jun. 2010.

[50] D. A. Staton, T. J. E. Miller and S. E. Wood, “Maximising the saliency ratio of the synchronous reluctance motor,” *IEE Proc. B- Elec. Power Appl.,* vol. 140, no. 4, pp. 249-259, Jul. 1993.

[51] J. Barta and C. Ondrusek, “Design and optimization of synchronous reluctance machine,” in *16th Int. Conf. Mechatron.*, Brno, Czech Republic, Dec. 3-5, 2014.

[52] F. Cupertino, G. Pellegrino, E. Armando and C. Gerada, “A SyR and IPM machine design methodology assisted by optimization algorithms,” in *ECCE*, Raleigh, NC, USA, 15-20 Sep., 2010.

[53] G. Pellegrino, F. Cupertino and C. Gerada, “Barriers shapes and minimum set of rotor parameters in the automated design of synchronous reluctance machines,” in *IEMDC*, Chicago, USA, May 12-15, 2013.

[54] K. Wang, Z. Q. Zhu, G.Ombach, M. Koch, S. Zhang and J. Xu, “Optimal slot/pole and flux-barrier layer number combinations for synchronous reluctance machines,” in *8th Int. Conf. EVER*, Monte Carlo, Monaco, Mar. 27-30, 2013.

[55] T. Matsuo and T. A. Lipo, "Rotor design optimization of synchronous reluctance machine," *IEEE Trans. Energy Convers.,* vol. 9, no. 2, pp. 359-365, Jun. 1994.

[56] R. R. Moghaddam and F. Gyllensten, "Novel high-performance SynRM design method: an easy approach for a complicated rotor topology," *IEEE Trans. Ind. Electron.,* vol. 61, no. 9, pp. 5058-5065, Jun. 2013.

[57] P. B. Reddy, A. M. El-Refaie, K. K. Huh, J. K. Tangudu and T. M. Jahns, "Comparison of interior and surface PM machines equipped with fractional-slot concentrated windings for hybrid traction applications," *IEEE Trans. Energy Convers.,* vol. 27, no. 3, pp. 593-602, May 2012.

[58] A. M. El-Refaie, T. M. Jahns and D. W. Novotny, "Analysis of surface permanent magnet machines with fractional-slot concentrated windings," *IEEE Trans. Energy Convers.,* vol. 21, no. 1, pp. 34-43, Feb. 2006.

[59] A. M. El-Refaie, "Fractional-slot concentrated-windings synchronous permanent magnet machines: opportunities and challenges," *IEEE Trans. Ind. Electron.,* vol. 57, no. 1, pp. 107-121, Sep. 2010.

[60] C. M. Spargo, B. C. Mecrow, J. D. Widmer and C. Morton, "Application of fractional-slot concentrated windings to synchronous reluctance motors," *IEEE Trans. Ind. Appl.,* vol. 51, no. 2, pp. 1446-1455, Jul. 2015.

[61] P. G. Barrass, B. C. Mecrow and A. C. Clothier, "Bipolar operation of fully-pitched winding switched reluctance drives," in *7th ICEMD*, Durham, UK, Sep. 11-13, 1995.

[62] B. C. Mecrow, "New winding configurations for doubly salient relutance machine," *IEEE Trans. Ind. Appl.,* vol. 32, no. 6, pp. 1348-1356, Dec. 1996.

[63] X. Ojeda, X. Mininger, M. Gabsi and M. Lecrivain, "Sinusoidal feeding for switched reluctance machine: application to vibration," in *18th ICEM*, Vilamoura, Portugal, Sep. 6-9, 2008.

[64] G. J. Li, X. Y. Ma, G. W. Jewell and Z. Q. Zhu, "Influence of conduction angles on single layer switched reluctance machines," *IEEE Trans. Magn.,* vol. 52, no. 12, pp. 1-11, Jul. 2016.

[65] F. Sahin, H. B. Ertan and K. Leblebicioglu, "Optimum geometry for torque ripple minimization of switched reluctance motors," *IEEE Trans. Energy Convers.,* vol. 15, no. 1, pp. 30-39, Mar. 2000.

[66] R. Mikail, I. Husain, Y. Sozer, M. S. Islam and T. Sebastian, "Torque-ripple minimization of switched reluctance machines through current profiling," *IEEE Trans. Ind. Appl.,* vol. 49, no. 3, pp. 1258-1267, Mar. 2013.

[67] R. Mikail, I. Husain, M. S. Islam, Y. Sozer and T. Sebastian, "Four-quadrant torque ripple minimization of switched reluctance machine through current profiling with mitigation of rotor eccentricity problem and sensor errors," *IEEE Trans. Ind. Appl.,* vol. 51, no. 3, pp. 2097-2104, May 2015.

[68] X. Liu, Z. Q. Zhu, M. Hasegawa, A. Pride and R. Deodhar, "Investigation of PWMs on vibration and noise in SRM with sinusoidal bipolar excitation," in *21st ISIE*, Hangzhou, China, May 28- 31, 2012.

[69] X. Liu, Z. Q. Zhu, M. Hasegawa, A. Pride, R. Deohar, T. Maruyama and Z. Q. Chen, "Performance comparison between unipolar and bipolar excitations in switched reluctance machine with sinusoidal and rectangular waveforms," in *ECCE*, Phoenix, AZ, USA, Sep. 17-22, 2011.

[70] G. J. Li, Z. Q. Zhu, X. Y. Ma and G. W. Jewell, "Comparative study of torque production in conventional and mutually coupled SRMs using frozen permeability," *IEEE Trans. Magn.,* vol. 52, no. 6, pp. 1-9, Jan. 2016.

[71] W. Hua, H. Hua, N. Dai, G. S. Zhao and M. Cheng, "Comparative study of switched reluctance machines with half-and full-teeth-wound windings," *IEEE Trans. Ind. Electron.,* vol. 63, no. 3, pp. 1414-1424, Feb. 2016.

[72] X. Y. Ma, G. J. Li, G. W. Jewell, Z. Q. Zhu and H. L. Zhan, "Performance comparison of doubly salient reluctance machine topologies supplied by sinewave currents," *IEEE Trans. Ind. Electron.,* vol. 63, no. 7, pp. 4086-4096, Mar. 2016.

[73] D. A. Staton, R. P. Deodhar, W. L. Soong and T. J. E. Miller, "Torque prediction using the flux-MMF diagram in AC, DC, and reluctance motors," *IEEE Trans. Ind. Appl.,* vol. 32, no. 1, pp. 180-188, Jan. 1996.

[74] Y. Hayashi and T. J. E. Miller, "A new approach to calculating core losses in the SRM," *IEEE Trans. Ind. Appl.,* vol. 31, no. 5, pp. 1039-1046, Sep./Oct. 1995.

[75] J. D. Lavers, P. P. Biringer and H. Hollitscher, "A simple method of estimating the minor loop hysteresis loss in thin laminations," *IEEE Trans. Magn.,* vol. 14, no. 5, pp. 386-388, Sep. 1978.

[76] P. N. Materu and R. Krishnan, "Estimation of switched reluctance motor losses," *IEEE Trans. Ind. Appl.,* vol. 28, no. 3, pp. 668-679, May/Jun. 1992.

[77] J. F. Liu, X. b. Zhang, H. J. Wang and J. F. Bao, "Iron loss characteristic for the novel bearingless switched reluctance motor," in *ICEM*, Busan, Korea, Oct. 26-29, 2013.

[78] S. D. Calverley, G. W. Jewell and R. J. Saunders, "Prediction and measurement of core losses in a high-speed switched-reluctance machine," *IEEE Trans. Magn.,* vol. 41, no. 11, pp. 4288-4298, Nov. 2005.

[79] G. J. Li, Z. Q. Zhu, W. Q. Chu, M. P. Foster and D. A. Stone, "Influence of flux gaps on electromagnetic performance of novel modular PM machines," *IEEE Trans. Energy Convers.,* vol. 29, no. 3, pp. 716-726, Sep. 2014.

[80] Z. Q. Zhu, "A simple method for measuring cogging torque in permanent magnet machines," in *PESGM*, Calgary, AB, Canada, Jul. 26-30, 2009.

[81] G. J. Li, X. Y. Ma, G. W. Jewell and Z. Q. Zhu, "Novel modular switched reluctance machines for performance improvement," *IEEE Trans. Energy Convers.,* Jan. 2018, (in press).

[82] E. Spooner, A. C. Williamson and G. Catto, "Modular design of permannet-magnet generators for wind turbines," *IEE Proc.- Elec. Power Appl.,* vol. 143, no. 5, pp. 388-395, Sep. 1996.

[83] S. P. Nikam and B. G. Fernandes, "Design of soft magnetic composite based modular four phase SRM for electirc vehicle application," in *ICEM*, Berlin, Germany, Sep. 2-5, 2014.

[84] N. R. Garrigan, W. L. Soong, C. M. Stephens, A. Storace and T. A. Lipo, "Radial force characteristics of a switched reluctance machine," in *IEEE Ind. Appl. Conf., 34th IAS Annual Meeting*, Phoenix, AZ, USA, Oct. 3-7, 1999.

[85] R. R. Moghaddam, F. Magnussen and C. Sadarangani, "Theoretical and experimental reevaluation of synchronous reluctance machine," *IEEE Trans. Ind. Electron.,* vol. 57, no. 1, pp. 6-13, Jan. 2010.

[86] A. Vagati, M. Pastorelli, G. Francheschini and S. C. Petrache, "Design of low-torque-ripple synchronous reluctance motors," *IEEE Trans. Ind. Appl.,* vol. 34, no. 4, pp. 758-765, Jul./Aug. 1998.

[87] G. Qi, J. T. Chen, Z. Q. Zhu, D. Howe, L. B. Zhou and C. L. Gu, "Influence of skew and cross-coupling on flux-weakening performance of permanent-magnet brushless AC machines," *IEEE Trans. Magn.,* vol. 45, no. 5, pp. 2110-2117, May 2009.

[88] T. A. Lipo, "Synchronous reluctance machines- a viable alternative for AC drives?," Electric Machines and Power Systems, Madison, USA, Nov. 1991.

[89] Q. Yu, B. Bilgin and A. Emadi, "Loss and efficiency analysis of switched reluctance machines using a new calculation method," *IEEE Tran. Ind. Electron.,* vol. 62, no. 5, pp. 3072-3080, May, 2015.

[90] W. L. Soong and T. J. E. Miller, "Field-weakening performance of brushless synchronous AC motor drives," *IEE Proc.- Elec. Power Appl.,* vol. 141, no. 6, pp. 331-340, Nov. 1994.

[91] J. Pyrhonen, T. Jokinen and V. Hrabovcova, Design of rotating electrical machines, Chichester, UK: John Wiley & Sons, 2008.

[92] T. S. Kwon and S. K. Sul, "Novel anti-windup of a current regular of a surface-mounted permanent-magnet motor for flux-weakening control," *IEEE Trans. Ind. Appl.,* vol. 42, no. 5, pp. 1293-1300, Sep./Oct. 2006.

[93] X. Y. Ma, G. J. Li, Z. Q. Zhu, G. W. Jewell and J. Green, "Investigation on synchronous reluctance machines with different rotor topologies and winding configurations," *IET Elec. Power Appl.,* vol. 12, no. 1, pp. 45-53, Jan. 2018.

[94] J. O. Fiedler, K. A. Kasper and R. W. D. Doncker, "Calculation of the acoustic noise spectrum of SRM using modal superposition," *IEEE Trans. Ind. Electron.,* vol. 57, no. 9, pp. 2939-2945, Mar. 2010.

[95] Z. Q. Zhu, X. Liu and Z. Pan, "Analytical model for predicting maximum reduction levels of vibration and noise in switched reluctance machine by active vibration cancellation," *IEEE Trans. Energy Convers.,* vol. 26, no. 1, pp. 36-45, Dec. 2010.

[96] N. Bianchi, H. Mahmoud and S. Bolognani, "Fast synthesis of permanent magnet assisted synchronous reluctance motors," *IET Elec. Power Appl.,* vol. 10, no. 5, pp. 312-318, Jun. 2016.

[97] Y. Guan, Z. Q. Zhu, I. A. A. Afinowi, J. C. Mipo and P. Farah, "Design of synchronous reluctance and permanent magnet synchronous reluctance machines for electric vehicle application," in *17th ICEMS*, Hangzhou, China, Oct. 22-25, 2014.

[98] X. Y. Ma, G. J. Li, G. W. Jewell and Z. Q. Zhu, "Quantitative analysis of contribution of air-gap field harmonics to torque production in three-phase 12-slot/8-pole doubly salient synchronous reluctance machines," *IEEE Trans. Magn.,* vol. 54, no. 9, pp. 1-11, Jul. 2018.

[99] Z. Q. Zhu and D. Howe, "Instantaneous magnetic field distribution in brushless permanent magnet dc motorss. III. effect of stator slotting," *IEEE Trans. Magn.,* vol. 29, no. 1, pp. 143-151, Jan. 1993.

[100] Z. Q. Zhu, L. Wu and Z. Xia, "An accurate subdomain model for magnetic field computation in slotted surface-mounted permanent-magnet," *IEEE Trans. Magn.,* vol. 47, no. 6, pp. 1100-1115, Apr. 2010.

[101] F. Dubas and C. Espanet, "Analytical solution of the magnetic field in permanent-magnet motors taking into account slotting effect: no-load," *IEEE Trans. Magn.,* vol. 45, no. 5, pp. 2097-2109, May 2009.

[102] Z. Q. Zhu and D. Howe, "Instantaneous magnetic field distribution in brushless permanent dc motors. II. armature reaction field.," *IEEE Trans. Magn.,* vol. 29, no. 1, pp. 136-142, Jan. 1993.

[103] T. Lubin, T. Hamiti, H. Razik and A. Rezzoug, "Comparison between finite-element analysis and winding function theory for inductances and torque calculation of a synchronous reluctance machine," *IEEE Trans. Magn.,* vol. 43, no. 8, pp. 3406-3410, Aug. 2007.

[104] G. Dajaku and D. Gerling, "Stator slotting effect on the magnetic field distribution of salient pole synchronous permanent-magnet machines," *IEEE Trans. Magn.,* vol. 46, no. 9, pp. 3676-3683, Sep. 2010.

[105] B. Gaussens, E. Hoang, O. d. l. Barriere, J. S. Michel, M. Lecrivain and M. Gabsi, "Analytical approach for air-gap modeling of field-excited flux-switching machine: no-load operation," *IEEE Trans. Magn.,* vol. 48, no. 9, pp. 2505-2517, Sep. 2012.

[106] B. Gaussens, E. Hoang, O. d. l. Barriere, J. S. Michel, P. Manfe, M. Lecrivain and M. Gabsi, "Analytical armature reaction field prediction in field-excited flux-switching machines using an exact relative permeance function," *IEEE Trans. Magn.,* vol. 49, no. 1, pp. 628-641, Aug. 2012.

[107] D. Zarko, D. Ban and T. A. Lipo, “Analytical calculation of magnetic field distribution in the slotted air gap of a surface permanent-magnet motor using complex relative air-gap permeance,” *IEEE Trans. Magn.,* vol. 42, no. 7, pp. 1828-1837, Jun. 2006.

APPENDIX

APPENDIX 1. PROTOTYPE BUILT

In order to validate the predictions, some prototypes have been built. Fig. I (a) shows the dimensional drawing of the 12-slot stator of the prototype SRMs/DSRMs. Fig. I (b) is the wound 12-slot stator of the SLC-SRM and SLMC-SRM. Fig. I (c) is the wound 12-slot stator of the DLC-SRM and DLMC-SRM. The two single/double layer SRMs can be realized with the same wound stator by reconnecting the coils as detailed in Fig. 2.3.

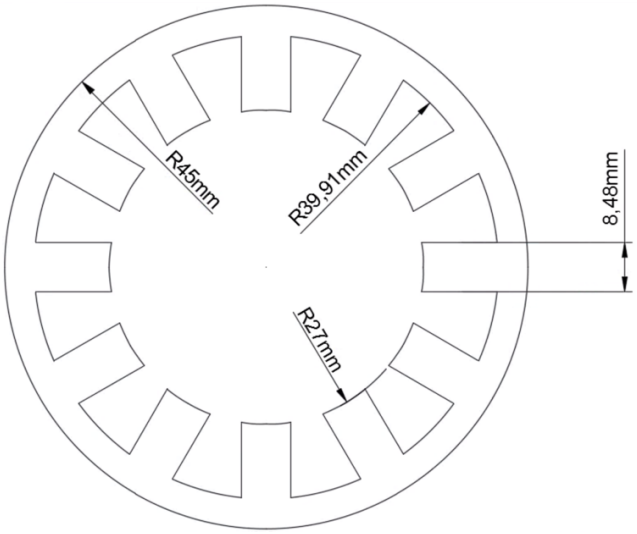

(a)

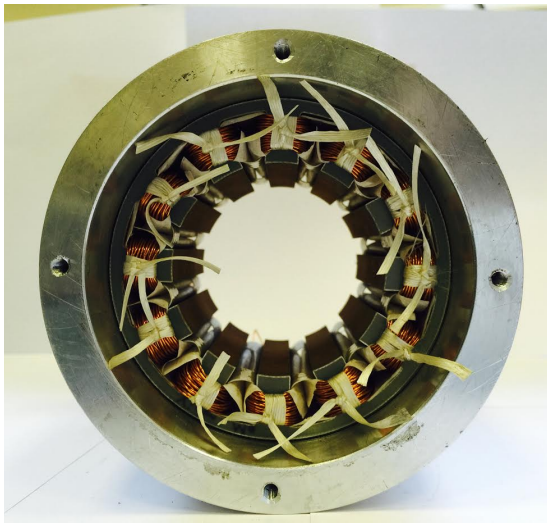

(b)

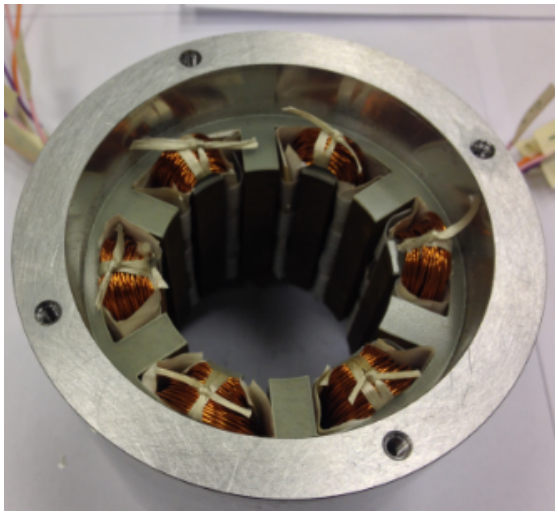

(c)

Fig. I. 12-slot stator of prototype SRMs/DSRMs. (a) Dimensional drawing, (b) DLC-DSRM or DLMC-DSRM stator, (c) SLC-DSRM or SLMC-DSRM stator.

Fig. II (a) shows the dimensional drawing of the 12-slot modular stator with FG=2mm and Fig. II (b) is the wound 12-slot modular stator of the prototype SRMs. Both the 8-pole and 14-pole rotors have been built, as shown in Fig. III and Fig. IV, respectively.

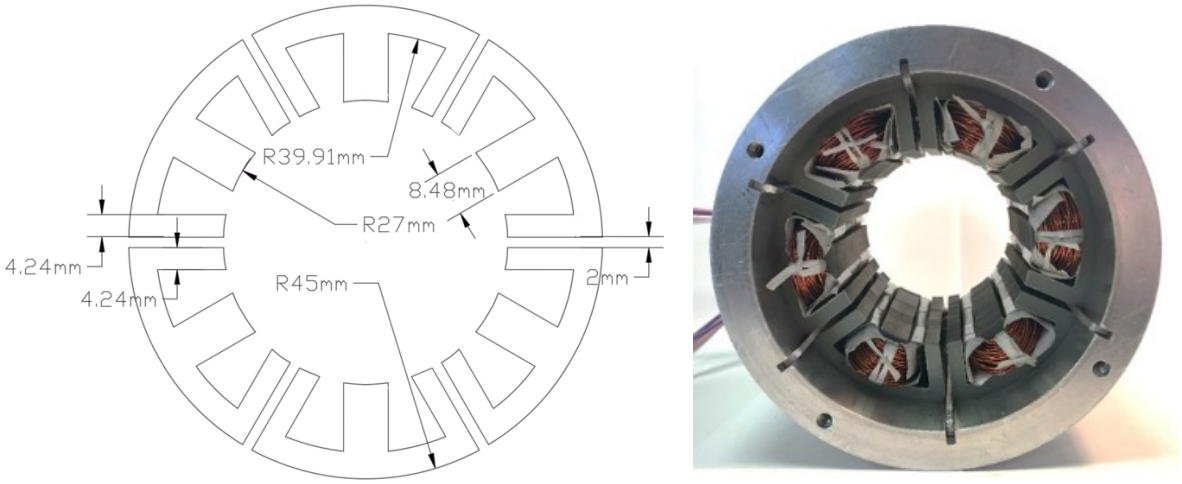

(a) (b)

Fig. II. 12-slot modular stator of prototype SRMs/DSRMs. (a) Dimensional drawing, (b) modular stator with FG=2mm.

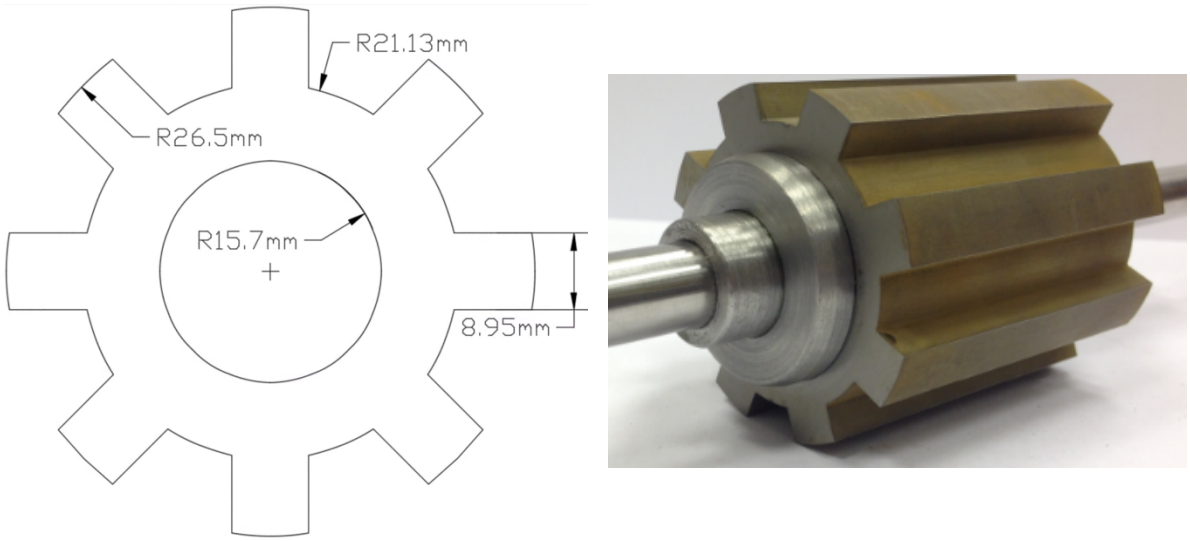

(a) (b)

Fig. III. 8-pole rotor of prototype SRMs/DSRMs. (a) Dimensional drawing, (b) 8-pole rotor.

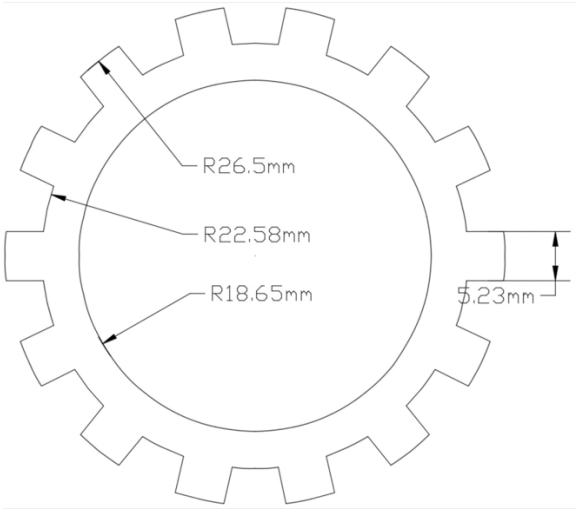

(a)

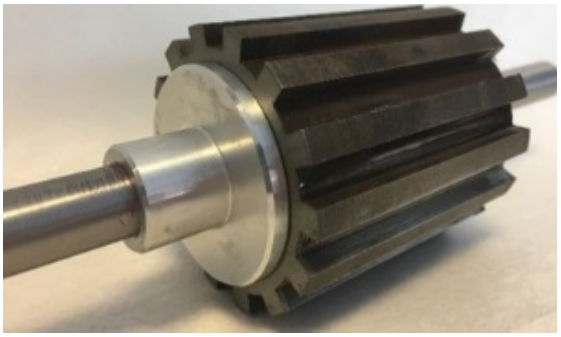

(b)

Fig. IV 14-pole rotor of prototype SRMs/DSRMs. (a) Dimensional drawing, (b) 14-pole rotor.

APPENDIX 2. SINGLE-PHASE AND 3-PHASE MMFS OF THE SLC

The winding arrangement of the SLC is similar to that of the DLC but with 2 coils per phase, and the coil magnetic polarities of the phase A of the SLC are NS. Therefore, its MMF against angular position θ, at t=0, can be calculated over a mechanical period, i.e. $[0, 2\pi]$:

$$MMF_a(\theta) = \begin{cases} \dfrac{2H\theta}{\beta_s\theta_s} & 0 \le \theta < \dfrac{\beta_s\theta_s}{2} \\ H & \dfrac{\beta_s\theta_s}{2} \le \theta < \theta_s(1-\dfrac{\beta_s}{2}) \\ \dfrac{-2H(\theta-\theta_s)}{\beta_s\theta_s} & \theta_s\left(1-\dfrac{\beta_s}{2}\right) \le \theta < \theta_s \\ 0 & \theta_s \le \theta < 6\theta_s \\ -\dfrac{2H(\theta-6\theta_s)}{\beta_s\theta_s} & 6\theta_s \le \theta < 6\theta_s + \dfrac{\beta_s\theta_s}{2} \\ -H & 6\theta_s + \dfrac{\beta_s\theta_s}{2} \le \theta < 7\theta_s - \dfrac{\beta_s\theta_s}{2} \\ \dfrac{-2H(\theta-7\theta_s)}{\beta_s\theta_s} & 7\theta_s - \dfrac{\beta_s\theta_s}{2} \le \theta < 7\theta_s \\ 0 & 7\theta_s \le \theta < 12\theta_s \end{cases} \quad \text{(I)}$$

Accordingly, () can be expanded into Fourier series over $[0, 2\pi]$ as

$$MMF_a(\theta, t=0) = \frac{2N_c I_{ph}}{\pi \beta_s \theta_s} \sum_{k=1}^{\infty} \frac{1}{k^2} \left(A_{a1,k} \sin(k\theta) + A_{a2,k} \cos(k\theta)\right) \quad \text{(II)}$$

where the coefficient $A_{a1,k}$ and $A_{a2,k}$ are shown in TABLE I and TABLE II, respectively. It can be found that the single-phase MMF of the SLC contains harmonic orders of 1, 3, 5, …, (2k-1), where k=1, 2, 3, … Accordingly, the magnitude of each harmonic in the single-phase MMF can be obtained.

TABLE I. COEFFICIENT $A_{a1,k}$ IN SINGLE-PHASE MMF OF THE SLC

$A_{a1,k}$	n
$(2-\sqrt{3})\sin(\frac{1}{2}n\beta_s\theta_s) + \cos\left(\frac{n\beta_s\theta_s}{2}\right) - 1$	$1+12(k-1)$
$2\sin(\frac{1}{2}n\beta_s\theta_s) + 2\cos\left(\frac{n\beta_s\theta_s}{2}\right) - 2$	$3+12(k-1)$
$(2+\sqrt{3})\sin(\frac{1}{2}n\beta_s\theta_s) + \cos\left(\frac{n\beta_s\theta_s}{2}\right) - 1$	$5+12(k-1)$
$(2+\sqrt{3})\sin(\frac{1}{2}n\beta_s\theta_s) - \cos\left(\frac{n\beta_s\theta_s}{2}\right) + 1$	$7+12(k-1)$
$2\sin(\frac{1}{2}n\beta_s\theta_s) - 2\cos\left(\frac{n\beta_s\theta_s}{2}\right) + 2$	$9+12(k-1)$
$(2-\sqrt{3})\sin(\frac{1}{2}n\beta_s\theta_s) - \cos\left(\frac{n\beta_s\theta_s}{2}\right) + 1$	$11+12(k-1)$

TABLE II. COEFFICIENT $A_{a2,k}$ IN SINGLE-PHASE MMF OF THE SLC

$A_{a2,k}$	n
$\sin(\frac{1}{2}n\beta_s\theta_s) + (2+\sqrt{3})[\cos\left(\frac{n\beta_s\theta_s}{2}\right) - 1]$	$1+12(k-1)$
$2\sin(\frac{1}{2}n\beta_s\theta_s) + 2\cos\left(\frac{n\beta_s\theta_s}{2}\right) - 2$	$3+12(k-1)$
$\sin(\frac{1}{2}n\beta_s\theta_s) + (2-\sqrt{3})[\cos\left(\frac{n\beta_s\theta_s}{2}\right) - 1]$	$5+12(k-1)$
$-\sin(\frac{1}{2}n\beta_s\theta_s) + (2-\sqrt{3})[\cos\left(\frac{n\beta_s\theta_s}{2}\right) - 1]$	$7+12(k-1)$
$-2\sin(\frac{1}{2}n\beta_s\theta_s) + 2\cos\left(\frac{n\beta_s\theta_s}{2}\right) - 2$	$9+12(k-1)$
$-\sin(\frac{1}{2}n\beta_s\theta_s) + (2+\sqrt{3})[\cos\left(\frac{n\beta_s\theta_s}{2}\right) - 1]$	$11+12(k-1)$

Supplied with 3-phase sinewave currents as shown in (6.6), the 3-phase MMF of the SLC can be calculated at different rotor positions as

$$MMF_{abc}(\theta,t)=\frac{3\sqrt{2}N_cI_{rms}}{\pi\beta_s\theta_s}\sum_{k=1}^{\infty}\frac{1}{k^2}(-A_{a1,k}\sin\beta_{a1}+A_{a2,k}\sin\beta_{a2}) \quad \text{(III)}$$

where

$$\beta_{a1}=\begin{cases}-n\theta+\omega t-\dfrac{\pi}{2} & n=1+6(k-1)\\ 0 & n=3+6(k-1)\\ n\theta+\omega t+\dfrac{\pi}{2} & n=5+6(k-1)\end{cases} \quad \text{(IV)}$$

and

$$\beta_{a2}=\begin{cases}-n\theta+\omega t & n=1+6(k-1)\\ 0 & n=3+6(k-1)\\ n\theta+\omega t & n=5+6(k-1)\end{cases} \quad \text{(V)}$$

APPENDIX 3. SINGLE-PHASE AND 3-PHASE MMFS OF THE SLMC

The winding arrangement of the SLMC is similar to that of the DLMC but with 2 coils per phase, and the coil magnetic polarities of the phase A of the SLC are NN. Therefore, its MMF against angular position θ, at t=0, can be calculated over a mechanical period, i.e. $[0, 2\pi]$

$$MMF_a(\theta)=\begin{cases}\dfrac{H}{2}-\delta_0 & 0\le\theta<\dfrac{\theta_s}{2}-\dfrac{\beta_s\theta_s}{2}\\ -\dfrac{H}{\beta_s\theta_s}(\theta-\theta_s)-\delta_0 & \dfrac{\theta_s}{2}-\dfrac{\beta_s\theta_s}{2}\le\theta<\dfrac{\theta_s}{2}+\dfrac{\beta_s\theta_s}{2}\\ -\dfrac{H}{2}-\delta_0 & \dfrac{\theta_s}{2}+\dfrac{\beta_s\theta_s}{2}\le\theta<\dfrac{11\theta_s}{2}-\dfrac{\beta_s\theta_s}{2}\\ \dfrac{H}{\beta_s\theta_s}(\theta-6\theta_s)-\delta_0 & \dfrac{11\theta_s}{2}-\dfrac{\beta_s\theta_s}{2}\le\theta<\dfrac{11\theta_s}{2}+\dfrac{\beta_s\theta_s}{2}\\ \dfrac{H}{2}-\delta_0 & \dfrac{11\theta_s}{2}+\dfrac{\beta_s\theta_s}{2}\le\theta<\dfrac{13\theta_s}{2}-\dfrac{\beta_s\theta_s}{2}\\ -\dfrac{H}{\beta_s\theta_s}(\theta-7\theta_s)-\delta_0 & \dfrac{13\theta_s}{2}-\dfrac{\beta_s\theta_s}{2}\le\theta<\dfrac{13\theta_s}{2}+\dfrac{\beta_s\theta_s}{2}\\ -\dfrac{H}{2}-\delta_0 & \dfrac{13\theta_s}{2}+\dfrac{\beta_s\theta_s}{2}\le\theta<\dfrac{23\theta_s}{2}-\dfrac{\beta_s\theta_s}{2}\\ \dfrac{H}{\beta_s\theta_s}(\theta-12\theta_s)-\delta_0 & \dfrac{23\theta_s}{2}-\dfrac{\beta_s\theta_s}{2}\le\theta<\dfrac{23\theta_s}{2}+\dfrac{\beta_s\theta_s}{2}\\ \dfrac{H}{2}-\delta_0 & \dfrac{23\theta_s}{2}+\dfrac{\beta_s\theta_s}{2}\le\theta<12\theta_s\end{cases} \quad \text{(VI)}$$

where

$$\delta_0=\frac{1}{T}\int_0^{12\theta_s}MMF_a\,(\theta,\delta_0=0)d\theta=-\frac{4\theta_sH}{12\theta_s}=-\frac{1}{3}H \quad \text{(VII)}$$

Accordingly, (VI) can be expanded into Fourier series over $[0,2\pi]$ as

$$MMF_a(\theta,t=0)=\frac{2N_cI_{ph}}{\pi\beta_s\theta_s}\sum_{k=1}^{\infty}\frac{1}{k^2}\left(B_{a,k}\cos(k\theta)\right) \quad \text{(VIII)}$$

where the coefficient $B_{a,k}$ is shown in TABLE IV. It can be found that the single-phase MMF of the SLMC contains harmonic orders of 2, 4, 6, …, (2k), where k=1, 2, 3, … Accordingly, the magnitude of each harmonic in the single-phase MMF can be obtained.

TABLE IV COEFFICIENT $B_{a,k}$ IN SINGLE-PHASE MMF OF THE SLMC

$B_{a,k}$	n
$2\sin(\frac{1}{2}n\beta_s\theta_s)$;	$2+24(k-1)$
$2\sqrt{3}\sin(\frac{1}{2}n\beta_s\theta_s)$	$4+24(k-1)$
$4\sin(\frac{1}{2}n\beta_s\theta_s)$	$6+24(k-1)$
$2\sqrt{3}\sin(\frac{1}{2}n\beta_s\theta_s)$	$8+24(k-1)$
$2\sin(\frac{1}{2}n\beta_s\theta_s)$	$10+24(k-1)$
$-2\sin(\frac{1}{2}n\beta_s\theta_s)$	$14+24(k-1)$
$-2\sqrt{3}\sin(\frac{1}{2}n\beta_s\theta_s)$	$16+24(k-1)$
$-4\sin(\frac{1}{2}n\beta_s\theta_s)$	$18+24(k-1)$
$-2\sqrt{3}\sin(\frac{1}{2}n\beta_s\theta_s)$	$20+24(k-1)$
$-2\sin(\frac{1}{2}n\beta_s\theta_s)$	$22+24(k-1)$

The 3-phase MMF of the SLMC can be calculated at different rotor positions as

$$MMF_{abc}(\theta,t)=\frac{3\sqrt{2}N_cI_{rms}}{\pi\beta_s\theta_s}\sum_{k=1}^{\infty}\frac{1}{k^2}(B_{a,k}\sin\beta_b) \tag{IX}$$

where

$$\beta_b=\begin{cases}n\theta+\omega t & n=2+6(k-1)\\ -n\theta+\omega t & n=4+6(k-1)\\ 0 & n=6+6(k-1)\end{cases} \tag{X}$$